

Dissertation zur Erlangung des Doktorgrades  
der Fakultät für Chemie und Pharmazie  
der Ludwig-Maximilians-Universität München

Morphology Control of Ordered Mesoporous Carbons  
for High Capacity Lithium Sulfur Batteries



**Jörg David Schuster**

**aus**

**Marktoberdorf**

**2011**

## **ERKLÄRUNG**

Diese Dissertation wurde im Sinne von § 13 Abs. 3 bzw. 4 der Promotionsordnung vom 29. Januar 1998 (in der Fassung der sechsten Änderungssatzung vom 16. August 2010) von Herrn Prof. Dr. Thomas Bein von der Fakultät für Chemie und Pharmazie betreut.

## **EHRENWÖRTLICHE VERSICHERUNG**

Diese Dissertation wurde selbständig, ohne unerlaubte Hilfe erarbeitet.

München, den 13.05.2011

.....

(Unterschrift des Autors)

Dissertation eingereicht am 13.05.2011

1. Gutachter: Prof. Dr. Thomas Bein
2. Gutachter: Prof. Dr. Christina Scheu

**Mündliche Prüfung am 07.06.2011**

## DANKSAGUNG

Zuallererst möchte ich mich natürlich bei meinem Doktorvater Prof. Thomas Bein bedanken. In seinem Arbeitskreis durfte ich die Welt der porösen Materialien kennen lernen, wobei er ein interessantes Forschungsthema von mir erkunden ließ, mich dabei immer mit neuen Ideen versorgte, mir aber auch die Freiheit ließ eigene Ideen zu verwirklichen. Dabei konnte ich von der exzellenten Ausstattung des Arbeitskreises profitieren, (der „Gerätepark“ sucht wahrscheinlich seinesgleichen), ich durfte für Untersuchungen mehrfach ans Synchrotron nach Triest fahren und meine Ergebnisse unter anderem in Erlangen, Varna (Bulgarien), Paris und San Francisco präsentieren. Besonderer Dank gilt auch Johannes Kobler. Er betreute mich zu Beginn meiner „Karriere“ im AK Bein, die bereits im Oktober 2005 mit einem Praktikum ihren Anfang nahm. Dabei fand ich nicht nur Gefallen am Forschungsgebiet sondern durfte auch einige meiner zukünftigen Kollegen kennen lernen. Johannes und ebenjene Kollegen überzeugten mich nicht nur durch kompetente Hilfe, sondern auch durch das positive Arbeitsklima, auch meine Masterarbeit im AK Bein durchzuführen. Bei den wöchentlichen Stammtischen war das Klima natürlich besonders positiv und auch kulinarische Bedürfnisse wurden zufrieden gestellt. In meiner Masterarbeit begann ich dann mit meinem aktuellen Forschungsthema, der Erforschung von mesoporösem Kohlenstoff, das dann in meiner Doktorarbeit vertieft wurde. Bedanken möchte ich mich hierbei bei den Mitgliedern meiner Subgroup, Ralf Köhn, Andreas Keilbach und Markus Döblinger, von denen ich in diesen vier Jahren sehr viel lernen konnte. Sie konnten mir stets helfen bei Fragen zur Synthese und Untersuchung meiner Proben und auch bei der Präsentation und Veröffentlichung meiner Ergebnisse. Besonders erfolgreich war die Anwendung meiner Kohlenstoff-Proben in Lithium-Schwefel-Batterien. Für die erfolgreiche Kooperation bei diesem Projekt möchte ich mich bei Prof. Linda Nazar und Guang He bedanken. Neue Erkenntnisse über die Strukturbildung der mesoporösen Kohlenstoffe bekam ich bei

Untersuchungen am Synchrotron in Triest. Für die hervorragende Betreuung an der „SAXS beamline“ und auch außerhalb möchte ich mich bei Heinz Amenitsch bedanken. Entscheidend für meine erfolgreiche Promotion war aber nicht zuletzt, dass ich immer gern zur Arbeit ging und dabei hatten meine Kollegen einen großen Anteil, von denen einige gute Freunde wurden. Besonders mit meinen Bürokollegen Axel Schlossbauer, Mirjam Dogru, Johann Szeifert und Andreas Keilbach konnte man gut auskommen und auch mal über andere Sachen als Chemie reden. Viel Spaß hatte ich auch auf allen Konferenzen und Winterschools, sowohl mit den „alten“ Kollegen, Hendrik, Johannes, Camilla, Monika, Johann oder Valentina, oder auch den „Jungen“, Benni, Basti, Christian, Hans, Norma, Flo Auras oder Flo Hinterholzinger. Eine große Hilfe und willkommene Abwechslung (und manchmal auch eine Herausforderung) waren auch meine zahlreichen Praktikanten, bzw. mein Masterand. Yizhen, Thilo, Christoph, Teresa, Jiadong, Rachel, Erik und Fabian erzielten tolle Ergebnisse die zum Teil auch veröffentlicht wurden. Ihnen wünsche ich weiterhin viel Glück, besonders Fabian, der mittlerweile seine Doktorarbeit im AK Bein begonnen hat. Großer Dank gilt auch unseren ständigen Mitarbeitern, Regina Huber, Tina Reuther und Steffen Schmidt, die die Konstanten im AK Bein darstellen und ohne die nix geht. Bei allen anderen im AK Bein die ich jetzt nicht namentlich genannt habe möchte ich mich natürlich auch bedanken, ihr habt stets für ein gutes Arbeitsklima gesorgt.

Ich möchte mich auch bei meinen Freunden außerhalb der Uni bedanken. Besonders mein Bruder Martin, aber auch Gregor Rossmanith, Jan Rothballer, Florian Forstmaier und der Rest vom SV Helios Daglfing sorgten für den sportlichen Ausgleich u.a. beim Fußball (spielen und schauen) und beim Erklimmen der höchsten Alpenpässe mit dem Rennrad. Wichtig ist für mich auch das gute Verhältnis zu meinen beiden Geschwistern Martin und Sonja mit denen ich auch mal in Urlauben ausspannen konnte (z.B. in Goa).

Für den seelischen Ausgleich sorgt seit zwei Jahren meine Freundin Simone (auch wenn sie wegen dieser Zeilen einen Abend auf mich verzichten muss). Besonders in der (stressigen) Endphase ist das sehr wichtig für mich.

Der größte Dank gilt allerdings meinen Eltern Heinz und Irmtraud Schuster, ohne deren stete Motivation und Förderung meine Ausbildung nicht möglich gewesen wäre. Sie haben mich immer unterstützt und mir die Freiheit gelassen meinen Beruf zu wählen und meine Ausbildung zu gestalten.

## ABSTRACT

The focus of this thesis concerns the morphology control of ordered mesoporous carbon (OMC) materials. Ordered mesoporous carbons with diverse morphologies, that are thin films, fibers – embedded in anodic alumina membranes and free-standing – or spherical nanoparticles, have been successfully prepared by soft-templating procedures. The mechanisms of structure formation and processing were investigated with *in-situ* SAXS measurements and their application in high capacity lithium-sulfur batteries was successfully tested in cooperation with Guang He and Linda Nazar from the University of Waterloo in Canada. The Li-S batteries receive increasing attention due to their high theoretical energy density which is 3 to 5 times higher than from lithium-ion batteries. For this type of battery the specific pore volume is crucial for the content of the active component (sulfur) in the cathode and therefore correlates with the capacity and gravimetric energy density of the battery.

At first, mesoporous thin films with 2D-hexagonal structure were obtained through organic-organic self-assembly of a preformed oligomeric resol precursor and the triblock copolymer template Pluronic P123. The formation of a condensed-wall material through thermopolymerization of the precursor oligomers resulted in mesostructured phenolic resin films. Subsequent decomposition of the surfactant and partial carbonization were achieved through thermal treatment in inert atmosphere. The films were crack-free with tunable homogenous thicknesses, and showed either 2D-hexagonal or lamellar mesostructure. An additional, yet unknown 3D-mesostructure was also found.

In the second part, cubic and circular hexagonal mesoporous carbon phases in the confined environment of tubular anodic alumina membrane (AAM) pores were obtained by self-

assembly of the mentioned resol precursor and the triblock copolymer templates Pluronic F127 or P123, respectively. Casting and solvent-evaporation were also followed by thermopolymerization, thermal decomposition of the surfactant and carbonization through thermal treatment at temperatures up to 1000 °C in an inert atmosphere. For both structures the AAM pores were completely filled and no shrinkage was observed, due to strong adhesion of the carbon wall material to the AAM pore walls. As a consequence of this restricted shrinkage effect, the mesophase system stayed almost constant even after thermal treatment at 1000 °C, and pore sizes of up to 20 nm were obtained.

In the third part, the aforementioned mesoporous films and embedded fibers in AAMs were further investigated concerning structure formation and carbonization in an *in-situ* SAXS study. The *in-situ* measurements revealed that for both systems the structure formation occurs during the thermopolymerization step. Therefore the process of structure formation differs significantly from the known evaporation-induced self-assembly (EISA) and may rather be viewed as thermally-induced self-assembly. As a result, the structural evolution strongly depends on the chosen temperature, which controls both the rate of the mesostructure formation and the spatial dimensions of the resulting mesophase.

In the fourth part the syntheses recipes for AAMs were applied on a presynthesized silica template for synthesis of freestanding mesoporous carbon nanofibers. The syntheses start with casting of carbon nanofibers with a silica precursor solution leading to a porous silica template after calcination with tubular pores mimicking the initial carbon nanofibers. A synthesis concept using triconstituent coassembly of resol, tetraethylorthosilicate as additional silica precursor and Pluronic F127 was applied here. The silica from the additional precursor was found to be beneficial, due to reduced shrinkage and created additional porosity after etching it. Those OMC nanofibers therefore exhibited a very large surface area and a high pore volume of 2486 m<sup>2</sup>/g and 2.06 cm<sup>3</sup>/g, respectively. Due to their extremely high porosity

values, those fibers were successfully applied as sulfur host and electrode material in lithium-sulfur batteries.

The fifth and last part focuses on the synthesis of spherical mesoporous carbon nanoparticles. Therefore the triconstituent coassembly was applied on a silica template with spherical pores, which was derived from the opal structure of colloidal crystals made from 400 nm PMMA spheres. The spherical ordered mesoporous carbon nanoparticles feature extremely high inner porosity of 2.32 cm<sup>3</sup>/g and 2445 m<sup>2</sup>/g, respectively. They were successfully applied as cathode material in Li-S batteries, where they showed high reversible capacity up to 1200 mAh/g and good cycle efficiency. The final product consists of spherical mesoporous carbon particles with a diameter of around 300 nm and 2D-hexagonal porosity. The particles could be completely separated by sonification to form stable colloidal suspensions. This could be the base for further applications such drug delivery.

## TABLE OF CONTENTS

Erklärung.....	ii
Ehrenwörtliche Versicherung.....	ii
Danksagung.....	iii
Abstract.....	vi
Table of Contents.....	ix
1. Introduction.....	1
1.1. Ordered Mesoporous Carbon Materials.....	2
1.2. Advances in Ordered Mesoporous Carbon Morphology Control.....	6
1.2.1. OMC Films.....	8
1.2.2. OMC Fibers Embedded in Anodic Alumina Membranes and Free Fibers.....	11
1.2.3. Spherical OMC Nanoparticles.....	15
1.3. Application as Sulfur Host and Electrode in Lithium Sulfur Batteries.....	19
1.4. Chapter References.....	22
2. Characterization Methods.....	26
2.1. X-Ray Scattering Techniques.....	26
2.1.1. One dimensional Small Angle X-Ray Scattering (1D-SAXS).....	28
2.1.2. 2D Small-Angle X-Ray Scattering (2D-SAXS).....	30
2.1.3. 2D Grazing Incidence Small Angle X-Ray Scattering (2D-GISAXS) <sup>51</sup> .....	32
2.2. Electron Microscopy <sup>54-55</sup> .....	34
2.2.1. Transmission Electron Microscopy (TEM).....	35
2.2.2. Scanning Electron Microscopy (SEM).....	39
2.3. Sorption Measurements.....	39
2.4. Ellipsometry.....	43
2.5. Dynamic Light Scattering (DLS).....	45
2.6. Infra-Red and Raman Spectroscopy.....	46
2.7. Chapter References.....	47
3. 2D-Hexagonal Periodic Mesoporous Polymer Resin Thin Films by Soft-Templating....	49
3.1. Introduction.....	50

3.2.	Experimental .....	54
3.3.	Results and Discussion .....	58
3.4.	Conclusions .....	71
3.5.	Chapter References.....	73
4.	Cubic and Hexagonal Mesoporous Carbon in the Pores of Anodic Alumina Membranes	75
4.1.	Introduction .....	76
4.2.	Results and Discussion .....	80
4.3.	Conclusion.....	91
4.4.	Experimental Section .....	91
4.5.	Chapter References.....	94
5.	<i>In Situ</i> SAXS Study on a New Mechanism for Mesostructure Formation of Ordered Mesoporous Carbons: Thermally-Induced Self-Assembly .....	97
5.1.	Introduction .....	98
5.2.	Experimental Section .....	100
5.3.	Results and Discussion.....	105
5.4.	Conclusions .....	118
5.5.	Chapter References.....	119
6.	Large Pore Ordered Mesoporous Carbon Nanofibers with Extremely High Porosity for Lithium-Sulfur Batteries .....	123
6.1.	Introduction .....	125
6.2.	Experimental Section .....	128
6.3.	Results and Discussion.....	131
6.4.	Conclusions .....	137
6.5.	Chapter References.....	137
7.	Spherical Ordered Mesoporous Carbon Nanoparticles with Extremely High Porosity for Lithium-Sulfur Batteries .....	140
7.1.	Introduction .....	141
7.2.	Experimental Section .....	143
7.3.	Results and Discussion.....	146
7.4.	Conclusions .....	151
7.5.	Chapter References.....	152

8. Conclusions and Outlook.....	154
9. Appendix.....	158
9.1. <i>In Situ</i> SAXS Study on a New Mechanism for Mesosstructure Formation of Ordered Mesoporous Carbons: Thermally-Induced Self-Assembly .....	158
10. Curriculum Vitae .....	178
11. List of Publications and Presentations .....	180
11.1. Publications .....	180
11.2. Oral Presentations.....	180
11.3. Poster Presentations.....	181
12. Bibliography .....	183



## 1. INTRODUCTION

Carbon is an outstanding element due to its diverse chemical properties, first of all the ability to form very long chains of interconnecting C-C bonds. This feature is the basis for organic chemistry and therefore a large field of industrial production and academic research.



**Figure 1.1:** Natural pure carbon materials: Diamond and Graphite.<sup>1</sup>

Despite the impact of organic compounds, “pure” carbon materials also have remarkable properties and are responsible for several records for material properties. When thinking about pure carbon, the two natural sources come to mind which are somewhat complementary in their properties: Diamond and graphite (Figure 1.1)

Diamond is the hardest material, transparent (with the highest refractive index), one of the best thermal conductors but an electrical insulator. On the other hand graphite is a soft material, highly light absorbing and therefore black, and it shows high electrical conductivity. Due to these properties, the applications of the two carbon allotropes are also diverse, diamonds are used as gemstones in jewelry or as abrasive (due to its hardness), graphite can be used as lubricant, for pencils or for electronic devices (due to its conductivity), e.g. as electrode material. Beside those two allotropes there are further forms of carbon such as nanotubes,<sup>2-3</sup> buckminsterfullerenes,<sup>4</sup> or graphene<sup>5</sup> which all exhibit remarkable new properties, the last two discoveries were even awarded with Nobel prizes (1996, 2010). Amorphous carbon on the other hand is not that famous but it is nonetheless a modification with a large number of industrial applications. Porous carbon materials are usually made of amorphous carbon having graphitic short range order. Not surprisingly, they can share some of the beneficial properties of graphite, including electrical conductivity as well as chemical and thermal stability. In addition, they have favorable qualities such as high specific surface areas and pore volumes and not least their unlimited availability. For these reasons they are employed extensively as electrode materials for batteries, supercapacitors and fuel cells, as sorbents for separation and gas storage, or as catalyst supports.

### **1.1. Ordered Mesoporous Carbon Materials**

Ordered mesoporous carbons (OMCs)<sup>6-8</sup> – i.e. carbon with a periodic arrangement of uniform mesopores – could offer advantages for several of these applications compared to traditional activated carbons, which typically consist of disordered microporous amorphous carbon. Possible advantages compared to the commonly applied activated microporous carbon are improved accessibility and mass transport due to large, continuous pores.

One of the first strategies for the synthesis of OMCs was the use of mesoporous silica, acting as hard template. An early example of periodic mesostructured carbon material was presented by Wu and Bein,<sup>9</sup> by filling the cylindrical mesopores of MCM-41 with polyacrylonitrile via radical polymerization, and subsequently creating conducting carbon nanowires through carbonization of the polymer. Ordered mesoporous carbon was first reported by Ryoo et al.<sup>10</sup>. They used the cubic mesoporous silica MCM-48 as hard template, sucrose as carbon precursor, and synthesized the carbon replica CMK-1 through pyrolysis of the included precursor. The silica template could be removed by etching with sodium hydroxide solution.

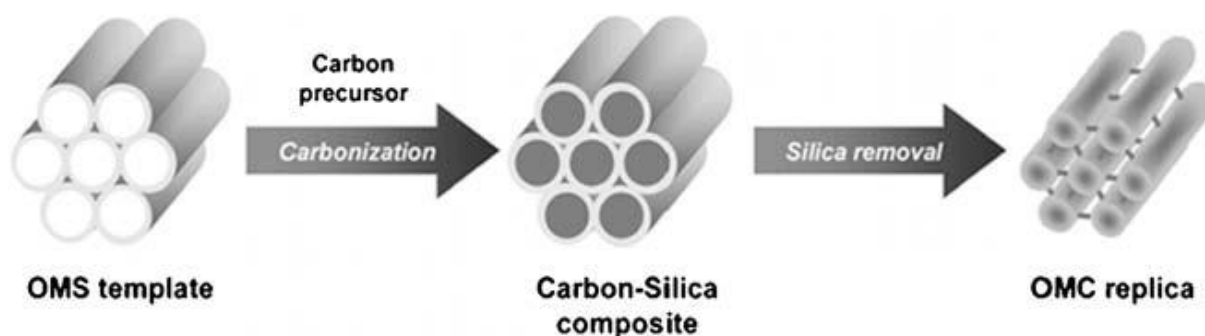


**Figure 1.2:** Illustration of the carbon synthesis by hard-templating<sup>8</sup> of an ordered mesoporous silica (OMS) template.

With this hard-templating method (Figure 1.2), also called nano-casting, various carbon mesostructures could be synthesized using silica templates with different symmetries, e.g. CMK-1<sup>10</sup> and SNU-1<sup>11</sup> as replicas of cubic MCM-48 or CMK-3<sup>12</sup> and CMK-5<sup>13</sup> from hexagonal SBA-15. Further work addressed the electronic and electrochemical properties of these materials<sup>9, 11, 14</sup> and their surface functionalization.<sup>15-18</sup>

A general drawback of hard-templating methods is the need for an inorganic template, and a process that involves several time-consuming and costly steps for the impregnation of the template, and selective etching of the silica with hydrofluoric acid or sodium hydroxide solution.

In contrast to hard templating methods, soft-templating strategies can directly produce the desired mesoporous carbon precursor structure. According to Liang et al.<sup>6</sup>, soft-templating approaches have four key requirements. They require (a) a polymerizable precursor system and (b) a suitable surfactant as structure-directing agent, which (c) sustains thermal treatments for curing the carbon yielding precursor but decomposes before or during carbonization. (d) The precursor system should form a stable polymeric wall material that can retain its mesostructure during template removal. Given these rather demanding requirements, it is not surprising that only a few systems have been reported so far for the synthesis of mesoporous carbon.

The first successful soft-templating approach towards mesoporous carbon was published in 1999 by Moriguchi et al.<sup>19</sup>. They synthesized organic mesophases of phenolic resin and cetyltrimethylammonium bromide (CTAB) acting as surfactant. However, the mesophases were not stable above 200 °C and thus no mesoporous carbon could be obtained. Thurn-Albrecht et al.<sup>20</sup> achieved the assembly of asymmetric large diblock copolymers of polystyrene (PS) and poly(methyl methacrylate) (PMMA) to form hexagonal mesostructured films, whose orientation could even be controlled with electric fields.

Liang et al.<sup>21</sup> achieved the self-assembly of a polystyrene-*b*-poly(4-vinylpyridine) block-copolymer (PS-*b*-P4VP) and resorcinol and formaldehyde as carbon sources, using a vapor infiltration method. Through a sequence of synthesis steps, they ultimately made mesoporous carbon thin films with hexagonally arranged 33 nm pores that were oriented normal to the surface.

In 2006, Meng et al.<sup>22</sup> introduced another promising soft-templating approach (Figure 1.3) by the self-assembly of a low-molecular-weight resol precursor and triblock copolymer templates with polyethylene and polypropylene blocks of variable lengths. The resol precursor is

synthesized according to a basic bakelite synthesis using phenol and formaldehyde as the educts.

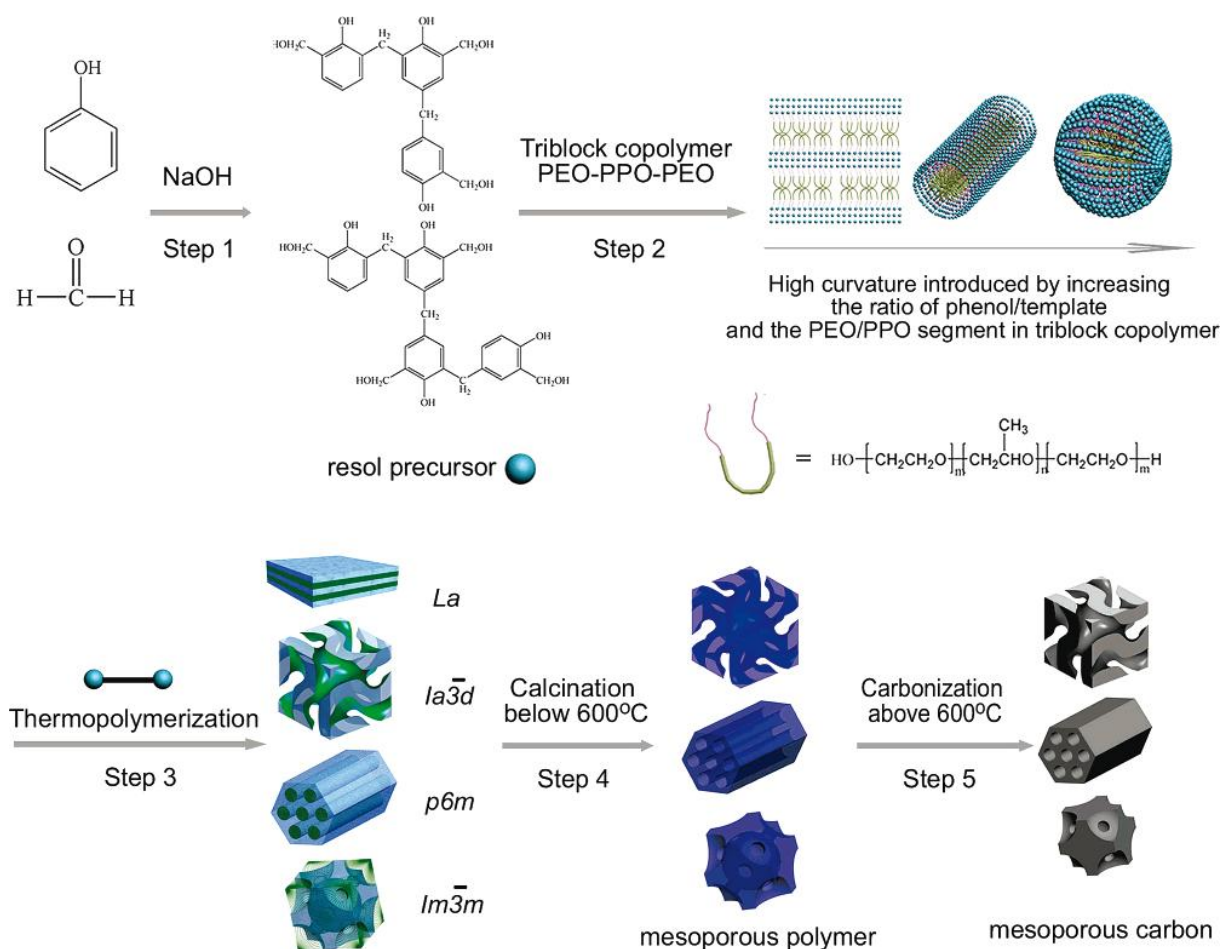


**Figure 1.3:** Synthesis of a low-molecular-weight resol precursor, self-assembly with block-copolymers, template removal and carbonization for different mesoporous systems.<sup>22</sup>

After thermopolymerization, template removal and carbonization Meng et al. obtained powders with two-dimensional hexagonal ( $p6m$ ), three-dimensional bicontinuous ( $Ia\bar{3}d$ ), body centered cubic ( $Im\bar{3}m$ ), and lamellar mesostructures. Thus mesoporous carbons with surface areas up to 1490 m<sup>2</sup>/g and thermal stability up to 1400 °C were realized.

Another effective approach<sup>23</sup> to produce OMCs with extremely high porosity is based on triconstituent self-assembly of resol as the carbon precursor, TEOS as the silica precursor and

the block copolymer Pluronic F127 as the structure directing agent. The whole process is illustrated in Figure 1.4.

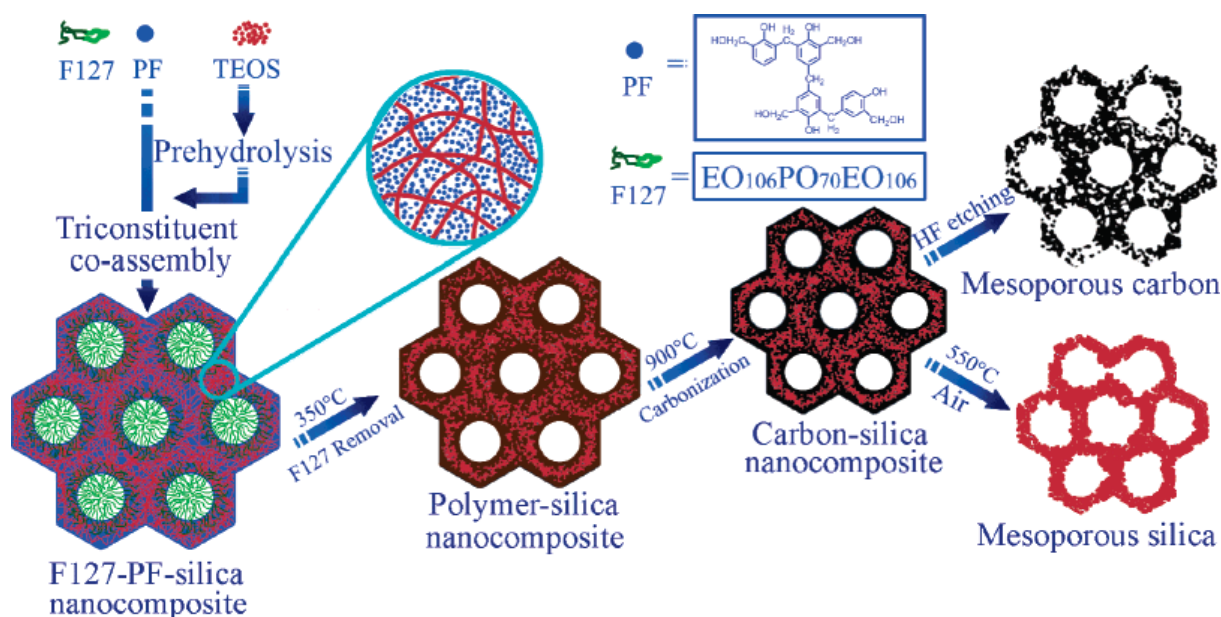


**Figure 1.4:** Triconstituent co-assembly to ordered mesoporous polymer-silica and carbon-silica nanocomposites, and the corresponding ordered mesoporous silica and carbon frameworks<sup>23</sup>

Carbonization is followed by etching of the silica in the carbon-silica nanocomposite with hydrofluoric acid. Through the silica in the walls, shrinkage during carbonization is reduced and additional porosity is produced by etching it, therefore mesoporous carbon with extremely high porosity above 2.0 cm<sup>3</sup>/g and 2000 m<sup>2</sup>/g, respectively is obtained.

## 1.2. Advances in Ordered Mesoporous Carbon Morphology Control

Great advances in the morphology control of ordered mesoporous carbons have been achieved in the past few years. A number of different morphologies have been successfully prepared or their properties were improved. However, various challenges, specific for the respective morphology, still remain.

Control of the OMC features in all three dimensions is challenging but critical for specific applications and the improvement of their properties, i.e., (i) the chemical composition and structure of the walls being decisive for the electronic properties and the reactivity, (ii) the mesoporous structure in terms of crystallographic symmetry, pore sizes, pore volumes and surface areas, and (iii) the OMC morphology, such as powders, thin films, nanofibers or nanoparticles, the latter two being decisive for molecular access to the pores. However, the optimization of one parameter often results in compromising other parameters. For example, high temperatures are needed for carbonization and good electrical conductivity but they can result in shrinkage or even collapse of the mesostructure.

The focus of this section concerns the recent advances in the synthesis of OMCs with controlled nano-morphologies, that is, thin films, filaments encapsulated within anodic alumina membrane pores, free nanofibers or spherical nanoparticles. Furthermore, the properties of OMC materials with respect to the aforementioned applications are discussed.

There are methods that are specific for selected morphologies, e.g., aerosol-based synthesis for spherical nanoparticles or electrospinning for nanofibers. However, for the majority of synthesis procedures, the 3D confinement in pre-synthesized porous templates is used to create the desired OMC-morphologies by evaporation-induced self-assembly (EISA) of precursor solutions. Consequently, the final OMC is a replica of the initial hard template. It turned out that 3D-confinements exhibit beneficial effects on the thermal stability and the shrinkage behavior of OMCs. As a main result from this restricted shrinkage effect, the OMCs exhibit larger pores, higher pore volumes and surface areas compared to bulk materials from the same precursor solutions.<sup>24-25</sup> The big advantage here is the applicability of recipes for bulk synthesis which are based on EISA processes.

### 1.2.1. OMC Films

OMC thin films with several structures have been reported so far. Usually mesoporous structures derived from polymers are called mesoporous carbon if they were carbonized at temperatures above 600 °C. Temperatures between 350 °C and 600 °C are sufficient to decompose the templates, and the resulting mesoporous structures are called mesoporous polymers or mesoporous polymer resins.<sup>22</sup> The reported films are either 2D-hexagonal with the pores perpendicular<sup>21</sup> or parallel<sup>26-27</sup> to the substrate or orthorhombic<sup>28</sup>. Apart from these stable porous films, films with lamellar structure<sup>26</sup> that did not survive template removal were synthesized. In general thin films are made by EISA of precursor solutions during spin- or dip-coating or simply by casting those solutions. The main challenge in the synthesis of thin films was found to be the low thermal stability compared to bulk powders. During template removal by pyrolysis of the surfactant and carbonization anisotropic shrinkage occurs, the films only shrink uniaxially perpendicular to the substrate because the other two dimensions are fixed if no cracking or delamination occurs. Therefore the initial structures are strongly distorted - usually the film thickness is decreasing up to 70 % even at moderate carbonization temperatures around 600 °C. The stress from this contraction can lead to the collapse of the mesostructure. The examples for OMC films that stand template removal and carbonization exhibit strongly distorted mesostructures and therefore elliptically shaped pores with reduced porosity.

The first mesoporous carbon thin films were realized by Liang et al.<sup>21</sup> using a vapor infiltration method. The mesoporous carbon thin films exhibited hexagonally arranged 33 nm pores oriented normal to the surface. A soft-templating pathway leading to thin films with face-centered orthorhombic (*Fmmm*) symmetry was reported by Tanaka et al.<sup>28</sup> Highly ordered mesoporous polymer resin thin films with a 2D-hexagonal order (*p6mm* shown in

Figure 1.5 left) made by a soft-templating method were reported by our group<sup>26</sup> and further investigated recently with *in-situ* GISAXS measurements during thermal treatments up to 1100 °C (Figure 1.5 right).

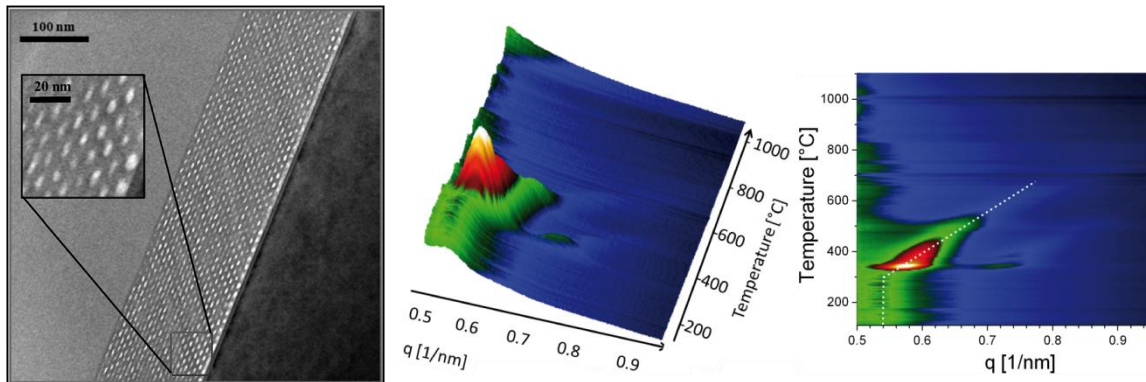


**Figure 1.5:** Left: TEM cross-section of a formerly 2D-hexagonal film after uniaxial shrinkage due to pyrolysis at 400 °C. Reproduced from Schuster et al.<sup>26</sup> Middle and Right: *In-situ* GISAXS measurement of the carbonization of this 2D-hexagonal film as plot of the carbonization temperature vs. radial integrated intensities. Shrinkage and intensity changes due to template removal and structural distortion are clearly visible.

In this study the structure formation and carbonization could be monitored *in-situ* for the 2D-hexagonal and in addition for orthorhombic thin films. The thin films were prepared by spin-coating a mixture of a preformed oligomeric resol precursor and a triblock copolymer template followed by thermopolymerization of the precursor oligomers. It was found that unlike in the case of mesostructured metal oxides (e.g. silica<sup>29</sup> or titania<sup>30</sup>) the structure formation for those systems does not occur during evaporation of the solvent (EISA) but during this thermopolymerization step and can therefore be called thermally-induced self-assembly. As a remarkable consequence, the mesostructure is still flexible and can be controlled in this step. An investigation of different thermopolymerization temperatures showed that higher temperatures result in increased unit cell parameters; it was also shown that the rate of the structure formation strongly depends on the thermopolymerization

temperature and on the block copolymer template. Template removal and carbonization were monitored up to 1100 °C, without total loss of structure. This surprisingly high thermal stability could be assigned to a faster ramp during carbonization. Nonetheless strong structural distortion was observed due to anisotropic shrinkage.

A study on thermal stability of 2D-hexagonal OMC thin films synthesized with the block copolymer templates Pluronic P123 and F127 was reported by Song and coworkers.<sup>27</sup> They found that the OMC films (or phenolic resin films, respectively at temperatures below 600 °C) made from different templates show differing thermal stabilities but identical crystallographic symmetry. The hexagonal films made with Pluronic F127 collapsed upon template removal by pyrolysis at 350 °C. In contrast, Pluronic P123 remained stable upon template removal at 350 °C and delivered well-ordered orthorhombic mesoporous films. The varying stabilities were assigned to different wall thicknesses – it was assumed that the thinner walls for F127 could not resist the uniaxial stress during shrinkage. In another study Song et al.<sup>31</sup> also studied carbon/silica composite thin films and the influence of the incorporated silica content on conductivity, porosity and structural distortion. This triconstitual approach already showed beneficial effects on shrinkage behavior and porosity for bulk powders.<sup>23</sup> The orthorhombic films (Figure 1.6) also showed reduced shrinkage during carbonization upon increased silica content. Whereas the pure carbon film exhibited shrinkage of 65 % after carbonization at 800 °C the films with the highest silica content (75 %) only showed shrinkage of 35 %.

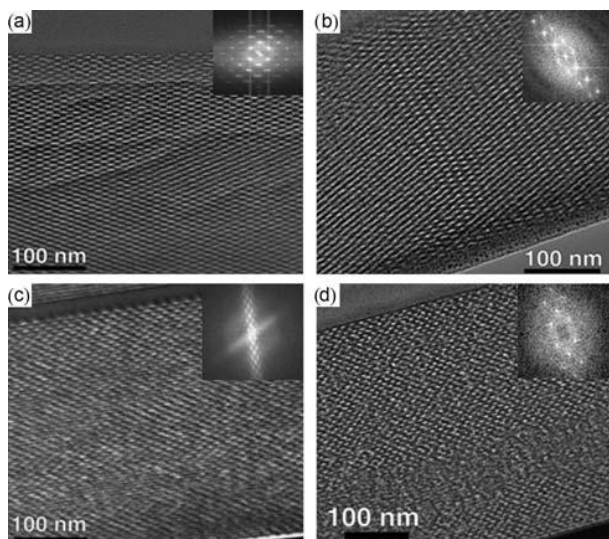


**Figure 1.6:** TEM micrographs of mesoporous carbon and carbon–silica nanocomposite films with orthorhombic structure (*Fmmm*) with varying silica composition after being pyrolyzed at 800 °C in nitrogen: (a) FDU-16-800, (b) CS-20-800, (c) CS-33-800 and (d) CS-51-800. Reproduced from Song et al.<sup>23</sup>

The reduced shrinkage resulted in higher porosity, which could be determined by refractive index change during adsorption of toluene in ellipsometric porosimetry measurements (from 13 % to 28 %). On the other hand, the increased silica content also resulted in lower conductivity (from 25.5 S/cm to 0.43 S/cm for 56 wt % SiO<sub>2</sub>).

### 1.2.2. OMC Fibers Embedded in Anodic Alumina Membranes and Free Fibers

The challenges for OMC fiber syntheses are completely different compared to thin films. While the carbonization of OMCs attached to plane substrates results in enormous anisotropic shrinkage, tubular confinements can show beneficial effects on the shrinkage behavior and the thermal stability. Free-standing anodic alumina membranes (AAMs) turned out to be suitable hosts due to high thermal stability and parallel alignment of the pores perpendicular to the surface as well as their commercial availability. Especially the oriented alignment of the pores is advantageous for characterization (e.g. SAXS and TEM) and offers new potential

applications such as separation of biomolecules through nanofiltration or the use as host material for the synthesis of nanostructures.

For the mentioned applications the control of symmetry, order and orientation of the ordered mesoporous carbon, and in addition high fill factors, accessibility and permeability along the AAM channels is essential and remains a challenge. For applications that require larger amounts of free fibers, the use of AAMs as template is not reasonable due to the high price in relation to the OMC yield. Thus other hard templates or methods should also be explored.

Early examples<sup>32-34</sup> of pure organic mesophases in AAMs were reported starting from 2007 and showed different mesoporous structures including the circular hexagonal structure.<sup>33</sup> A new restriction effect of hard templates for the shrinkage during carbonization was first reported by Zheng and coworkers<sup>24</sup> for OMC in AAMs. The embedded fibers were carbonized at different temperatures and investigated with nitrogen sorption as isolated fibers after etching. As illustrated in Figure 1.7 they could show that the pore sizes did not shrink but instead increased upon higher carbonization temperatures. These increased pore sizes are explained by a combination of strong adhesion of the carbon to the alumina walls and shrinkage of the pore walls during carbonization. Due to this restricted shrinkage effect they could exhibit large pores up to 15 nm, high surface areas and pore volumes (1154 m<sup>2</sup>/g and 3.44 cm<sup>3</sup>/g), which were much larger than those of the corresponding bulk material FDU-16-700.

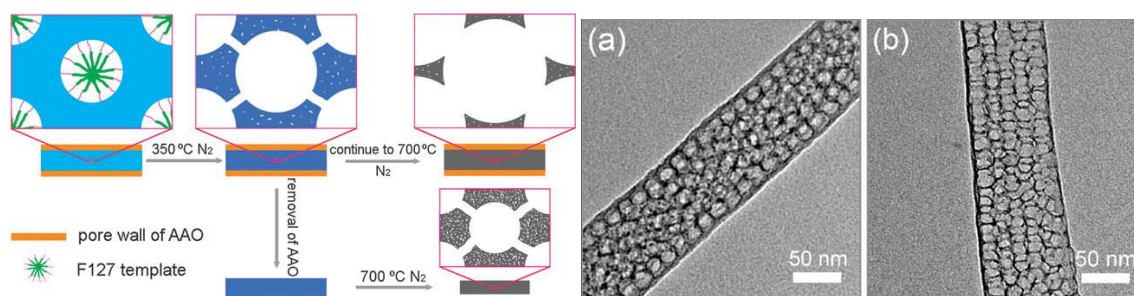


**Figure 1.7:** Schematic illustration of the restriction effect of AAO for the shrinkage of mesoporous polymer during carbonization. TEM images of (a) MPNF-350 and (b) MCNF-700 obtained by using AAO with an average pore diameter of 90 nm as template and pyrolysis at 350 °C and 700 °C, respectively. Reproduced from Zheng et al.<sup>24</sup>

Mesoporous carbon in AAMs showing for the first time a cubic symmetry (space group  $Im\bar{3}m$ ) was reported recently.<sup>25</sup> The membranes showed excellent fill factors and highly ordered mesoporous structures up to 1000 °C.

The aforementioned restricted shrinkage effect was also found here and resulted in excellent porosity properties. The high fill factor together with the cubic structure (which is an open pore structure) should make this system a very attractive candidate for application as membrane e.g. for bio-separations. The cubic system was further investigated with *in-situ* SAXS measurements during structure formation and carbonization (together with a circular hexagonal structure). As observed for OMC films, it was found that the structure forms not during EISA but during the thermopolymerization step and that the thermopolymerization temperature influences the dimensions of the cubic unit cell. To gain further control of the symmetry of the structure and its orientation in the membrane manipulation in this thermopolymerization step should be the starting point.

An alternative macroporous template was recently introduced by Liu et al.<sup>35</sup>

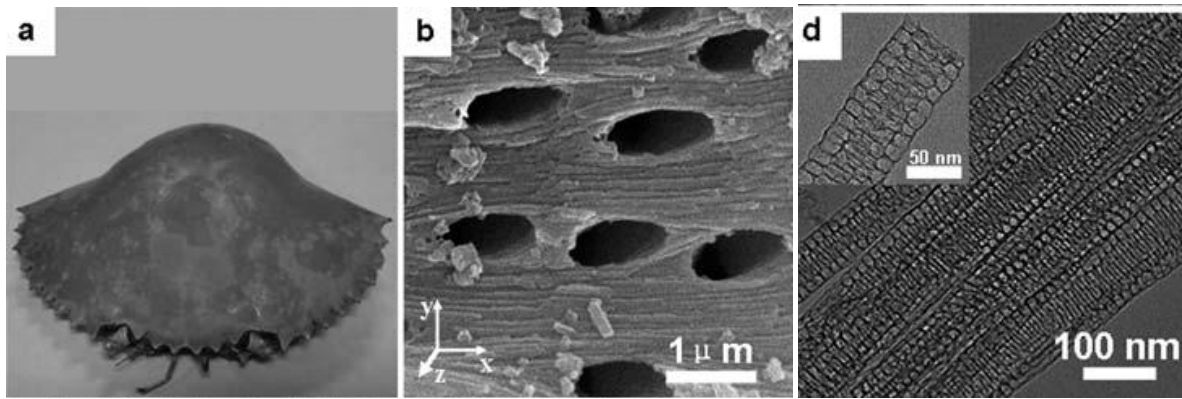


**Figure 1.8:** Photograph of natural scylla serrata crab shell (a) and SEM image (b) after calcination; (d) TEM images, the high-magnification TEM of single mesoporous carbon nanofiber is inserted. Reproduced from Liu et al.<sup>35</sup>

Here a calcined crab shell was used as hard template that consists of  $\text{CaCO}_3$  with disordered pores of 70 nm in diameter. The  $\text{CaCO}_3$  could be dissolved in hydrochloric acid to free the fibers. The capacitance performance of the fibers as an electrode material for supercapacitors and the electrocatalytic activity as a supporting medium for platinum in direct methanol fuel cells were also investigated here and beneficial effects of the fibrous morphology and the high porosity due to the restriction effect of the confinement were found. Recently we developed another approach for free fibers, which used solid carbon nanofibers for the synthesis of a porous silica template. The silica template was imbibed with different OMC precursor solutions, carbonized up to 1000 °C and finally etched in hydrofluoric acid to free the mesoporous carbon nanofibers. The fibers exhibited large pore sizes up to diameters of 9 nm and porosities up to 2486  $\text{m}^2/\text{g}$  and 2.06  $\text{cm}^3/\text{g}$ , respectively. The fibers were applied as sulfur host and electrode material in lithium-sulfur batteries and resulted in much higher capacities than the related bulk material. An alternative synthesis procedure that has potential for industrial application is electrospinning. Electrospinning uses an electric charge to draw very fine (down to the nanoscale) fibers from a liquid and can be in principle applied for the

precursor solutions of OMCs. The applicability as a continuous process could make it superior over hard template based syntheses for large scale applications although the fibers synthesized in that way would not show the beneficial effects of the tubular confinements on the shrinkage behavior. Nevertheless porous carbon fibers made by electrospinning are rare and the reported fibers<sup>36-38</sup> do neither gain the good porosity properties nor the high crystallographic symmetries by far of the mentioned OMC fibers from template based syntheses.

### **1.2.3. Spherical OMC Nanoparticles**

The morphology of spherical nanoparticles is potentially advantageous due to higher accessibility that results from reduced diffusion lengths compared to bulk materials. Accordingly, processes that depend on transport of guest species through porous hosts can often be improved. In addition nanoparticles can be used for new applications such as drug delivery if the particles can be separated and can form colloidal suspensions.

While most of the syntheses for OMC bulk materials, thin films or fibers use sol-gel syntheses followed by thermal treatments for template removal and carbonization, nanoparticle syntheses for other materials than carbon are normally solution based. In those solvothermal syntheses nucleation and particle growth can be controlled by concentrations and reaction times. Therefore the big challenge here is to either create solution based OMC nanoparticle syntheses or to adapt the established sol-gel methods to nanoparticles. Due to these difficulties only few examples for OMC nanoparticles are reported so far using varying concepts for nanoparticle synthesis.

The first examples for mesoporous carbon nanoparticles used the voids of close-packed PMMA spheres as template,<sup>39</sup> were aerosol assisted<sup>40</sup> or used ultrasonic emulsification.<sup>41</sup>

Those carbon materials all exhibited relatively small porosities values ( $< 610 \text{ m}^2/\text{g}$ ,  $< 0.86 \text{ cm}^3/\text{g}$ ) compared to already known bulk materials.

Kim et al.<sup>42</sup> used mesoporous silica nanoparticles as hard template to get the inverse carbon structures with very high surface area up to  $2000 \text{ m}^2/\text{g}$  and a pore volume of  $1.2 \text{ cm}^3/\text{g}$  for small mesopores of 2.4 nm. They could also show that the particles could serve as a transmembrane carrier and exhibit low cytotoxicity and could therefore be potentially used for drug delivery. Ordered arrays of mesoporous carbon spheres were reported by Liu et al.<sup>43</sup> They used close packed polystyrene spheres for synthesis of a silica inverse opal structure and in the second step this silica inverse opal was imbibed with the OMC precursors. They obtained fused particles with porosity properties of  $601 \text{ m}^2/\text{g}$  and  $1.70 \text{ cm}^3/\text{g}$  including textural porosity. The material was investigated regarding the electrochemical properties as an electrode material for supercapacitor applications and showed high capacity and cycling stability. A hydrothermal synthesis for nanoparticles at variable size from 20 nm up to 140 nm was introduced recently by Fang et al.<sup>44</sup>

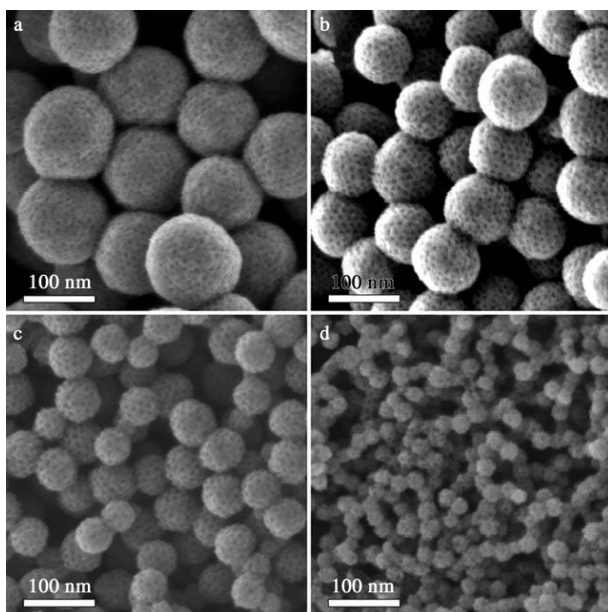


**Figure 1.9:** HRSEM images of the ordered mesoporous carbon nanospheres prepared by a low-concentration hydrothermal method at 130°C: a) MCN-140 with a diameter of 140 nm; b) MCN-90 with a diameter of 90 nm; c) MCN-50 with a diameter of 50 nm, and d) MCN-20 with a diameter of 20 nm. Reproduced from Fang et al.<sup>44</sup>

The highly ordered particles gained porosities up to 1100 m<sup>2</sup>/g and 1.52 cm<sup>3</sup>/g (including textural porosity), respectively. Application as drug carrier was also investigated for those mesoporous carbon nanospheres, they showed low cytotoxicity, excellent cell permeability and showed a good adsorption capacity for ibuprofen. Recently Lei et al.<sup>45</sup> reported synthesis of mesoporous carbon nanospheres with diameters of 65 nm, porosity of 2.7 nm mesopores and high textural porosity and therefore very high porosity up to a surface area of 2400 m<sup>2</sup>/g and a total pore volume of 2.9 cm<sup>3</sup>/g. The nanospheres made through hardtemplating of mesoporous silica spheres showed high energy density and cyclability as electrode material in a supercapacitor. Nanoparticles with extremely high porosity could be synthesized recently by our group. The spherical mesoporous carbon nanoparticles were obtained by a two step casting process. An opal structure of PMMA spheres was imbibed with a silica precursor solution to form the inverse silica structures. The macroporous silica structure is then used as

template for a triconstituent precursor solution containing resol, TEOS and the block copolymer Pluronic F127. Carbonization at 900 °C is followed by etching of the silica templates and the silica in the carbon/silica nanocomposite walls with hydrofluoric acid and OMC nanoparticles with extremely high inner porosity of 2.32 cm<sup>3</sup>/g and 2445 m<sup>2</sup>/g, respectively are obtained. To our knowledge this is the highest reported inner porosity for mesoporous carbon nanoparticles. The particles (Figure 1.10) show a highly ordered 2D-hexagonal mesostructure and particles sizes of 300 nm and could form stable colloidal suspensions.

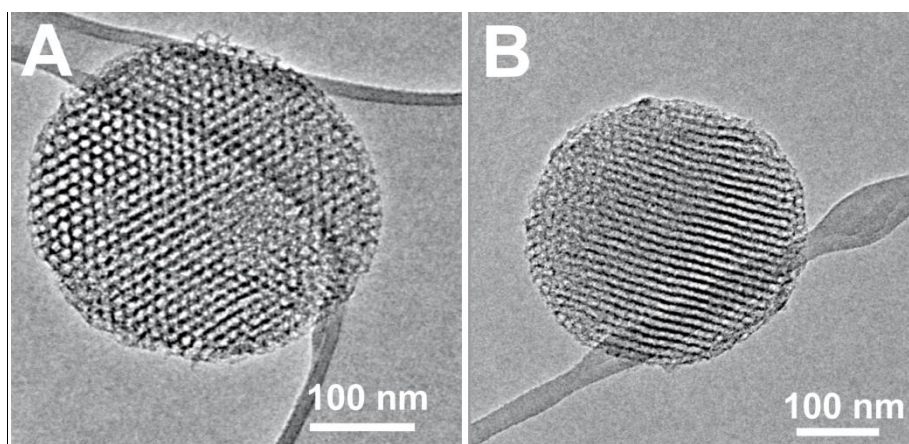


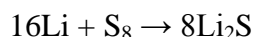
**Figure 1.10:** TEM micrographs of spherical OMC nanoparticles showing the 2D-hexagonal structure: A) projected along the columns; B) tilted out of the columnar projection.

The high pore volume makes the particles interesting as host material for sulfur in rechargeable Lithium Sulfur batteries. This type of energy storage system attracts increasing attention due to its theoretical energy density which is 3 to 5 times higher than for Li ion batteries based on intercalation reactions.<sup>46</sup> The particles were tested for this application and showed significantly higher reversible capacities than the bulk material<sup>23</sup> made from the same precursor solution up to 1200 mAh/g and low capacity fading.

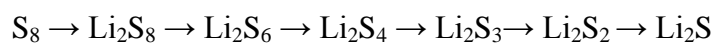
### 1.3. Application as Sulfur Host and Electrode in Lithium Sulfur Batteries

Rechargeable lithium sulfur batteries are attracting increasing attention due to their high theoretical specific energy density, which is 3 to 5 times higher than that of lithium-ion batteries based on intercalation chemistry. Recent advances were discussed by Ji and Nazar.<sup>46</sup>

The lithium sulfur battery is based on the reaction of lithium and sulfur to lithium sulfide:



The electrodes in this cell (Figure 1.11) mainly consist of metallic lithium (negative electrode, anode during discharging) and sulfur (positive electrode, cathode during discharging). During discharge lithium is oxidized, the  $\text{Li}^+$  ions are dissolved in the solvent and move towards the cathode. There, they react with reduced sulfur to finally produce  $\text{Li}_2\text{S}$  via several intermediates (the polysulfides).



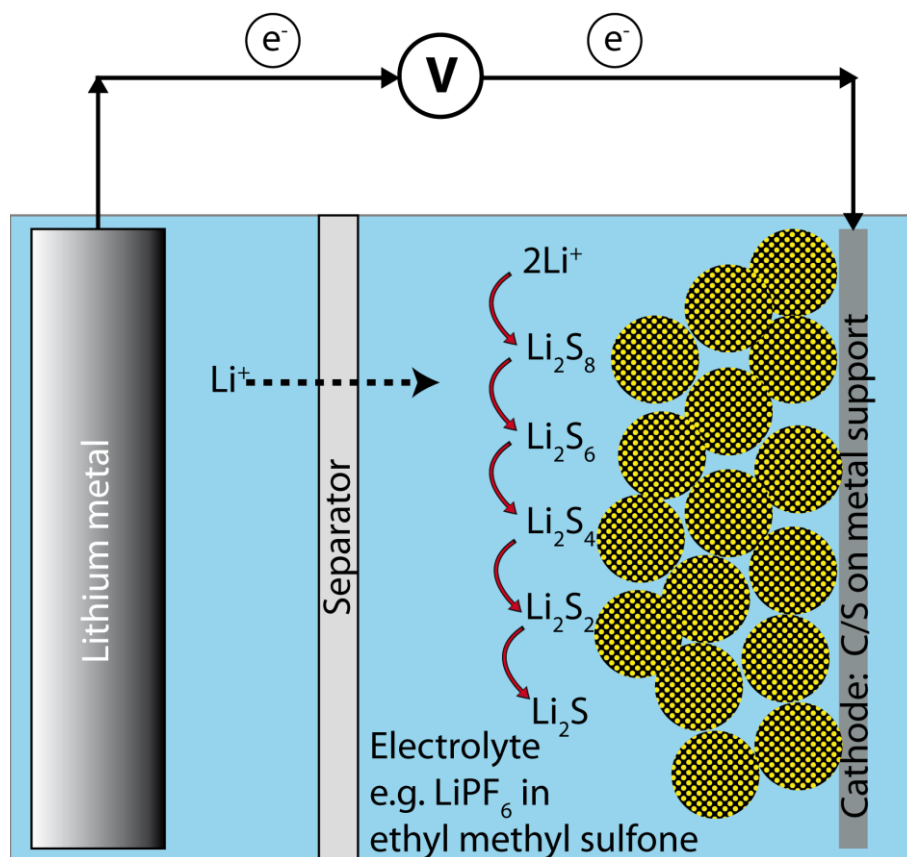


**Figure 1.11:** Basic components and the discharge reactions in a lithium sulfur battery with a cathode of carbon-sulfur composite spheres

The theoretical capacity for the sulfur electrode is 1675 mAh/g which is extremely high compared to cathodes in Li-ion batteries, e.g. one of the best,  $\text{LiCoO}_2$ , offers only 275 mAh/g. This exceptionally high capacity – in fact the highest value for all solid cathode materials – together with the average voltage of 2.15 V results in a theoretical energy density of 2500 Wh/kg. Sulfur as a raw material has the advantage that it is very cheap and therefore suitable for mass production, but it lacks electrical conductivity. Therefore the electrochemical reactions must take place close (meaning few nanometers) to the surface of a conductive electrode, thus a sulfur host is needed. Porous carbons turned out to be suitable for this purpose due to their high specific pore volume, their chemical stability and electrical

conductivity, and the affinity of sulfur to adsorb at the hydrophobic carbon surface. A high specific pore volume is essential here, because it correlates with the amount of sulfur that can be adsorbed in the pores and therefore with the capacity of the cathode. A pore volume of  $1 \text{ cm}^3/\text{g}$  allows an electrode of 50 % sulfur, whereas  $2.1 \text{ cm}^3/\text{g}$  can provide electrodes with 70 % sulfur.

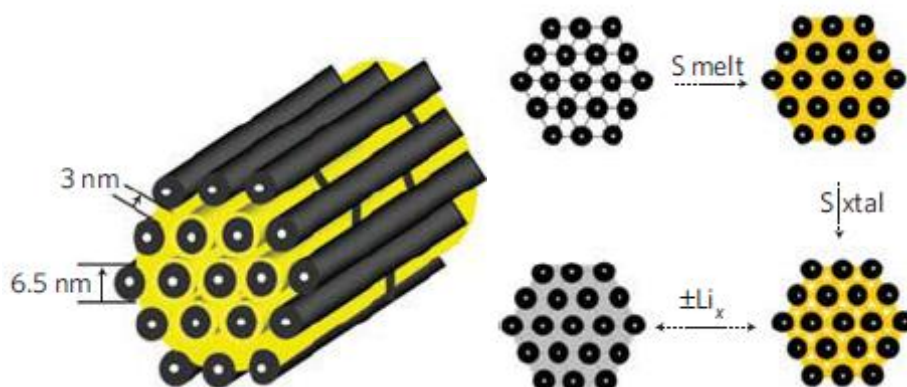


**Figure 1.12:** Left: Schematic diagram<sup>47</sup> of the sulfur (yellow) confined in the interconnected pore structure of mesoporous carbon, CMK-3. Right: Schematic diagram<sup>47</sup> of composite synthesis by impregnation of molten sulfur, followed by its densification on crystallization.

One of the primary shortfalls of most Li-S cells is the reactivity of the intermediates with the electrolytes. While  $\text{S}_8$  and  $\text{Li}_2\text{S}$  are rather insoluble in most electrolytes, the intermediary polysulfides are not. As a result, the dissolution of  $\text{LiS}_n$  into the electrolyte causes irreversible loss of active sulfur. For this reason the porous carbons should not only provide electrical conductivity and allow diffusion of the lithium ions but also capture the polysulfides. The challenge here is to find the carbon material with appropriate pore sizes and also morphologies that match those purposes best.

The best electrochemical properties showed a CMK-3 material in the form of small particles reported by Ji et al.<sup>47</sup> The OMC exhibits high surface area and pore volume of  $1976 \text{ m}^2/\text{g}$  and  $2.1 \text{ cm}^3/\text{g}$ , respectively and could therefore build C/S composites with 70 % sulfur content.

The measured reversible capacities based on the mass of sulfur were up to 1000 mAh/g for the bare CMK-3 and even higher up to 1320 mAh/g after functionalization with PEG-chains (polyethylene glycol). Those chains served to trap the polysulfides by providing a highly hydrophilic surface chemical gradient that preferentially solubilizes them in relation to the electrolyte. The PEG functionalization also reduced the capacity fading due to polysulfide dissolution.

#### 1.4. Chapter References

1. <http://en.wikipedia.org/wiki/File:Diamond-and-graphite-with-scale.jpg>.
2. Dresselhaus, M.; Endo, M., Relation of Carbon Nanotubes to Other Carbon Materials. In *Carbon Nanotubes*, Dresselhaus, M.; Dresselhaus, G.; Avouris, P., Eds. Springer Berlin / Heidelberg: 2001; Vol. 80, pp 11-28.
3. [http://en.wikipedia.org/wiki/Carbon\\_nanotube](http://en.wikipedia.org/wiki/Carbon_nanotube).
4. Kroto, H. W.; Heath, J. R.; O'Brien, S. C.; Curl, R. F.; Smalley, R. E., *Nature* **1985**, *318* (6042), 162-163.
5. Geim, A. K.; Novoselov, K. S., *Nat Mater* **2007**, *6* (3), 183-191.
6. Liang, C.; Li, Z.; Dai, S., *Angew. Chem., Int. Ed.* **2008**, *47* (20), 3696-3717.
7. Wan, Y.; Shi, Y.; Zhao, D., *Chem. Mater.* **2008**, *20* (3), 932-945.
8. Chang, H.; Joo, S. H.; Pak, C., *J. Mater. Chem.* **2007**, *17* (30), 3078-3088.
9. Wu, C.-G.; Bein, T., *Science* **1994**, *266* (5187), 1013-15.
10. Ryoo, R.; Joo, S. H.; Jun, S., *J. Phys. Chem. B* **1999**, *103* (37), 7743-7746.
11. Lee, J.; Yoon, S.; Hyeon, T.; Oh, S. M.; Kim, K. B., *Chem. Commun.* **1999**, (21), 2177-2178.
12. Jun, S.; Joo, S. H.; Ryoo, R.; Kruk, M.; Jaroniec, M.; Liu, Z.; Ohsuna, T.; Terasaki, O., *J. Am. Chem. Soc.* **2000**, *122* (43), 10712-10713.

13. Kruk, M.; Jaroniec, M.; Kim, T.-W.; Ryoo, R., *Chem. Mater.* **2003**, *15* (14), 2815-2823.
14. Xing, W.; Bai, P.; Li, Z. F.; Yu, R. J.; Yan, Z. F.; Lu, G. Q.; Lu, L. M., *Electrochim. Acta* **2006**, *51* (22), 4626-4633.
15. Li, Z.; Dai, S., *Chem. Mater.* **2005**, *17* (7), 1717-1721.
16. Bazula, P. A.; Lu, A.-H.; Nitz, J.-J.; Schueth, F., *Microporous Mesoporous Mater.* **2008**, *108* (1-3), 266-275.
17. Wang, X.; Liu, R.; Waje, M. M.; Chen, Z.; Yan, Y.; Bozhilov, K. N.; Feng, P., *Chem. Mater.* **2007**, *19* (10), 2395-2397.
18. Vinu, A.; Hossian, K. Z.; Srinivasu, P.; Miyahara, M.; Anandan, S.; Gokulakrishnan, N.; Mori, T.; Ariga, K.; Balasubramanian, V. V., *J. Mater. Chem.* **2007**, *17* (18), 1819-1825.
19. Moriguchi, I.; Ozono, A.; Mikuriya, K.; Teraoka, Y.; Kagawa, S.; Kodama, M., *Chem. Lett.* **1999**, (11), 1171-1172.
20. Thurn-Albrecht, T.; DeRouchey, J.; Russell, T. P.; Jaeger, H. M., *Macromolecules* **2000**, *33* (9), 3250-3253.
21. Liang, C.; Hong, K.; Guiochon, G. A.; Mays, J. W.; Dai, S., *Angew. Chem., Int. Ed.* **2004**, *43* (43), 5785-5789.
22. Meng, Y.; Gu, D.; Zhang, F.; Shi, Y.; Cheng, L.; Feng, D.; Wu, Z.; Chen, Z.; Wan, Y.; Stein, A.; Zhao, D., *Chem. Mater.* **2006**, *18* (18), 4447-4464.
23. Liu, R.; Shi, Y.; Wan, Y.; Meng, Y.; Zhang, F.; Gu, D.; Chen, Z.; Tu, B.; Zhao, D., *J. Am. Chem. Soc.* **2006**, *128* (35), 11652-11662.
24. Zheng, M.; Ji, G.; Wang, Y.; Cao, J.; Feng, S.; Liao, L.; Du, Q.; Zhang, L.; Ling, Z.; Liu, J.; Yu, T.; Cao, J.; Tao, J., *Chem. Commun.* **2009**, (33), 5033-5035.

25. Schuster, J.; Keilbach, A.; Koehn, R.; Doeblinger, M.; Doerfler, T.; Dennenwaldt, T.; Bein, T., *Chem. Eur. J.* *In press*.
26. Schuster, J.; Koehn, R.; Keilbach, A.; Doeblinger, M.; Amenitsch, H.; Bein, T., *Chem. Mater.* **2009**, *21* (24), 5754-5762.
27. Song, L.; Feng, D.; Fredin, N. J.; Yager, K. G.; Jones, R. L.; Wu, Q.; Zhao, D.; Vogt, B. D., *ACS Nano* **2009**, *4* (1), 189-198.
28. Tanaka, S.; Katayama, Y.; Tate, M. P.; Hillhouse, H. W.; Miyake, Y., *J. Mater. Chem.* **2007**, *17* (34), 3639-3645.
29. Brinker, C. J.; Lu, Y.; Sellinger, A.; Fan, H., *Adv. Mater.* **1999**, *11* (7), 579-585.
30. Smarsly, B.; Grosso, D.; Brezesinski, T.; Pinna, N.; Boissière, C.; Antonietti, M.; Sanchez, C., *Chem. Mater.* **2004**, *16* (15), 2948-2952.
31. Song, L.; Feng, D.; Campbell, C. G.; Gu, D.; Forster, A. M.; Yager, K. G.; Fredin, N.; Lee, H.-J.; Jones, R. L.; Zhao, D.; Vogt, B. D., *J. Mater. Chem.* **2010**, *20* (9), 1691-1701.
32. Steinhart, M.; Liang, C.; Lynn, G. W.; Goesele, U.; Dai, S., *Chem. Mater.* **2007**, *19* (10), 2383-2385.
33. Wang, K.; Zhang, W.; Phelan, R.; Morris, M. A.; Holmes, J. D., *J. Am. Chem. Soc.* **2007**, *129* (44), 13388-13389.
34. Zheng, M.; Cao, J.; Ke, X.; Ji, G.; Chen, Y.; Shen, K.; Tao, J., *Carbon* **2007**, *45* (5), 1111-1113.
35. Liu, H.-J.; Wang, X.-M.; Cui, W.-J.; Dou, Y.-Q.; Zhao, D.-Y.; Xia, Y.-Y., *J. Mater. Chem.* **2010**, *20* (20), 4223-4230.
36. Peng, M.; Li, D.; Shen, L.; Chen, Y.; Zheng, Q.; Wang, H., *Langmuir* **2006**, *22* (22), 9368-9374.

37. Kim, C.; Ngoc, B. T. N.; Yang, K. S.; Kojima, M.; Kim, Y. A.; Kim, Y. J.; Endo, M.; Yang, S. C., *Adv. Mater.* **2007**, *19* (17), 2341-2346.
38. Im, J. S.; Jang, J.-S.; Lee, Y.-S., *Journal of Industrial and Engineering Chemistry* **2009**, *15* (6), 914-918.
39. Wang, Z.; Li, F.; Stein, A., *Nano Letters* **2007**, *7* (10), 3223-3226.
40. Yan, Y.; Zhang, F.; Meng, Y.; Tu, B.; Zhao, D., *Chem. Commun.* **2007**, (27), 2867-2869.
41. Tonanon, N.; Intarapanya, W.; Tanthapanichakoon, W.; Nishihara, H.; Mukai, S.; Tamon, H., *Journal of Porous Materials* **2008**, *15* (3), 265-270.
42. Kim, T.-W.; Chung, P.-W.; Slowing, I. I.; Tsunoda, M.; Yeung, E. S.; Lin, V. S. Y., *Nano Letters* **2008**, *8* (11), 3724-3727.
43. Liu, H.-J.; Cui, W.-J.; Jin, L.-H.; Wang, C.-X.; Xia, Y.-Y., *J. Mater. Chem.* **2009**, *19* (22), 3661-3667.
44. Fang, Y.; Gu, D.; Zou, Y.; Wu, Z.; Li, F.; Che, R.; Deng, Y.; Tu, B.; Zhao, D., *Angew. Chem.* **2010**, *122* (43), 8159-8163.
45. Lei, Z.; Christov, N.; Zhang, L. L.; Zhao, X. S., *J. Mater. Chem.* **2011**, *21* (7), 2274-2281.
46. Ji, X.; Nazar, L. F., *J. Mater. Chem.* **2010**, *20* (44), 9821-9826.
47. Ji, X.; Lee, K. T.; Nazar, L. F., *Nat Mater* **2009**, *8* (6), 500-506.

## 2. CHARACTERIZATION METHODS

A comprehensive understanding of the synthesized mesoporous carbons requires knowledge of diverse properties, such as mesoporous structure, porosity, morphology as well as chemical, optical and electronic properties. As a consequence, a large number of characterization techniques are required to analyze the material. To study the mesostructures and their morphologies a combination of small angle x-ray scattering and electron microscopy techniques is used. Nitrogen sorption measurements are employed to characterize the porosity properties. By ellipsometry the film thicknesses and optical constants can be measured whereas infrared and Raman spectroscopies are used to get information about the composition of the material and the template during synthesis and thermal treatment. Dynamic Light Scattering (DLS) can be used to determine the particle size distribution of colloidal suspensions.

### 2.1. X-Ray Scattering Techniques

Diffraction can occur if the distances in a periodic lattice are of the same dimension as the wavelength of the impinging beam. Therefore crystals act as a three dimensional diffraction lattice for the X-rays. The lattice planes of this diffraction lattice are formed through periodic variations in the electron density. The angles for constructive or destructive interference depend on the distances of the lattice planes. Figure 2.1 illustrates the condition for constructive interference. Only if the optical retardation  $\delta$  equals a multiple of the wavelength of the X-rays  $\lambda$ , constructive interference takes place and a reflection can be recorded at a scattering angle  $2\theta$ .

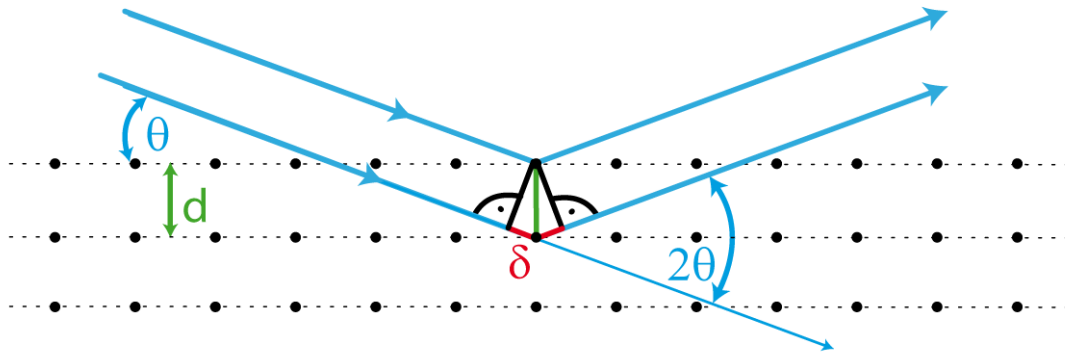


**Figure 2.1:** X-ray diffraction can be regarded as reflection of X-rays at lattice planes that fulfill the Bragg condition. (2.1).

The Bragg relation summarizes this condition:

$$n\lambda = 2d_{hkl} \sin\theta \quad (2.1)$$

In this equation  $n$  is the order of diffraction,  $d_{hkl}$  the distances of the lattice planes and  $\theta$  is the angle of constructive interference, also called Bragg angle.

The right part of this equation defines the optical retardation  $\delta$  of two X-rays diffracted at two parallel lattice planes with distance  $d$ . Those  $d$ -values are associated with the lattice constants  $\mathbf{a}$ ,  $\mathbf{b}$  and  $\mathbf{c}$  and the Miller indices  $h$ ,  $k$  and  $l$ . Each index denotes a plane orthogonal to a direction  $(h, k, l)$  in the basis of the reciprocal lattice vectors. For a cubic lattice the relation is simple because the lattice parameters  $\mathbf{a}$ ,  $\mathbf{b}$  and  $\mathbf{c}$  are equal, so the relation can be written as:

$$d_{hkl} = \frac{a}{\sqrt{h^2+k^2+l^2}} \quad (2.2)$$

For a hexagonal structure  $\mathbf{a}$  and  $\mathbf{b}$  are equal and the relation is:

$$d_{hkl} = \frac{a}{\sqrt{\frac{4}{3}(h^2+hk+k^2)+\frac{a^2}{c^2}l^2}} \quad (2.3)$$

For the 2D-hexagonal structure **a** and **b** are equal and **c** is not defined. The relation is reduced as follows:

$$d_{hk} = \frac{a}{\sqrt{\frac{4}{3}(h^2+hk+k^2)}} \quad (2.4)$$

Thus by measuring d-values of different lattice planes, information about the unit cell parameters and their symmetry can be obtained. Many mesoporous materials do not exhibit atomic periodicity but only periodically ordered pores. Hence the distances of the lattice planes are much larger ( $\approx 2$  to 10 nm) than the atomic distances in a crystal, and the corresponding diffraction angles are very small (typically 0.5 to 5  $^\circ(2\theta)$ ). Appropriate diffraction techniques usually require special setups; they are summarized under the term small angle X-ray scattering (SAXS) techniques.

### 2.1.1. One dimensional Small Angle X-Ray Scattering (1D-SAXS)

In this work, a line collimation instrument (Scintag XDS 2000) was used for one dimensional SAXS measurements. It uses copper  $K_\alpha$  radiation with a wavelength of  $\lambda = 1.54 \text{ \AA}$ . The setup is measuring in reflection mode in  $\theta - \theta$  geometry, meaning that the sample is stationary while the X-ray tube and the detector are rotated around it, while the angle of incidence and reflection are the same. This setup can be used for measurements of powders or films on planar substrates. With this technique only reflections from lattice planes parallel to the substrate plane ( $0^\circ$ ) can be detected. Powders usually consist of randomly oriented crystallites and therefore also the lattice planes are oriented randomly. Some of them are always oriented parallel to the substrate plane and therefore fulfill the Bragg relation. Mesoporous thin films often exhibit one specific orientation with respect to the substrate, with rotational freedom around the substrate normal and therefore only one reflection and its

higher orders can be detected. The resulting XRD pattern of a thin film with 2D-hexagonal structure in [01]-orientation regarding the substrate is depicted in Figure 2.2.

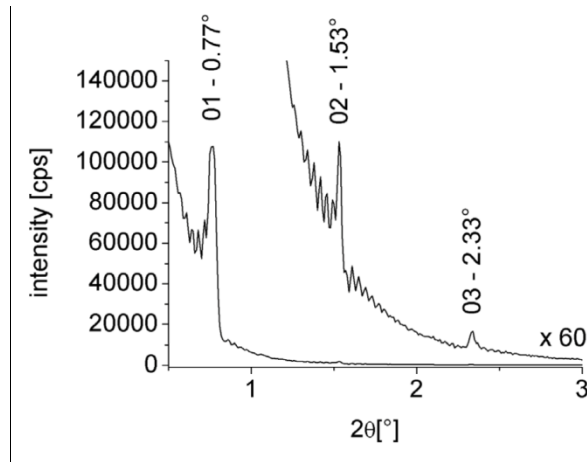


**Figure 2.2:** 1D-SAXS pattern of a thin film with periodic mesostructure. To illustrate higher order reflections the right part of the curve is 60 times magnified.

It shows several orders of a sharp reflection indexed according to a 2D hexagonal structure. In this pattern also Kiessig fringes<sup>48-49</sup> can be observed, which could be used to determine the film thickness. Kiessig fringes result from reflections between the film surface and the interface of film and substrate. In the case of very thin and homogenous films several orders of these surface wave reflections can be observed. The reflection angles  $\theta_m$  and  $\theta_{m+1}$  of two consecutive fringes are related to the film thickness T by the formula:

$$T = \frac{\lambda}{2 \sin \theta_{m+1} - \sin \theta_m} \quad (2.5)$$

The width of the reflections ( $\Delta 2\theta_{FWHM}$  : full width at half maximum = FWHM) can be related to the domain size D according to the Scherrer equation.<sup>50</sup>

$$\Delta 2\theta_{FWHM} = \frac{K\lambda}{D \cdot \cos \theta} \quad (2.6)$$

In addition the width of a reflection depends on the angle of incidence  $\theta$  and the wavelength  $\lambda$ . The constant K can normally be set as 0.9 and depends on the experimental setup. According

to this formula, a very sharp reflection indicates a well-ordered structure with large domain sizes. For films, the domain size is limited by the film thickness. Consequently, the sharpness of the observed reflections is also limited by the film thickness.

### **2.1.2. 2D Small-Angle X-Ray Scattering (2D-SAXS)**

For 2D-SAXS measurements in transmission two setups with point collimation sources were used. First, a lab instrument the SAXSess system by Anton Paar, in combination with a CCD detector system (Roper Scientific). Second, the beamline BL 5.2 L at the Synchrotrone Elettra (Trieste, Italy). The wavelength of the incident beam was 0.15498 nm (8 keV) in both cases. Figure 1 depicts a schematic picture of the experimental setup for SAXS measurements in transmission.

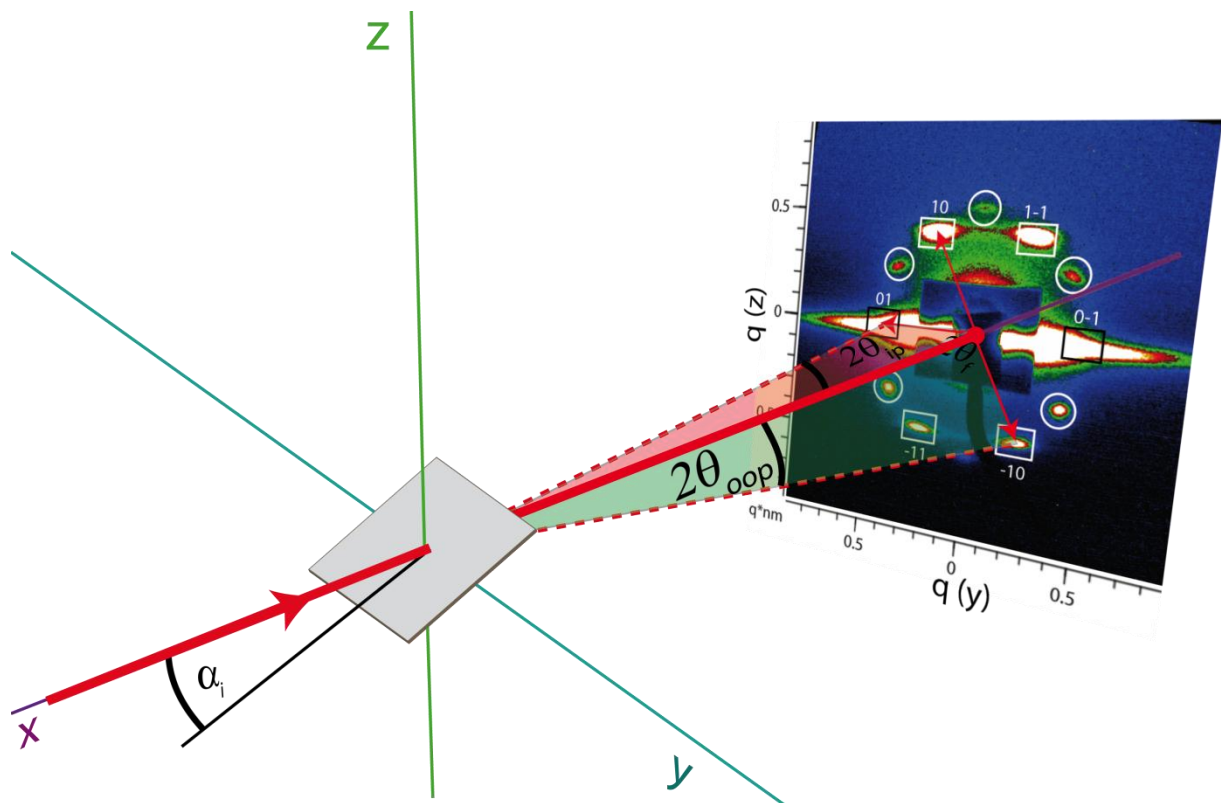


**Figure 2.3:** Experimental setup for a SAXS measurement in transmission mode and the resulting diffraction pattern indexed according to a circular hexagonal structure in the pores of an anodic alumina membrane (AAM).

The specimen (e.g. an AAM) is brought into the monochromatic point-collimated X-ray beam under a desired angle  $\alpha_i$  which was normally set to  $10^\circ$ . As all X-rays in the recorded diffraction pattern are passing through the sample, it has to be thin enough to allow transmission. Most of the X-rays pass the sample without being scattered. To avoid overexposure, the primary beam usually has to be blocked or reduced in intensity by the beam-stop. In SAXS measurements, the wavevector  $\mathbf{q}$  is commonly used to indicate the position of Bragg reflections. The q-value is the norm of the wavevector  $\mathbf{q}$ ; it is related to the distances of lattice planes  $d$  (as commonly used in wide-angle XRD) via

$$d = 2\pi/q_{\text{peak}} \quad (2.7)$$

The orientation of  $\mathbf{q}$  is always parallel to the lattice plane normal; it can be split in the components  $q_z$  and  $q_y$ . In 2D-SAXS, the reflection spots on the horizontal axis of the pattern ( $q_z = 0$ ) are called in-plane reflections (ip) and refer to lattice planes that are parallel to the xz-plane. Out-of-plane reflections (oop,  $q_z \neq 0$ ) refer to all other lattice planes parallel to the x-axis. 2D-SAXS in transmission can only be used for powders, thin films on thin substrates such as 40  $\mu\text{m}$  thick silicon wafers or mesoporous structures confined within thin substrates such as in AAMs, while normal silicon wafers completely absorb the X-ray beam.

### **2.1.3. 2D Grazing Incidence Small Angle X-Ray Scattering (2D-GISAXS)<sup>51</sup>**

Different to 2D-SAXS in transmission, 2D-GISAXS uses reflection of X-rays and thus films on planar substrates can be probed and 2D diffraction patterns can be obtained. These 2D diffraction patterns also show reflections from lattice planes that are not parallel to the substrate and give therefore much more information about the structure than 1D XRD patterns. The 2D-GISAXS experiments were performed at the beamline BL 5.2 L at Sincrotrone Elettra (Trieste, Italy). The experimental setup and the resulting diffraction pattern of an orthorhombic thin film are illustrated in Figure 2.4.

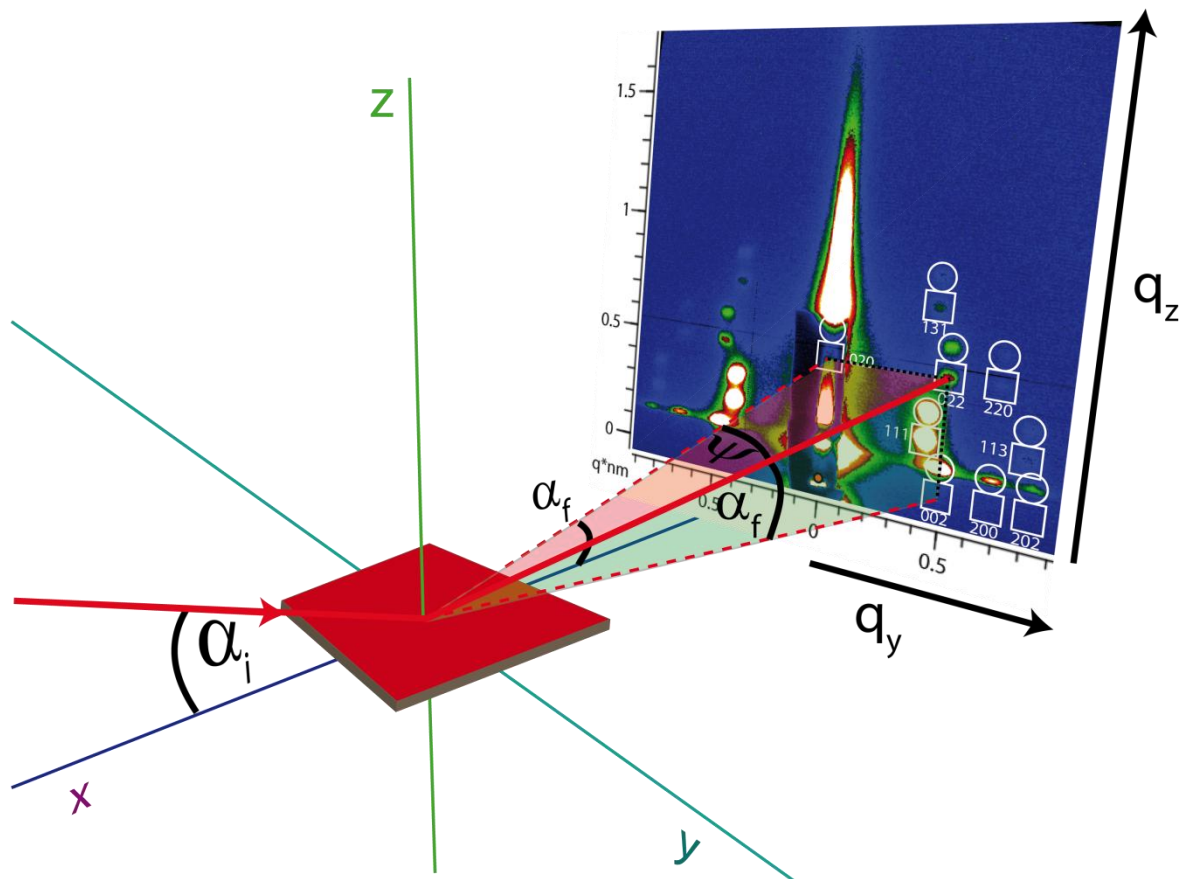


**Figure 2.4:** Schematic picture of the experimental set-up for 2D-GISAXS and a resulting pattern indexed according to an orthorhombic mesostructure. The reflections are doubled due to diffraction of the incident beam reflected at the film substrate interface.

In contrast to SAXS, the angle of incidence of the X-Ray beam on the substrate ( $\alpha_i$ ) is very small. The method is therefore called grazing incidence SAXS. According to Müller-Buschbaum<sup>51</sup> the denotation for 2D-GISAXS is slightly different compared to 2D-SAXS in transmission. The so-called scattering plane is defined by the incident and the exit angles  $\alpha_i$  and  $\alpha_f$  (xz-plane) and all reflections on this vertical axis are denoted as in-plane reflections ( $q_y = 0$ ). Scattering outside this plane is described by an out-of plane angle  $\psi$ . Specular scattering fulfills the condition  $\alpha_i = \alpha_f$  and  $\psi = 0$ , all other cases are called off-specular or diffuse scattering. Specular scattering is typically much more intense compared to off-specular scattering and has to be shielded. Measurements for  $\alpha_i \neq \alpha_f$  and  $\psi = 0$  are called

conventional diffuse scattering, they can be performed with a point detector or a line collimation instrument because they do not require  $q_y$ -resolution. For GISAXS also  $q_y$ -resolution is necessary for information about lattice planes that are not parallel to the substrate plane and therefore result in out-of plane scattering ( $\psi \neq 0$ ). In the interpretation of GISAXS images some complication arises in the scattering, when the incident angle is close to the critical angle of the substrate. In this case, the reflected beam from the substrate has a similar strength as the incident beam and thus the scattering of the reflected beam can give rise to a doubling of scattering features in the perpendicular direction. This doubling is strongly influenced by the incidence angle  $\alpha_i$  in intensity and distance of the two peaks. A second artifact is the so called Yoneda peak.<sup>52</sup> In case the exit angle  $\alpha_f$  of the scattered beam is close to the critical angle, signal enhancement due to the Vineyard effect<sup>53</sup> occurs, resulting in a bright band of intensity at the critical angle.

## 2.2. Electron Microscopy<sup>54-55</sup>

Charged particles such as electrons can be accelerated in electric fields. In the nonrelativistic approximation, the kinetic energy of an electron in an electric field and therefore its velocity  $v$  are related to the acceleration voltage  $U$  by

$$E_{kin} = \frac{1}{2} m_e v^2 = e \cdot U \quad (2.8),$$

$$v = \sqrt{\frac{2 \cdot eU}{m_e}} \quad (2.9),$$

where  $m_e$  is the mass of the electron and  $e$  is the elemental charge. Due to the wave-particle dualism particles have wave properties and the other way around. According to the de-Broglie equation, a wavelength  $\lambda$  can be related to the momentum  $p$  of a moving particle, which can be derived from the acceleration voltage from the latter equations by

$$\lambda = \frac{h}{p} = \frac{h}{m_e v} = \frac{h}{\sqrt{2m_e \cdot e \cdot V}} \quad (2.10),$$

where  $h$  is the Planck constant.

In modern electron microscopes acceleration voltages up to three megavolts are feasible. The theoretical resolution limit for such a microscope is smaller than  $0.1 \text{ \AA}$ . Even though this resolution could not be reached yet due to the lack of good electromagnetic lenses, atomic resolution is possible. Electron microscopes can be used to make structures visible which are much smaller than the resolution limit of optical microscopes, which is about  $200 \text{ nm}$  for visible light. According to Williams and Carter,<sup>55</sup> several types of signal are generated when a high energy electron beam interacts with matter of a thin specimen (Figure 2.5).

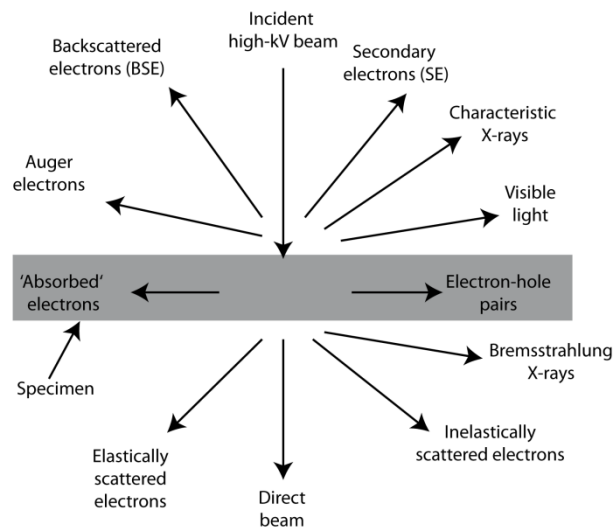


**Figure 2.5:** Signals generated when a high-kV electron beam interacts with a thin specimen.

Adapted from Williams and Carter.<sup>55</sup>

### 2.2.1. Transmission Electron Microscopy (TEM)

In a TEM, electrons directly transmitted through an ultra-thin specimen are detected. Schemes of the experimental setup and of the optical path are illustrated in Figure 2.6. In most cases, an

electron beam is generated either by thermal emission (using a tungsten filament or a LaB<sub>6</sub>-crystal) or by thermally assisted field emission (Schottky field emitter) producing a beam of electrons whose wavelength depends on the acceleration voltage (usually between 80 and 400 kV). A complex lens system is needed for the illumination and the imaging process. The lens systems can be subdivided in three main components. With the condenser lens system various illumination conditions can be chosen. In normal TEM mode, a rather parallel illumination of an area whose size depends on the actual magnification usually is required. Within the sample the intensity of the electron beam is modulated by interaction of the electrons with the specimen atoms. Behind the specimen the objective lens focuses the modulated electron beam again and creates the first magnified image of the sample. Finally the projector lenses further magnify the image and project it on a fluorescent screen or a CCD camera.

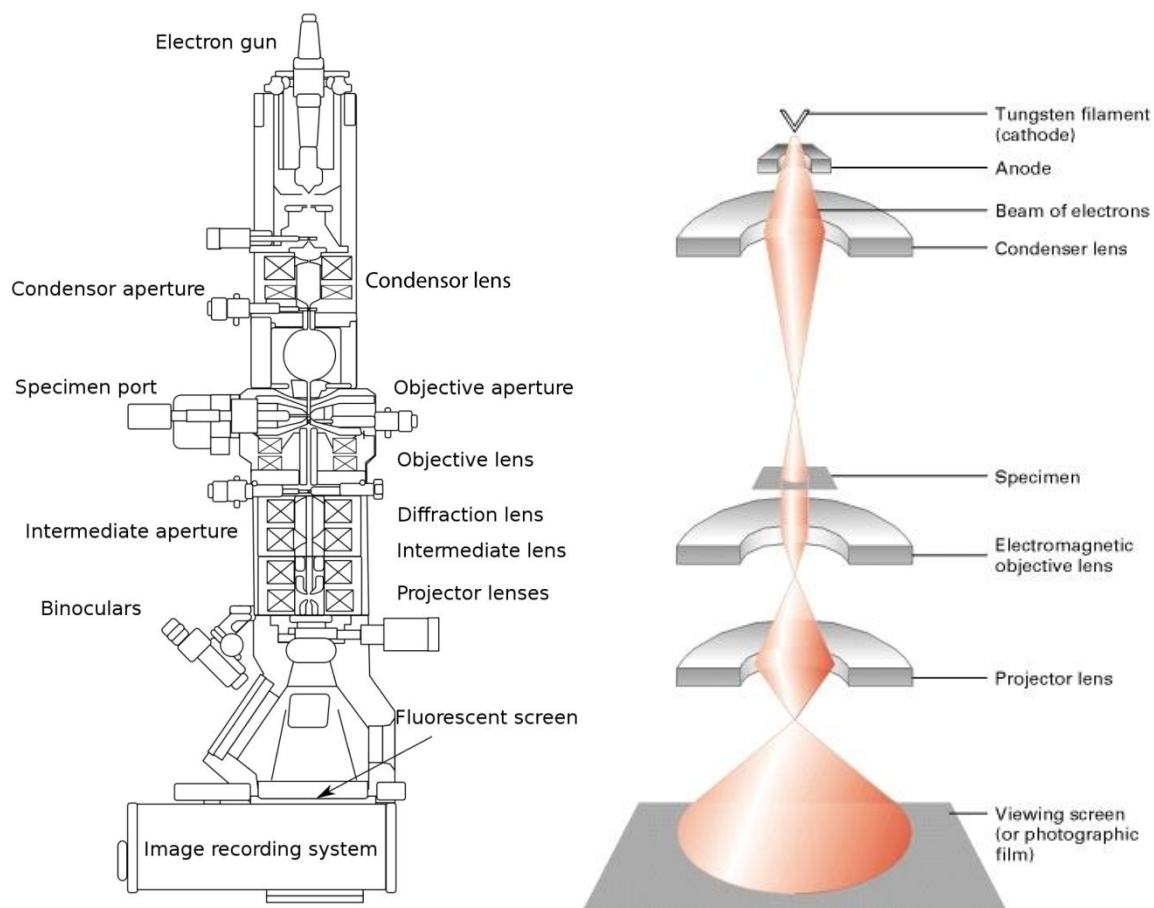


**Figure 2.6:** Scheme of the components (left)<sup>56</sup> in a transmission electron microscope and the optical path (right).<sup>57</sup>

In Scanning transmission electron microscopy (STEM) mode, the electron beam is focused into a spot on the sample which is then scanned over a rectangular area of the sample. The transmitted electrons can then be detected as a function of the scattering angle. Bright-field (BF) imaging uses the direct beam, annular dark-field (ADF) imaging uses scattered electrons close to the direct beam and high-angle annular dark-field (HAADF) uses electrons scattered to even higher angles. By using STEM in this HAADF mode, it is possible to form atomic resolution images whose contrast is approximately proportional to the square of the atomic number (Z-contrast image). Therefore, HAADF-STEM images allow a rather direct interpretation as compared to conventional TEM images. The TEM measurements were made with a JEOL JEM 2011 at an acceleration voltage of 200 kV or a with a FEI TITAN 80-300

microscope at an acceleration voltage of 300 kV. HAADF-STEM images were recorded with a TITAN 80-300 microscope at an acceleration voltage of 300 kV. Due to the need for ultra-thin specimens, sample preparation for TEM is usually quite complex and time-consuming. The preparation process for thin films on plane substrates such as silicon wafers is displayed in Figure 2.7.

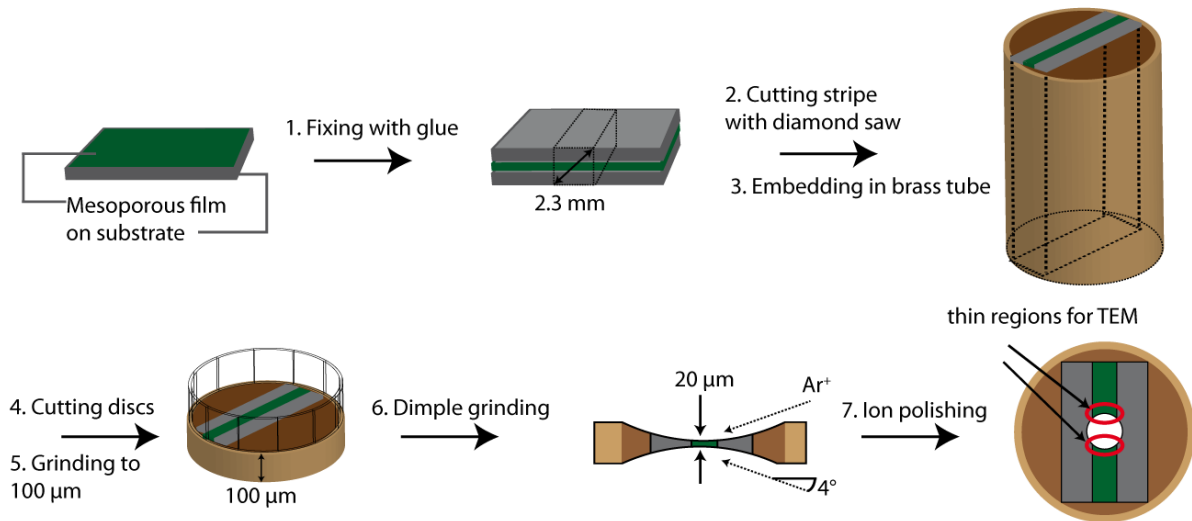


**Figure 2.7:** TEM cross-section preparation of thin films on substrates (e.g. silicon wafers)

Two pieces of the same film are fixed together with epoxy glue. Out of this stack, a thin stripe is cut with a diamond saw which is then embedded in a brass tube again with epoxy glue. With the diamond saw, discs of ca. 300 μm are cut and ground to 100 μm thickness. Dimple grinding from both sides is then used to thin the discs to 20 μm in the center of the discs. Finally the hole is created by ion polishing, usually by an argon ion beam. Normally the ions are accelerated by voltages between 0.3 keV and 5 keV hitting the sample at incident angles between 4° and 8°, until a tiny hole is visible. The edges are then thin enough for transmission of electrons and can be investigated with TEM.

### 2.2.2. Scanning Electron Microscopy (SEM)

Scanning electron microscope (SEM) images are recorded by scanning the sample surface with a high-energy electron beam in a raster scan pattern. In a SEM, the electron beam is also generated by an electron gun (tungsten filament, LaB<sub>6</sub>-crystal, field emission gun) but with much smaller accelerating voltages of 0.1 – 30 kV compared to TEM. Unlike TEM, the most common signal used in SEM are secondary electrons ( $E_{\text{kin}} < 50\text{eV}$ ) generated by the incident electrons, for imaging the surface of a specimen. Due to the imaging of the sample surface in SEM, the requirements for the specimens are not as strict as for TEM samples and the preparation is less extensive.

### 2.3. Sorption Measurements

Sorption measurements are commonly used for characterization of micro- and mesoporous materials regarding their specific surface area, pore volume, and pore size distribution. A common gas sorption measurement starts with the adsorption. For this purpose the porous sample (adsorbent) is first heated while it is exposed to a vacuum system to completely remove all adsorbed molecules from the surface. Then the adsorption isotherm is measured by adjusting distinct relative pressures ( $p/p_0$ ; absolute pressure/saturation vapor pressure) of the probe gas (or adsorptive) at constant temperature (usually nitrogen at 77 K). During the measurement the relative pressure is increased close to  $p_0$  and then decreased again for measurement of the desorption isotherm. The adsorbed and desorbed volumes of gas (in  $\text{cm}^3/\text{g}$ ) on the sample surface are calculated for varying relative pressures. Adsorption and desorption isotherms are usually not identical due to hysteresis. Experimental gas-adsorption isotherms are categorized by IUPAC into six categories<sup>58</sup> shown in Figure 2.8.

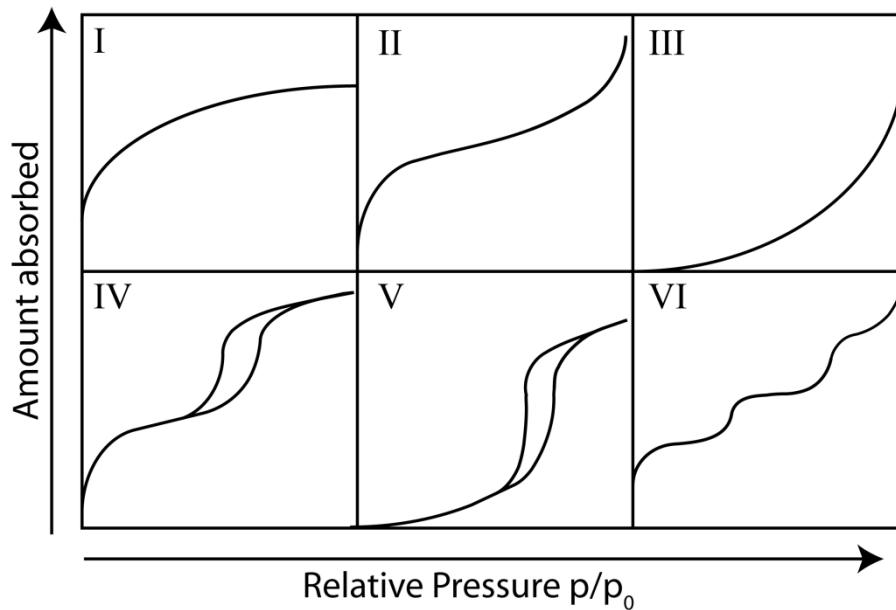


**Figure 2.8:** Classification of sorption isotherms as defined by IUPAC.<sup>58</sup> Type I isotherms are characteristic for microporous materials or chemisorption. Isotherms following type II are obtained from macro- or nonporous materials with a high heat of adsorption. Nonporous materials with low adsorption enthalpies follow type III. Type IV and V isotherms with a steep second slope (capillary condensation step) are characteristic for mesoporous materials with high (IV) or low (V) adsorption enthalpies; they often show a hysteresis loop. Type VI isotherms are attributed to several possibilities, e.g., layer-by-layer adsorption.

The shapes of isotherms strongly depend on the size of the pores which are therefore classified<sup>58</sup> according to their sizes:

- (i) pores with widths  $\leq 2$  nm are called micropores;
- (ii) pores of widths between 2 nm and 50 nm are called mesopores;
- (iii) pores with widths  $\geq 50$  nm (0.05  $\mu\text{m}$ ) are called macropores.

The most important isotherms for gas adsorption on porous solids are those of a shape following type I, II, and IV. Isotherms of type I are related to sorption experiments on microporous materials, with micropore filling taking place during the steep slope at low relative pressures. Type II isotherms represent sorption on macroporous/nonporous materials. A frequent feature of the Type IV isotherm is a hysteresis loop, which is associated with capillary condensation taking place in mesopores. In Type IV isotherms the gas absorption proceeds via multilayer adsorption followed by capillary condensation in mesopores (steep steps in the isotherms).

Data evaluation. The sorption isotherms reveal information about the specific surface area and the pore size distribution of a porous solid. For determination of the surface area the Brunauer-Emmett-Teller (BET) method has become the most widely used standard procedure. The BET method is an extension of the Langmuir theory, the theory for monolayer adsorption. The BET method is based on the assumptions that a) the gas molecules physically adsorb on a solid in multilayers with an infinite number of layers, b) there is no interaction between the particles in each adsorption layer and c) the Langmuir theory can be applied for each layer, meaning the adsorption enthalpy for all layers is the same except the first layer, where the enthalpy is only based on interactions between the adsorbent and the adsorptive.

These assumptions are described by the BET equation (in the linear form):

$$\frac{p}{n^a \cdot (p^0 - p)} = \frac{1}{n_m^a \cdot C} + \frac{(C-1)p}{n_m^a \cdot C \cdot p^0} \quad (2.11)$$

Here  $n^a$  is the amount adsorbed at the relative pressure  $p/p^0$  and  $n_m^a$  is the monolayer capacity.  $C$  is the BET constant, which is related to the enthalpy of adsorption in the first monolayer. In the region of multilayer adsorption ( $0.05 < p/p^0 < 0.35$ )  $\frac{p}{n^a \cdot (p^0 - p)}$  is proportional to  $\frac{p}{p^0}$  which can be shown in the BET plot. The slope and the y-intercept of the line in this plot can then be

used to calculate the monolayer capacity  $n_m^a$  and the BET constant  $C$ , which can be subsequently used for calculation of the specific surface area.

The pore size distribution (PSD) is the distribution of pore volume with respect to pore size. The classical computation of pore size distribution is the Barret-Joyner-Halenda method (BJH) which uses a modified form of the Kelvin equation.

$$\frac{1}{r_1} + \frac{1}{r_2} = -\frac{RT}{\sigma^{lg}v^l} \ln \frac{p}{p^0} \quad (2.12)$$

It relates the principal radii,  $r_1$  and  $r_2$ , of the curvature of the liquid meniscus in the pore to the relative pressure,  $p/p^0$ , at which condensation occurs; here  $\sigma^{lg}$  is the surface tension of the liquid condensate and  $v^l$  is its molar volume.

The Kelvin equation describes the change in vapor pressure due to a curved liquid/vapor interface (meniscus) with radius  $r$  (e.g. in a capillary). This can be applied on the capillary condensation in mesopores.

In using this approach to obtain the pore radius or pore width, it is necessary to assume a model for the pore shape. The pore shape is generally assumed to be either cylindrical or slit-shaped which is not always realistic for mesoporous materials. In addition, the concept is not valid for very narrow pores, such as micropores or also small mesopores, where the thermodynamic concept of a smooth liquid/vapor interface and a bulk-like pore fluid is no longer a realistic description of the system. Thus significant divergences from the real pore sizes have to be taken into account. Modern methods use Density Functional Theory (DFT) calculations and Grand Canonical Monte Carlo (GCMC) simulations. These microscopic methods correctly describe the local field structure near curved walls. Those DFT based models give correct results for all pore size ranges from micropores to large mesopores and

should therefore be preferred to the classical BJH method. The DFT models (or kernels) are highly specific, they can be tailored regarding the sorbent material and the pore geometry (e.g. spherical or cylindrical pores) and can be applied on the adsorption as well as for the desorption branch. For this reason the full set of kernels does not exist yet for all materials, e.g., for carbon there are no kernels for calculation of the PSD from the adsorption branches. Nevertheless it is better in principle to use a silica-DFT kernel also for mesoporous carbon instead of using the BJH method. For better comparison with literature data the pore sizes calculated with the BJH model should also be listed.

In this thesis, the nitrogen-sorption measurements on powdered mesoporous materials were performed with a NOVA 4000e Surface area & Pore Size Analyzer or an Autosorb-1 by Quantachrome Instruments. All samples were outgassed at 150 °C for 12 hours prior to measurement.

## **2.4. Ellipsometry**

Ellipsometry is a technique that measures the change of polarization of light upon reflection (or transmission) of a sample. In general, linearly or circularly polarized light is used which is usually elliptically polarized after reflection at an interface. Ellipsometry is commonly used to measure film thicknesses for single layers or complex multilayer stacks ranging from a few angstroms or tenths of a nanometer to several micrometers with an excellent accuracy. It can be further used to determine the optical constants (complex refractive index and complex permittivity). The schematic setup is depicted in Figure 2.9.

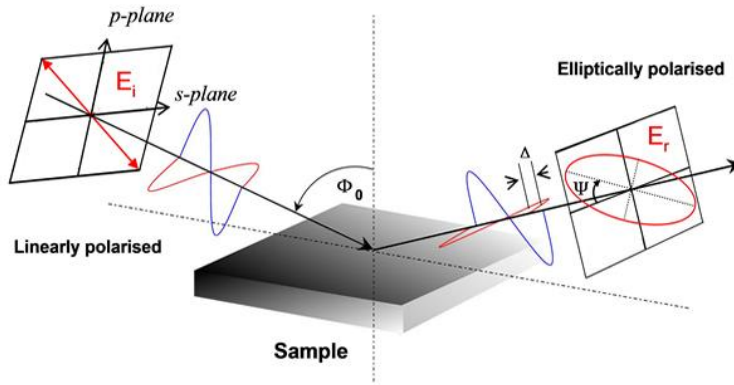


**Figure 2.9:** Schematic setup of an ellipsometric measurement.<sup>59</sup>

Linearly polarized light is reflected from a sample and gets elliptically polarized due to different reflectivity for the components of the incident beam that are perpendicular (s-plane) and parallel (p-plane) to plane of incidence. The amplitudes of the s and p components, after reflection and normalization to their initial values, are denoted by  $r_s$  and  $r_p$ , respectively (Figure 2.10).

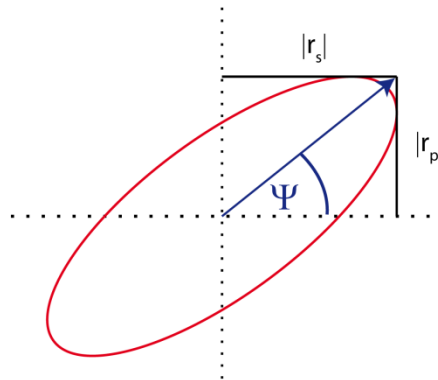


**Figure 2.10:** Field vector of elliptically polarized light and the components  $r_s$  and  $r_p$

The change of polarization can be described through the ratio  $\rho$  of the reflection coefficients  $r_s$  and  $r_p$ , which are the basis for the fundamental equation of ellipsometry:

$$\rho = \frac{r_p}{r_s} = \tan \Psi e^{i\Delta} \quad (2.13)$$

Thus,  $\tan \Psi$  is the amplitude ratio upon reflection, and  $\Delta$  is the phase shift (difference). Since ellipsometry is measuring the ratio of two values, it is very accurate and reproducible, relatively insensitive to scattering and fluctuations, and requires no standard sample or reference beam. Ellipsometry is an indirect method, i.e., in general the optical constants of the sample cannot be calculated directly from the measured  $\Psi$  and  $\Delta$ . Normally, a layer model must be constructed, which considers the optical constants and the thickness of all individual layers of the sample including the correct layer sequence. Using an iterative procedure, the unknown optical constants and thickness parameters are varied, and  $\Psi$  and  $\Delta$  values are calculated using the Fresnel equations. The calculated  $\Psi$  and  $\Delta$  values that match the experimental data best are then used to calculate the optical constants and thickness parameters of the sample.

## **2.5. Dynamic Light Scattering (DLS)**

Dynamic light scattering (also known as Photon Correlation Spectroscopy or Quasi-Elastic Light Scattering) is a technique that can be used to determine the size distribution of small particles in suspension or polymers in solution. When light hits particles that are small compared to the wavelength (below 250 nm) the light scatters in all directions (Rayleigh scattering). If the light source is a laser, and is therefore monochromatic and coherent, then one observes a time-dependent fluctuation in the scattering intensity. These fluctuations take place due to the fact that the small particles in solutions are undergoing Brownian motion and so the distance between the scatterers in the solution is constantly changing with time. The light scattered at different particles then interferes either constructively or destructively, and information is derived about the time scale of movement of the scatterers. The smaller the particles are, the faster they diffuse and thus the faster the intensity changes. The dynamic information of the particle movement can be derived from an autocorrelation of the measured

intensity. The second order autocorrelation function can be directly generated from the intensity trace:

$$g^{II}(q; \tau) = \frac{\langle I(t)I(t+\tau) \rangle}{\langle I(t)^2 \rangle} \quad (2.14)$$

$q$  is the wave vector,  $\tau$  is the delay time and  $I$  is the intensity.

For short time delays, the particles could not move to far from the initial state, thus the correlation is high. For longer time delays the correlation decreases exponentially to zero, this means after a long time there is no correlation between the scattered intensities. This exponential decay is related to the diffusion coefficients of the particles and can be fitted.

The Stokes-Einstein equation describes the relation of the diffusion coefficient  $D$  to the radius  $r$  of a spherical particle in a liquid phase with viscosity  $\eta$  and temperature  $T$ .

$$D = \frac{kT}{6\pi\eta r} \quad (2.15)$$

## 2.6. Infra-Red and Raman Spectroscopy

FT-IR and Raman spectroscopy are methods to investigate the chemical bonding in materials by excitation of vibrational modes.

At greater wavelengths than the visible part of electromagnetic radiation follows the infra-red part with wavelengths from 780 nm to 1 mm (or in wavenumbers:  $12800 \text{ cm}^{-1}$  to  $10 \text{ cm}^{-1}$ ). A photon of radiation in this range has an energy that can excite vibrations of chemical bonds and/or rotations of molecules. The infra-red region is subdivided in three parts. The first part is the near infra-red (NIR, 780 nm – 2.5  $\mu\text{m}$ ,  $12800 \text{ cm}^{-1}$  –  $4000 \text{ cm}^{-1}$ ), where mainly higher harmonics are located. The fundamental vibrations occur from 2.5  $\mu\text{m}$  to 50  $\mu\text{m}$  ( $4000 \text{ cm}^{-1}$  –

200  $\text{cm}^{-1}$ ) in the mid-infra-red (MIR). In far infra-red (FIR, 50  $\mu\text{m}$  to 1000  $\mu\text{m}$ , 200  $\text{cm}^{-1}$  – 10  $\text{cm}^{-1}$ ) only phonon modes and rotations are excited. In this thesis thin films on silicon substrates were investigated, therefore the spectra were measured with FT-RAIR (reflection absorption infra-red) with a Bruker IFS 66v/s instrument.

The Raman effect is based on the inelastic scattering of light. The scattered light can show either a shift towards lower frequencies (Stokes shift), that corresponds to an energy loss, or towards higher frequencies (anti-Stokes shift), that corresponds to an energy gain from the sample. The variety of bands in a Raman spectrum can be assigned to various vibrational modes in the molecule and thus can help to identify it. The selection rules for IR and Raman spectroscopy are completely different and therefore IR-active vibrations are often not Raman active and the other way round. For IR a vibrational mode is detectable if the dipole moment of the molecule changes during this vibration. For Raman spectroscopy the polarizability of the molecules changes during a Raman-active vibration.

## 2.7. Chapter References

48. Kiessig, H., *Ann. Phys.* **1931**, *10*, 715-68.
49. Kiessig, H., *Ann. Phys.* **1931**, *10*, 769-788.
50. Patterson, A. L., *Physical Review* **1939**, *56* (10), 978.
51. Müller-Buschbaum, P., Structure Determination in Thin Film Geometry Using Grazing Incidence Small-Angle Scattering. In *Polymer Surfaces and Interfaces*, Stamm, M., Ed. Springer Berlin Heidelberg: 2008; pp 17-46.
52. Yoneda, Y., *Physical Review* **1963**, *131* (5), 2010.
53. Vineyard, G. H., *Physical Review B* **1982**, *26* (8), 4146.

54. Goodhew, P. J.; Humphreys, J.; Beanland, R., *Electron microscopy and analysis*. 3rd ed. ed.; Taylor & Francis: London, 1988.
55. Williams, D. B.; Carter, C. B., *Transmission electron microscopy : a textbook for materials science : I : basics*. Plenum: New York, 1996.
56. [http://en.wikipedia.org/wiki/File:Scheme\\_TEM\\_en.svg](http://en.wikipedia.org/wiki/File:Scheme_TEM_en.svg).
57. <http://www.ncbi.nlm.nih.gov/books/NBK21629/>.
58. Sing, K. S. W.; Everett, D. H.; Haul, R. A. W.; Moscou, L.; Pierotti, R. A.; Rouquerol, J.; Siemieniewska, T., *Pure Appl. Chem.* **1985**, 57 (4), 603-619.
59. <http://www.tcd.ie/Physics/Surfaces/ellipsometry2.php>.

### 3. 2D-HEXAGONAL PERIODIC MESOPOROUS POLYMER RESIN THIN FILMS BY SOFT-TEMPLATING

This chapter is based on the article “2D-Hexagonal Periodic Mesoporous Polymer Resin Thin Films by Soft-Templating”,<sup>26</sup> *Chemistry of Materials* **2009**, 21 (24), 5754-5762. from Jörg Schuster, Ralf Köhn, Andreas Keilbach, Markus Doeblinger, Heinz Amenitsch and Thomas Bein

#### ABSTRACT

2D-hexagonal (plane group,  $p6mm$ ) mesoporous polymer resin thin films were obtained through evaporation-induced organic-organic self-assembly of a preformed oligomeric resol precursor and the triblock copolymer template pluronic P123. The polymer resin films were prepared on silicon wafers by spin-coating a mixture of precursor and surfactant in ethanol. Evaporation-induced self-assembly is followed by the formation of a condensed-wall material through thermopolymerization of the precursor oligomers, resulting in mesostructured phenolic resin films. Subsequent decomposition of the surfactant and partial carbonization were achieved through thermal treatment in inert atmosphere. The films are crack-free with tunable homogenous thicknesses, and show either 2D-hexagonal or lamellar mesostructure. An additional, yet unknown 3D-mesostructure was also found. The mesoporous polymer resin films can serve as precursors for various mesoporous carbon structures.

### 3.1. Introduction

Porous carbon materials are omnipresent and essential for a large number of modern applications. Beneficial properties such as high surface area, large pore volume, chemical inertness or electrical conductivity make them highly desirable for uses such as electrode materials for batteries, supercapacitors and fuel cells, as sorbents for separation and gas storage, or as catalyst supports.

Ordered mesoporous carbons (OMCs)<sup>6-8</sup> could offer advantages for several of these applications compared to traditional activated carbons, which typically consist of disordered microporous amorphous carbon. Possible disadvantages of activated microporous carbon include limited mass transport in the micropores and low conductivity due to defects.<sup>6</sup>

One of the first strategies for the synthesis of OMCs was the use of mesoporous silica, acting as hard template. An early example of periodic mesostructured carbon material was presented by Wu and Bein<sup>9</sup>, by filling the cylindrical mesopores of MCM-41 with polyacrylonitrile via radical polymerization, and subsequently creating conducting carbon nanowires through carbonization of the polymer. Ordered mesoporous carbon was first reported by Ryoo et al.<sup>10</sup>. They used the cubic mesoporous silica MCM-48 as hard template, sucrose as carbon precursor, and synthesized the carbon replica CMK-1 through pyrolysis of the included precursor. The silica template could be removed by etching with sodium hydroxide solution. With this hard-templating method, also called nano-casting, various carbon mesostructures could be synthesized using silica templates with different symmetries, e.g. CMK-1<sup>3</sup> and SNU-1<sup>11</sup> as replicas of cubic MCM-48 or CMK-3<sup>12</sup> and CMK-5<sup>13</sup> from hexagonal SBA-15. Further work addressed the electronic and electrochemical properties of these materials<sup>9, 11, 14</sup> and their surface functionalization<sup>15-17</sup>.

A general drawback of hard-templating methods is the need for an inorganic template, and a process that involves several time-consuming and costly steps for the impregnation of the template, and selective etching of the silica with hydrofluoric acid or sodium hydroxide solution.

While many mesoporous carbon materials have been made in bulk, it appears that the preparation of thin films following this strategy is more challenging. A major issue is the weak adhesion of the resulting carbon film after etching of the silica template.<sup>28</sup> In an alternative approach, mesoporous carbon films were prepared by spin-coating of sucrose and silica nanoparticles and subsequent removal of the silica.<sup>60</sup> However, these films contained a disordered pore system.

In contrast to hard templating methods, soft-templating strategies can directly produce the desired mesoporous carbon precursor structure. According to Liang et al.<sup>6</sup>, soft-templating approaches have four key requirements. They require (a) a polymerizable precursor system and (b) a suitable surfactant as structure-directing agent, which (c) sustains thermal treatments for curing the carbon yielding precursor but decomposes before or during carbonization. (d) The precursor system should form a stable polymeric wall material that can retain its mesostructure during template removal. Given these rather demanding requirements, it is not surprising that only a few systems have been reported so far for the synthesis of mesoporous carbon.

The first successful soft-templating approach towards mesoporous carbon was published in 1999 by Moriguchi et al.<sup>19</sup>. They synthesized organic mesophases of phenolic resin and cetyltrimethylammonium bromide (CTAB) acting as surfactant. However, the mesophases were not stable above 200 °C and thus no mesoporous carbon could be obtained. Thurn-Albrecht et al.<sup>20</sup> achieved the assembly of asymmetric large diblock copolymers of

polystyrene (PS) and poly(methyl methacrylate) (PMMA) to form hexagonal mesostructured films, whose orientation could even be controlled with electric fields.

Liang et al.<sup>21</sup> achieved the self-assembly of a polystyrene-*b*-poly(4-vinylpyridine) block-copolymer (PS-*P*4VP) and resorcinol and formaldehyde as carbon sources, using a vapor infiltration method. Through a sequence of synthesis steps, they ultimately made mesoporous carbon thin films with hexagonally arranged 33 nm pores that were oriented normal to the surface.

In 2006 Meng et al.<sup>22</sup> introduced another promising soft-templating approach by the self-assembly of a low-molecular-weight resol precursor and triblock copolymer templates with polyethylene and polypropylene blocks of variable lengths. They obtained powders with two-dimensional hexagonal ( $P6mm$ ), three-dimensional bicontinuous ( $Ia\bar{3}d$ ), body centered cubic ( $Im\bar{3}m$ ), and lamellar mesostructures. Thus mesoporous carbons with surface areas up to 1490 m<sup>2</sup>/g and thermal stability up to 1400 °C were realized.

Recently two new approaches were published. Dai et al.<sup>61</sup> made OMCs with even higher thermal stability, up to 2600 °C. They accomplished the self-assembly of resorcinol/formaldehyde with block-copolymer templates (e.g. Pluronic F127) under highly acidic conditions. An extremely small shrinkage during this high temperature treatment is another remarkable property of these OMCs. A single-step procedure for self-assembly in aqueous solution was accomplished by Lu et al.<sup>62</sup>

Despite these great achievements in the soft-templating of bulk mesoporous carbon materials, the synthesis of mesoporous carbon thin films is still a significant challenge. So far only very few, successful approaches were published. The vapor infiltration method was used for the above-mentioned resorcinol/formaldehyde/(PS-*P*4VP) system,<sup>21</sup> resulting in ordered

mesoporous carbon structures. However, the very large block-copolymers employed in this study are extremely expensive. Very recently a similar approach was used for a resorcinol/formaldehyde/F127 system<sup>63</sup>. Different unknown mesostructures were found with electron microscopy. A soft-templating pathway leading to thin films with face-centered orthorhombic (*Fmmm*) symmetry was reported by Tanaka et al.<sup>28</sup> They used evaporation-induced self-assembly (EISA) during spin-coating of synthesis mixtures with resorcinol, phloroglucinol and formaldehyde as carbon precursors, and Pluronic F127 as surfactant template under acidic conditions. The authors report a surface area and pore volume of 436 m<sup>2</sup>/g and 0.39 cm<sup>3</sup>/g for a sample carbonized at 400 °C, respectively, obtained by nitrogen adsorption of a scratched film. Despite these recent achievements, the variety of structures, the thermal stability, and the high surface areas and pore volumes of bulk OMCs have not been matched in thin films yet.

Here we report the synthesis of highly ordered mesoporous polymer resin thin films with 2D-hexagonal (*p6mm*) order through evaporation-induced organic-organic self-assembly, using only easily available reagents. These films were pyrolyzed to 400 °C and showed spectroscopic signatures of beginning carbonization at this temperature. The polymer resin films were deposited onto silicon wafers through spin-coating of a pre-synthesized oligomeric resol precursor and the triblock copolymer template Pluronic P123, followed by thermal treatments in inert atmosphere for thermopolymerization, template removal and partial carbonization. 2D-hexagonal (*p6mm*), lamellar and another yet unknown mesostructure were observed, depending on the template-to-precursor ratio in the synthesis. The films are crack-free with tunable homogeneous thicknesses of about 60 to 200 nm.

## 3.2. Experimental

**Chemicals.** Formalin (37 wt% formaldehyde in water) and the triblock copolymer Pluronic P123 ( $M_w = 5800$ , EO<sub>20</sub>-PO<sub>70</sub>-EO<sub>20</sub>) were purchased from BASF AG, and phenol from Merck KGaA. All chemicals were used without further purification. Silicon Wafers were donated by Siltronic AG.

### Synthesis.

*Resol precursor.* A low molecular weight precursor for the organic framework was synthesized in a reaction of phenol and formaldehyde in a base-catalyzed process according to Meng et al.<sup>22</sup>. The molecular weight average of the resol precursor is expected to be smaller than 500 g/mol (GPC<sup>22</sup>). For the synthesis, 6.1 g of phenol (0.064 mol) were molten in a flask with 1.3 g of 20 wt % sodium hydroxide solution (0.0065 mol). The mixture was heated up to 50 °C and then 10.5 g formalin (37 wt % formaldehyde in water, 0.1295 mol) were added dropwise. The molar ratio of phenol / formaldehyde / NaOH was 1 : 2 : 0.1. The clear, lightly yellow colored solution was stirred at 75 °C for one hour and then cooled down to room temperature. The precursor solution was neutralized with 1 M hydrochloric acid and the water was removed by vacuum evaporation below 50 °C. The resulting product was redissolved in ethanol to a total weight of 50 g.

*SDA Solution.* 1.00 g P123 (0.17 mmol) was dissolved in 20.0 g (0.45 mol) ethanol to give a 4.76 wt % solution. For a double concentrated (9.52 wt %) template solution, 1.00 g P123 (0.17 mmol) were dissolved in 9.5 g ethanol.

*Synthesis of Mesoporous Polymer Resin films with 2D-Hexagonal structure (p6mm).*

2D-hexagonal films were obtained in the molar ratio range of phenol / formaldehyde / NaOH / P123 = 1 : 2 : 0.1 : 0.0063-0.0095, which is equivalent to weight ratios of the SDA and precursor solution from 1 : 1 to 1.5 : 1. In a typical preparation, 1 g of the precursor solution was mixed with 1 g template solution (molar ratio phenol / formaldehyde / NaOH / P123 = 1 : 2 : 0.1 : 0.0063). After stirring for 10 min, a homogeneous solution was obtained. The mesostructured films were synthesized on polished silicon wafers. The wafers were cut into smaller pieces, washed with ethanol, and cleaned in an oxygen-plasma for one minute. The mixed precursor and SDA solutions were dropped on the wafers through a syringe filter (CHROMAFIL PET-20/15 MS, pore size 0.20  $\mu\text{m}$ ), and spin coated at 3000 rpm with an acceleration of 1260 rpm/s. The films were tempered at 100 °C for 24 h. For template removal and partial carbonization, the films were heated in a nitrogen flow with a ramp of 1 °C/min to the final temperature (400 °C) with a dwell time of 3 h at that temperature.

#### *Synthesis of Polymer films with Lamellar Mesostructure.*

The synthesis parameters for lamellar films were in the range of phenol / formaldehyde / NaOH / P123 = 1 : 2 : 0.1 : 0.0126-0.0189 (weight ratio: 2 : 1 to 3 : 1). In a typical preparation, 1 g of the precursor solution was mixed with 2.5 g template solution (1 : 2 : 0.1 : 0.0157).

After the same procedures of solvent evaporation during spin-coating and thermal treatment, mesostructured lamellar films were obtained.

#### *Synthesis of Polymer films with an unknown 3D mesostructure.*

The synthesis parameters for this structure were phenol / formaldehyde / NaOH / P123 = 1 : 2 : 0.1 : 0.0221 (weight ratio: 3.5 : 1). In a typical preparation, 1 g of the

precursor solution was mixed with 3.5 g template solution. For these films the same procedures of solvent evaporation during spin-coating and thermal treatment were performed.

#### *Variation of film thickness.*

To obtain thinner films, the mixtures of precursor and template were diluted with ethanol by weight. The degree of dilution (D1 to D11) represents the total weight of the diluted solution compared with the parent solution (D1). The solutions were spin-coated and tempered as the other samples described before. The double concentrated SDA-solution was used to get thicker films. These solutions are denoted Dconc. Even thicker films could be made by casting. For this purpose, the solutions were dropped onto silicon wafers without spin-coating. The resulting films were dried at room temperature.

#### *Nomenclature.*

The films are denoted S-D-T. S represents the structure; H for hexagonal, L for lamellar or U for the unknown phase. D stands for the degree of dilution and T represents the carbonization temperature. For example H-D2-400 °C denotes a film with hexagonal structure, degree of dilution D2 and pyrolyzed at 400 °C.

#### **Characterization.**

X-ray diffraction (XRD) of the films measurements were performed on a Scintag XDS 2000 in  $\theta$ - $\theta$  geometry (Cu-K $\alpha$ ;  $\lambda = 1.54 \text{ \AA}$ ).

The thicknesses of the films were determined by so-called Kiessig fringes which result from reflections between the film surface and the interface of film and substrate. In the case of very thin and homogenous films several orders of these surface wave reflections can be observed.

The reflection angles  $\theta_m$  and  $\theta_{m+1}$  of two consecutive fringes are related to the film thickness  $D$  by the formula:

$$D = \frac{\lambda}{2 \sin \theta_{m+1} - \sin \theta_m}$$

Grazing incidence small angle X-ray scattering (GISAXS) experiments were performed at beamline BL 5.2 L at Synchrotrone Elettra (Trieste, Italy). The wavelength of the incident beam was 0.15498 nm (8 keV), and the sample-detector distance was 1105 mm.

Transmission electron microscopy (TEM) data were obtained on a JEOL JEM 2011 microscope at an acceleration voltage of 200 kV. The HAADF-STEM images (high angle annular dark field scanning transmission electron microscopy) were recorded with a TITAN 80-300 microscope at an acceleration voltage of 300 kV. Cross-sections were prepared by dimple-grinding and ion-polishing. Raman spectra were recorded on a Jobin Yvon Horiba HR800 UV Raman Microscope using a HeNe laser emitting at 632.8 nm. IR-spectra were measured in reflection mode with a Bruker IFS 66v/s instrument.

### 3.3. Results and Discussion

One of the key parameters for the final structure in the EISA processes is the template/precursor ratio. Here, the ratio is denoted as weight ratio of the precursor and the template solutions, which can also be translated into the molar ratio of the educts phenol, formaldehyde and Pluronic P123. Mesoporous films could be obtained in a range of 1 : 1 to 3.5 : 1 for the template/precursor ratio.

The XRD-patterns of the as-synthesized films H-D1-100 °C, L-D1-100 °C and U-D1-100 °C are shown in Figure 3.1, ordered with respect to increasing template/precursor ratios 1 : 1, 2 : 1 and 3.5 : 1, respectively. Figure S 3.1 shows the XRD pattern of H-cast-100 °C. Sharp peaks between  $0.7$  and  $0.8^\circ(2\theta)$  can be observed in the patterns with full widths at half maximum between  $0.05$  (A, B) and  $0.08^\circ(2\theta)$  (C). They correspond to well-defined d-values of 11.5 to 11.9 nm of ordered matter parallel to the substrate. The reflections at higher angles can be indexed as the corresponding higher orders of these first reflections. The intensive and very sharp reflections in combination with the observation of higher diffraction orders confirm the formation of highly ordered mesoporous films. The absence of peaks for further lattice planes reveals the homogenous orientation of the mesoporous structures parallel to the substrate plane (with rotational freedom around the substrate normal).

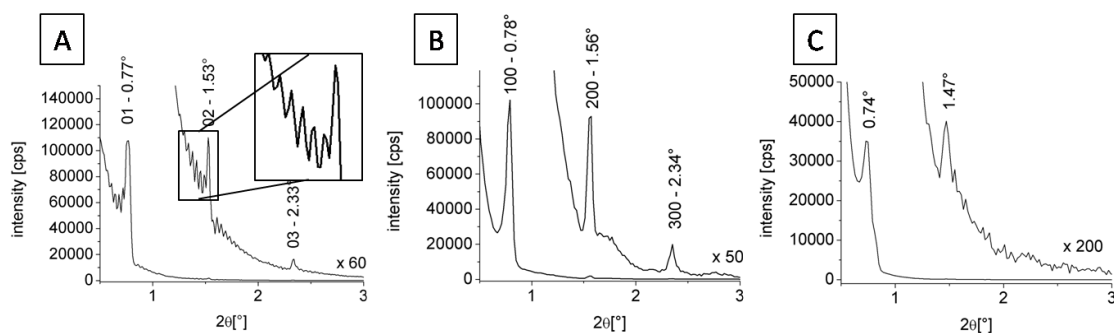


**Figure 3.1:** XRD-patterns of the as-synthesized samples A) H-D1-100 °C, B) L-D1-100 °C and C) U-D1-100 °C. The patterns are magnified in the region of the higher order reflections according to the number on top of the magnified graphs. Pattern A contains an inset showing Kiessig fringes.

For most of the patterns Kiessig fringes<sup>48-49</sup> could be observed (e.g. inset in pattern A), which could be used for film thickness calculations. With ellipsometry, the thicknesses of films with low intensity or without Kiessig fringes could also be measured. The measured values of both methods are in good agreement with each other. Table 3.1 shows the thicknesses measured with ellipsometry of a dilution series of the hexagonal and lamellar samples (H, L) with template / precursor ratios 1 : 1 and 2.5 : 1, respectively.

**Table 3.1:** Thickness variation through dilution of the synthesis mixtures

Sample name	Ratio [template/precursor]	Dilution [wt]	Specific volume [D1 = 1]	Thickness [nm] (Ellipsometry)
H-Dconc-100 °C	1 : 1	Conc.	0.738	360
H-D1-100 °C	1 : 1	0	1	294
H-D2-100 °C	1 : 1	1	2.05	140
H-D3-100 °C	1 : 1	2	3.102	73
L-D1-100 °C	2.5 : 1	0	1	238
L-D2-100 °C	2.5 : 1	1	2	108
L-D3-100 °C	2.5 : 1	2	3	67

The film thickness decreases with increasing dilution with ethanol for both the hexagonal and the lamellar films. The lamellar films are slightly thinner, due to the lower concentration of the precursor. The relationship between the thickness and the specific volume is plotted in Figure 3.2. We define the specific volume as equal to the volume ratio of ethanol to the parent solutions (D1), which can be slightly different to the weight ratios due to different densities of ethanol and the parent solutions.

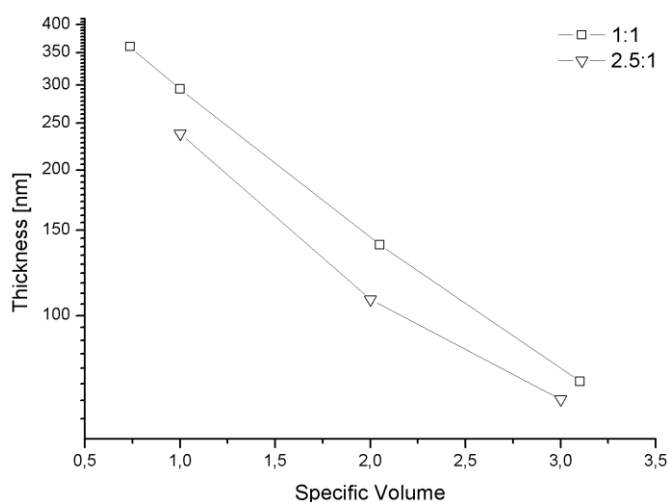


**Figure 3.2:** Mesosstructured film thickness (logarithmic scale) as a function of the specific volume for hexagonal (squares) and lamellar (triangles) films

The measured film thickness follows a logarithmic function with respect to the specific volume in the precursor solution. This allows the prediction of necessary dilution for other desired thicknesses.

## 2D-Hexagonal Mesostructure (plane group $p6mm$ ).

All the films were crack-free and showed homogeneous thickness after pyrolysis at 400 °C. The samples H-D1-400 °C still showed reflections in the diffraction patterns (Figure 3.3), while no remaining structure could be observed for the samples L-D1-400 °C and U-D1-400 °C. This already indicates that only a low template/precursor ratio results in a 3-dimensionally connected wall material. For the higher template/precursor ratios mesostructures without a self-supporting wall material were observed, such as a lamellar or an inverse micellar structure.

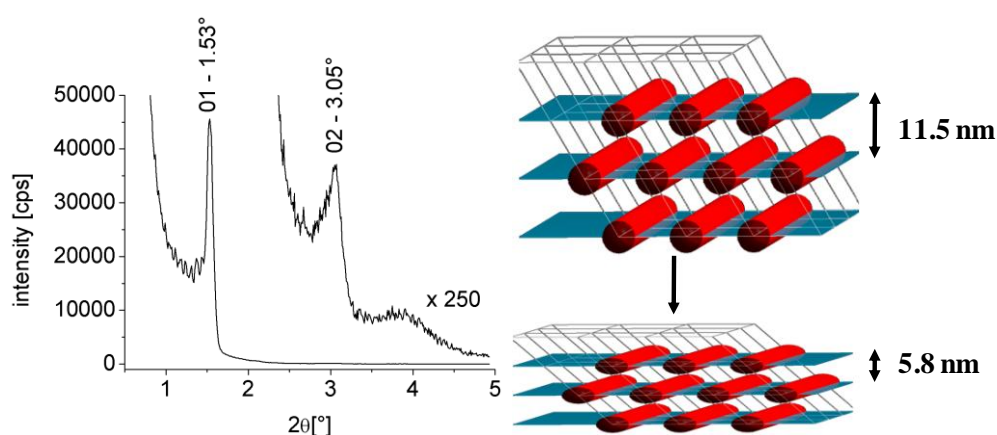


**Figure 3.3:** XRD-pattern of the sample H-D1-400 °C after pyrolysis. The reflections are shifted to higher angles due to shrinkage. The scheme illustrates the shrinkage during the partial carbonization process.

The measured  $d_{01}$ -value of 5.8 nm corresponds to shrinkage of around 50 % normal to the surface. Shrinkage during carbonization is a well-known process;<sup>22, 28</sup> it takes place due to pyrolysis of the template and condensation reactions in the evolving wall material. For one specific sample H-D1-100 °C, the overall thickness decreased from 294 to 140 nm, which is equivalent to a shrinkage of 52.5 %, and a similar 50 %-shrinkage for the lattice plane

distances from 11.5 nm to 5.8 nm could be extracted from the diffraction data, which can be viewed equivalent considering the measurement accuracy. The films were still crack-free which shows that the dimensions parallel to the wafer were fixed and shrinkage in these directions did not occur. Therefore an overall decrease of the film volume can only be caused by thickness shrinkage. For an initial 2D-hexagonal structure with  $p6mm$  symmetry the uniaxial shrinkage results in the plane group  $c2mm$ . In projection along the columns the pore shape becomes elliptical. Films heated to 600 °C do not show periodic order in XRD measurements, in contrast to the mesoporous carbon powders reported by Meng et al.<sup>22</sup>, which were stable up to 1400 °C. We note that the distortion for thin films can only occur in the direction perpendicular to the substrate, thus the distortion of the initial unit cell is large, and finally results in the collapse of the periodic mesostructure. For powders the initial unit cell can shrink in all directions, which implies that it does not necessarily have to be distorted. Synchrotron GISAXS experiments were carried out to identify the highly-ordered 2D hexagonal mesostructure as averaged structural information of the whole film, and to specify the unit cell parameters in terms of distortion during the thermal treatments. The patterns depicted in Figure 3.4 for the samples H-cast-100 °C, H-D1-100 °C and H-D1-400 °C show diffraction spots that can be attributed to a 2D hexagonal lattice of cylinders with the cylinders being oriented parallel to the substrate.

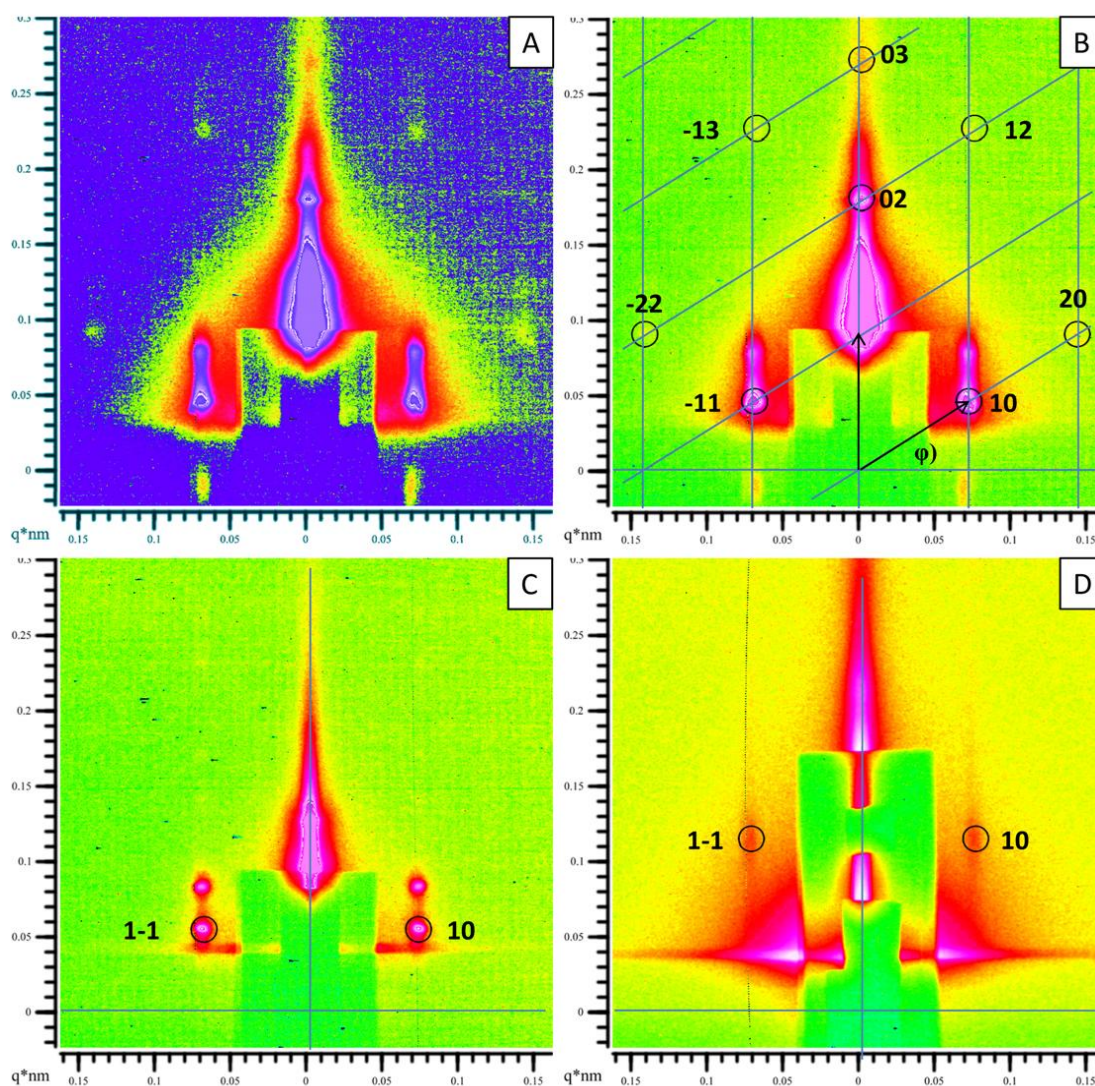


**Figure 3.4:** 2D-GISAXS patterns: A) Contrast enhanced image of H-cast-100 °C where the higher order reflections can be observed easily B) H-cast-100 °C with a linear intensity scaling visualizing the reciprocal lattice of the 2D-hexagonal structure, the peaks are indexed in a 2D-hexagonal unit cell. C) H-D1-100 °C before and D) H-D1-400 °C after pyrolysis. The indexing according to a 2D-hexagonal unit cell was retained, although it was distorted during template removal and pyrolysis. The most intense reflections in patterns A-C are doubled due to the grazing incidence geometry, the first peak is resulting from the X-rays scattered at the lattice planes and the second on top is a specular reflection of the first one.

All the patterns show very intense reflections, which can be analyzed regarding their d-values and angles  $\varphi$ , defined as angle between the connection of a peak with the zero beam and the horizontal axis. The peaks at  $\varphi = 90^\circ$  come from the lattice planes parallel to the surface, and their positions correspond to the data obtained in the one-dimensional experiments. Peaks along other directions ( $\varphi < 90^\circ$ ) are related to lattice planes that cut the substrate plane at the angle  $(90^\circ - \varphi)$ . The sample H-cast-100 °C showed the most intense pattern with several higher order reflections (A). Similar patterns have been reported for 2D-hexagonal silica films<sup>64-65</sup>. All the reflections lie on a reciprocal lattice of a slightly distorted 2D-hexagonal structure and could be indexed according to corresponding lattice planes. For the 2D-hexagonal structure,  $\varphi$  is nominally  $30^\circ$  for the 01 and the -11-reflection, respectively but strains, e.g., through shrinkage, can change these angles. In pattern (B),  $\varphi$  is around  $32^\circ$ , which is close to ideal considering the measurement accuracy. In pattern C, for sample H-D1-100 °C, the equivalent reflections could be observed, which reveals the hexagonal structure. This pattern does not show higher orders, due to its lower thickness of around 140 nm. In this pattern, the position of the zero beam cannot be defined very accurately, therefore the reflections are somewhat shifted and a quantitative evaluation of the d-values and angles from Pattern C was not possible. However, the same structure is expected here due to coincident d-values from the XRD patterns and the similar GISAXS patterns. For the cast film H-cast-100 °C in Figure 3.4A and B, the  $d_{10}$ -value (11.6 nm) and  $\varphi$  in combination with the  $d_{01}$ -value (11.2 nm) were used to calculate the unit cell parameters after the thermopolymerization. The results are illustrated in Figure 3.5. In the same figure we also show a unit cell, which was modified in terms of shrinkage by 50%, and exclusively perpendicular to the substrate.

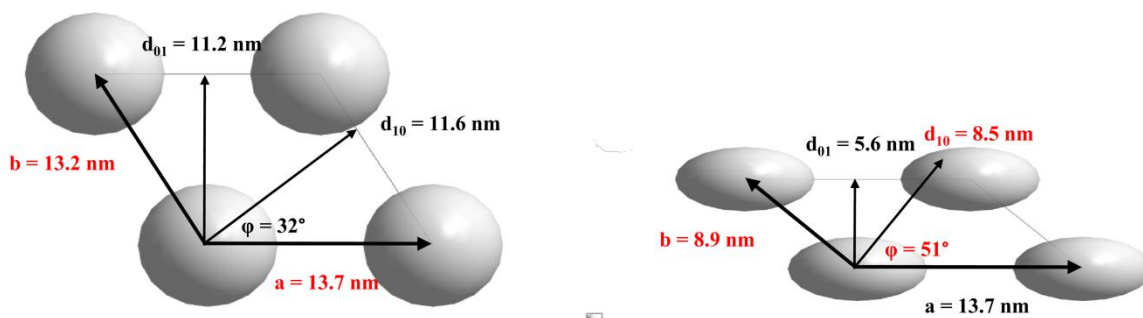


**Figure 3.5:** Unit cell parameters from of GISAXS data for the hexagonal cast film before (left), and after pyrolysis (right), applying shrinkage of  $d_{01}$  by 50 % and a constant parameter  $a$ . The calculated values are marked in red.

The unit cell parameter  $a$  is parallel to the substrate and therefore should not be changed by shrinkage. Figure 3.4D shows the GISAXS pattern after pyrolysis. The decrease of the  $d$ -values and the increase of  $\varphi$  show the distortion of the unit cell in agreement with the calculated unit cell in Figure 3.5.

Figure 3.6 displays a TEM-cross-section of the sample H-D1-400 °C, showing the 2D-hexagonal structure projected along the columns (A) and tilted out of the columnar projection (B). The images reveal the highly homogenous mesoporous structure, the constant film thickness, and the elliptically shaped pores.

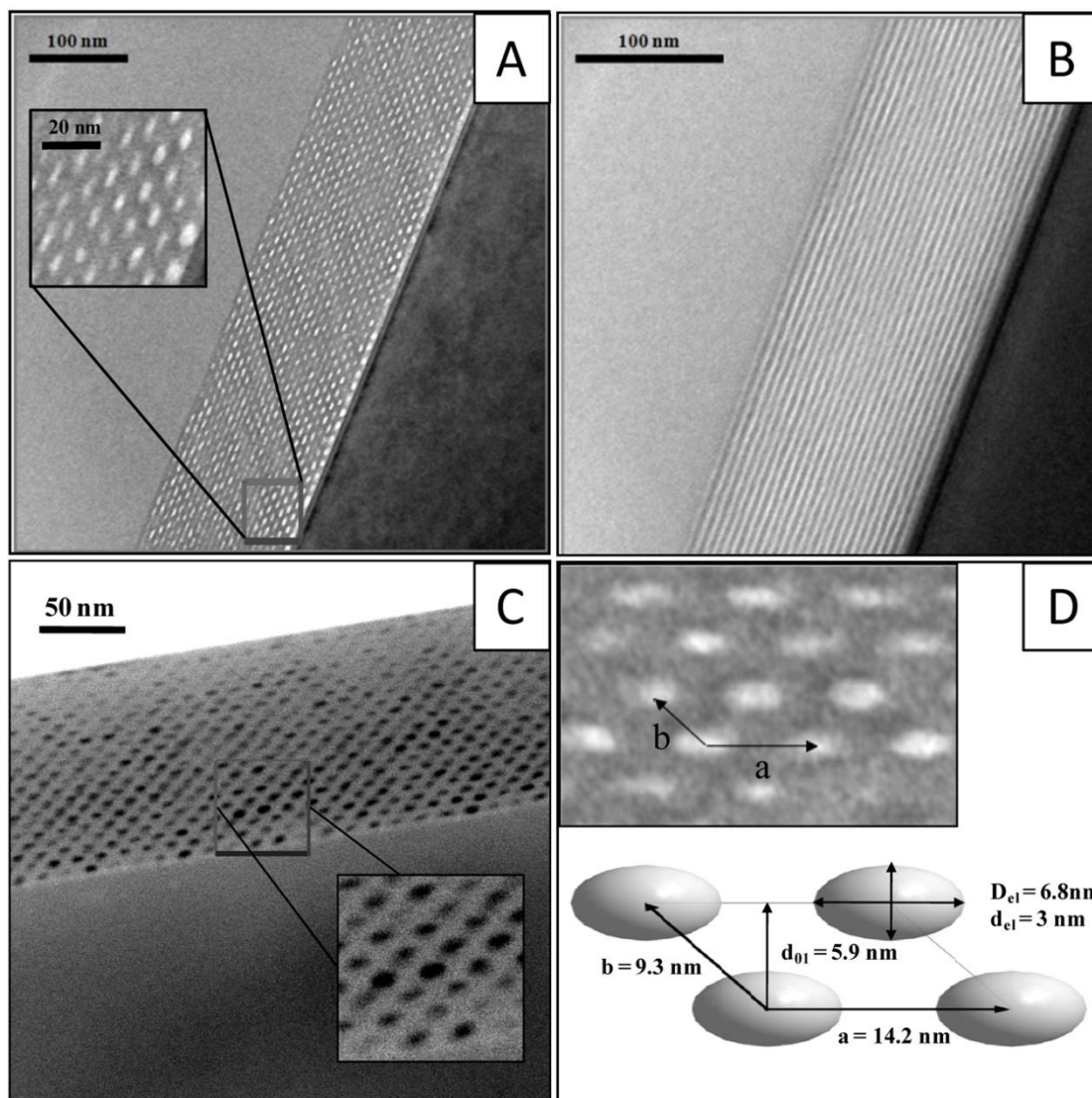


**Figure 3.6:** TEM cross-section of the sample H-D1-400 °C showing the formerly 2D-hexagonal structure A) projected along the columns, with an inset at higher magnification and B) tilted out of the columnar projection. C) HAADF-STEM image recorded along the columns. The white area in the image stems from the silicon wafer. D) The base vectors are depicted in the TEM-micrograph and in the unit cell. The estimated dimensions of the elliptically shaped pores are also depicted.

Image (A) was recorded along the columns with a small underfocus. At first approximation, the low resolution required allows for an interpretation in terms of mass-thickness contrast.

The FWHM of the intensity variations perpendicular and parallel to the film surface were used to estimate an average pore size and average cell parameters from more than 20 pores in each case. The values for the minor and the major axis as determined by TEM were in the range of  $3 \text{ nm} \pm 0.4 \text{ nm}$  and  $6.8 \text{ nm} \pm 0.6 \text{ nm}$ . These results were confirmed by complementary HAADF-STEM images (C), which allow a direct interpretation in first approximation. The ratio of minor axis to major axis is 0.5, which is equivalent with a shrinkage factor of 50 % assuming a perfect hexagonal columnar pore system and disc-like cross-sections of the pores before pyrolysis and thermopolymerization. This ratio is in good agreement with the shrinkage observed in the XRD measurements and is also in the accuracy range of the pore diameters determined from the TEM image (Figure 6A).

The unit cell dimensions extracted from these measurements are displayed in part D of Figure 3.6. They are in good agreement with the calculated unit cell from the GISAXS measurements shown before. The open porosity of the mesoporous films is indicated by large contrast variation (Figure 3.6C). The elliptical shape of the pores is also clearly visible. We note the lower contrast for pores that are near the wafer and thus far away from the surface of the film. Some of the pores are not completely empty. We suppose that some of the pyrolysis products could not leave the pores during the pyrolysis.

### **Framework constitution: 2D-Hexagonal Mesosstructure.**

The constitution of the wall material and the template were investigated with IR-spectroscopy. As discussed below, the peaks can be related to vibrations of functional groups.<sup>22, 66</sup> The comparison of films before and after thermal treatment at 400 °C is depicted in Figure 3.7.

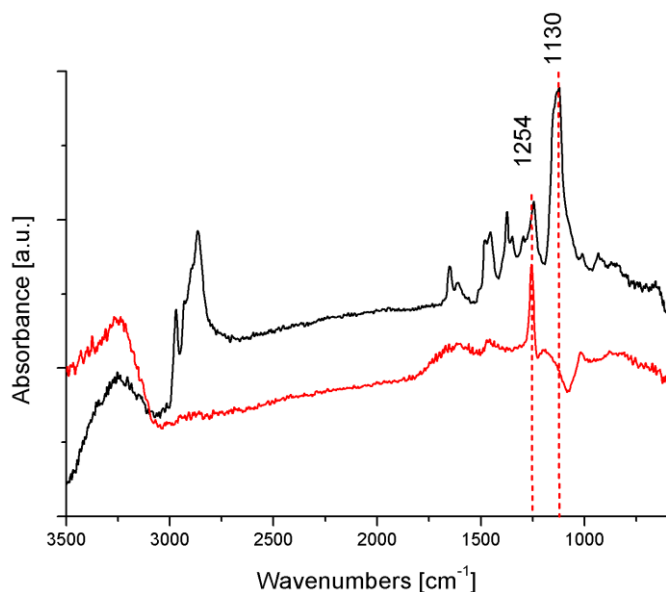


**Figure 3.7:** IR-spectra of an as-synthesized thin film (H-D1-100 °C) (black), and after template removal and pyrolysis at 400 °C (red) (H-D1-400 °C). The peak related to the template at 1130  $\text{cm}^{-1}$  vanished due to pyrolysis of the template.

The spectra are comparable to the spectra of polymer resin powders synthesized with the same template / precursor ratio synthesized by Meng et al.<sup>22</sup> The composite of the phenolic resin and the template shows several peaks related to vibrations of substituted benzene rings.<sup>66</sup> The broad band around 3300  $\text{cm}^{-1}$  arises from O-H-stretching of phenolic or aliphatic hydroxyl groups. The peaks around 3000  $\text{cm}^{-1}$  can be related to the aromatic and aliphatic C-H-stretching. The peak at 1611  $\text{cm}^{-1}$  is caused by carbon-carbon bond stretching of tri-substituted benzene rings. The band near 1475  $\text{cm}^{-1}$  is caused by C-H-bending of an aliphatic bridge structure. The intense band at 1130  $\text{cm}^{-1}$  can be related to C-O stretching in the template. All the bands nearly vanished after the heat treatment, especially the bands for aliphatic C-H stretching and the C-O stretching modes in the template, which confirms the decomposition and removal of the surfactant template. Only one band at 1254  $\text{cm}^{-1}$  remains or is even increasing in intensity for all samples heated to 400 °C. According to Trick et al.<sup>66</sup> it is

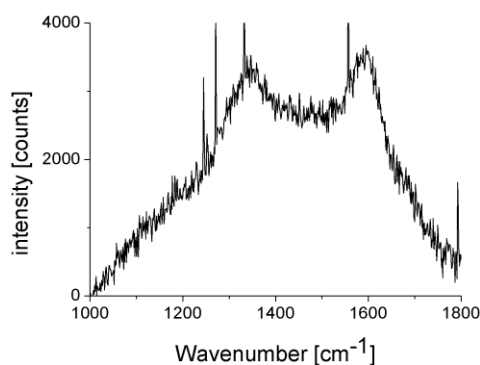
related to diphenyl ether bridges which are formed at temperatures around 400 °C, giving evidence of the increasing degree of cross-linking.

Figure 3.8 shows two films on glass slides, a colorless one before and a brown one after pyrolysis.



**Figure 3.8:** Films on glass slides as-synthesized H-D1-100 °C (right) and H-D1-400 °C after pyrolysis at 400 °C (left).

The absorption of light in a broad energy range is caused by the evolving amorphous carbon containing small graphitic domains. Even after pyrolysis the films stay transparent, which we attribute to their small thickness of only 140 nm, while powders are already deep black after pyrolysis at 400 °C. Raman spectroscopy has proven to be useful for the investigation of the microstructure of amorphous or graphitic carbon materials.<sup>67</sup> A Raman-spectrum of a pyrolyzed film is shown in Figure 3.9.



**Figure 3.9:** Raman spectrum of the sample H-D1-400 °C, pyrolyzed at 400 °C showing the broad carbon D and G bands at 1358  $\text{cm}^{-1}$  and 1600  $\text{cm}^{-1}$ ; the spikes are detector artifacts.

The well-known broad D and G bands of partially graphitic carbon are visible at 1358  $\text{cm}^{-1}$  and 1600  $\text{cm}^{-1}$ , respectively. The D-band is a breathing mode of six-carbon aromatic rings, which is forbidden in perfect graphene sheets and thus it is associated with small domain sizes. The G-band is a vibrational mode of in-plane bond stretching of pairs of  $\text{sp}^2$  carbon atoms, which is symmetry-allowed in ideal graphene sheets. The presence of the two bands at almost equal intensity is typical for nanocrystalline graphitic carbon generated by pyrolysis of organic precursor materials.<sup>22, 28</sup>

### **Lamellar Phase and an unknown Mesostructure.**

GISAXS patterns for the samples L-D1-100 °C and U-D1-100 °C are presented in Figure 3.10.

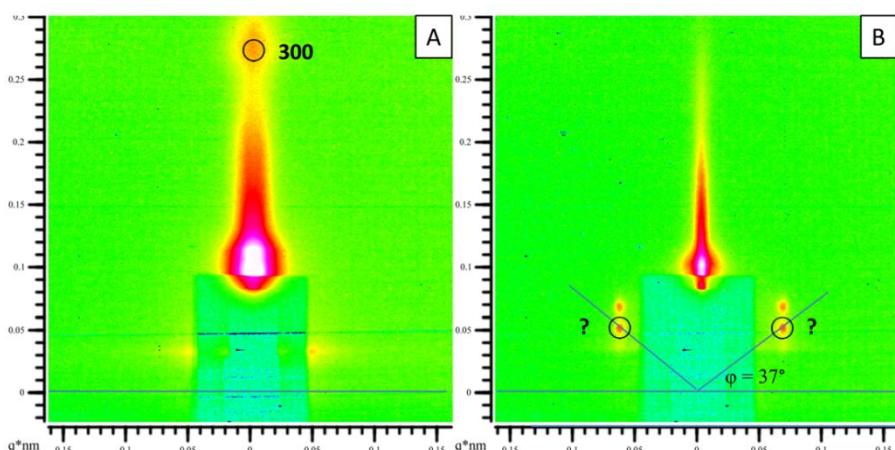


**Figure 3.10:** GISAXS patterns of a lamellar structured film L-D1-100 °C (A) and a film for higher template concentration with an unknown mesostructure U-D1-100 °C (B).

Only peaks on the vertical axis ( $\varphi = 90^\circ$ ) are visible in part A, which proves the lamellar structure of the film. Lamellar structures are commonly formed for the highest template / precursor ratios with Pluronic P123 as template<sup>22</sup>. Thus it is surprising that for a sample with an even higher template/precursor ratio (U-D1-100 °C) further reflections became visible. Because the structure was not stable upon template removal, and the ratio was higher than for the lamellar structure, we tentatively propose the formation of an inverse micellar structure in this sample. For example, possible structures include a reverse micellar arrangement of three-dimensionally ordered spheres of the carbon precursor surrounded by the template, or a hexagonal arrangement of carbon cylinders surrounded by the template, respectively. The GISAXS peak positions of this sample are similar to the pattern of the 2D-hexagonal structure, suggesting the formation of an inverse micellar structure having  $p6mm$  symmetry.

### 3.4. Conclusions

In this work we have demonstrated the synthesis of highly ordered mesoporous polymer resin thin films through partial carbonization of organic-organic composite films. Using a soft-

templating method, thin films with several mesostructures were formed during the evaporation-induced self-assembly of a preformed precursor and a block-copolymer template at variable molar ratios. The template removal upon pyrolysis from films with low template / precursor ratios leads to a compressed but still highly ordered mesostructure. The structural distortion during pyrolysis (from plane group  $p6mm$  to  $c2mm$ ) through uniaxial shrinkage along the substrate normal was followed with GISAXS measurements for the 2D-hexagonal phase. The structural parameters and the porosity could be directly visualized with TEM and HAADF-STEM images of cross-sections in columnar projection. This soft-templating approach represents a simple and inexpensive source for mesoporous polymer resin and carbon films, which can serve as a structural platform for various applications requiring highly stable mesoporous channel structures.

### Supporting Information:

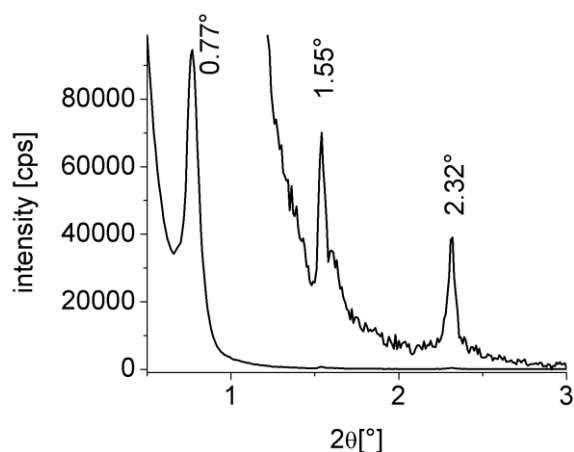


**Figure S 3.1:** X-ray diffraction pattern for the film H-cast-100°C.

### 3.5. Chapter References

6. Liang, C.; Li, Z.; Dai, S., *Angew. Chem., Int. Ed.* **2008**, *47* (20), 3696-3717.
7. Wan, Y.; Shi, Y.; Zhao, D., *Chem. Mater.* **2008**, *20* (3), 932-945.
8. Chang, H.; Joo, S. H.; Pak, C., *J. Mater. Chem.* **2007**, *17* (30), 3078-3088.
9. Wu, C.-G.; Bein, T., *Science* **1994**, *266* (5187), 1013-15.
10. Ryoo, R.; Joo, S. H.; Jun, S., *J. Phys. Chem. B* **1999**, *103* (37), 7743-7746.
11. Lee, J.; Yoon, S.; Hyeon, T.; Oh, S. M.; Kim, K. B., *Chem. Commun.* **1999**, (21), 2177-2178.
12. Jun, S.; Joo, S. H.; Ryoo, R.; Kruk, M.; Jaroniec, M.; Liu, Z.; Ohsuna, T.; Terasaki, O., *J. Am. Chem. Soc.* **2000**, *122* (43), 10712-10713.
13. Kruk, M.; Jaroniec, M.; Kim, T.-W.; Ryoo, R., *Chem. Mater.* **2003**, *15* (14), 2815-2823.
14. Xing, W.; Bai, P.; Li, Z. F.; Yu, R. J.; Yan, Z. F.; Lu, G. Q.; Lu, L. M., *Electrochim. Acta* **2006**, *51* (22), 4626-4633.
15. Li, Z.; Dai, S., *Chem. Mater.* **2005**, *17* (7), 1717-1721.
16. Bazula, P. A.; Lu, A.-H.; Nitz, J.-J.; Schueth, F., *Microporous Mesoporous Mater.* **2008**, *108* (1-3), 266-275.
17. Wang, X.; Liu, R.; Waje, M. M.; Chen, Z.; Yan, Y.; Bozhilov, K. N.; Feng, P., *Chem. Mater.* **2007**, *19* (10), 2395-2397.
19. Moriguchi, I.; Ozono, A.; Mikuriya, K.; Teraoka, Y.; Kagawa, S.; Kodama, M., *Chem. Lett.* **1999**, (11), 1171-1172.
20. Thurn-Albrecht, T.; DeRouchey, J.; Russell, T. P.; Jaeger, H. M., *Macromolecules* **2000**, *33* (9), 3250-3253.
21. Liang, C.; Hong, K.; Guiochon, G. A.; Mays, J. W.; Dai, S., *Angew. Chem., Int. Ed.* **2004**, *43* (43), 5785-5789.

22. Meng, Y.; Gu, D.; Zhang, F.; Shi, Y.; Cheng, L.; Feng, D.; Wu, Z.; Chen, Z.; Wan, Y.; Stein, A.; Zhao, D., *Chem. Mater.* **2006**, *18* (18), 4447-4464.
26. Schuster, J.; Koehn, R.; Keilbach, A.; Doeblinger, M.; Amenitsch, H.; Bein, T., *Chem. Mater.* **2009**, *21* (24), 5754-5762.
28. Tanaka, S.; Katayama, Y.; Tate, M. P.; Hillhouse, H. W.; Miyake, Y., *J. Mater. Chem.* **2007**, *17* (34), 3639-3645.
48. Kiessig, H., *Ann. Phys.* **1931**, *10*, 715-68.
49. Kiessig, H., *Ann. Phys.* **1931**, *10*, 769-788.
60. Pang, J.; Li, X.; Wang, D.; Wu, Z.; John, V. T.; Yang, Z.; Lu, Y., *Adv. Mater.* **2004**, *16* (11), 884-886.
61. Wang, X.; Liang, C.; Dai, S., *Langmuir* **2008**, *24* (14), 7500-7505.
62. Lu, A.-H.; Spliethoff, B.; Schueth, F., *Chem. Mater.* **2008**, *20* (16), 5314-5319.
63. Kataoka, S.; Yamamoto, T.; Inagi, Y.; Endo, A.; Nakaiwa, M.; Ohmori, T., *Carbon* **2008**, *46* (10), 1358-1360.
64. Gibaud, A.; Grosso, D.; Smarsly, B.; Baptiste, A.; Bardeau, J. F.; Babonneau, F.; Doshi, D. A.; Chen, Z.; Brinker, C. J.; Sanchez, C., *J. Phys. Chem. B* **2003**, *107* (25), 6114-6118.
65. Smarsly, B.; Gibaud, A.; Ruland, W.; Sturmayer, D.; Brinker, C. J., *Langmuir* **2005**, *21* (9), 3858-3866.
66. Trick, K. A.; Saliba, T. E., *Carbon* **1995**, *33* (11), 1509-15.
67. Ferrari, A. C.; Robertson, J., *Phys. Rev. B* **2000**, *61* (20), 14095-14107.

## 4. CUBIC AND HEXAGONAL MESOPOROUS CARBON IN THE PORES OF ANODIC ALUMINA MEMBRANES

This chapter is based on the article “Cubic and Hexagonal Mesoporous Carbon in the Pores of Anodic Alumina Membranes”,<sup>25</sup> accepted by *Chemistry – a European Journal* from Jörg Schuster, Andreas Keilbach, Ralf Köhn, Markus Doeblinger, Thilo Dörfler, Teresa Dennenwaldt und Thomas Bein.

### ABSTRACT

Cubic and circular hexagonal mesoporous carbon phases in the confined environment of Anodic Alumina Membranes (AAM) pores were obtained by organic-organic self-assembly of a preformed oligomeric resol precursor and the triblock copolymer templates Pluronic F127 or P123, respectively. Casting and solvent-evaporation were followed by self-assembly and the formation of a condensed wall material by thermopolymerization of the precursor oligomers, resulting in mesostructured phenolic resin phases. Subsequent thermal decomposition of the surfactant and carbonization were achieved through thermal treatment at temperatures up to 1000 °C in an inert atmosphere. The resulting hierarchical mesoporous composite materials were characterized by small-angle X-ray scattering and nitrogen sorption measurements. The structural features were directly imaged in TEM cross-sections of the composite membranes. For both structures the AAM pores were completely filled and no

shrinkage was observed, due to strong adhesion of the carbon wall material to the AAM pore walls. As a consequence, the pore size of the mesophase system stays almost constant even after thermal treatment at 1000 °C.

#### **4.1. Introduction**

Porous carbon materials are intensively used and indispensable for a large number of modern applications. They are employed as electrode materials for batteries, supercapacitors and fuel cells, as sorbents for separation and gas storage, or as catalyst supports due to their favorable properties such as high specific surface area and pore volume, chemical inertness or electrical conductivity.

Ordered mesoporous carbons (OMCs)<sup>6-8</sup> – tailor-made in terms of macroscopic morphology and properties of the periodic mesopore system – could be advantageous for several of these applications compared to conventional activated carbons, which typically consist of disordered microporous amorphous carbon. Possible drawbacks of activated microporous carbon include limited mass transport within the micropores and low conductivity due to defects.<sup>6</sup> One of the first strategies for the synthesis of OMCs was the use of periodic mesoporous silica as hard template leading to carbon replicas of the original silica structures. An early example of periodic mesostructured carbon was presented by Wu and Bein,<sup>9</sup> by replicating the cylindrical mesopores of MCM-41 with polyacrylonitrile via radical polymerization followed by carbonization of the polymer to yield conducting carbon nanowires. Ordered mesoporous carbon was introduced by Ryoo et al.<sup>10</sup> With this hard-templating method, also called nano-casting, various carbon mesostructures could be synthesized using silica templates with different symmetries, e.g. CMK-1<sup>10</sup> and SNU-1<sup>11</sup> as replicas of cubic MCM-48 or CMK-3<sup>12</sup> and CMK-5<sup>13</sup> from hexagonal SBA-15. Further work

focused on the electronic and electrochemical properties of these bulk materials<sup>9, 11, 14</sup> and their surface functionalization.<sup>15-18</sup>

While various mesoporous carbon phases have been synthesized in bulk form by hard-templating, it appears that their preparation within confined environments – as thin films on planar substrates or as fibers within the pores of anodic alumina membranes – following this strategy is more challenging. A major issue is the weak adhesion of the resulting carbon material after etching of the silica template.<sup>28</sup> In contrast to hard templating methods, soft-templating strategies – using liquid crystal phases of surfactants or block copolymers as templates – can directly produce the designated mesoporous carbon precursor structure.

The first successful soft-templating method on the way to mesoporous carbon was published in 1999 by Moriguchi et al.<sup>19</sup> However, the mesophases were not stable above 200 °C and thus no ordered mesoporous carbon could be obtained. A mesostructured composite that survives template removal and carbonization was first realized by Liang et al.<sup>21</sup> through the self-assembly of a polystyrene-*b*-poly(4-vinylpyridine) block-copolymer (PS-*P4VP*) and resorcinol and formaldehyde as carbon sources, using a vapor infiltration method. Through a sequence of synthesis steps, they finally prepared mesoporous carbon thin films with hexagonally arranged 33 nm pores that were oriented normal to the surface. In 2006 Meng et al.<sup>22</sup> introduced another promising soft-templating approach by the self-assembly of a low-molecular-weight resol precursor and triblock copolymer templates with polyethylene and polypropylene blocks of variable lengths, leading to OMC bulk materials with variable symmetries. Further progress concerning high thermal stability or easier synthesis conditions for bulk materials were achieved by Wang<sup>61</sup> and Lu.<sup>62</sup>

A soft-templating pathway leading to thin films with face-centered orthorhombic (*Fmmm*) symmetry was reported by Tanaka et al.<sup>28</sup> Recently we reported a soft-templating

method for highly ordered mesoporous polymer resin thin films with a 2D-hexagonal order ( $p6mm$ ).<sup>26</sup>

Mesoporous phases within the pores of Anodic Alumina Membranes (AAM) were first achieved with mesoporous silica. In 2003, Yang et al.<sup>68</sup> synthesized a circular hexagonal mesoporous silica. Here the mesopores form circles around the axis of the columnar AAM pores (or the membrane normal). Yamaguchi et al.<sup>69</sup> realized a columnar hexagonal silica phase, here the mesopores are oriented along the axis of the AAM pores. Platschek et al. systematically investigated the influence of surfactant concentration and humidity<sup>70</sup> on the ratio of circular to columnar phase and showed that the ratio of these phases can be tuned towards pure columnar phases. The authors also found a strongly favorable effect of the addition of inorganic salts on the phase formation process in combination with reduced shrinkage.<sup>71</sup> The kinetics of the mesostructure formation and phase transformations between the two hexagonal phases were investigated by *in-situ* GISAXS measurements.<sup>72</sup> Further progress on the way to confined mesoporous organic phases was accomplished by Keilbach et al.<sup>73</sup> by synthesizing periodic mesoporous organosilicas (PMOs) in AAM pores. Two phases could be found, a circular hexagonal one and a cubic phase with  $Im\bar{3}m$  symmetry, which had never been reported before in AAMs.

The first examples of pure organic mesophases in AAMs were reported in 2007. Zheng et al.<sup>34</sup> showed a self-assembly process to core-shell mesoporous carbon nanofibers using an oligomeric resol precursor and Pluronic F127 as template, followed by carbonization up to 700 °C. After etching away the alumina, the structure and porosity of the fibers could be characterized with electron microscopy and nitrogen sorption. Steinhart et al.<sup>32</sup> synthesized mesoporous carbon fibers by solvent-free infiltration of a precursor mixture into porous alumina and carbonization at moderate temperatures of 500 °C. Wang et al.<sup>33</sup> achieved the

synthesis of circular hexagonal mesoporous carbon in AAM pores that had contact to a silicon wafer. The fibers could be isolated as free-standing mesoporous carbon nanofiber arrays through a supercritical CO<sub>2</sub> drying process. TEM micrographs of the fibers showed columnar oriented mesochannels in the middle of some fibers surrounded by the circular phase. The same group also reported a detailed study on the synthesis of mesoporous carbon in AAMs with a resol precursor and several templates resulting in variable ordered and disordered mesostructures.<sup>74</sup> They could also characterize the conductivity of the carbon fibers by conductive atomic force microscopy (C-AFM). Recently, Zheng et al.<sup>24</sup> investigated the restricted shrinkage in AAMs for the first time for mesoporous carbon by nitrogen sorption of the isolated fibers carbonized at different temperatures. They could show that the pore size did not shrink but instead increased due to a strong adhesion to the alumina walls during carbonization. An alternative macroporous template was recently introduced by Liu et al.<sup>35</sup> Here a calcined crab shell was used as hard template, which consists of CaCO<sub>3</sub> with disordered pores of 70 nm in diameter.

Despite these recent achievements, control of symmetry, order and orientation of ordered mesoporous carbon in confined environments remains a challenge. Due to high processing temperatures during carbonization, OMCs often encounter significant shrinkage and distortion of their initial structures. As a consequence most of the hierarchical composite systems offer poor fill factors after template removal and carbonization, which can be a knock-out criterion for applications, e.g., for separation of biomolecules through nanofiltration. Moreover, for many applications accessibility and permeability of the mesostructures along the AAM channels are key features of paramount importance. Thus, to achieve molecular access into the pore system, the discovery of new open mesoporous structures is required.

Here we report on the soft-templating synthesis procedure of highly ordered mesoporous carbon phases in the pores of AAMs showing for the first time a cubic symmetry (space group

$Im\bar{3}m$ ) allowing access into the pore system. This system is compared to mesoporous carbon phases showing the circular hexagonal symmetry (plane group  $p6mm$ ), and obtained at similarly high carbonization temperatures. The still embedded OMC nanofibers were characterized by nitrogen sorption, two-dimensional small-angle X-ray scattering (2D-SAXS) and transmission electron microscopy (TEM) regarding their porosity, fill-factor and order and orientation of the mesostructures. Both hierarchical systems offer excellent fill factors in the alumina channels and very high surface areas. No shrinkage of the mesopore system was observed upon carbonization up to about 800 °C, due to the strong adhesion of the carbon wall material to the AAM pore walls, while a small shrinkage occurred at 1000 °C. As a consequence, the pore size of the mesophase system stays almost constant even after thermal treatment at 1000 °C.

## 4.2. Results and Discussion

**Mesoporous Polymer Resin and Carbon in AAOs with Cubic Structure.** 2D-SAXS measurements were carried out to identify the cubic mesostructures as averaged structural information of the membrane, to specify the unit cell parameters, and their evolution during thermal treatments. Figure 4.1 shows the SAXS patterns for the samples Cub-400, Cub-600 and Cub-1000. All the SAXS patterns show the very intense reflections (squares) that are characteristic for a highly ordered body centered cubic structure.<sup>73</sup> They can be indexed according to the cubic  $Im\bar{3}m$  mesostructure showing only reflections perpendicular to two possible zone axes, [01-1] and the [11-2], which was also confirmed by the following TEM micrographs (Figure 4.2). Due to the measurement geometry with a tilt angle of 10°, the 01-1 reflection, which would be on the vertical axis, cannot be observed.

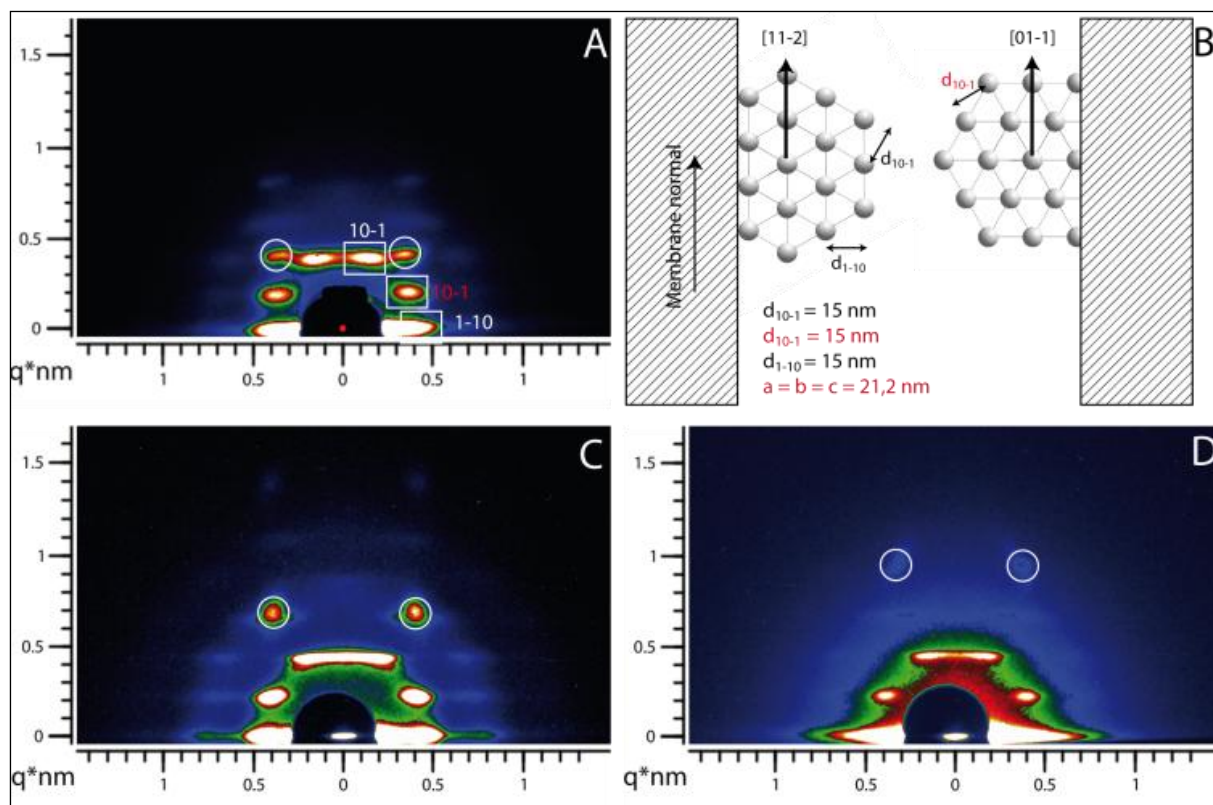


**Figure 4.1:** (A) SAXS pattern for the sample Cub-400 indexed according to the cubic ( $Im\bar{3}m$ ) unit cell; (B) corresponding unit cell viewed along  $[111]$  and its possible orientations along the membrane normal,  $[11-2]$  and  $[01-1]$ ; SAXS pattern for the sample (C) Cub-600, and (D) SAXS pattern for the sample Cub-1000. The circles show reflections from a top layer on the membrane.

At 400 °C the unit cell (Figure 4.1B) is undistorted. This is related to a restricted shrinkage behavior in contrast to thin films, where uniaxial shrinkage of around 50 % occurs.<sup>26</sup> From 400 °C to 600 °C (Figure 4.1C) only small peak shifts to higher angles are visible, while no further shrinkage to 1000 °C (Figure 4.1D) can be observed. Even at 1000 °C (Figure 4.1D) the SAXS pattern shows intense peaks and higher order reflections. Reflections assigned to a top layer on the membrane (circles) show a much larger peak shift as the temperature increases from 400 °C to 600 °C and to 1000 °C, respectively.

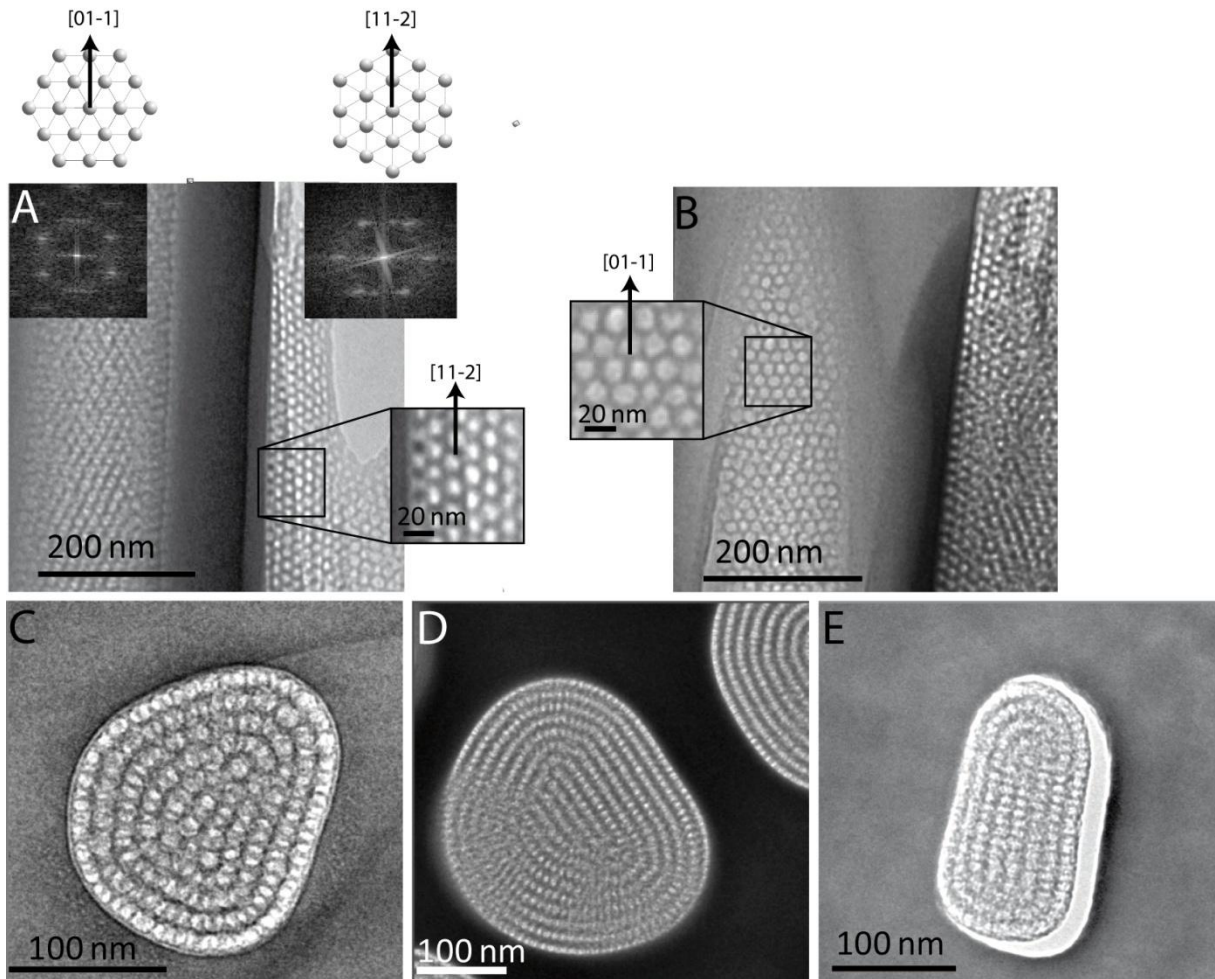


**Figure 4.2:** TEM micrographs of the sample Cub-400 (A, B) in cross-section with FFT insets of the left and the right part of image A, revealing the two different orientations of the cubic unit cell; The insets in image A and B show the two orientations at higher magnification. ; Samples Cub-400 (C), Cub-600 (D) and Cub-1000 (E) in plan view recorded in [11-2] zone axis.

The cubic structure can also be observed in TEM micrographs. For the sample Cub-400, the cross-section in Figure 4.2A reveals the two possible orientations of the  $Im\bar{3}m$  unit cell regarding the membrane normal. Both the left and the right fiber are recorded in [111] zone axis. However, the membrane normal of the left fiber is along [01-1] while the right fiber is

along [11-2]. The two fibers are tilted by 30° around [111] with respect to each other. The combination of both 2D-Fourier transforms (FFTs) of the images shows peaks at positions corresponding to the SAXS diffraction pattern in Figure 4.1A, illustrating that the SAXS pattern matches the structural elements seen in the TEM cross-section. The two different orientations are also clearly visible in the higher magnified insets of Figure 4.2A and 2B. The two different orientations were observed for several fibers, even both orientations in only one fiber were occasionally observed. The [11-2] orientation seems to be preferred at the interface to the AAO walls, while the [01-1] orientation was found mostly in the center of the pores. The plan view images (Figure 4.2C, D, E) of the samples Cub-400, Cub-600 and Cub-1000 reveal a high fill factor, all the membrane pores are filled, while no delamination from the membrane walls occurred at 600 °C. At a carbonization temperature of 1000 °C, delamination is visible for the majority of pores.

The sample Cub-800 (not shown) still showed a high fill-factor and no delamination. All the plan view images show a circular pattern looking like “pearls on a string” that would match both the [01-1] and the [11-2] orientation, which are difficult to distinguish. However, the parallel orientation of this “string” regarding the AAO walls and the related distances of about 15 nm determine the [11-2] orientation. The cell dimensions in all TEM images are in good agreement with the aforementioned SAXS data.

The porosity properties (Table 4.1) were determined by nitrogen sorption measurements of the OMC/AAM composites. Figure 4.3 depicts the isotherms of the samples Cub-400, Cub-600 and Cub-1000 with their respective pore size distributions. The isotherms all show the typical type-IV shape commonly observed for mesoporous materials, with a large adsorption-desorption hysteresis for the samples carbonized at 400 °C and 600 °C. These wide hysteresis loops can be attributed to large pores connected by smaller windows. This effect appears to be less distinct for higher carbonization temperatures, indicating that the

entrances to the large pores are widening up. The calculation of the pore-size distributions was done using NLDFT methods using a silica kernel for cylindrical and spherical pores for the adsorption branch. This model is the best compromise for this system, as corresponding models for carbon materials do not yet exist.

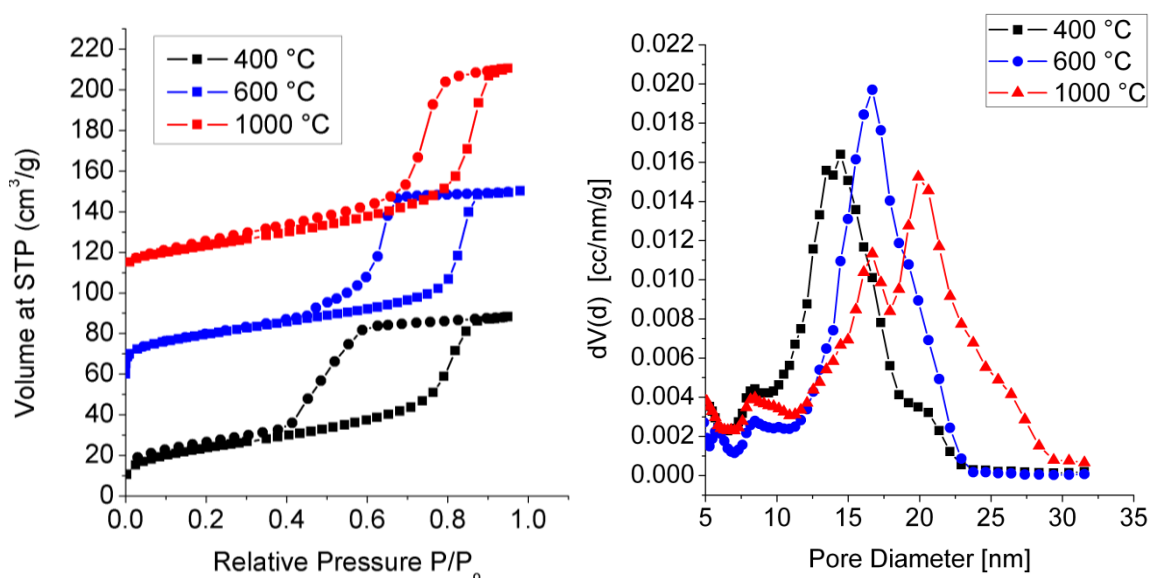


**Figure 4.3:** Nitrogen sorption isotherms (left) for the OMC/AAM composites Cub-400, Cub-600 and Cub-1000 and their pore size distributions (right) from the adsorption branches; the isotherms of Cub-600 and Cub-1000 are offset vertically by 50 and 100 cm<sup>3</sup>/g, respectively.

Sample Cub-400 shows a very large hysteresis loop and a small gap between adsorption and desorption branches of the isotherm at low pressures between 0.0 and 0.4  $p/p_0$ . We attribute this gap to an incomplete template decomposition, resulting in very long times needed for equilibration during desorption. The samples Cub-600 and Cub-1000 show higher surface areas and pore volumes. The pore size distributions show an increase in pore diameter from 400 °C to 1000 °C. This can be explained by the template decomposition and, more importantly, by the shrinkage of the walls due to carbonization, as the strong adhesion of the

OMC material to the AAM walls results in a restricted shrinkage<sup>24</sup> of the material. Two maxima are visible for Cub-1000, at 16 nm and at 20 nm. The bimodal pore size distribution is tentatively attributed to delamination and resulting shrinkage of some fibers, while others could not shrink due to the intact strong adhesion. For better comparison with literature data the pore sizes calculated with the BJH model from the adsorption branches are also listed in Table 4.1. The model is known to largely underestimate the pore diameters.

The composite membranes contain 7-15 wt% porous carbon; thus the mesoporous carbon fibers alone (without the alumina mold) show high specific surface areas of up to 1130 m<sup>2</sup>/g and specific pore volumes of up to 2.3 cm<sup>3</sup>/g (calculated for sample Cub-1000).

**Table 4.1:** Porosity properties for OMC/AAM composites Cub-400, Cub-600 and Cub-1000

Sample Name	wt% Carbon	BET surface area [m <sup>2</sup> /g]	Specific BET <sup>a</sup> area [m <sup>2</sup> /g]	Pore volume [cc/g]	Specific volume <sup>b</sup> [cc/g]	Pore size <sup>c</sup> NLDFT [nm]	Pore size BJH <sup>d</sup> [nm]
Cub-400	15.2	85	559	0.135	0.88	14	11
Cub-600	11.5	103.8	902	0.153	1.33	17	15.5
Cub-1000	7.3	82.5	1130	0.165	2.26	20, 16	15.5

[a] Calculated from the total BET surface area of the composite related to the carbon content.

[b] Calculated from the total pore volume of the composite related to the carbon content. [c]

Calculated by the NLDFT model adsorption branch model for cylindrical and spherical pores

with silica as adsorbent [d] Calculated by the BJH model from the adsorption branches

### Mesoporous Polymer Resin and Carbon in AAOs with Circular Hexagonal Structure.

In the second set of samples, the circular hexagonal structure could be identified with 2D-SAXS measurements as a highly ordered major phase in the membranes (Figure 4.4).

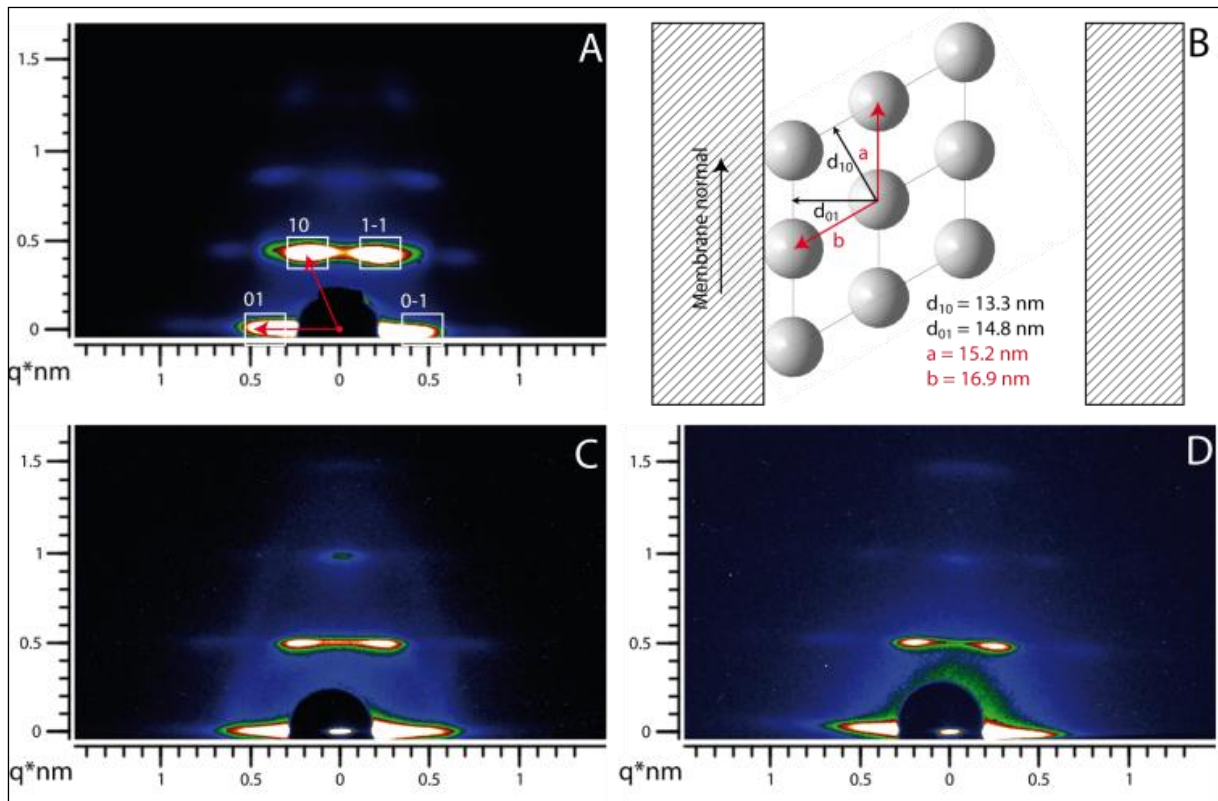


**Figure 4.4:** (A) SAXS pattern for the sample Hex-400 indexed in the circular hexagonal ( $p6mm$ ) unit cell; (B) unit cell for Hex-400 and its orientations regarding the AAM pore walls; (C) SAXS pattern for the sample Hex-600 and (D) SAXS pattern for the sample Hex-1000.

Up to 1000 °C all the SAXS patterns show very intense reflections (indicated by squares) characteristic for the circular hexagonal structure.<sup>70</sup> Figure 4.4A can be indexed according to a zone axis parallel to the hexagonal axis of the unit cell (plane group  $p6mm$ , Figure 4.4B). Again this small shrinkage can be attributed to confinement. From 400 to 600 °C (Figure 4.4C) only small peak shifts to higher angles are visible, while no further shrinkage can be observed for up to 1000 °C (Figure 4.4D). Even after heating to 1000 °C under nitrogen atmosphere the SAXS pattern shows intense peaks and higher order reflections.

The circular hexagonal structure in these samples can also be observed as the major phase in TEM micrographs. For the sample Hex-400, the cross-section in Figure 4.5A shows mesostructure with thin walls and large pores in hexagonal order, while the plan view image (Figure 4.5B) reveals the circular arrangement of the pores.

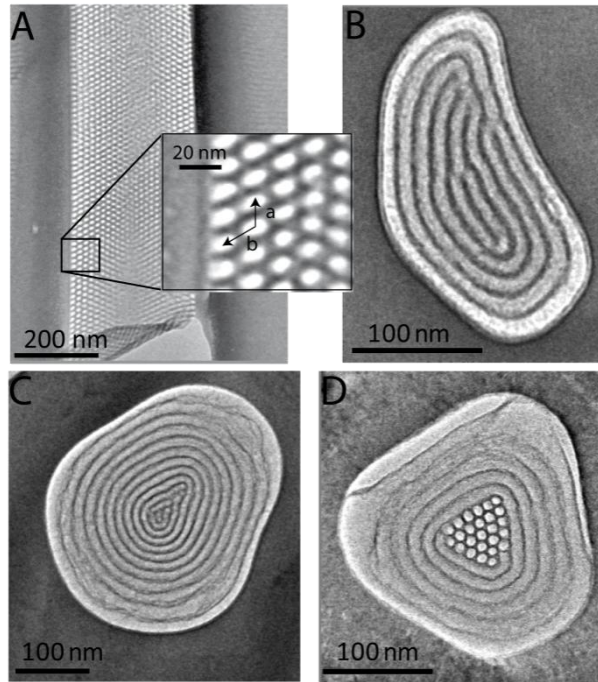


**Figure 4.5:** TEM micrographs of the sample Hex-400 (A, B) in cross-section (A) with an inset at higher magnification and in plan view (B); Samples Hex-600 (C) and Hex-1000 (D) in plan view.

The membranes show a high fill factor, all the pores are filled. Even after temperature treatment of up to 1000 °C, no significant delamination was observed. Plan view images for the samples heated above 600 °C (Figure 4.5C, D) all show a stretching of the pore diameters close to the membrane pore walls and shrinkage in the pore centers. This can explain the slight distortion found in the SAXS patterns (Figure 4.4). As a minor phase, the columnar hexagonal structure could be observed in several TEM plan views, e.g., in Figure 4.5D for Hex-1000. The mesoporous carbon fibers show circular hexagonal order close to the alumina

walls and some show columnar hexagonal order in the pore centers. We believe that the size and the shape of the membrane pores have a strong influence on the orientation of the hexagonal mesostructures. Nevertheless, the circular structure was found as majority phase in all samples of this group. The cell dimensions are in good agreement with the aforementioned SAXS data.

The porosity properties (Table 4.2) were also determined by nitrogen sorption measurements of the OMC/AAM composites. Figure 4.6 depicts the isotherms of the samples Hex-400, Hex-600 and Hex-1000 with their corresponding pore size distributions. Similar to the cubic samples, Hex-400 shows a very large hysteresis loop and a small gap between the adsorption and desorption branch of the isotherm at low pressure ranges. Due to the relatively large hysteresis, the NLDFT model for cylindrical pores of the adsorption branch was chosen. Again, this model is only available for silica as the adsorbent.

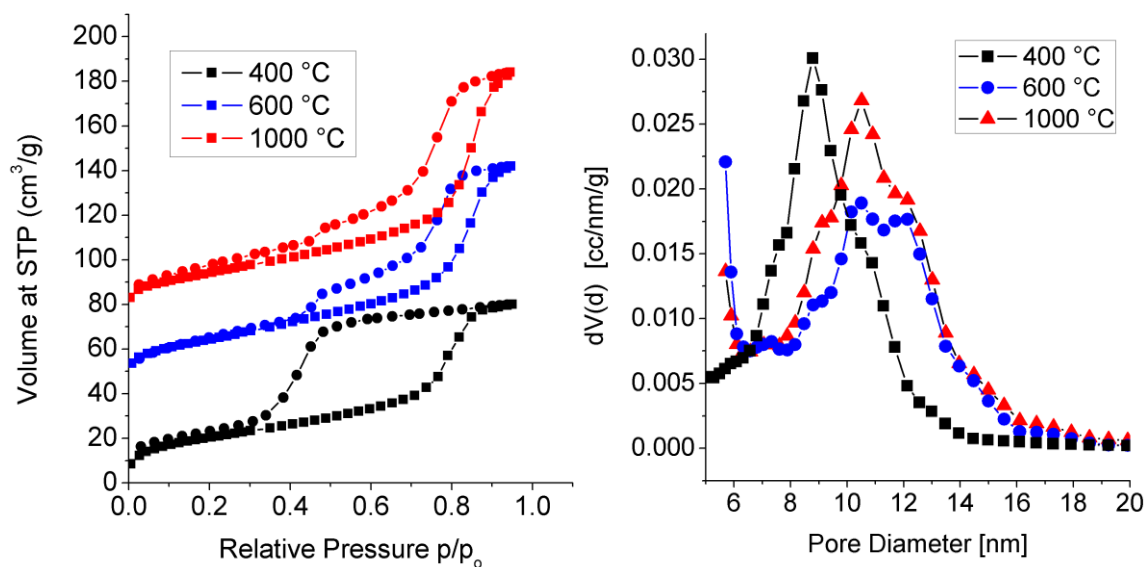


**Figure 4.6:** Nitrogen sorption isotherms (left) for the OMC/AAM composites Hex-400, Hex-600 and Hex-1000 and the corresponding pore size distributions (right); the isotherms of Hex-600 and Hex-1000 are offset vertically by 30 and 70 cm<sup>3</sup>/g, respectively.

As already discussed above for the cubic samples, we attribute the slightly incomplete equilibration for sample Hex-400 to the incomplete removal of the structure-directing agent (SDA) at this rather low temperature. The large hysteresis loop for samples pyrolyzed at 400 °C can also be attributed to an incomplete SDA removal, leading to partial blocking of the large pores (ca. 8.7 nm). The steep slope in the desorption curve at around 0.4  $p/p_0$  is specific for the cavitation of the adsorptive nitrogen in small mesopores. The samples Hex-600 and Hex-1000 show higher surface areas and pore volumes with a less distinct hysteresis. Their desorption isotherms show two steps, the first around 0.75  $p/p_0$  which is related to capillary condensation in accessible large mesopores and a second step around 0.4  $p/p_0$ , which is related to the adsorptive nitrogen. At this partial pressure, all the remaining blocked mesopores are completely emptied by cavitation. Thus, the desorption isotherms could only be used from 0.5 to 1.0  $p/p_0$  for the calculation of the pore sizes. The pore size distributions show an increase in the average pore diameter from 400 °C to 600 °C. This can be readily explained by the proceeding template decomposition as well as the shrinkage of the walls due to carbonization. The shrinkage of the carbon fibers is again restricted due to strong adhesion to the AAO walls; as a consequence, also the shrinkage of the mesopores themselves is restricted. In the pore-size distribution of Hex-600, two distinct maxima at 11 nm and 12 nm are visible.

**Table 4.2:** Porosity properties for OMC/AAM composites Hex-400, Hex-600 and Hex-1000

Sample Name	wt% Carbon	BET surface area [m <sup>2</sup> /g]	Specific BET <sup>a</sup> area [m <sup>2</sup> /g]	Pore volume [cc/g]	Specific volume <sup>b</sup> [cc/g]	Pore size NLDFT [nm]	Pore size BJH <sup>e</sup> [nm]
Hex-400	14	75	536	0.121	0.87	9 <sup>c</sup>	9.5
Hex-600	15	120	800	0.173	1.16	11 <sup>d</sup> , 12	12.5
Hex-1000	7.0	86	1230	0.169	2.41	11 <sup>d</sup>	12.5

[a] Calculated from the total BET surface area of the composite related to the carbon content.

[b] Calculated from the total pore volume of the composite related to the carbon content.

[c] Calculated by the NLDFT adsorption branch model for cylindrical pores with silica as

adsorbent [d] Calculated by the NLDFT equilibrium branch model for cylindrical pores with

carbon as adsorbent for the partial pressures 0.5 to 1.0 [e] Calculated by the BJH model from

the adsorption branches

A similar distribution is obtained for Hex-1000, with the only difference that the peak at 12.0 nm is decreased to a shoulder. This bimodal pore size distribution can be explained by shrinkage of the pores in the centers of the fibers, while the pores are “stretched” in the outer parts. This effect was already observed in TEM images as depicted in Figure 4.5. The pore sizes were also determined with the BJH model from the adsorption branches for better comparison with literature data; there, the same trends were observed (Table 4.2). As already mentioned above, the OMC/AAM composites contain 7-15 wt% porous carbon; thus the carbon fibers show high specific surface areas up to 1230 m<sup>2</sup>/g and high specific pore volumes up to 2.4 cm<sup>3</sup>/g (Hex-1000).

### 4.3. Conclusion

We have demonstrated the synthesis of highly ordered hierarchical mesoporous carbon structures in the confined environment of anodic aluminum oxide pores with either cubic or circular hexagonal order. The carbon phases were obtained by organic-organic self-assembly of a preformed oligomeric resol precursor and the triblock copolymer templates Pluronic F127 or P123, respectively. Subsequent thermal decomposition of the surfactant and carbonization were achieved by thermal treatment up to 1000 °C in an inert atmosphere with minimal structural distortion due to strong adhesion of the carbon wall material to the AAM pore walls. As a consequence, the pore size of the mesophase system stays almost constant even after thermal treatment at 1000 °C. The symmetry and orientations of the mesoporous phases were characterized in detail by SAXS measurements and could be directly visualized by TEM micrographs of cross-sections and plan views. Large pore sizes and large specific surface areas and pore volumes could be determined with nitrogen sorption measurements. The carbon phases exhibit pore sizes of up to 20 nm for the cubic phase and 12 nm for the hexagonal phase and specific surface areas and pore volumes of up to 1130 m<sup>2</sup>/g and 2.3 cm<sup>3</sup>/g (cubic) and 1230 m<sup>2</sup>/g and 2.4 cm<sup>3</sup>/g, respectively (hexagonal). This soft-templating approach represents an effective approach for OMC/AAM composite membranes or isolated OMC fibers with accessible pores that could be used for applications such as membranes for bio-separations or electrode materials for batteries. The highly desirable porosity features of these hierarchical systems as well as their high thermal stability should make them very attractive candidates for these applications.

### 4.4. Experimental Section

**Chemicals:** Formalin (37 wt% formaldehyde in water) and the triblock copolymers Pluronic P123 ( $M_w = 5800$ , EO<sub>20</sub>-PO<sub>70</sub>-EO<sub>20</sub>) and Pluronic F127 ( $M_w = 12600$ , EO<sub>106</sub>-PO<sub>70</sub>-EO<sub>106</sub>)

were purchased from BASF AG, and phenol from Merck KGaA. All chemicals were used without further purification. Whatman Anodiscs® (25 mm and 47 mm diameter, nominal pore diameter 0.02 µm) were used as porous alumina substrates.

**Synthesis: Resol precursor.** A low molecular weight precursor for the organic framework was synthesized in a reaction of phenol and formaldehyde in a base-catalyzed process according to Meng et al.<sup>22</sup>. The molecular weight average of the resol precursor is expected to be smaller than 500 g/mol. For the synthesis, 6.1 g of phenol (0.064 mol) were molten in a flask with 1.3 g of 20 wt % sodium hydroxide solution (0.0065 mol). The mixture was heated up to 50 °C and then 10.5 g formalin (37 wt % formaldehyde in water, 0.1295 mol) were added dropwise. The molar ratio of phenol / formaldehyde / NaOH was 1 : 2 : 0.1. The clear, lightly yellow colored solution was stirred at 75 °C for one hour and then cooled down to room temperature. The precursor solution was neutralized with 1 M hydrochloric acid and the water was removed by vacuum evaporation below 50 °C. The resulting product was redissolved in ethanol to a total weight of 50 g.

**SDA solutions.** Pluronic F127: 1.00 g F127 (0.08 mmol) was dissolved in 20.0 g (0.45 mol) ethanol to give a 4.76 wt % solution. Pluronic P123: 1.00 g P123 (0.17 mmol) was dissolved in 9.5 g (0.21 mol) ethanol to give a 9.52 wt % solution.

**Synthesis of Mesoporous Polymer Resin and Carbon in AAOs with Cubic Structure.** The cubic phase was obtained for a molar ratio of phenol / formaldehyde / NaOH / F127 = 1 : 2 : 0.1 : 0.0044, which is equivalent to a weight ratio of the SDA and precursor solution of 1.5 : 1. In a typical preparation, 1 g of the precursor solution was mixed with 1.5 g template solution. After stirring for 10 min, a homogeneous solution was obtained. The mixed solutions – 0.75 ml for the 47 mm membrane and 0.25 ml for the 25 mm

membrane, respectively – were dropped on the membrane, followed by evaporation of the solvent over night. The impregnated membranes were tempered at 100 °C for 24 h. For template removal and carbonization, the membranes were heated in a nitrogen flow with a ramp of 1 °C/min to the final temperature with a dwell time of 3 h at that temperature.

### **Synthesis of Mesoporous Polymer Resin and Carbon in AAOs with Circular Hexagonal**

**Structure.** The circular hexagonal phase was obtained for a molar ratio of phenol / formaldehyde / NaOH / P123 = 1 : 2 : 0.1 : 0.0095, which is equivalent to a weight ratio of the SDA and precursor solution of 0.75 : 1. In a typical preparation, 1 g of the precursor solution was mixed with 0.75 g template solution. After stirring for 10 min, a homogeneous solution was obtained. The mixed solutions – 0.75 ml for the 47 mm membrane and 0.25 ml for the 25 mm membrane, respectively – were dropped on the Anodiscs, followed by evaporation of the solvent over night. The procedure for thermopolymerization and carbonization is identical as for the cubic phase described in the section above.

**Nomenclature:** The sample are denoted S-T. S represents the structure; Hex for the circular hexagonal, Cub for the cubic phase. T represents the carbonization temperature. For example Hex-400 is a composite with circular hexagonal structure, carbonized at 400 °C.

**Characterization:** Transmission electron microscopy (TEM) data were obtained on a JEOL JEM 2011 microscope at an acceleration voltage of 200 kV. Nitrogen sorption isotherms were obtained at -196 °C using a Quantachrome Nova 4000e or a Quantachrome Autosorb-1. 2D small angle X-ray scattering experiments were carried out using the SAXSess system by Anton Paar in combination with a CCD detector system (Roper Scientific). The wavelength of the incident beam is 0.154056 nm ( $\text{Cu}_{K\alpha}$ ), the sample-detector distance was set to 308 mm. Samples were measured with a tilt angle of 10° with respect to the primary beam.

## 4.5. Chapter References

6. Liang, C.; Li, Z.; Dai, S., *Angew. Chem., Int. Ed.* **2008**, *47* (20), 3696-3717.
7. Wan, Y.; Shi, Y.; Zhao, D., *Chem. Mater.* **2008**, *20* (3), 932-945.
8. Chang, H.; Joo, S. H.; Pak, C., *J. Mater. Chem.* **2007**, *17* (30), 3078-3088.
9. Wu, C.-G.; Bein, T., *Science* **1994**, *266* (5187), 1013-15.
10. Ryoo, R.; Joo, S. H.; Jun, S., *J. Phys. Chem. B* **1999**, *103* (37), 7743-7746.
11. Lee, J.; Yoon, S.; Hyeon, T.; Oh, S. M.; Kim, K. B., *Chem. Commun.* **1999**, (21), 2177-2178.
12. Jun, S.; Joo, S. H.; Ryoo, R.; Kruk, M.; Jaroniec, M.; Liu, Z.; Ohsuna, T.; Terasaki, O., *J. Am. Chem. Soc.* **2000**, *122* (43), 10712-10713.
13. Kruk, M.; Jaroniec, M.; Kim, T.-W.; Ryoo, R., *Chem. Mater.* **2003**, *15* (14), 2815-2823.
14. Xing, W.; Bai, P.; Li, Z. F.; Yu, R. J.; Yan, Z. F.; Lu, G. Q.; Lu, L. M., *Electrochim. Acta* **2006**, *51* (22), 4626-4633.
15. Li, Z.; Dai, S., *Chem. Mater.* **2005**, *17* (7), 1717-1721.
16. Bazula, P. A.; Lu, A.-H.; Nitz, J.-J.; Schueth, F., *Microporous Mesoporous Mater.* **2008**, *108* (1-3), 266-275.
17. Wang, X.; Liu, R.; Waje, M. M.; Chen, Z.; Yan, Y.; Bozhilov, K. N.; Feng, P., *Chem. Mater.* **2007**, *19* (10), 2395-2397.
18. Vinu, A.; Hossian, K. Z.; Srinivasu, P.; Miyahara, M.; Anandan, S.; Gokulakrishnan, N.; Mori, T.; Ariga, K.; Balasubramanian, V. V., *J. Mater. Chem.* **2007**, *17* (18), 1819-1825.
19. Moriguchi, I.; Ozono, A.; Mikuriya, K.; Teraoka, Y.; Kagawa, S.; Kodama, M., *Chem. Lett.* **1999**, (11), 1171-1172.

21. Liang, C.; Hong, K.; Guiochon, G. A.; Mays, J. W.; Dai, S., *Angew. Chem., Int. Ed.* **2004**, *43* (43), 5785-5789.
22. Meng, Y.; Gu, D.; Zhang, F.; Shi, Y.; Cheng, L.; Feng, D.; Wu, Z.; Chen, Z.; Wan, Y.; Stein, A.; Zhao, D., *Chem. Mater.* **2006**, *18* (18), 4447-4464.
24. Zheng, M.; Ji, G.; Wang, Y.; Cao, J.; Feng, S.; Liao, L.; Du, Q.; Zhang, L.; Ling, Z.; Liu, J.; Yu, T.; Cao, J.; Tao, J., *Chem. Commun.* **2009**, (33), 5033-5035.
25. Schuster, J.; Keilbach, A.; Koehn, R.; Doeblinger, M.; Doerfler, T.; Dennenwaldt, T.; Bein, T., *Chem. Eur. J. In press*.
26. Schuster, J.; Koehn, R.; Keilbach, A.; Doeblinger, M.; Amenitsch, H.; Bein, T., *Chem. Mater.* **2009**, *21* (24), 5754-5762.
28. Tanaka, S.; Katayama, Y.; Tate, M. P.; Hillhouse, H. W.; Miyake, Y., *J. Mater. Chem.* **2007**, *17* (34), 3639-3645.
32. Steinhart, M.; Liang, C.; Lynn, G. W.; Goesele, U.; Dai, S., *Chem. Mater.* **2007**, *19* (10), 2383-2385.
33. Wang, K.; Zhang, W.; Phelan, R.; Morris, M. A.; Holmes, J. D., *J. Am. Chem. Soc.* **2007**, *129* (44), 13388-13389.
34. Zheng, M.; Cao, J.; Ke, X.; Ji, G.; Chen, Y.; Shen, K.; Tao, J., *Carbon* **2007**, *45* (5), 1111-1113.
35. Liu, H.-J.; Wang, X.-M.; Cui, W.-J.; Dou, Y.-Q.; Zhao, D.-Y.; Xia, Y.-Y., *J. Mater. Chem.* **2010**, *20* (20), 4223-4230.
61. Wang, X.; Liang, C.; Dai, S., *Langmuir* **2008**, *24* (14), 7500-7505.
62. Lu, A.-H.; Spliethoff, B.; Schueth, F., *Chem. Mater.* **2008**, *20* (16), 5314-5319.
68. Yang, Z.; Niu, Z.; Cao, X.; Yang, Z.; Lu, Y.; Hu, Z.; Han, C. C., *Angew. Chem., Int. Ed.* **2003**, *42* (35), 4201-4203.
69. Yamaguchi, A.; Uejo, F.; Yoda, T.; Uchida, T.; Tanamura, Y.; Yamashita, T.; Teramae, N., *Nature Materials* **2004**, *3* (5), 337-341.
70. Platschek, B.; Petkov, N.; Bein, T., *Angew. Chem., Int. Ed.* **2006**, *45* (7), 1134-1138.

71. Platschek, B.; Petkov, N.; Himsl, D.; Zimdars, S.; Li, Z.; Koehn, R.; Bein, T., *J. Am. Chem. Soc.* **2008**, *130* (51), 17362-17371.
72. Platschek, B.; Koehn, R.; Doeblinger, M.; Bein, T., *Langmuir* **2008**, *24* (9), 5018-5023.
73. Keilbach, A.; Doeblinger, M.; Koehn, R.; Amenitsch, H.; Bein, T., *Chemistry--A European Journal* **2009**, *15* (27), 6645-6650, S6645/1-S6645/3.
74. Wang, K.; Birjukovs, P.; Ertz, D.; Phelan, R.; Morris, M. A.; Zhou, H.; Holmes, J. D., *J. Mater. Chem.* **2009**, *19* (9), 1331-1338.

## 5. *IN SITU* SAXS STUDY ON A NEW MECHANISM FOR MESOSTRUCTURE FORMATION OF ORDERED MESOPOROUS CARBONS: THERMALLY-INDUCED SELF-ASSEMBLY

### ABSTRACT

A new mechanism for mesostructure formation of ordered mesoporous carbons (OMCs) was investigated with *in situ* SAXS measurements: Thermally-induced self-assembly. Unlike for the well-established evaporation-induced self-assembly (EISA) the structure formation for organic-organic self-assembly of an oligomeric resol precursors and the block-copolymer templates Pluronic P123 and F127 does not occur during evaporation but only in the following thermopolymerization step at temperatures above 100 °C.

The systems investigated here were cubic ( $Im\bar{3}m$ ), orthorhombic ( $Fmmm$ ) and 2D-hexagonal (plane group  $p6mm$ ) mesoporous carbon phases in confined environments, as thin films and within the pores of anodic alumina membranes (AAM), respectively. The thin films were prepared by spin-coating mixtures of the resol precursor and the surfactants in ethanol followed by thermopolymerization of the precursor oligomers. The carbon phases within the pores of AAMs were made by imbibition of the latter solutions followed by solvent evaporation and thermopolymerization within the solid template. This thermopolymerization step was investigated in detail with *in situ* GISAXS (for films) and *in situ* SAXS (for AAMs).

It was found that the structural evolution strongly depends on the chosen temperature, which controls both the rate of the mesostructure formation and the spatial dimensions of the resulting mesophase. Therefore the process of structure formation differs significantly from the known evaporation-induced self-assembly (EISA) and may rather be viewed as thermally-induced self-assembly. The complete process of structure formation, template removal and shrinkage during carbonization up to 1100 °C could be monitored in this *in situ* SAXS study.

## 5.1. Introduction

Porous carbon materials are essential for many modern applications. They are employed as electrode materials for batteries, supercapacitors and fuel cells, as sorbents for separation and gas storage, or as catalyst supports due to their favorable properties including high specific surface area and pore volume, chemical inertness and electrical conductivity.

Conventional activated carbons presently in use typically consist of disordered microporous amorphous carbon. The main drawback of these activated microporous carbons is limited accessibility and mass transport within the micropores.<sup>6</sup> Ordered mesoporous carbons (OMCs)<sup>6-8</sup> – tailor-made in terms of morphology and properties of the periodic mesopore system – could be beneficial for several of the aforementioned applications. Ordered mesoporous carbon in bulk or powder form are commonly synthesized either by hard-templating,<sup>9-13</sup> where periodic mesoporous silica is filled with carbon precursors followed by carbonization and removal of the silica, or by soft-templating,<sup>22, 61-62</sup> using the self-assembly of soluble carbon precursors with liquid crystalline phases of surfactants or block copolymers acting as soft templates.

The examples for OMC thin films<sup>21, 26-28, 31</sup> or OMC phases still embedded in AAM hosts<sup>24-25, 32-34, 74-75</sup> are limited to soft-templating methods. Hard-templating methods for ordered

mesoporous carbon based on porous silica templates have yet not been implemented for these morphologies, which is mainly attributed to weak adhesion of the resulting carbon material to the substrate after etching of the silica template.<sup>28, 76</sup> The few examples using hard-templating of mesoporous silica for AAMs either result in mesostructured carbon/silica composites<sup>9, 76</sup> and/or in freestanding fibers.<sup>76</sup> An alternative approach for mesoporous carbon films uses spin-coating of sucrose and silica nanoparticles and subsequent removal of the silica.<sup>60</sup> However, these films contained a disordered pore system. While the final carbon structure obtained *via* hard-templating is controlled by the solid template, the final structures made by soft-templating are much more sensitive to experimental conditions such as concentrations, temperature or humidity during structure formation. Therefore, the understanding and control of structure formation processes for soft-templating methods concerning mesostructural symmetry, morphology and orientation of the desired mesoporous carbon phases is essential, especially for syntheses in confined environments.

*In-situ* GISAXS characterization of thin films and *in-situ* SAXS of AAM/OMC composites are powerful tools to investigate structural changes during all steps of structure formation and processing – self-assembly, template removal and the final carbonization. Some examples for *in-situ* SAXS studies regarding the structure formation with evaporation-induced self-assembly (EISA)<sup>29, 72, 77</sup> and thermal processing<sup>30, 78</sup> of mesoporous systems other than mesoporous carbon have already been reported.

The self-assembly mechanisms for OMC materials made by soft-templating have not yet been investigated in detail. Liang et al.<sup>21</sup> described the self-assembly of a polystyrene-*b*-poly(4-vinylpyridine) block-copolymer (PS-*P4VP*) with resorcinol and formaldehyde as carbon sources, as solvent-induced self-assembly. For other OMC systems – mainly for the popular resol-Pluronic system<sup>6, 22, 27, 40, 79</sup> – the structure formation is mostly described as evaporation-

induced self-assembly (EISA), such as for mesostructured metal oxides (e.g., silica<sup>29</sup> or titania<sup>30</sup>) followed by a thermopolymerization step to crosslink the precursor oligomers.

Herein we report an *in-situ* SAXS study on a new mechanism for mesostructure formation of OMCs in the form of thin films and confined within the pores of anodic alumina membranes:

#### Thermally-induced self-assembly

The OMC phases were obtained by solvent evaporation of mixtures of a preformed oligomeric resol precursor and the triblock copolymer templates Pluronic P123 and F127, respectively followed by a thermopolymerization step at temperatures at intermediate temperatures (> 100 °C) and finally carbonization at high temperatures (> 600 °C) in inert atmosphere. We found that unlike in the case of mesostructured metal oxides and also different to literature on those soft-templated OMCs, the structure formation in these systems does not occur during evaporation of the solvent (EISA) but during the thermopolymerization step, and should therefore rather be called thermally-induced self-assembly. As a consequence, the mesostructure is still flexible and can be controlled during the thermopolymerization step. Different thermopolymerization temperatures resulted in changed unit cell parameters for the final OMC structures. Template removal and carbonization of thin films and AAM composites were monitored up to 1100 °C, with mesopore order still retained at this temperature. We observed strong structural distortion for the thin films due to anisotropic shrinkage upon carbonization, but no distortion was found for the AAM composites due to the restricted shrinkage effect of the confining alumina wall.

## 5.2. Experimental Section

**Chemicals.** Formalin (37 wt% formaldehyde in water) and the triblock copolymers Pluronic P123 ( $M_w = 5800$ , EO<sub>20</sub>-PO<sub>70</sub>-EO<sub>20</sub>) and Pluronic F127 ( $M_w = 12600$ , EO<sub>106</sub>-PO<sub>70</sub>-EO<sub>106</sub>)

were purchased from BASF AG. Phenol was obtained from Merck KGaA. All chemicals were used without further purification. Whatman Anodiscs® (25mm and 47 mm diameter, nominal pore diameter 0.02 µm) were used as porous alumina substrates. Silicon Wafers were kindly donated by Siltronic AG.

**Synthesis. Resol precursor.** A low molecular weight precursor for the organic framework was synthesized in a reaction of phenol and formaldehyde in a base-catalyzed process according to Meng et al.<sup>22</sup> The molecular weight average of the resol precursor is expected to be smaller than 500 g/mol. For the synthesis, 6.1 g of phenol (0.064 mol) were molten in a flask with 1.3 g of 20 wt % sodium hydroxide solution (0.0065 mol). The mixture was heated up to 50 °C and then 10.5 g formalin (37 wt % formaldehyde in water, 0.1295 mol) were added dropwise. The molar ratio of phenol : formaldehyde : NaOH was 1 : 2 : 0.1. The clear, lightly yellow colored solution was stirred at 75 °C for one hour and then cooled down to room temperature. The precursor solution was neutralized with 1 M hydrochloric acid and the water was removed by vacuum evaporation below 50 °C. The resulting product was redissolved in ethanol to a total weight of 50 g.

*SDA solutions.* Pluronic F127: 1.00 g F127 (0.08 mmol) was dissolved in 20.0 g (0.45 mol) ethanol to give a 4.76 wt % solution. Pluronic P123: 1.00 g P123 (0.17 mmol) was dissolved in 20.0 g (0.45 mol) ethanol to give a 4.76 wt % solution. For a double concentrated (9.52 wt %) template solution, 1.00 g P123 (0.17 mmol) was dissolved in 9.5 g ethanol.

*Synthesis of Mesoporous Polymer and Carbon films with 2D-Hexagonal structure.*<sup>26</sup>

2D-hexagonal films were prepared with a molar ratio of phenol : formaldehyde : NaOH : P123 = 1 : 2 : 0.1 : 0.0063, which is equivalent to a weight ratio of the SDA (4.76 wt % P123) and precursor solution of 1 : 1. In a typical preparation, 1 g of the precursor

solution was mixed with 1 g template solution (molar ratio phenol : formaldehyde : NaOH : P123 = 1 : 2 : 0.1 : 0.0063). After stirring for 10 min, a homogeneous solution was obtained. The mesostructured films were synthesized on polished silicon wafers. The wafers were cut into smaller pieces, washed with ethanol, and cleaned in an oxygen-plasma for one minute. The mixed precursor and SDA solutions were dropped on the wafers through a syringe filter (CHROMAFIL PET-20/15 MS, pore size 0.20  $\mu\text{m}$ ), and spin-coated at 3000 rpm with an acceleration of 1260 rpm/s.

*Synthesis of Mesoporous Polymer and Carbon films with Orthorhombic Structure.*

Orthorhombic films were obtained with a molar ratio of phenol : formaldehyde : NaOH : P123 = 1 : 2 : 0.1 : 0.0029, which is equivalent to a weight ratio of the SDA (4.76 wt % F127) and precursor solution from 1 : 1. In a typical preparation, 1 g of the precursor solution was mixed with 1 g template solution (molar ratio phenol / formaldehyde / NaOH / P123 = 1 : 2 : 0.1 : 0.0063). For these films the same procedure as described above for solvent evaporation during spin-coating was performed.

*Synthesis of Mesoporous Polymer Resin and Carbon in AAOs with Circular Hexagonal Structure.*<sup>25</sup> The circular hexagonal phase was obtained for a molar ratio of phenol : formaldehyde : NaOH : P123 = 1 : 2 : 0.1 : 0.0095, which is equivalent to a weight ratio of the SDA (9.52 wt % P123) and precursor solution of 0.75 : 1. In a typical preparation, 1 g of the precursor solution was mixed with 0.75 g template solution. After stirring for 10 min, a homogeneous solution was obtained. The mixed solutions – 0.75 ml for the 47 mm membrane and 0.25 ml for the 25 mm membrane, respectively – were spread over the membrane, followed by evaporation of the solvent over night.

The cubic phase was obtained for a molar ratio of phenol : formaldehyde : NaOH : F127 = 1 : 2 : 0.1 : 0.0044, which is equivalent to a weight ratio of the SDA and precursor solution of 1.5 : 1. In a typical preparation, 1 g of the precursor solution was mixed with 1.5 g template solution. For these membranes the same procedure of solvent evaporation was performed as described for the hexagonal structure.

*Thermopolymerization:* The solvent evaporation was followed by thermopolymerization at temperatures between 90 °C and 180 °C on a Bruker DHS 1100 heating plate until strong reflections were visible in the *in-situ* recorded GISAXS patterns.

*Carbonization:* After thermopolymerization the samples were heated in the Bruker DHS 1100 heating chamber in nitrogen atmosphere with a ramp of 6 °C/min up to the defined limit of 1100 °C.

*Nomenclature:* The thin films are denoted Film-S-T and the AAMs are denoted AAM-S-T. S represents the structure; -Hex for the hexagonal, -Or for orthorhombic and -Cub for the cubic phase. T represents the thermopolymerization temperature reached at a ramp of 20 °C/min. For example AAM-Hex-110 is a composite with circular hexagonal structure, heated with a ramp of 20 °C/min and to the thermopolymerization temperature of 110 °C. Samples thermopolymerized using a faster ramp of 100 °C/min get the suffix fast, e.g. Film-Hex-180fast.

## Characterization

GISAXS and SAXS experiments were performed at beamline BL 5.2 L at Synchrotrone Elettra (Trieste, Italy). The wavelength of the incident beam was 0.15498 nm (8 keV), and the sample-detector distance was 1563 mm, 1490 mm and 1430 mm, respectively for the different

sessions at the synchrotron. The samples were heated in a Bruker DHS 1100 heating chamber. The films were measured with GISAXS at incident angles of  $0.3^\circ$ . The AAMs were measured with SAXS in transmission at an incident angle of  $5^\circ$ . For this purpose they were placed on a grooved copper plate (groove width 0.5 cm, depth 0.5 cm) on top of the heating plate. For temperatures above  $200^\circ\text{C}$  the DHS 1100 was equipped with the provided graphite dome or with a self-made top, which consists of a rectangular steel tube with windows made from a  $10\ \mu\text{m}$  thin polyethylene terephthalate film (Kalle GmbH, Wiesbaden, Germany). The film was found to have a negligible contribution to the measured signal in contrast to the graphite dome, which produces an intense diffuse background at small angles. The sample temperature was verified with the  $\alpha$ - $\beta$  phase transition of quartz at  $573^\circ\text{C}$ .<sup>80-81</sup> The quartz jump was determined by a peak shift of the 101 reflection (Figure S9.1). For this purpose, quartz crystals were placed on an AAM on top of the grooved copper plate. The set temperature at the phase transition was  $569^\circ\text{C}$ , thus  $4^\circ\text{C}$  ( $< 1\%$  error) lower than the real sample temperature.

### 5.3. Results and Discussion

#### *Mesoporous Structures.*

Four OMC systems – two thin films and two in AAMs – were investigated in this *in-situ* GISAXS study. The thin films were obtained through organic-organic self-assembly of a preformed oligomeric resol precursor and the triblock copolymer templates Pluronic P123 (hexagonal) and Pluronic F127 (orthorhombic), respectively. The 2D-hexagonal (plane group,  $p6mm$ ) mesoporous carbon thin films have already been investigated in a combined GISAXS and TEM study.<sup>26</sup> The structure can be described by cylindrical pores arranged in a hexagonal stacking parallel to the substrate. These films are denoted Film-Hex-T. A typical GISAXS pattern for the orthorhombic thin films – denoted as Film-Or-T – is depicted in Figure 5.1. The pattern shows a differing arrangement of reflections compared to the 2D-hexagonal structure that can be indexed according to a face-centered orthorhombic unit cell ( $Fmmm$ ) with the (010) plane parallel to the substrate.

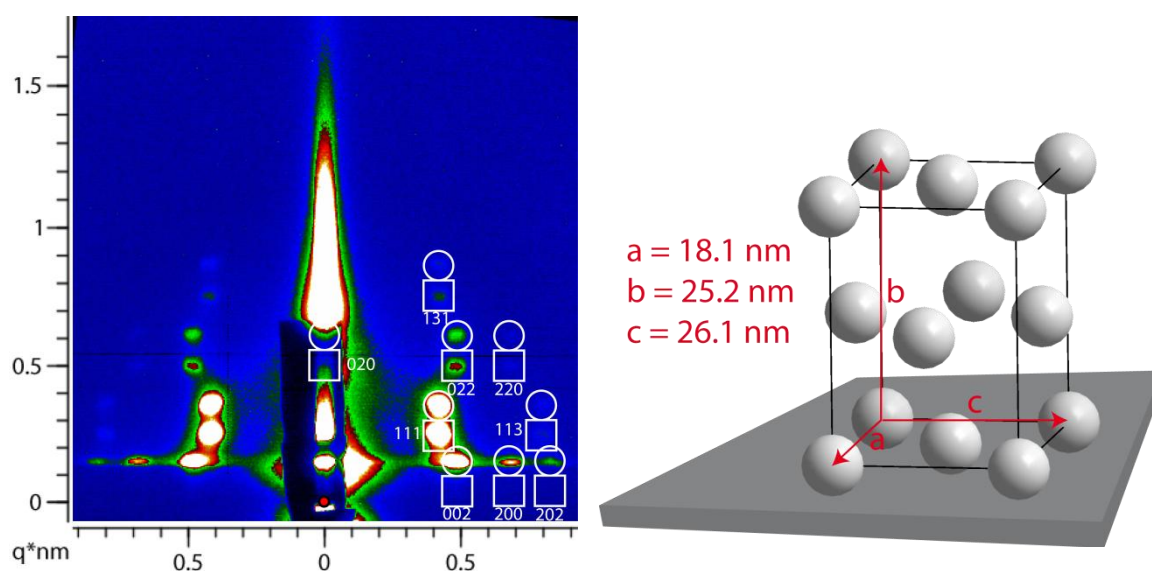


**Figure 5.1:** GISAXS pattern (left) of Film-Or-100 indexed according to the face-centered orthorhombic unit cell ( $Fmmm$ ), with (010) plane parallel to the substrate (right)

Films possessing the above space group and orientation with respect to the substrate were already reported for carbon and metal oxides.<sup>28, 31, 78, 82</sup> OMC phases synthesized with the surfactant Pluronic F127 usually show cubic  $Im\bar{3}m$  symmetry but this can be changed to an orthorhombic  $Fmmm$  symmetry due to distortion. The symmetry change from cubic  $Im\bar{3}m$  to orthorhombic  $Fmmm$  is also described by Falcaro et al.<sup>78</sup>

Circular hexagonal and cubic AAM phases – denoted as AAM-Hex-T and AAM-Cub-T – were obtained by organic-organic self-assembly of a preformed oligomeric resol precursor and the triblock copolymer templates Pluronic P123 (hexagonal) and Pluronic F127 (cubic), respectively. These mesostructures have been investigated before by combined SAXS and TEM.<sup>25</sup> Solvent-casting and -evaporation were followed by self-assembly and by thermopolymerization of the precursor oligomers, resulting in the mesostructured phenolic resin phases. A typical SAXS pattern for the circular hexagonal structure is presented in Figure 5.2 (left) for the sample AAM-Hex-160. It can be indexed according to a zone axis parallel to the hexagonal axis of the unit cell (plane group  $p6mm$ , Figure 5.2 right) with  $[2\bar{1}]$  orientation regarding the membrane normal. The squares show the reflections from the mesophases in the AAM pores while the circles show reflections from a top layer on the membrane. This top layer also shows a 2D-hexagonal structure but with  $[01]$  orientation regarding the membrane normal.

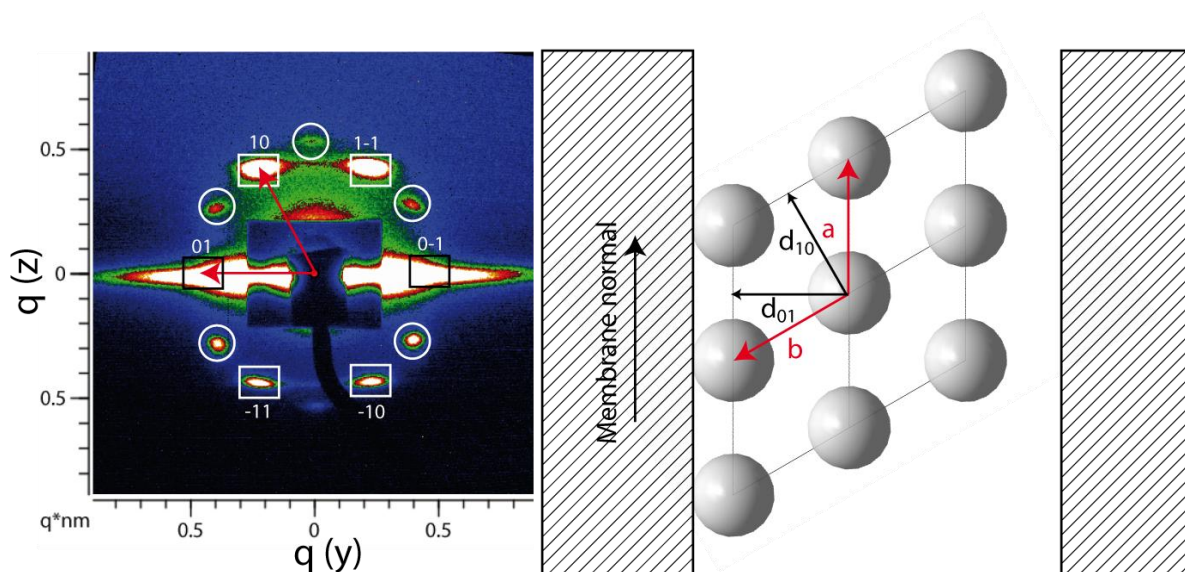


**Figure 5.2:** SAXS pattern (left) for the sample AAM-Hex-160 indexed in the circular hexagonal ( $p6mm$ ) unit cell (right). The squares show the reflections from the mesophases in the AAM pores while the circles show reflections from a top layer on the membrane.

A typical SAXS pattern for the cubic structure is presented in Figure 5.3 (left) for the sample AAM-Cub-180. This pattern can be indexed according to the cubic  $Im\bar{3}m$  unit cell (right) showing only reflections perpendicular to two possible zone axes,  $[01-1]$  and the  $[11-2]$ .

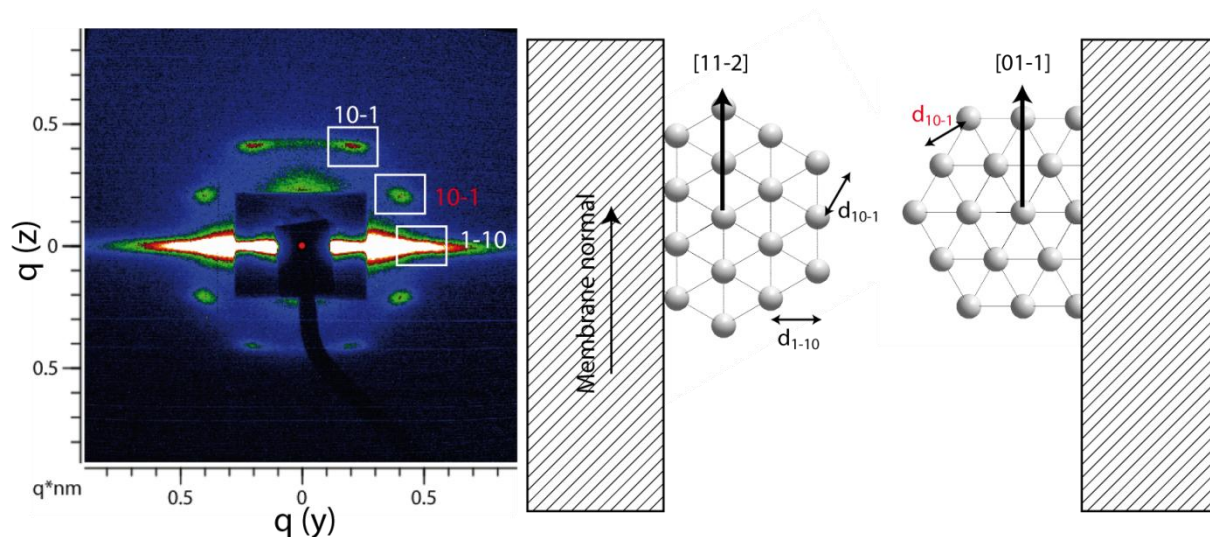


**Figure 5.3:** SAXS pattern (left) for the sample AAM-Cub-180 indexed in the cubic unit cell unit cell ( $Im\bar{3}m$ ). (Right) corresponding unit cell viewed along  $[111]$  and its possible orientations along the membrane normal,  $[11-2]$  and  $[01-1]$ .

*Structure Formation by Thermally-Induced Self-Assembly.*

The structure formation by thermally-induced self-assembly could be monitored *in-situ* for all four systems. The corresponding GISAXS data are presented in the supporting information (Appendix), Figure S9.2-6 Film-Hex-T), Figure S9.8-13 (Film-Or-T), Figure S9.15-20 (AAM-Hex-T) and Figure S9.23-29 (AAM-Cub-T) for temperatures between 90 °C and 220 °C. Exemplary *in-situ* GISAXS measurements for thin films (Film-Hex-100) and in AAMs (AAM-Hex-130) are depicted in Figure 5.4 and Figure 5.5, respectively.

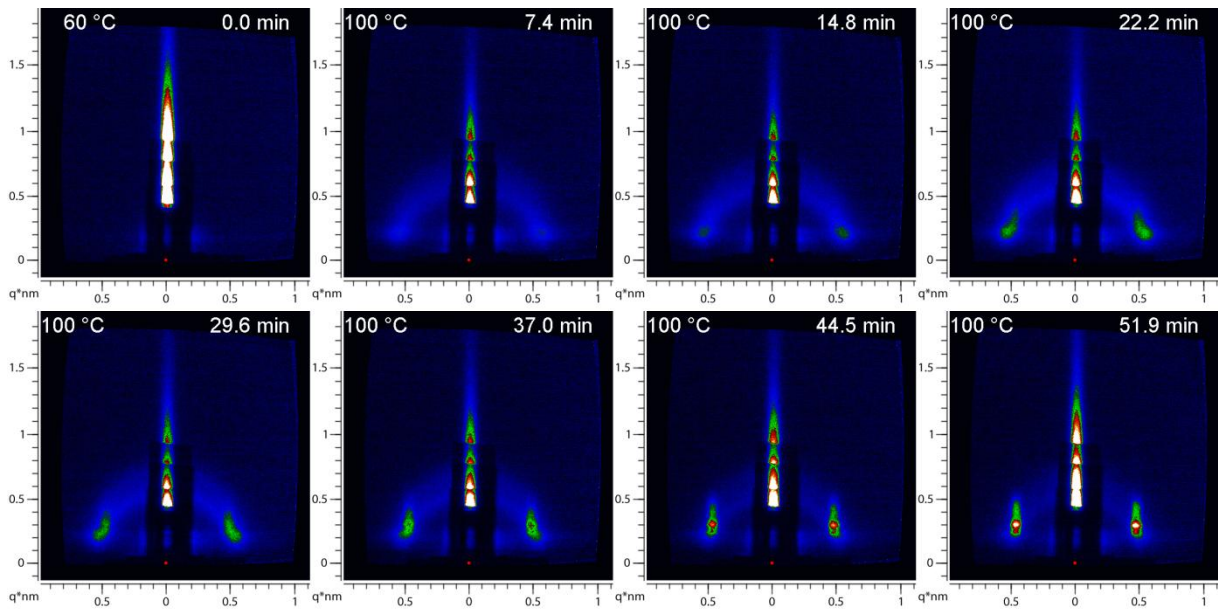


**Figure 5.4:** In-situ GISAXS of Film-Hex-100: Structure formation during thermopolymerization at 100 °C.

In the first picture (0.0 min) only specular intensities and diffuse scattering along the vertical axis is visible, thus no periodic structure is formed yet. The maxima along the vertical axis result from the staggered arrangement of multiple layers of aluminum foil acting as absorber. Therefore, the reflections on the vertical axis (e.g.  $d_{01}$ ) cannot be observed. After a few minutes a diffuse ring and Yoneda reflections<sup>52</sup> become visible and increase in intensity, due to an evolving mesostructure, which is oriented randomly at that stage. During continued heating, the evolution of distinct reflections related to an oriented hexagonal mesostructure occurs between 25 and 40 min after starting the heating at 60 °C. After 60 minutes, the reflections became more distinct and intense, but no further structural changes were visible. Remarkably, the time of structural evolution is much shorter than the well-established thermopolymerization time of 24 h used for bulk samples and films.<sup>22, 26</sup> The processes in the thermally-induced structure formation in AAMs are illustrated for AAM-Hex-130 in Figure 5.5.

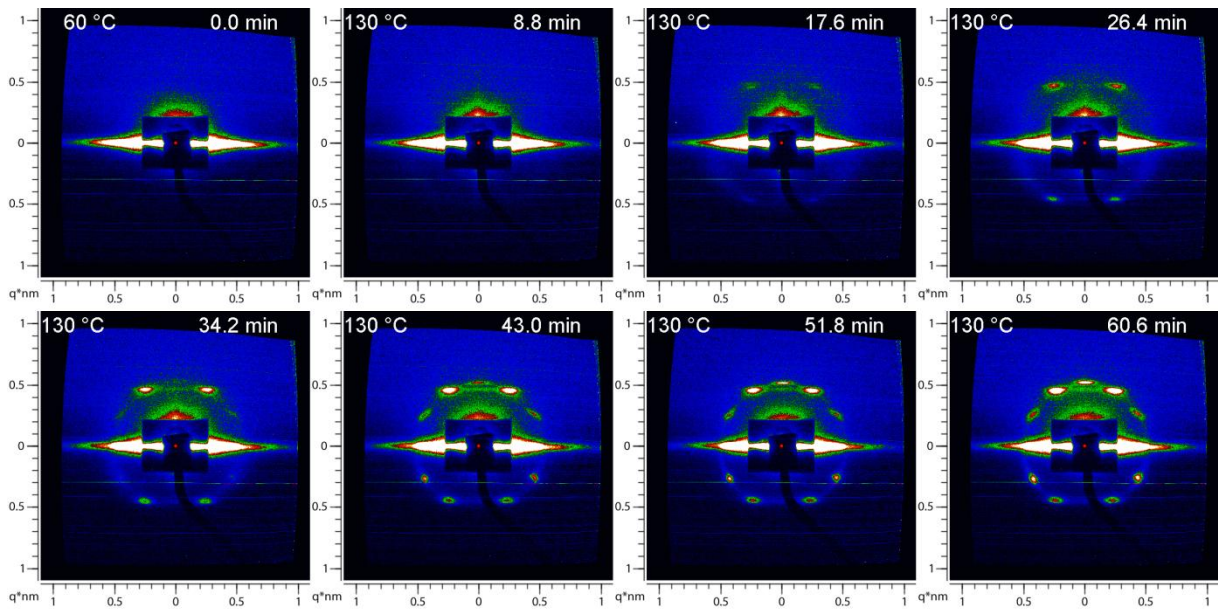


**Figure 5.5:** In-situ SAXS of AAM-Hex-130: Structure formation during thermopolymerization at 130 °C.

After heating for 15 minutes at 130 °C, the first reflections related to a circular hexagonal structure start to appear. A diffuse ring attributed to a random orientation is also visible, thus some parts are oriented randomly while others already show the final orientation. Upon further heating the intensity of the reflection spots increases, and the structure becomes completely circular hexagonal. Some additional reflections appear after 39 min, corresponding to a hexagonally ordered top-layer on the membrane. Figure 5.6 summarizes the thermopolymerization process for all four OMC systems.

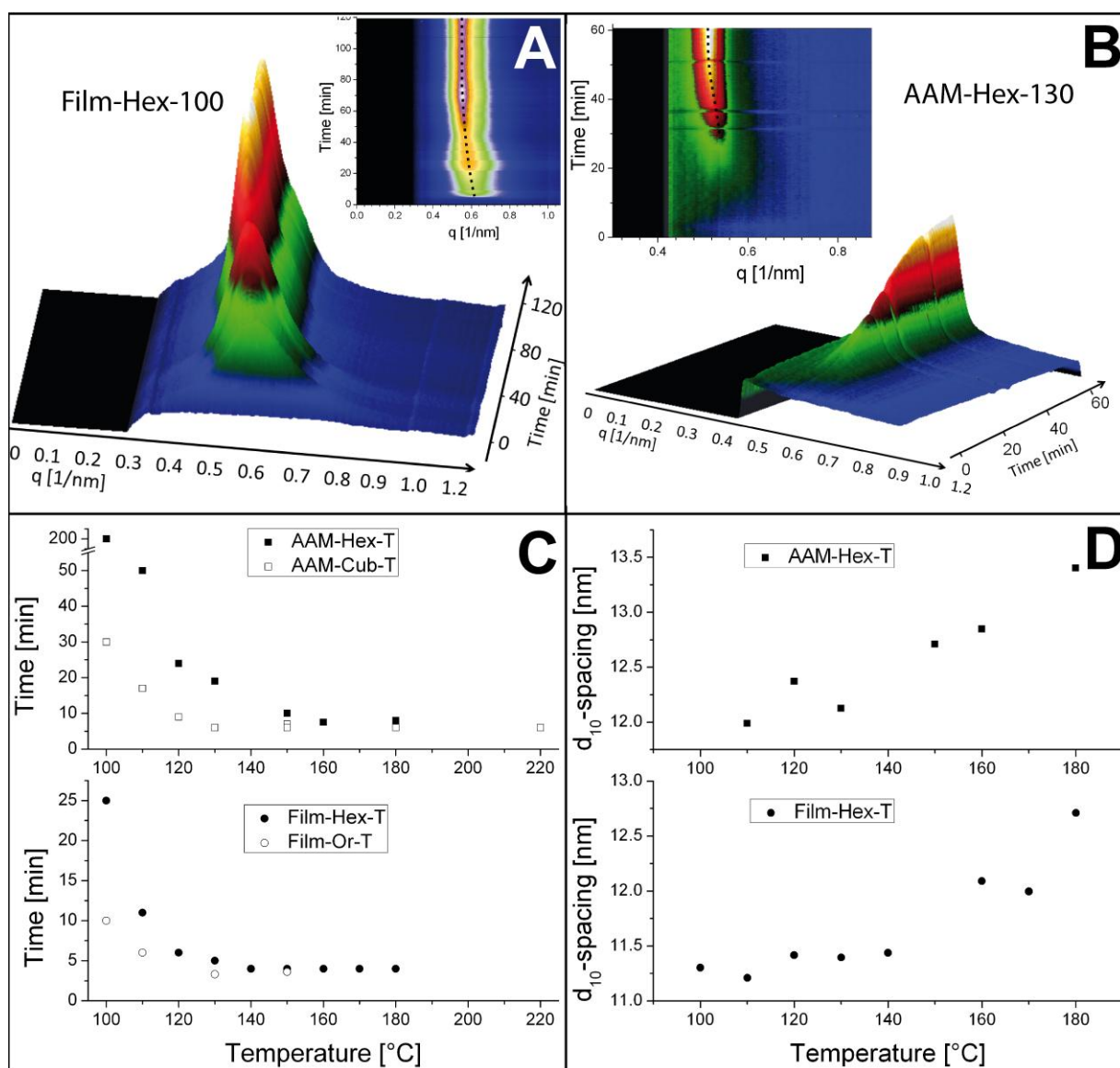


**Figure 5.6:** Evolution of structure during thermopolymerization. A) Plot of thermopolymerization time vs. radially integrated intensities for Film-Hex-100 in 3D-projection with an inset of the 2D projection. In-plane intensity (on the vertical axis) was masked due to extremely high intensities from specular and diffuse scattering. B) Plot of thermopolymerization time vs. radially integrated intensities for AAM-Hex-130 C) Time of structure formation for samples AAM-Hex-T, AAM-Cub-T (top), Film-Hex-T and Film-Or-T (bottom); Time (start of the 20 °C/min ramp at 60 °C until the first  $d_{10}$ - or  $d_{111}$ -reflections can be observed) vs. the final thermopolymerization temperature. D)  $d_{10}$ -spacings after thermopolymerization for the samples AAM-Hex-T (top) and Film-Hex-T (bottom).

Figure 5.6A shows the structural evolution for Film-Hex-100 as plot of radially integrated intensities. The maximum of out-of plane intensity ( $d_{10}$ -reflection) is moving to smaller  $q$ -values until 60 min after the start and stays constant even after cooling down. This indicates a swelling of the micelles during structure formation and condensation and therefore larger  $d$ -spacings of the oriented hexagonal mesostructure compared to the randomly oriented phase. The same effect could be observed for AAM-Hex-130 in Figure 5.6B. The intensity is increasing and at the same time the maximum shifts to smaller  $q$ -values (inset). The minimum temperature to obtain highly ordered mesostructures within a few hours was 100°C for all four systems. At higher temperatures up to 220 °C the structure formation was much faster. Figure 5.6C illustrates the observed decrease of the time for the first structure formation with increasing thermopolymerization temperature for thin films (bottom) and for AAMs (top). The thermopolymerization times for the thin films Film-Hex-T and Film-Or-T were between 25 and 4 minutes, the lower limit being caused by the relatively slow heating ramp of 20 °C/min. For temperatures above 140 °C the reflections can be observed before the desired temperature is reached at this heating rate. Figure S9.6 shows an in-situ GISAXS measurement (Film-Hex-180fast) where the film was heated with a ramp of 100 °C/min; here the structure formation started already after 1.6 minutes. The thermopolymerization times for the samples AAM-Hex-T and AAM-Cub-T are also shorter at higher temperatures, but compared to thin films the structure formation is much slower. This effect of the tubular confinement is attributed to higher surface energies of the resulting mesophase. Apparently, the block copolymers cannot form the phase with the lowest energy but they have to allow circular distortion because the block copolymers have to adapt to the curved alumina surface. We note that this effect should be strong for the investigated mesophases due to their

relatively large unit cells (constants between 13 and 21 nm) compared to the tubular pores (ca. 200 nm in diameter).

It appears that the structure formation for orthorhombic films is faster than the formation of the hexagonal films at equal thermopolymerization temperatures, and that the cubic phase forms faster than the hexagonal phase in AAMs, which is probably caused by the different surfactants used. In both cases OMC phases made from Pluronic F127 form faster than with Pluronic P123.

Interestingly, the final patterns are also slightly different concerning the positions of the reflection spots, which is shown in Figure 5.6D for Film-Hex-T (bottom) and AAM-Hex-T (top). Higher thermopolymerization temperatures result in larger d-spacings – the reflections move closer to the beam center. Thus the swelling effect during structure formation and condensation shown in Figure 5.6A and Figure 5.6B is temperature-dependent. We explain this effect by thermal expansion of the liquid crystalline block-copolymer phase during structure formation, which is then fixed in its dimensions due to condensation of the precursor oligomers in the walls. Thermal expansion of block copolymers was also investigated for smectic phases of diblock copolymers with polyethylene oxide and polymethacrylate with azobenzene blocks (PEOm-b-PMA(Az)).<sup>83</sup> While for Film-Hex-T (Figure 5.6C, bottom) the changes between 100 °C and 140 °C are negligible ( $d_{10} \sim 11.4$  nm), a significant increase of the  $d_{10}$  d-spacings can be observed between 160 °C and 180 °C, reaching 12.7 nm. The larger d-spacings result from smaller  $q(y)$  wavevectors, while the  $q(z)$  values remain constant (Figure S9.7A, B). Thus the corresponding unit cells differ mainly in the substrate-plane (xy-plane) and not perpendicular to it (z-direction). This effect could be caused by a compensation of the swelling liquid crystal phase and uniaxial (z) shrinkage of the resol network. For AAM-Hex-T (Figure 5.6C, top) we show the shift of the 10 reflection to lower angles with increasing thermopolymerization temperature; the distribution to y and z components is shown in Figure

S9.21. Both the  $q(y)$  and  $q(z)$  values decrease with higher thermopolymerization temperatures. The decreasing  $q(y)$  reveal larger lattice plane distances parallel to the membrane wall, while the  $q(z)$  values show stretched d-spacings along the membrane normal. The differences are up to 10 % in both cases. This shows swelling of the complete unit cells of the liquid crystal structures during structure formation with increasing thermopolymerization temperatures, but no significant distortion. The final mesostructures of the samples AAM-Cub-T also differ in unit cell parameters. Figure S9.30 depicts the d-spacing of the 10-1 reflection (perpendicular to [11-2]), which is shifted to lower angles with increasing thermopolymerization temperature. The same trend as for the circular hexagonal phase is visible here; the d-spacings grow larger for higher thermopolymerization temperatures due to swelling of the liquid crystal mesostructures during thermopolymerization.

### *Carbonization*

The carbonization of a thin film is illustrated for sample Film-Hex-110 during heating in nitrogen to 1090 °C (ramp of 6 °C/min) with a series of GISAXS patterns in Figure 5.7 and a plot of radially integrated intensities in Figure 5.8.

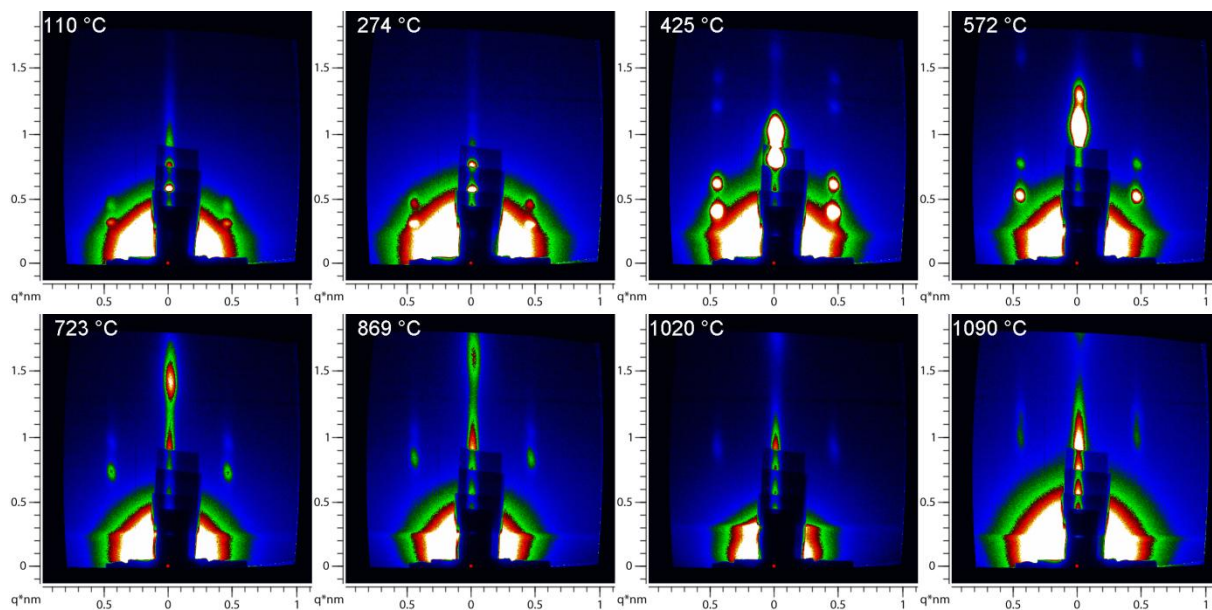


**Figure 5.7:** Carbonization of Film-Hex-110 presented in a series of GISAXS patterns: the most intense reflections are doubled due to the grazing incidence geometry (the lower reflection results from Bragg diffraction, and the second reflection on top of the first one is a specular reflection of the corresponding Bragg reflection). The strongly increased diffuse scattering as compared to the patterns in Figure 5.4 stems from the graphite dome on the heating chamber. Directions:  $q(z)$ : vertical,  $q(y)$ : horizontal.

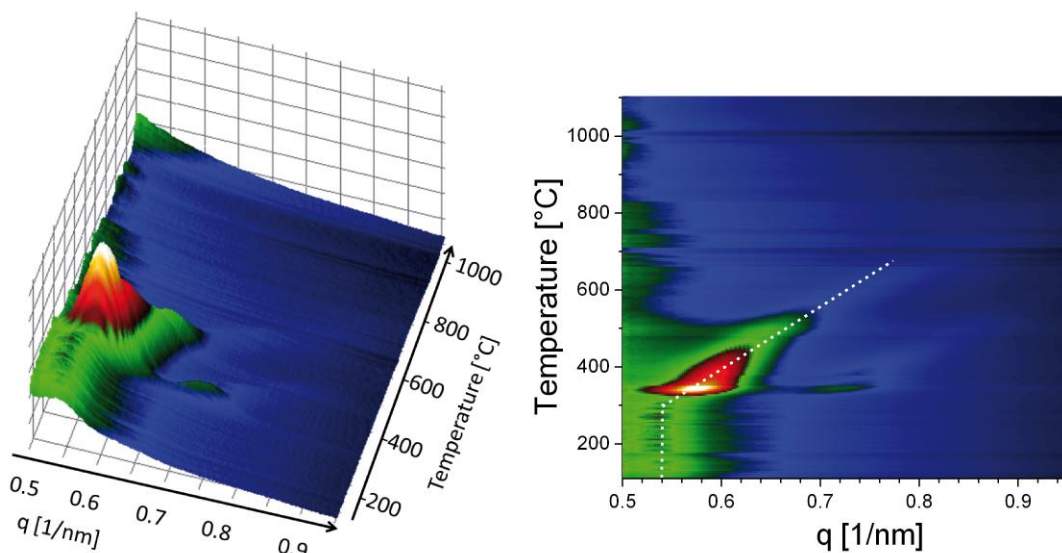


**Figure 5.8:** Carbonization of Film-Hex-110 as plot of the radial intensities: Plot of carbonization temperature vs. radially integrated intensities (3D: left; 2D: right, in-plane intensity and intensity from scattering of the graphite dome are masked). The main intensity is related to the 10-reflection. The dotted line indicates the position of the reflection maximum.

In Figure 5.7 we observe parallel movement of the reflections along  $q(z)$ , demonstrating the uniaxial shrinkage of the pore system along the substrate normal during carbonization. The first changes to the initial mesostructure are visible at around 330 °C, subsequently the intensity of the reflections increases drastically and higher order reflections arise, due to template removal and the resulting greater contrast in electron density. The reflections also shift to higher  $q$ -values along the vertical axis due to unit cell shrinkage perpendicular to the surface of the film. The intensity plot in Figure 5.8 shows that the maximum intensity is already reached around 350 °C, where the structure is only slightly distorted. At higher temperatures the reflection intensity decreases strongly while continuously shifting to higher  $q(z)$ -values. These observations show that the structure becomes less ordered at higher carbonization temperature. The reflections of the mesostructure remain visible up to 1090 °C

(Figure 5.7), thus the mesostructure did not collapse completely. We note that the structure is retained at the high temperatures due to the relatively fast heating ramp of 6°C/min; low ramp rates such as 1°C/min will lead to structural collapse at lower temperatures.<sup>26</sup> The carbonization process for the orthorhombic film Film-Or-100 was also followed *in-situ* with GISAXS as depicted in Figure S9.14. The film was heated up to 1050 °C in nitrogen with a ramp of 6 °C/min. The film shows the same behavior of uniaxial shrinkage and carbonization as the hexagonal films. Thus, the orthorhombic films can also be carbonized to highly ordered mesoporous carbon films at temperatures above 600 °C and they can even resist high temperatures up to 1050 °C for several hours.

The carbonization of sample AAM-Hex-100 was monitored *in-situ* up to 1000 °C (Figure 5.9, a more detailed series in Figure S9.22).

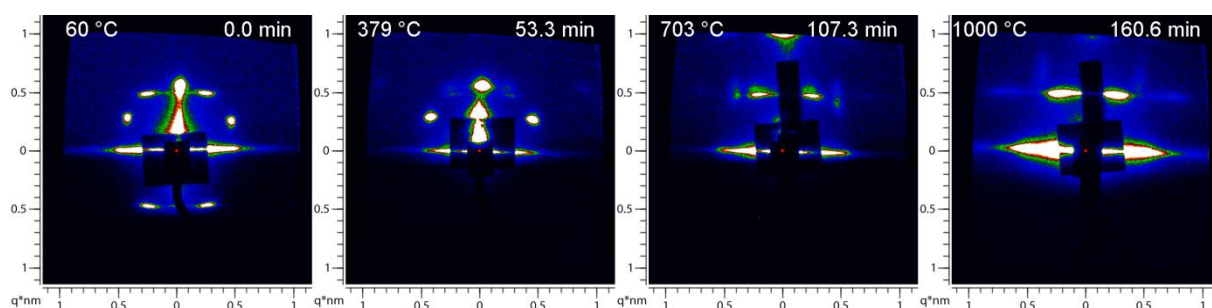


**Figure 5.9:** Carbonization of AAM-Hex-100: The reflections related to the top layer are moving due to shrinkage and vanish completely. In contrast, the reflections originating from the mesophase in the AAM pores do not shift; the shrinkage is restricted due to the confinement effect.

The initial pattern shows reflections related to the circular hexagonal structure and also reflections from a top-layer (compare Figure 5.2). The measurement shows the carbonization of the circular hexagonal structure up to 1000 °C, the shift of the reflections from the top layer due to shrinkage and the restricted shrinkage effect due to the confinement of the AAM pores.

It also illustrates the striking effect of confinement on the thermal stability, as the reflections

from the top layer completely vanish but the reflections from the mesostructure even increase in intensity up to 1000 °C. The carbonization of the sample AAM-Cub-100 could also be followed *in-situ*, which is shown in Figure S9.31. The restricted shrinkage due to confinement can also be observed here; the reflections increase drastically in intensity and higher order reflections become visible due to template removal, but no change in position is observed due to the restricted shrinkage effect of the confining AAM pores.

## 5.4. Conclusions

In this *in-situ* SAXS study we have investigated a new mechanism for the mesostructure formation of OMC phases in confined environments: thermally-induced self-assembly. The OMC phases – 2D-hexagonal and orthorhombic for thin films and cubic and circular hexagonal for anodic alumina membranes (AAMs) – were obtained by organic-organic self-assembly of a pre-formed oligomeric resol precursor and the triblock copolymer templates Pluronic P123 and F127, respectively. Importantly, we show that unlike for mesostructured metal oxides and also different to literature on those soft-templated OMCs, the structure formation for the studied OMC systems does not occur during the evaporation process but during a thermopolymerization step and can thus be called thermally-induced self-assembly. As a remarkable consequence the mesostructure is not fixed but still flexible and can be controlled during this step. Moreover, we find that higher thermopolymerization temperatures result in increased unit cell parameters, caused by swelling of the liquid crystal structures of the block copolymer templates. Interestingly, the distortion of the unit cell for hexagonal thin films mainly originates from an increase of the cell parallel to the substrate plane and is therefore not visible in standard detector scans. We also find that the rate of the structure formation strongly depends on the thermopolymerization temperature and on the block copolymer template.

Template removal and carbonization of thin films and AAMs were monitored *in situ* up to 1100 °C, without total loss of structure. In both cases, the template decomposition started at temperatures around 330 °C, indicated by a strong intensity increase in the GISAXS patterns. Strong structural distortion of the thin films was observed due to anisotropic shrinkage. In striking contrast, the confined OMC-phases in the AAM hosts were not subject to distortion even at the high carbonization temperatures reached in this study.

The new mechanism discovered here offers additional opportunities for mesostructure control. We have demonstrated the influence of different temperatures during this thermally-induced self-assembly on the final mesostructure, and we suppose that the change of other synthesis parameters such as the vapor atmosphere will also show significant effects and should thus be subject of further studies.

## 5.5. Chapter References

6. Liang, C.; Li, Z.; Dai, S., *Angew. Chem., Int. Ed.* **2008**, *47* (20), 3696-3717.
7. Wan, Y.; Shi, Y.; Zhao, D., *Chem. Mater.* **2008**, *20* (3), 932-945.
8. Chang, H.; Joo, S. H.; Pak, C., *J. Mater. Chem.* **2007**, *17* (30), 3078-3088.
9. Wu, C.-G.; Bein, T., *Science* **1994**, *266* (5187), 1013-15.
10. Ryoo, R.; Joo, S. H.; Jun, S., *J. Phys. Chem. B* **1999**, *103* (37), 7743-7746.
11. Lee, J.; Yoon, S.; Hyeon, T.; Oh, S. M.; Kim, K. B., *Chem. Commun.* **1999**, (21), 2177-2178.
12. Jun, S.; Joo, S. H.; Ryoo, R.; Kruk, M.; Jaroniec, M.; Liu, Z.; Ohsuna, T.; Terasaki, O., *J. Am. Chem. Soc.* **2000**, *122* (43), 10712-10713.
13. Kruk, M.; Jaroniec, M.; Kim, T.-W.; Ryoo, R., *Chem. Mater.* **2003**, *15* (14), 2815-2823.

21. Liang, C.; Hong, K.; Guiochon, G. A.; Mays, J. W.; Dai, S., *Angew. Chem., Int. Ed.* **2004**, *43* (43), 5785-5789.
22. Meng, Y.; Gu, D.; Zhang, F.; Shi, Y.; Cheng, L.; Feng, D.; Wu, Z.; Chen, Z.; Wan, Y.; Stein, A.; Zhao, D., *Chem. Mater.* **2006**, *18* (18), 4447-4464.
24. Zheng, M.; Ji, G.; Wang, Y.; Cao, J.; Feng, S.; Liao, L.; Du, Q.; Zhang, L.; Ling, Z.; Liu, J.; Yu, T.; Cao, J.; Tao, J., *Chem. Commun.* **2009**, (33), 5033-5035.
25. Schuster, J.; Keilbach, A.; Koehn, R.; Doeblinger, M.; Doerfler, T.; Dennenwaldt, T.; Bein, T., *Chem. Eur. J. In press*.
26. Schuster, J.; Koehn, R.; Keilbach, A.; Doeblinger, M.; Amenitsch, H.; Bein, T., *Chem. Mater.* **2009**, *21* (24), 5754-5762.
27. Song, L.; Feng, D.; Fredin, N. J.; Yager, K. G.; Jones, R. L.; Wu, Q.; Zhao, D.; Vogt, B. D., *ACS Nano* **2009**, *4* (1), 189-198.
28. Tanaka, S.; Katayama, Y.; Tate, M. P.; Hillhouse, H. W.; Miyake, Y., *J. Mater. Chem.* **2007**, *17* (34), 3639-3645.
29. Brinker, C. J.; Lu, Y.; Sellinger, A.; Fan, H., *Adv. Mater.* **1999**, *11* (7), 579-585.
30. Smarsly, B.; Grosso, D.; Brezesinski, T.; Pinna, N.; Boissière, C.; Antonietti, M.; Sanchez, C., *Chem. Mater.* **2004**, *16* (15), 2948-2952.
31. Song, L.; Feng, D.; Campbell, C. G.; Gu, D.; Forster, A. M.; Yager, K. G.; Fredin, N.; Lee, H.-J.; Jones, R. L.; Zhao, D.; Vogt, B. D., *J. Mater. Chem.* **2010**, *20* (9), 1691-1701.
32. Steinhart, M.; Liang, C.; Lynn, G. W.; Goesele, U.; Dai, S., *Chem. Mater.* **2007**, *19* (10), 2383-2385.
33. Wang, K.; Zhang, W.; Phelan, R.; Morris, M. A.; Holmes, J. D., *J. Am. Chem. Soc.* **2007**, *129* (44), 13388-13389.

34. Zheng, M.; Cao, J.; Ke, X.; Ji, G.; Chen, Y.; Shen, K.; Tao, J., *Carbon* **2007**, *45* (5), 1111-1113.
40. Yan, Y.; Zhang, F.; Meng, Y.; Tu, B.; Zhao, D., *Chem. Commun.* **2007**, (27), 2867-2869.
52. Yoneda, Y., *Physical Review* **1963**, *131* (5), 2010.
60. Pang, J.; Li, X.; Wang, D.; Wu, Z.; John, V. T.; Yang, Z.; Lu, Y., *Adv. Mater.* **2004**, *16* (11), 884-886.
61. Wang, X.; Liang, C.; Dai, S., *Langmuir* **2008**, *24* (14), 7500-7505.
62. Lu, A.-H.; Spliethoff, B.; Schueth, F., *Chem. Mater.* **2008**, *20* (16), 5314-5319.
72. Platschek, B.; Koehn, R.; Doeblinger, M.; Bein, T., *Langmuir* **2008**, *24* (9), 5018-5023.
74. Wang, K.; Birjukovs, P.; Ertz, D.; Phelan, R.; Morris, M. A.; Zhou, H.; Holmes, J. D., *J. Mater. Chem.* **2009**, *19* (9), 1331-1338.
75. Tanaka, S.; Doi, A.; Nakatani, N.; Katayama, Y.; Miyake, Y., *Carbon* **2009**, *47* (11), 2688-2698.
76. Cott, D. J.; Petkov, N.; Morris, M. A.; Platschek, B.; Bein, T.; Holmes, J. D., *J. Am. Chem. Soc.* **2006**, *128* (12), 3920-3921.
77. Grosso, D.; Babonneau, F.; Albouy, P.-A.; Amenitsch, H.; Balkenende, A. R.; Brunet-Bruneau, A.; Rivory, J., *Chem. Mater.* **2002**, *14* (2), 931-939.
78. Falcaro, P.; Grosso, D.; Amenitsch, H.; Innocenzi, P., *J. Phys. Chem. B* **2004**, *108* (30), 10942-10948.
79. Geranmayeh, S.; Abbasi, A.; Badiei, A., *E-J. Chem.* **2011**, *8* (1), 196-200.
80. Ghiorso, M.; Carmichael, I.; Moret, L., *Contrib. Mineral. Petrol.* **1979**, *68* (3), 307-323.
81. Tucker, M. G.; Keen, D. A.; Dove, M. T., *Mineral. Mag.* **2001**, *65* (4), 489-507.

82. Tate, M. P.; Urade, V. N.; Kowalski, J. D.; Wei, T.-c.; Hamilton, B. D.; Eggiman, B. W.; Hillhouse, H. W., *J. Phys. Chem. B* **2006**, *110* (20), 9882-9892.
83. Watanabe, R.; Iyoda, T.; Yamada, T.; Yoshida, H., *Journal of Thermal Analysis and Calorimetry* **2006**, *85* (3), 713-717.

## 6. LARGE PORE ORDERED MESOPOROUS CARBON NANOFIBERS WITH EXTREMELY HIGH POROSITY FOR LITHIUM-SULFUR BATTERIES

This chapter is based on a cooperation with Linda Nazar and Guang He from the University of Waterloo in Canada. The electrode preparation and electrochemical characterization was done there.

### ABSTRACT

Mesoporous carbon nanofibers featuring very large pores up to 13.3 nm or extremely high inner porosity of 2.06 cm<sup>3</sup>/g and 2486 m<sup>2</sup>/g, respectively were obtained in a two-step casting process. The fibers were successfully applied as cathode material in Li-S batteries, where they showed high reversible capacity up to 1050 mAh/g and good cycle efficiency. The synthesis starts with casting of commercial carbon nanofibers (MF-150, Ø ≈ 150 nm) with a silica precursor solution leading to a macroporous silica template after calcination. The silica template is then imbibed with three different precursor solutions for ordered mesoporous carbon, the samples are carbonized up to 1000 °C and finally etched in hydrofluoric acid to free the mesoporous carbon nanofibers (MCNF). The samples MCNF-F127 and MCNF-P123 were obtained by organic-organic self-assembly of a preformed oligomeric resol precursor and the triblock copolymer templates Pluronic F127 or P123, respectively. The fibers exhibited large pore sizes up to diameters of 13.3 nm which is much larger than the related bulk synthesis and can be explained by a restricted shrinkage effect of the tubular confinement. For the third sample MCNF-C-36\*, a triconstituent precursor solution containing resol, TEOS as additional silica precursor and the block copolymer Pluronic F127

was used. After carbonization and etching those OMC nanofibers exhibit large pores of ~6.0 nm from the block copolymer template and additional smaller pores from the removal of the silica from the walls of the composite and feature therefore a very large surface area and a high inner pore volume of 2486 m<sup>2</sup>/g and 2.06 cm<sup>3</sup>/g, respectively. All fibers exhibit diameters of 50 to 100 nm and lengths of several micrometers. The process only involves the use of low-cost materials; especially the synthesis of the macroporous silica template is more cost-effective than the commonly used anodic alumina membranes and might therefore be superior for lab synthesis at the gram scale or even suitable for large-scale applications.

## 6.1. Introduction

A large number of modern applications are dependent on porous carbon materials. Porous carbons are employed as sorbents for separation and gas storage, as catalyst supports and as electrode material for fuel cells, supercapacitors and batteries. The highly favorable properties such as high specific surface area and pore volume, chemical and thermal stability or electrical conductivity make porous carbons suitable for those purposes.

Ordered mesoporous carbons (OMCs)<sup>6-8</sup> – tailor-made in terms of macroscopic morphology and properties of the periodic mesopore system – could be superior for several of these applications compared to classically used activated carbons. As the mass transport to the surface depends on both, the pore sizes of the mesopores (or micropores) and the length of the diffusion paths inside those pores, hierarchical porosity could be beneficial. Morphology control is therefore an important issue in OMC synthesis. In the literature there are numerous examples for mesoporous bulk materials made either by hard-templating<sup>9-13</sup> or soft-templating,<sup>22-23, 61-62</sup> and several examples for OMCs prepared as thin films<sup>21, 26, 28, 31</sup> or as nanoparticles,<sup>39, 42, 44</sup> as fibers embedded in membranes,<sup>24-25, 32-34, 74</sup> or as free fibers.<sup>24, 33, 35</sup> Most of the syntheses self-assembly of oligomeric carbon precursors and block copolymers followed by thermal treatments for template removal (>350 °C) and carbonization (>600 °C). The OMCs synthesized like this normally suffer from serious shrinkage during carbonization which results in reduced pore sizes and volumes. Tubular confinements can have highly beneficial effects<sup>24-25</sup> on the shrinkage behavior and the thermal stability on the embedded fibers. Due to strong adhesion of the carbon to the pore walls of the confinement (e.g. alumina), the mesoporous structure cannot shrink; only the carbon pore walls of the mesostructured carbon can shrink. Therefore this restricted shrinkage effect results not only in much larger pore sizes compared to bulk syntheses from equivalent precursor solutions but

also in increasing pore sizes at higher carbonization temperatures. Zheng et al.<sup>24</sup> observed pore sizes up to 15 nm for carbonization at 700 °C and as further consequence very high porosity of 1154 m<sup>2</sup>/g and 3.44 cm<sup>3</sup>/g. Recently, Schuster and coworkers<sup>25</sup> reported a cubic OMC phase embedded in AAMs with a pore size for the spherical pores of 20 nm for carbonization at 1000 °C, also showing very high porosity up to 1130 m<sup>2</sup>/g and 2.3 cm<sup>3</sup>/g. For applications that require larger amounts of free fibers the use of AAMs as template is not reasonable due to the high cost in relation to the OMC yield. Thus other hard templates with tubular pores should also be explored. A different approach to reduce shrinkage, introduced by Liu et al.<sup>23</sup> uses coassembly of resol as carbon precursor and tetraethylorthosilicate (TEOS) as silica precursor for synthesis of mesoporous carbon/silica nanocomposites. The silica in the walls has two beneficial effects, it reduced the shrinkage and creates additional porosity by etching it. Thus several mesoporous carbon materials with varying carbon/silica contents could be synthesized that showed pore sizes around 6 nm and extremely high porosities up to 2470 m<sup>2</sup>/g and 2.0 cm<sup>3</sup>/g, respectively. The synthesis of those highly porous OMCs in the form of nanofibers could enhance the accessibility of the pores and therefore have beneficial effects for applications dependent on diffusion of guests.

Rechargeable lithium sulfur (Li-S) batteries require carbon materials with extremely high accessible porosity.<sup>46</sup> They are attracting increasing attention due to their high theoretical specific energy density, which is 3 to 5 times higher than that of lithium-ion batteries based on intercalation reactions. In lithium sulfur batteries the OMCs act as cathode material and host for sulfur, which is reacting to Li<sub>2</sub>S. They have to provide electron transport to the isolating sulfur; therefore the sulfur has to be in the range of few nanometers from the carbon surface. For this purpose the OMCs for Li-S batteries need extremely high surface areas and even more important extremely high pore volumes. Beside this Li-S batteries usually show

capacity fading due to dissolution of intermediates – the polysulfides  $\text{LiS}_n$  – in the electrolyte, which causes irreversible loss of active sulfur. Thus, the used OMCs should also trap the polysulfides. For those reasons control over the diffusion of both, the Li-ions and the polysulfides is necessary. The diffusion is controlled by pore sizes and geometries, but also the external morphology, which defines the accessibility of the inner pore structure and the length of diffusion paths.

Herein we report on the synthesis of mesoporous carbon nanofibers and their application in lithium-sulfur batteries. The fibers were obtained by a two step casting process. First commercial carbon nanofibers (MF-150,  $\text{Ø} \approx 150$  nm) were cast with a silica precursor solution leading to a silica template with tubular pores after calcination. The silica template was then cast in a second step with three different precursor solutions, carbonized up to 1000 °C and finally etched in hydrofluoric acid to free the mesoporous carbon nanofibers (MCNF). The samples MCNF-F127 and MCNF-P123 were obtained by self-assembly of the preformed oligomeric resol and the triblock copolymer templates Pluronic F127 or P123, respectively. The fibers exhibited large pore sizes up to diameters of 13 nm, which is much larger than the related bulk synthesis and can be explained by the restricted shrinkage effect of the confinement which was found for OMCs in anodic alumina membranes (AAMs) before. For the third sample MCNF-C-36\*, a triconstituent precursor solution containing resol, TEOS as additional silica precursor and the block copolymer Pluronic F127 was used. After carbonization and etching those OMC nanofibers also exhibit pores of ~6 nm from the block copolymer template and additional smaller pores from the removal of the silica from the walls of the composite and showed therefore a very large surface area and a high pore volume of 2486 m<sup>2</sup>/g and 2.06 cm<sup>3</sup>/g, respectively. All fibers exhibit diameters of 50 to 100 nm and lengths of several micrometers. The process only involves the use of low-cost materials; especially the synthesis of the macroporous silica template is more cost-effective than the

commonly used anodic alumina membranes and might therefore be superior for lab synthesis at the gram scale or even suitable for large scale applications. As a proof of principle, the fibers were successfully applied as cathode material in Li-S batteries, where they showed high reversible capacity up to 1050 mAh/g.

## 6.2. Experimental Section

**Chemicals.** Formalin (37 wt% formaldehyde in water) and the triblock copolymers Pluronic P123 ( $M_w = 5800$ , EO<sub>20</sub>-PO<sub>70</sub>-EO<sub>20</sub>) and Pluronic F127 ( $M_w = 12600$ , EO<sub>106</sub>-PO<sub>70</sub>-EO<sub>106</sub>) were purchased from BASF AG, phenol from Merck KGaA and TEOS (Tetraethylorthosilicate, C<sub>8</sub>H<sub>20</sub>O<sub>4</sub>Si) from Sigma Aldrich GmbH. All chemicals were used without further purification. Carbon nanofibers MF-C150 were received from YOUR-TOOL GmbH ( $\varnothing = 80 - 150$  nm, length 2-25  $\mu\text{m}$ ).

### Synthesis.

#### *Macroporous Silica.*

For a silica sol-gel solution 4 ml of ethanol were mixed with 6 ml TEOS (26.9 mmol), 3 ml water and 1 ml concentrated hydrochloric acid (1.19 g, 12 mmol HCl). The carbon nanofibers MF-C150 were suspended in ethanol and filtered on a Büchner funnel. While applying vacuum to the funnel the silica sol-gel solution is dripped over the surface to completely wet the nanofibers. The silica/carbon composite is heated to 1000 °C with a ramp of 2 °C/min and calcined for 3 h. The silica yield is normally around 25 wt % of the initial carbon fibers.

*Resol precursor.* A low molecular weight precursor for the organic framework was synthesized in a reaction of phenol and formaldehyde in a base-catalyzed process according to

Meng et al.<sup>22</sup>. For the synthesis, 6.1 g of phenol (0.064 mol) were molten in a flask with 1.3 g of 20 wt % sodium hydroxide solution (0.0065 mol). The mixture was heated up to 50 °C and then 10.5 g formalin (37 wt % formaldehyde in water, 0.1295 mol) were added drop wise. The molar ratio of phenol / formaldehyde / NaOH was 1 : 2 : 0.1. The clear, lightly yellow colored solution was stirred at 75 °C for one hour and then cooled down to room temperature. The precursor solution was neutralized with 1 M hydrochloric acid and the water was removed by vacuum evaporation below 50 °C. The resulting product (10 g) was redissolved in ethanol to a total weight of 50 g (20 wt %).

*Synthesis of Mesoporous Carbon Nanofibers (MCNF).* Three different precursor solutions were mixed for the samples MCNF-F127, MCNF-P123 and MCNF-C36\*, respectively. The precursor solutions for MCNF-F127 and MCNF-P123 are based on our previous work<sup>25</sup> for OMCs in anodic alumina membranes for the samples Cub-1000 and Hex-1000, respectively. MCNF-F127 was obtained for a molar ratio of phenol / formaldehyde / NaOH / F127 = 1 : 2 : 0.1 : 0.0044. In a typical preparation, 1 g of the resol precursor solution was mixed with 1.5 g template solution (4.76 wt % Pluronic F127 in ethanol). After stirring for 10 min, a homogeneous solution was obtained. MCNF-P123 was obtained for a molar ratio of phenol / formaldehyde / NaOH / P123 = 1 : 2 : 0.1 : 0.0095. In a typical preparation, 1 g of the precursor solution was mixed with 0.75 g template solution (9.52 wt % Pluronic P123 in ethanol).

The preparation of the precursor solutions for MCNF-C36\* is based on Liu et al.<sup>23</sup> for the sample MP-C-36\* with the mass ratio F127/resol/TEOS/EtOH/HCl/H<sub>2</sub>O) 1:0.5:2.08:12:0.0073:1.0. In a typical preparation, 1.0 g of Pluronic F127, 10.0 g of ethanol, and 1.0 g of 0.2 M HCl were mixed well at 40 °C. Then 2.08 g TEOS and 2.5 g of the 20 wt-% resol solution were added, and stirring was continued for 5 h at 40 °C.

The precursor solutions were cast in glass vials together with the macroporous silica template with a mass ratios for precursor solution/porous silica of 20:1 for MCNF-F127 and MCNF-P123 and 40:1 for MCNF-C36\*, which are equivalent with the ratios for precursor solution to the initial fibers MF-C150 of 5:1 and 10:1 for a silica yield of 25 %.

The ratio for MCNF-F127 and MCNF-P123 is based on the assumption that the final porous carbon product has a density which is up to three times lower than the density of the non porous nanofibers MF-C150 and therefore needs up to three times more space. The OMC yield of the precursor solution MCNF-F127 is 4 % and for MCNF-P123 it is 5.7 %. This means the weight ratio of the precursor solutions to OMC are 25:1 (MCNF-F127) and 17.5:1 (MCNF-P123). Due to three times higher density of the carbon fibers MF-C150, the maximum ratio for precursor solutions to the initial fibers MF-C150 should be below 25:3 (MCNF-F127) and 17.5:3 (MCNF-P123). The chosen ratios of 5:1 were much lower.

The ratio for MCNF-C36\* is based on the assumption that the final porous carbon product has a density which is up to five times lower than the density of the non porous nanofibers MF-C150 and therefore needs up to five times more space. The OMC yield of the precursor solution of MCNF-C36\* it is only 1.5 %. Therefore the weight ratio of the precursor solution to OMC 66:1. Due to five times higher density of the carbon fibers MF-C150, the maximum ratio for precursor solutions to the initial fibers MF-C150 should be below 66:5 or 13:1. The chosen ratio of 10:1 was much lower.

The solvent was evaporated and the composites were thermopolymerized for 24 h at 100 °C. Afterwards, the materials were carbonized at 1000 °C in nitrogen for MCNF-F127 and MCNF-P123, or at 900 °C for MCNF-C-36\*, respectively. The heating ramp was 1 °C/min

and the dwell time 3 h. After carbonization the carbon-silica nanocomposites were immersed in 10 wt % HF solution for 24 h.

#### *Electrode preparation.*

The C/S nanocomposites were prepared following a melt-diffusion strategy. Mesoporous carbon was ground together with sulfur with a mass ratio of 1 : 1 and then heated to 155 °C for overnight. The C/S cathode materials were slurry-cast from cyclopentanone onto a carbon-coated aluminum current collector. Typically, 82 wt% of C/S composite, 10 wt% Super S carbon and 8 wt% poly(vinylidene fluoride) (PVDF) were mixed with cyclopentanone. The slurries were coated on aluminum current collectors and dried at 60 °C overnight. The electrochemical performance of the prepared cathodes was evaluated using 2325 coin cells cycled at room temperature between 1.5 V and 3.0 V, with lithium metal foil as the anode. The electrolyte used was 1 M bis-(trifluoromethane)sulfonimide lithium (LiTFSI) in a mixed solvent of dimethoxyethane (DME) and dioxolane (DOL) with a volume ratio of 1 : 1.

#### **Characterization**

Transmission electron microscopy (TEM) data were obtained on a JEOL JEM 2011 microscope at an acceleration voltage of 200 kV or a TITAN 80-300 microscope at an acceleration voltage of 300 kV. Scanning electron microscopy (SEM) was performed on a JEOL JSM-6500F scanning electron microscope equipped with a field emission gun, at 4 kV. Nitrogen sorption isotherms were obtained at -196 °C using a Quantachrome Nova 4000e or a Quantachrome Autosorb-1.

### **6.3. Results and Discussion**

SEM and TEM measurements were carried out to investigate the morphology and the mesoporous structure of the OMC nanofibers. Figure 6.1 shows SEM and TEM micrographs of the three different samples MCNF-F127, MCNF-P123 and MCNF-C36\*.

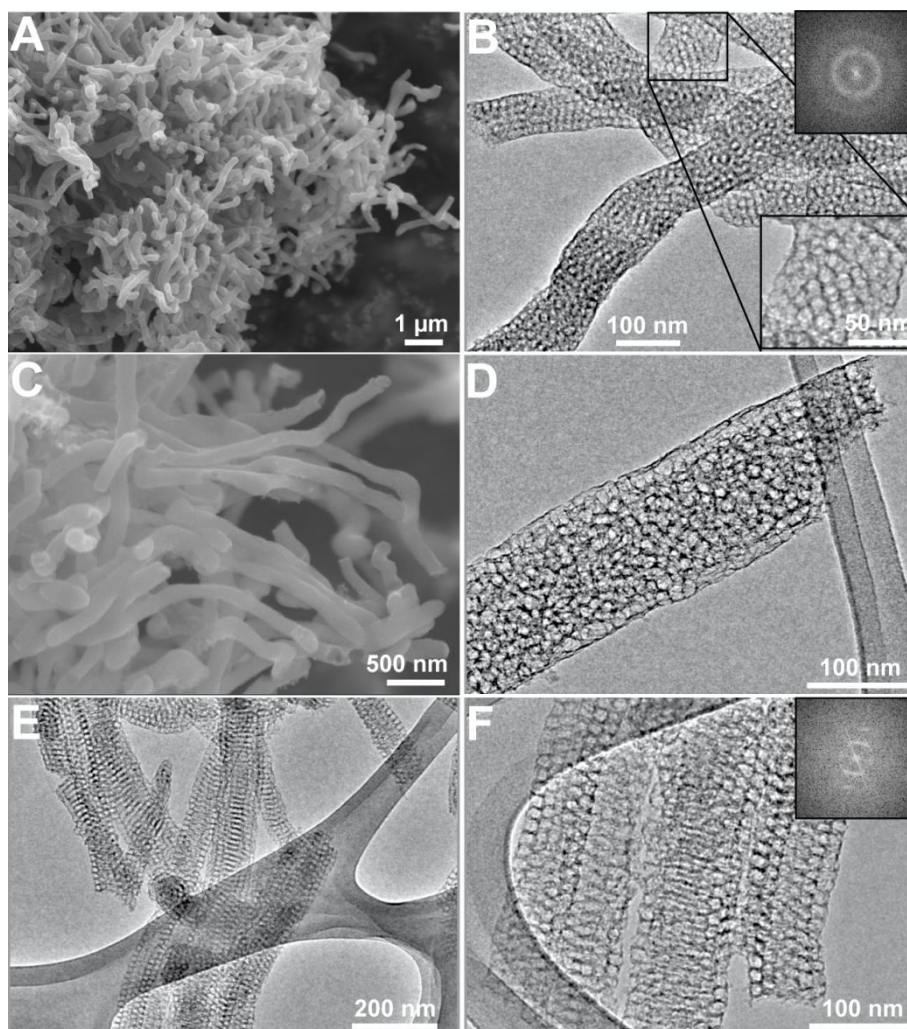


**Figure 6.1:** SEM (A, C) and TEM (B, D, E, F) micrographs of MCNF-F127 (A, B), MCNF-P123 (C, D) and MCNF-C36\* (E, F) with insets at higher magnification or Fast-Fourier-Transformations (FFT) of the images

The fiber morphology can be clearly seen in the left column (Figure 6.1A, C, E). The observed fibers are several micrometers long and exhibit diameters of 50 to 100 nm and are therefore thinner than the initial carbon nanofibers (MF-C150,  $\varnothing = 80 - 150$  nm) that were

used for the synthesis of the macroporous silica template. The silica is heated up to 1000 °C during calcinations and therefore shrinkage occurred. The fibers are not completely straight, they exhibit curvatures. In the right column (Figure 6.1B, D, F), the fibers are depicted in high resolution and the mesoporous structures can be observed. For MCNF-F127 (Figure 6.1B), the fibers exhibit an ordered mesostructure with small domain sizes but uniform d-spacings of 12.4 nm (inset FFT). The fibers are probably too thin to allow the order of a highly oriented cubic phase which was found for the same precursor solution in AAMs.<sup>25</sup> MCNF-P123 does not show any ordered mesoporous structure, again the fibers are probably too thin to allow the order of the highly oriented circular hexagonal structure which was found for the precursor solution used in AAMs.<sup>25</sup> The fibers MCNF-C36\* clearly show a highly ordered mesostructure with defined large pores and uniform d-spacing of ca. 12.2 nm (inset FFT). A 2D-hexagonal structure was found with this precursor solution for bulk material<sup>23</sup>, therefore a hexagonal structure was expected. The fibers are probably ordered in a circular hexagonal structure, which is indicated by a different orientation near the fiber edges and in the center of the fibers.

The porosity properties (Table 6.1) were determined by nitrogen sorption measurements of the free OMC fibers.

**Table 6.1.** Porosity properties for mesoporous nanofibers

Sample Name	BET area [m <sup>2</sup> /g]	Pore volume [cc/g]	Pore size NLDFT [nm]	Pore size BJH <sup>c</sup> [nm]
MCNF-F127	690	0.73	13.3 <sup>a</sup>	9.6
MCNF-P123	700	0.77	7.0, 8.6 <sup>b</sup>	9.4
MCNF-C36*	2486	2.06	2.7 - 6.0 <sup>b</sup>	-

[a] Calculated by the NLDFT adsorption branch model for cylindrical and spherical pores with silica as adsorbent [b] NLDFT adsorption branch model for cylindrical pores with silica as adsorbent [c] Calculated by the BJH model from the adsorption branches

Figure 6.2 depicts the isotherms of the samples MCNF-F127, MCNF-P123 and MCNF-C36\* with their respective pore size distributions.

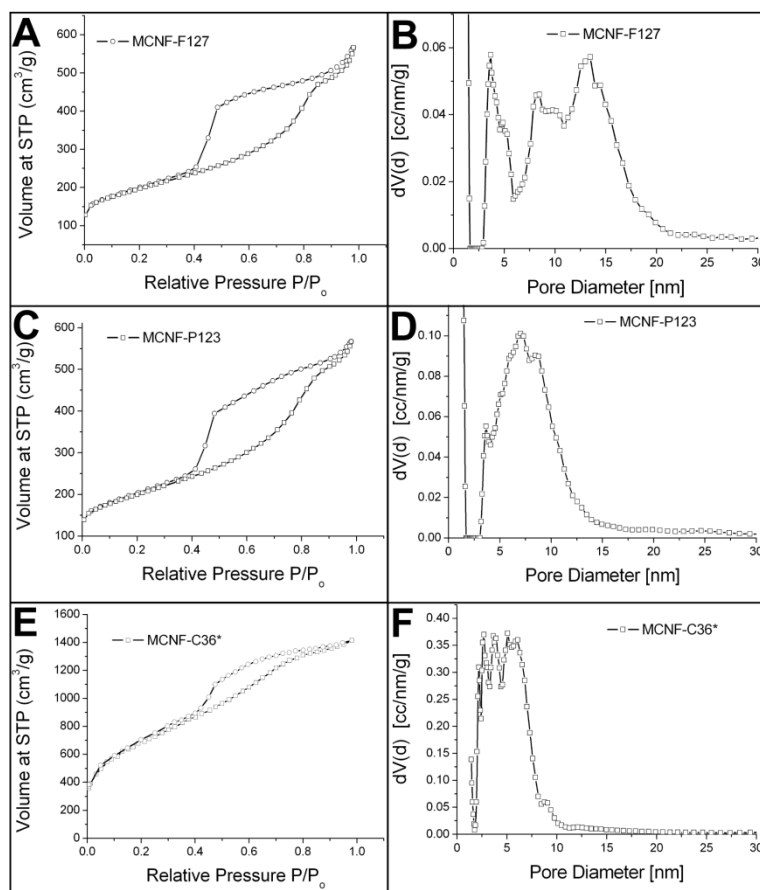


**Figure 6.2:** Nitrogen-sorption measurements (A, C, E) and pore size distributions (B, D, F) for MCNF-F127 (A, B), MCNF-P123 (C, D) and MCNF-C36\* (E, F). The pore size distributions are calculated by NLDFT methods from the adsorption branches.

For MCNF-F127 the calculation of the pore sizes was done using a NLDFT silica kernel for spherical and cylindrical pores from the adsorption branch. This kernel was chosen due to the

expected spherical pores typical for a cubic structure that was found for the precursor solution used in AAMs.<sup>25</sup> The calculation of the pore-size distributions for MCNF-P123 and MCNF-C36\* was done with a NLDFT method using a silica kernel for cylindrical pores for the adsorption branch due to pore blocking. The silica kernels are the best compromises for those systems, as corresponding models for carbon materials do not yet exist. For better comparison with literature data the pore sizes calculated with the BJH model from the adsorption branches are also listed in Table 6.1.

MCNF-F127 and MCNF-P123 (Figure 6.2A, C) show adsorption at high relative pressures (0.75 – 0.85  $p/p_0$ ), which can be attributed to condensation in large mesopores and a large hysteresis loop due to narrow pore entrances. In addition, adsorption above 0.85  $p/p_0$  can be observed, which can be attributed to textural porosity and clearly confirms the fiber morphology found in SEM and TEM micrographs in Figure 6.1.

MCNF-F127 and MCNF-P123 exhibit large mesopores up to 13.3 nm and 8.6 nm, respectively with relatively wide distributions (Figure 6.2B, D). The fibers show similar surface areas ( $\sim 700 \text{ m}^2/\text{g}$ ) but higher pore volumes ( $\sim 0.77 \text{ cm}^3/\text{g}$ ) and much larger pores than the corresponding bulk materials<sup>22</sup> synthesized with the same precursor solutions (FDU-16, FDU-15). This clearly shows the beneficial effect of restricted shrinkage due to the confinement of the macroporous silica template, which was already found in AAMs.<sup>25</sup> The shrinkage of the carbon fibers is restricted due to strong adhesion to the silica walls; as a consequence, also the shrinkage of the mesopores themselves is restricted. Compared to the cubic and circular hexagonal phase in AAMs the restricted shrinkage effect is not that pronounced, there even larger pore sizes were observed. MCNF-C36\* shows much higher porosity (Figure 6.2E), a very large surface area and a high inner pore volume of  $2486 \text{ m}^2/\text{g}$  and  $2.06 \text{ cm}^3/\text{g}$  ( $p/p_0 = 0.85$ , pores  $< 15 \text{ nm}$ ) and a total pore volume of  $2.2 \text{ cm}^3/\text{g}$

( $p/p_0 = 0.98$ ), respectively. Those extremely high porosity values are caused by the coassembly of the carbon and the silica precursor which reduces shrinkage and gives additional porosity by etching the silica. The fibers exhibit a broad pore size distribution (Figure 6.2F) with pore sizes between 2.7 and 6 nm.

### Lithium-Sulfur Batteries:

The three samples were tested as cathode material and sulfur host in Li-S batteries and investigated concerning reversible capacities and cycling stability up to 400 cycles, which is depicted in Figure 6.3.

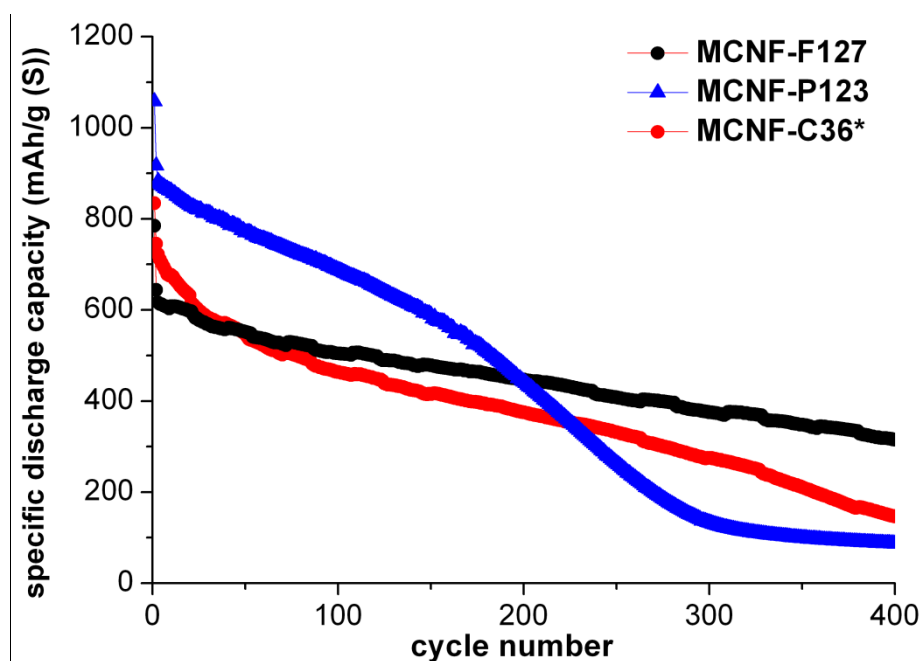


**Figure 6.3:** Cycling stability up to 400 cycles of carbon/sulfur composites of the mesoporous carbon nanofibers MCNF-F127 and MCNF-P123 and MCNF-C36\*.

The three nanofibers showed differing behavior concerning reversible capacities and cycling stability. The highest reversible capacity up to 1050 mAh/g was achieved with the sample MCNF-C36\*. But the capacity dropped strongly after ca. 150 cycles down to 90 mAh/g after

400 cycles which is only 8 % of the initial capacity. The samples MCNF-F127 and MCNF-P123 on the other hand showed much lower initial capacities of around 800 mAh/g, however the cycling stability was much higher and the capacities follow a linear decrease. After 400 cycles the highest specific capacity was obtained for MCNF-F127 with 325 mAh/g, equivalent to 41 % of the initial capacity. The reasons for the strongly differing behavior are not clear yet. The different pore sizes and/or pore morphologies seem to have significant effects on the diffusion of the polysulfides. For clarification of these effects further investigations are needed.

#### 6.4. Conclusions

We have demonstrated the synthesis of mesoporous carbon nanofibers and their application as cathode and sulfur host in high capacity Li-S batteries. The fibers MCNF-F127 and MCNF-P123 showed large pores up to 13.3 nm due to the restricted shrinkage effect of the tubular pores of the silica template. MCNF-C36\* exhibited extremely high porosity, of 2486 m<sup>2</sup>/g and 2.06 cm<sup>3</sup>/g, respectively due to the coassembly approach of a carbon and silica precursor that reduces shrinkage and gives additional porosity by etching the silica. The fibers showed interesting first results as cathode material in Li-S batteries with capacities up to 1050 mAh/g and high cycling efficiency with a retained capacity of 41 % even after 400 cycles, which serves as proof of principle. Further experiments are needed to clarify the reasons for the strongly differing behavior for capacity fading.

#### 6.5. Chapter References

6. Liang, C.; Li, Z.; Dai, S., *Angew. Chem., Int. Ed.* **2008**, *47* (20), 3696-3717.
7. Wan, Y.; Shi, Y.; Zhao, D., *Chem. Mater.* **2008**, *20* (3), 932-945.
8. Chang, H.; Joo, S. H.; Pak, C., *J. Mater. Chem.* **2007**, *17* (30), 3078-3088.

9. Wu, C.-G.; Bein, T., *Science* **1994**, *266* (5187), 1013-15.
10. Ryoo, R.; Joo, S. H.; Jun, S., *J. Phys. Chem. B* **1999**, *103* (37), 7743-7746.
11. Lee, J.; Yoon, S.; Hyeon, T.; Oh, S. M.; Kim, K. B., *Chem. Commun.* **1999**, (21), 2177-2178.
12. Jun, S.; Joo, S. H.; Ryoo, R.; Kruk, M.; Jaroniec, M.; Liu, Z.; Ohsuna, T.; Terasaki, O., *J. Am. Chem. Soc.* **2000**, *122* (43), 10712-10713.
13. Kruk, M.; Jaroniec, M.; Kim, T.-W.; Ryoo, R., *Chem. Mater.* **2003**, *15* (14), 2815-2823.
21. Liang, C.; Hong, K.; Guiochon, G. A.; Mays, J. W.; Dai, S., *Angew. Chem., Int. Ed.* **2004**, *43* (43), 5785-5789.
22. Meng, Y.; Gu, D.; Zhang, F.; Shi, Y.; Cheng, L.; Feng, D.; Wu, Z.; Chen, Z.; Wan, Y.; Stein, A.; Zhao, D., *Chem. Mater.* **2006**, *18* (18), 4447-4464.
23. Liu, R.; Shi, Y.; Wan, Y.; Meng, Y.; Zhang, F.; Gu, D.; Chen, Z.; Tu, B.; Zhao, D., *J. Am. Chem. Soc.* **2006**, *128* (35), 11652-11662.
24. Zheng, M.; Ji, G.; Wang, Y.; Cao, J.; Feng, S.; Liao, L.; Du, Q.; Zhang, L.; Ling, Z.; Liu, J.; Yu, T.; Cao, J.; Tao, J., *Chem. Commun.* **2009**, (33), 5033-5035.
25. Schuster, J.; Keilbach, A.; Koehn, R.; Doeblinger, M.; Doerfler, T.; Dennenwaldt, T.; Bein, T., *Chem. Eur. J.* *In press*.
26. Schuster, J.; Koehn, R.; Keilbach, A.; Doeblinger, M.; Amenitsch, H.; Bein, T., *Chem. Mater.* **2009**, *21* (24), 5754-5762.
28. Tanaka, S.; Katayama, Y.; Tate, M. P.; Hillhouse, H. W.; Miyake, Y., *J. Mater. Chem.* **2007**, *17* (34), 3639-3645.

31. Song, L.; Feng, D.; Campbell, C. G.; Gu, D.; Forster, A. M.; Yager, K. G.; Fredin, N.; Lee, H.-J.; Jones, R. L.; Zhao, D.; Vogt, B. D., *J. Mater. Chem.* **2010**, *20* (9), 1691-1701.
32. Steinhart, M.; Liang, C.; Lynn, G. W.; Goesele, U.; Dai, S., *Chem. Mater.* **2007**, *19* (10), 2383-2385.
33. Wang, K.; Zhang, W.; Phelan, R.; Morris, M. A.; Holmes, J. D., *J. Am. Chem. Soc.* **2007**, *129* (44), 13388-13389.
34. Zheng, M.; Cao, J.; Ke, X.; Ji, G.; Chen, Y.; Shen, K.; Tao, J., *Carbon* **2007**, *45* (5), 1111-1113.
35. Liu, H.-J.; Wang, X.-M.; Cui, W.-J.; Dou, Y.-Q.; Zhao, D.-Y.; Xia, Y.-Y., *J. Mater. Chem.* **2010**, *20* (20), 4223-4230.
39. Wang, Z.; Li, F.; Stein, A., *Nano Letters* **2007**, *7* (10), 3223-3226.
42. Kim, T.-W.; Chung, P.-W.; Slowing, I. I.; Tsunoda, M.; Yeung, E. S.; Lin, V. S. Y., *Nano Letters* **2008**, *8* (11), 3724-3727.
44. Fang, Y.; Gu, D.; Zou, Y.; Wu, Z.; Li, F.; Che, R.; Deng, Y.; Tu, B.; Zhao, D., *Angew. Chem.* **2010**, *122* (43), 8159-8163.
46. Ji, X.; Nazar, L. F., *J. Mater. Chem.* **2010**, *20* (44), 9821-9826.
61. Wang, X.; Liang, C.; Dai, S., *Langmuir* **2008**, *24* (14), 7500-7505.
62. Lu, A.-H.; Spliethoff, B.; Schueth, F., *Chem. Mater.* **2008**, *20* (16), 5314-5319.
74. Wang, K.; Birjukovs, P.; Erts, D.; Phelan, R.; Morris, M. A.; Zhou, H.; Holmes, J. D., *J. Mater. Chem.* **2009**, *19* (9), 1331-1338.

## **7. SPHERICAL ORDERED MESOPOROUS CARBON NANOPARTICLES WITH EXTREMELY HIGH POROSITY FOR LITHIUM-SULFUR BATTERIES**

This chapter is based on a cooperation with Linda Nazar and Guang He from the University of Waterloo in Canada. The electrode preparation and electrochemical characterization was done there.

### **ABSTRACT**

Spherical ordered mesoporous carbon nanoparticles featuring extremely high inner porosity (pore volume of  $2.32 \text{ cm}^3/\text{g}$  and surface area of  $2445 \text{ m}^2/\text{g}$ ) were synthesized in a two-step casting process. They were successfully applied as cathode material in Li-S batteries, where they showed high reversible capacity up to  $1200 \text{ mAh/g}$  and good cycle efficiency. Starting from a cast PMMA opal structure an inverse opal silica structure was obtained. This material was used as a silica template for casting a triconstituent precursor solution of resol, tetraethylorthosilicate (TEOS) and Pluronic F127. Through carbonization a carbon/silica nanocomposite was formed in the large pores of the silica inverse opal structure. Afterwards, both the inverse opal silica template and the silica of the nanocomposite mesostructure were removed by etching with hydrofluoric acid. The final product consists of spherical mesoporous carbon particles with a diameter of around  $300 \text{ nm}$  and 2D-hexagonal porosity.

The particles exhibit large pores of ~6 nm from the block copolymer template and smaller pores from the removal of the silica inside the walls of the composite. The particles could be completely separated by sonification and form stable colloidal suspensions of the single particles in water, which could be the base for further applications such drug delivery.

## 7.1. Introduction

Following up the introduction of the previous chapter, the morphology of OMCs as spherical nanoparticles is also attracting increasing attention. While most of the syntheses for OMC bulk materials, thin films or fibers use sol-gel chemistry followed by thermal treatments for template removal and carbonization, nanoparticle syntheses for other materials are normally solution based syntheses where nucleation and particle growth can be controlled by concentrations and reaction times. Therefore it is a big challenge to either create solution based OMC nanoparticle syntheses or to adapt the established EISA methods to nanoparticles. Due to these difficulties only few examples for OMC nanoparticles are reported so far using varying concepts for nanoparticle synthesis. Wang et al.<sup>39</sup> synthesized OMCs in the voids of a macroporous template of close packed PMMA spheres. After removing the template they obtained OMC nanoparticles of spherical or cubic morphology. Yan and coworkers<sup>40</sup> used an aerosol assisted approach to synthesize OMC micro- and nanoparticles with relatively broad size distributions and porosity up to 427 m<sup>2</sup>/g and 0.42 cm<sup>3</sup>/g, respectively. Kim et al.<sup>42</sup> used mesoporous silica nanoparticles as template for inverse carbon structures with very high surface area up to 2000 m<sup>2</sup>/g and a pore volume of 1.2 cm<sup>3</sup>/g for small mesopores of 2.4 nm. They could also show that the particles could serve as a transmembrane carrier. Tonanon and coworkers<sup>41</sup> used ultrasonic emulsification to create submicron mesoporous carbon spheres. Nanoparticles at variable size from 20 nm up to 140 nm were obtained in a hydrothermal synthesis by Fang et al.<sup>46</sup> They gained porosities up to 1100 m<sup>2</sup>/g and 1.52 cm<sup>3</sup>/g,

respectively. Ordered arrays of mesoporous carbon spheres were reported by Liu et al.<sup>43</sup> They used close packed PMMA spheres for the synthesis of a silica inverse opal structure and in the second step this silica inverse opal was imbibed with the OMC precursors. They obtained fused particles with porosity properties of  $601 \text{ m}^2/\text{g}$  and  $1.70 \text{ cm}^3/\text{g}$  including textural porosity. Recently Lei et al.<sup>45</sup> reported the synthesis of mesoporous carbon nanospheres with diameters of 65 nm, hierarchical porosity of 2.7 nm mesopores and high textural porosity and therefore very high porosity up to a surface area of  $2400 \text{ m}^2/\text{g}$  and a total pore volume of  $2.9 \text{ cm}^3/\text{g}$ . The nanospheres made through hard-templating of mesoporous silica spheres showed high energy density and cyclability as electrode material in a supercapacitor.

Herein we report the synthesis of spherical OMC nanoparticles of 300 nm in diameter, which can be dispersed in water by sonification to form stable colloidal suspensions. The spherical mesoporous carbon nanoparticles were obtained by a two step casting process. An opal structure of PMMA spheres was cast with a silica precursor solution to form a silica inverse opal. The inverse opal is then used as template for a triconstituent precursor solution<sup>23</sup> containing resol as the carbon precursor, TEOS as the silica precursor and the block copolymer Pluronic F127 as the structure directing agent. Carbonization is followed by etching of the silica template and the silica in the carbon/silica nanocomposite with hydrofluoric acid, resulting in the formation of OMC with hierarchical porosity. Through the silica in the walls, shrinkage during carbonization is reduced and additional porosity is produced by etching it, therefore OMC with extremely high mesoporosity is created. To the best of our knowledge the material shows one of the highest inner pore volumes for mesoporous carbon nanoparticles of  $2.32 \text{ cm}^3/\text{g}$  and also one of the highest surface areas of  $2445 \text{ m}^2/\text{g}$  with a bimodal pore size distribution of large and small mesopores of 6 nm and 3.1 nm. As proof of principle the particles were investigated as cathode material and sulfur

host in lithium sulfur batteries where they showed high reversible capacity up to 1200 mAh/g and good cycle efficiency.

## 7.2. Experimental Section

**Chemicals.** Formalin (37 wt% formaldehyde in water) and the triblock copolymer Pluronic F127 ( $M_w = 12600$ , EO<sub>106</sub>-PO<sub>70</sub>-EO<sub>106</sub>) were purchased from BASF AG, and phenol from Merck KGaA. TEOS (Tetraethylorthosilicate, C<sub>8</sub>H<sub>20</sub>O<sub>4</sub>Si), SDS (sodium dodecyl sulfate, NaC<sub>12</sub>H<sub>25</sub>O<sub>4</sub>S), MMA (methyl methacrylate, C<sub>5</sub>H<sub>8</sub>O<sub>2</sub>) and Potassium persulfate (K<sub>2</sub>S<sub>2</sub>O<sub>8</sub>) were purchased from Sigma Aldrich GmbH. All chemicals were used without further purification.

### Synthesis.

*PMMA colloidal crystals.* For the preparation of PMMA spheres 98 ml of distilled water were degassed with nitrogen for 15 minutes. 5 mg SDS (288.4 g/mol, 0.017 mmol) and 35.5 g MMA (100.1 g/mol, 0.35 mmol) were added. The mixture was held at 90 °C for 1 h under reflux conditions in nitrogen atmosphere. The initiator solution containing 56 mg K<sub>2</sub>S<sub>2</sub>O<sub>8</sub> (270.3 g/mol, 0.21 mmol) in 2 ml distilled water was added to the suspension. The white colloidal suspension was washed three times by centrifugation (20 min, 20000 rpm) and redispersed in water. To remove small amounts of larger spheres (> 500 nm), an additional centrifugation and washing step was performed (2 min, 5000 rpm). The final solution exhibited a sphere concentration of about 20 wt%. The colloidal stock solution was dried in a plastic petri dish for 12 h at 60 °C. The obtained pieces of densely packed colloidal crystals had a size of several mm<sup>3</sup> and are directly used for further liquid impregnation of a silica sol-gel solution.

*Silica inverse opal.*<sup>84</sup> For silica sol-gel solution 4 ml of ethanol were mixed with 6 ml TEOS (26.9 mmol), 3 ml water and 1 ml concentrated hydrochloric acid (1.19 g, 12 mmol HCl). The colloidal crystal structures were crushed to powders and put on a filter paper in a Büchner funnel. While applying vacuum to the funnel, the silica sol-gel solution was dripped over the surface to completely wet the PMMA. The silica/PMMA composite was heated to 550 °C with a ramp of 1 °C/min and calcined for 5 h. The density of the silica inverse opal is much lower than for the PMMA opal, therefore the yield was only around 10 %.

Resol precursor.<sup>22</sup> A low molecular weight precursor for the organic framework was synthesized in a reaction of phenol and formaldehyde in a base-catalyzed process according to Meng et al.<sup>22</sup> For the synthesis, 6.1 g of phenol (0.064 mol) were molten in a flask with 1.3 g of 20 wt % sodium hydroxide solution (0.0065 mol). The mixture was heated up to 50 °C and then 10.5 g formalin (37 wt % formaldehyde in water, 0.1295 mol) were added dropwise. The molar ratio of phenol / formaldehyde / NaOH was 1 : 2 : 0.1. The clear, lightly yellow colored solution was stirred at 75 °C for one hour and then cooled down to room temperature. The precursor solution was neutralized with 1 M hydrochloric acid and the water was removed by vacuum evaporation below 50 °C. The resulting product (10 g) was redissolved in ethanol to a total weight of 50 g (20 wt %).

Synthesis of Ordered Mesoporous Polymer-Silica and Carbon-Silica Nanocomposites. A precursor solution was mixed according to Liu et al.<sup>23</sup> for the sample MP-CS-36\* with the mass ratio F127/resol/TEOS/EtOH/HCl/H<sub>2</sub>O) 1:0.5:2.08:12:0.0073:1.0.

In a typical preparation, 1.0 g of Pluronic F127, 10.0 g of ethanol, and 1.0 g of 0.2 M HCl were mixed well at 40 °C. Then 2.08 g TEOS and 2.5 g of the 20 wt % resol solution were added, and stirring was continued for 5 h at 40 °C. The precursor solution was cast in a glass

vial together with the silica inverse opal with a mass ratio for precursor solution/silica of 100:1 which is equivalent with a ratio for precursor solution to initial PMMA spheres of 10:1 for a silica yield of 10 %.

The ratio is based on the assumption that the final porous carbon product has a density which is up to five times lower than the density of the non porous non porous PMMA spheres and therefore needs up to five times more space. The OMC yield of the precursor solution is only 1.5 %. Therefore the weight ratio of the precursor solution to OMC 66:1. Due to five times higher density of the PMMA spheres, the maximum ratio for precursor solutions to the initial PMMA spheres should be below 66:5 or 13:1. The chosen ratio of 10:1 was much lower.

The solvent evaporated and the composite was thermopolymerized for 24 h at 100 °C. Afterwards, the material was carbonized at 900 °C in nitrogen, the heating sequence was 1 °C/min to 350 °C (3 h dwell time), then 1 °C/min to 600 °C and 5 °C/min to 900 °C (2 h).

*Etching of the silica.* After carbonization the carbon-silica nanocomposites were immersed in 10 wt % HF solution for 24 h. Afterwards the carbon was filtered and washed with water.

*Ultrasonic treatment.* 10 mg of the OMC nanoparticles could be dispersed in 200 ml water by sonification for 60 minutes in an ice cooled ultrasonic bath and for 10 minutes with an ultrasonic generator (Vibra Cell model VC 250, 20 kHz with 13 mm tip) at 50 % power.

*Electrode preparation.*

The C/S nanocomposites were prepared following a melt-diffusion strategy. Mesoporous carbon was ground together with sulfur with a mass ratio of 1 : 1 and then heated to 155 °C for overnight. The C/S cathode materials were slurry-cast from cyclopentanone onto a carbon-coated aluminum current collector. Typically, 82 wt% of C/S composite, 10 wt% Super S carbon and 8 wt% poly(vinylidene fluoride) (PVDF) were mixed with cyclopentanone. The

slurries were coated on aluminum current collectors and dried at 60 °C overnight. The electrochemical performance of the prepared cathodes was evaluated using 2325 coin cells cycled at room temperature between 1.5 V and 3.0 V, with lithium metal foil as the anode. The electrolyte used was 1 M bis-(trifluoromethane)sulfonimide lithium (LiTFSI) in a mixed solvent of dimethoxyethane (DME) and dioxolane (DOL) with a volume ratio of 1 : 1.

### **Characterization.**

Transmission electron microscopy (TEM) data were obtained on a JEOL JEM 2011 microscope at an acceleration voltage of 200 kV. Scanning electron microscopy (SEM) was performed on a JEOL JSM-6500F scanning electron microscope equipped with a field emission gun, at 4 kV. Nitrogen sorption isotherms were obtained at -196 °C using a Quantachrome Autosorb-1. The sample mass in the measurement was 36.7 mg. The calculation of the pore-size distribution was done with a NLDFT method using a silica kernel for cylindrical pores for the adsorption branch. This model is the best compromise for this system, as corresponding models for carbon materials do not yet exist. Dynamic light scattering (DLS) was performed using a Malvern Zetasizer-Nano equipped with a 4 mW He-Ne laser (633 nm) and an avalanche photodiode detector. The scattering data were weighted based on particle volume.

## **7.3. Results and Discussion**

The scanning electron microscopy (SEM) images in Figure 7.1 depict the morphologies at different steps of synthesis. The PMMA spheres close packed in opal structure (Figure 7.1A) are used as template for a silica precursor solution, thus after calcination a silica inverse opal

structure (Figure 7.1B) is formed. The silica is then used in a second casting step as template for an artificial opal made of OMC spheres (Figure 7.1C, D).

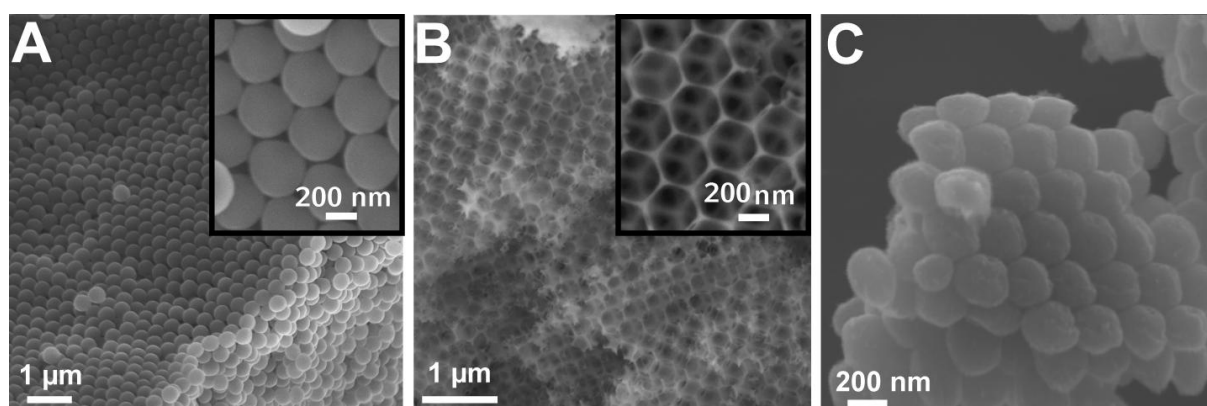


**Figure 7.1:** SEM images: A) PMMA spheres ordered in close packing with an inset at higher magnification; B) Silica inverse opal structure with an inset at higher magnification; C) OMC spheres ordered in opal structure

The PMMA spheres with diameters of ca. 400 nm assembled in an opal structure (Figure 7.1A) show the typical play of color of a photonic crystal. The silica inverse opal structure (Figure 7.1B) obtained from infiltration of the PMMA opal structure is also highly ordered. The pore size (ca. 320 nm) in the inverse opal is smaller than the PMMA particle size due to shrinkage of the structure as the walls condense during calcination at 550 °C. The particle size of the OMC spheres (Figure 7.1C) is around 300 nm. Thus further shrinkage occurred during carbonization of the carbon-silica composite at 900 °C. The OMC spheres still show the close packing of the PMMA spheres and the silica inverse opal.

The representative TEM micrographs in Figure 7.2 reveal the 2D-hexagonal mesostructure ( $p6mm$ ) of the OMC nanoparticles. In agreement with SEM results, the mean particle size was found to be around 300 nm  $\pm$  40 nm.

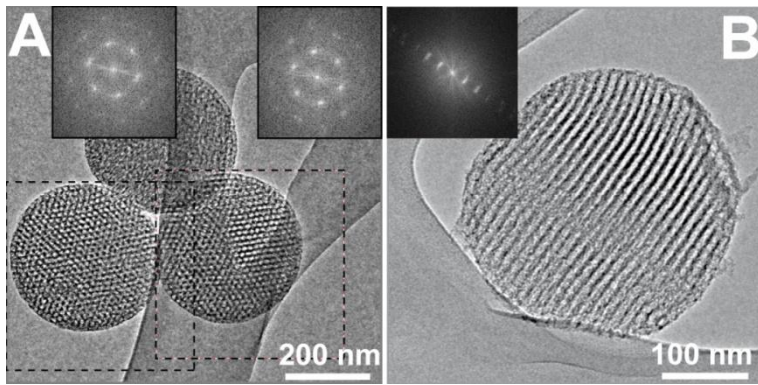


**Figure 7.2:** TEM micrographs of spherical OMC nanoparticles showing the 2D-hexagonal structure: A) projected along the columns, with insets of Fast Fourier Transformations (FFT) of the squares; B) tilted out of the columnar projection with FFT inset.

Figure 7.2A depicts the hexagonal structure projected along the columns. The FFTs clearly show the hexagonal symmetry of the projections with d-spacings of 12.5 nm. Tilting up to 30° showed that no other zone axis can be found which excludes a 3D structure and verifies the 2D-hexagonal mesostructure. Figure 7.2B shows the 2D-hexagonal structure tilted out of the columnar projection, where the cylindrical pores can be clearly observed. Thus the spherical nanoparticles exhibit the same structure as the bulk material described by Liu and coworkers<sup>23</sup> synthesized from the same precursor solution. After grinding for TEM preparation, the OMC opal aggregates were separated into small clusters (e.g. in Figure 7.2A) or even as single particles (e.g. in Figure 7.2B), which already indicates that they are only loosely bound together and could be separated. Complete separation could be obtained by sonification. The DLS measurement in Figure 7.3 shows an average particle size of 255 nm and its narrow distribution.

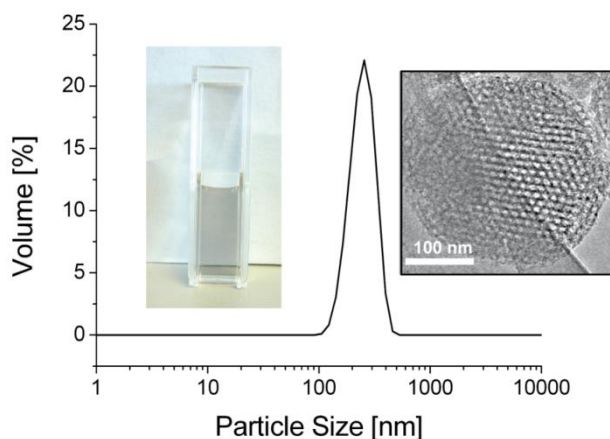


**Figure 7.3:** DLS measurement of OMC spheres in water after sonification with insets of the stable colloidal suspension and a TEM micrograph showing the intact 2D-hexagonal mesostructure.

The mean particle size here is even smaller than the aforementioned particle size of 300 nm found in SEM and TEM. Thus the spheres could be separated out of the close packing of the opal structure and could form stable colloidal suspensions of single nanoparticles. The left inset shows a colloidal suspension of the spheres in water, which was still stable after one week. The TEM micrograph in the right inset shows that even after the relatively harsh ultrasonic treatment the particles still exhibit the 2D-hexagonal mesostructure.

The OMC spheres show excellent porosity properties as Figure 7.4 illustrates.

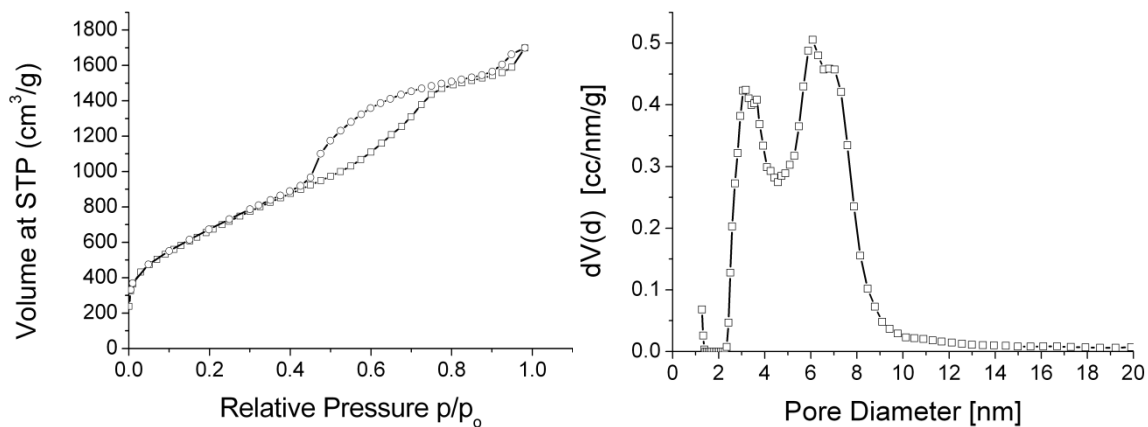


**Figure 7.4:** Nitrogen sorption isotherm (left) and pore size distribution (right, NLDFT adsorption branch) of the spherical OMC nanoparticles.

They exhibit a BET surface area of  $2445 \text{ m}^2/\text{g}$ , an inner pore volume of  $2.32 \text{ cm}^3/\text{g}$  ( $p/p_0 = 0.82$ , pores  $< 13 \text{ nm}$ ) and a total pore volume of  $2.63 \text{ cm}^3/\text{g}$  ( $p/p_0 = 0.98$ ). The Type IV isotherm shows hysteresis due to capillary condensation in mesopores. The bimodal pore size distribution (NLDFT adsorption branch) shows a maximum for large pores of  $6.0 \text{ nm}$  but also smaller pores with a maximum of  $3.1 \text{ nm}$ . This can be explained by porous walls that were formed through etching the silica out of the former carbon/silica nanocomposite walls. For better comparison with literature data the pore sizes were also determined with the BJH model, which gives maxima at  $5.3$  and  $2 \text{ nm}$ . In addition the isotherm shows adsorption at very high partial pressures due to textural porosity of the packed  $300 \text{ nm}$  spheres. Due to their high pore volume and surface area the nanoparticles were tested as cathode material in Li-S batteries. Figure 7.5 depicts the cycling stability up to 400 cycles.

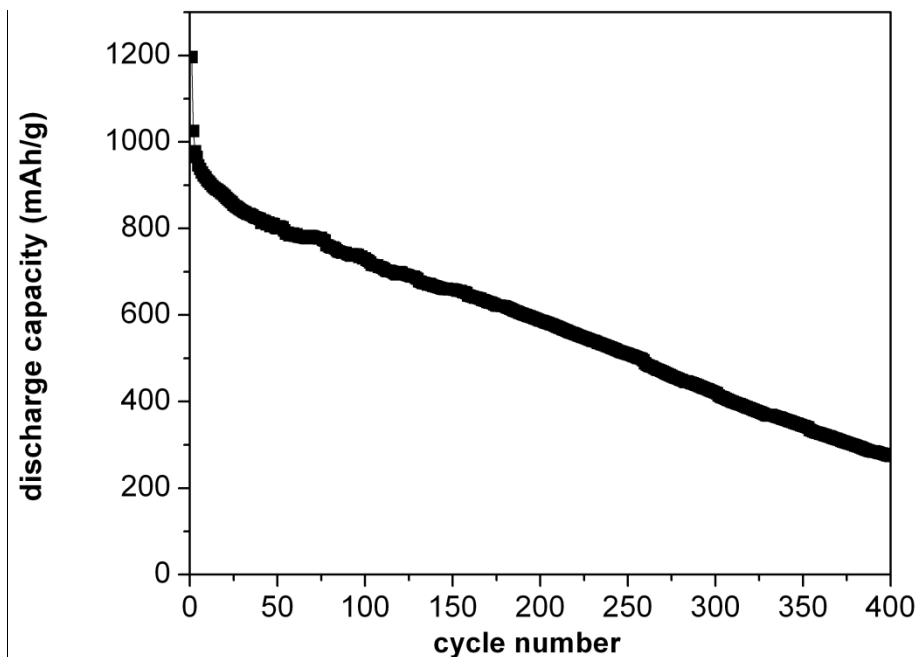


**Figure 7.5:** Cycling stability of carbon/sulfur composites of the spherical mesoporous carbon nanoparticles.

The spheres show even higher initial capacities than all fibers in Figure 6.3 and in addition higher cycling stability than the fibers MCNF-C36\*. The spheres show reversible capacity up to 1200 mAh/g and 730 mAh/g even after 100 cycles (61 % initial capacity). Afterwards the capacity decrease followed a linear trend down to 275 mAh/g (17 % initial capacity) after 400 cycles.

These are already promising first result, which serve as proof of principle. However they have to be reproduced and further investigated in terms of mechanisms for capacity fading.

#### 7.4. Conclusions

We have demonstrated the synthesis of spherical OMC nanoparticles of 300 nm in diameter with a 2D-hexagonal mesostructure, which could be dispersed in water by sonification to form stable colloidal suspensions. The material shows one of the highest inner pore volumes

for mesoporous carbon nanoparticles of 2.32 cm<sup>3</sup>/g and also one of the highest surface areas of 2445 m<sup>2</sup>/g with a bimodal pore size distribution of large and small mesopores of 6 nm and 3.1 nm. As proof of principle the particles were successfully applied as cathode material and sulfur host in lithium sulfur batteries and showed high reversible capacity up to 1200 mAh/g and good cycling capacity.

Beside the successful application in Li-S batteries the dispersed particles could be used as platform for variable host-guest systems, e.g. for drug delivery and could therefore be beneficial in terms of loading, stability and toxicity.

### 7.5. Chapter References

22. Meng, Y.; Gu, D.; Zhang, F.; Shi, Y.; Cheng, L.; Feng, D.; Wu, Z.; Chen, Z.; Wan, Y.; Stein, A.; Zhao, D., *Chem. Mater.* **2006**, *18* (18), 4447-4464.
23. Liu, R.; Shi, Y.; Wan, Y.; Meng, Y.; Zhang, F.; Gu, D.; Chen, Z.; Tu, B.; Zhao, D., *J. Am. Chem. Soc.* **2006**, *128* (35), 11652-11662.
39. Wang, Z.; Li, F.; Stein, A., *Nano Letters* **2007**, *7* (10), 3223-3226.
40. Yan, Y.; Zhang, F.; Meng, Y.; Tu, B.; Zhao, D., *Chem. Commun.* **2007**, (27), 2867-2869.
41. Tonanon, N.; Intarapanya, W.; Tanthapanichakoon, W.; Nishihara, H.; Mukai, S.; Tamon, H., *Journal of Porous Materials* **2008**, *15* (3), 265-270.
42. Kim, T.-W.; Chung, P.-W.; Slowing, I. I.; Tsunoda, M.; Yeung, E. S.; Lin, V. S. Y., *Nano Letters* **2008**, *8* (11), 3724-3727.
43. Liu, H.-J.; Cui, W.-J.; Jin, L.-H.; Wang, C.-X.; Xia, Y.-Y., *J. Mater. Chem.* **2009**, *19* (22), 3661-3667.

45. Lei, Z.; Christov, N.; Zhang, L. L.; Zhao, X. S., *J. Mater. Chem.* **2011**, *21* (7), 2274-2281.
84. Holland, B. T.; Blanford, C. F.; Stein, A., *Science* **1998**, *281* (5376), 538-540.

## 8. CONCLUSIONS AND OUTLOOK

In the course of this thesis, variable morphologies of ordered mesoporous carbons have been prepared and investigated in terms of structure formation and applicability in high capacity Lithium Sulfur batteries. These ordered mesoporous carbons have been prepared via soft-templating procedures in the forms of thin films, fibers – embedded in anodic alumina membranes and free-standing – or spherical nanoparticles.

Aiming at a more extended control of morphology, self-assembly procedures for ordered mesoporous carbons in the form of bulk powders were refined and adapted to nanomorphologies. In chapter 3 mesoporous thin films with 2D-hexagonal structure were obtained in a self-assembly procedure of an oligomeric resol precursor and the block copolymer template Pluronic P123. Spin-coating, followed by different thermal treatments for thermopolymerization, template removal and carbonization were used for the synthesis of these highly ordered mesoporous films with variable thicknesses.

This self-assembly process could also be transferred to the confined environment of tubular anodic alumina membrane (AAM) pores in Chapter 4. Thus, cubic and circular hexagonal mesoporous carbon phases embedded within anodic alumina membranes could be synthesized. The embedded fibers showed extremely high thermal stability up to 1000 °C and contrary to bulk powders, the mesostructures did not show any shrinkage, the pore sizes even increased upon higher carbonization temperatures. This restricted shrinkage effect is caused by strong adhesion of the carbon to the aluminum oxide walls of the tubular membrane pores.

As a consequence these fibers exhibited very high surface areas and pore volumes and pore sizes up to 20 nm. Here the morphology control really had a beneficial effect due to this restricted shrinkage effect of the tubular confinement.

In order to gain further understanding on the mechanisms of structure formation, the OMC thin films and fibers introduced in the two latter chapters were further investigated concerning mechanisms of structure formation. Chapter 5 shows the *in situ* SAXS study, which was accomplished for this purpose at the Synchrotrone Elettra (Trieste, Italy) in cooperation with Heinz Amenitsch from the Austrian Academy of Sciences in Graz. The *in-situ* SAXS measurements revealed that unlike for the well-established evaporation-induced self-assembly (EISA), the structure formation for organic-organic self-assembly does not occur during evaporation but only in the following thermopolymerization step at temperatures above 100 °C. Therefore, the process of structure formation should rather be called thermally-induced self-assembly. The understanding of the mechanisms for structure formation can be critical for advances in the synthesis control. The discovery of this new mechanism reveals the key step for structure formation, in this thermopolymerization step changes in the synthesis parameters should have the highest impact on the resulting structures.

In chapter 6, variable freestanding mesoporous carbon nanofibers were made by imbibing a presynthesized silica template, and explored as cathode material in lithium sulfur batteries. Beside the self-assembly of resol oligomers and Pluronic block copolymers, a synthesis concept using triconstituent co-assembly of resol, tetraethylorthosilicate as additional silica precursor and the block copolymer template Pluronic F127 was investigated here. The silica from the additional precursor was found to be beneficial, due to reduced shrinkage and created additional porosity after etching it.

The fibers differed strongly regarding their pore sizes and pore structures and also their specific surface areas and pore volumes. Those variations had a strong effect on the capacity and the cycle stability of the batteries. The highest reversible capacity of 1000 mAh/g was achieved for the sample MCNF-C36\* made by the mentioned triconstituent coassembly which had the highest porosity of 2486 m<sup>2</sup>/g and 2.06 cm<sup>3</sup>/g and cylindrical pores. The slowest capacity decay upon cycling on the other hand was observed by the sample MCNF-F127, which exhibited larger cage-like pores.

Even higher capacities in Lithium Sulfur batteries were achieved with the spherical mesoporous carbon nanoparticles introduced in chapter 7. These nanoparticles featured extremely high inner porosity of 2.32 cm<sup>3</sup>/g and 2445 m<sup>2</sup>/g and showed high reversible capacity up to 1200 mAh/g and good cycle efficiency. Here the triconstituent coassembly approach was adapted to a silica template with spherical pores, a silica inverse opal structure. The particles could be completely separated by sonification to form stable colloidal suspensions, which could be the base for further applications such drug delivery.

The application of OMCs as cathode material and sulfur host in Li-S batteries is of great interest. Rechargeable lithium sulfur batteries are attracting increasing attention due to their high theoretical specific energy density, which is 3 to 5 times higher than for all lithium-ion batteries based on intercalation chemistry. The tested OMC nanomorphologies already showed much higher capacities than bulk powders made from the same precursor solutions. Nevertheless, the reduction of capacity fading is the big challenge for Li-S batteries and our project is just at the beginning. One of the primary shortfalls of most Li-S cells is reactions of the intermediates with the electrolytes, the dissolution of intermediary polysulfides into the electrolyte, which causes irreversible loss of active sulfur.

Therefore, the OMCs should trap the polysulfides but allow diffusion of Li-ions. Our results suggest that the fibers and spheres can be optimized with respect to several important features, including tuning of the nanomorphologies in terms of fiber diameters and particle sizes, tailoring of the mesostructure and porosity and functionalization of the surface.

Looking at possible further developments, the ultimate sulfur host could be an OMC material where the external surface is coated with a Li<sup>+</sup>-conducting material, such as sulfide glasses (e.g. Li<sub>2</sub>S-SiS<sub>2</sub> or Li<sub>2</sub>S-P<sub>2</sub>S<sub>5</sub>). For this purpose the carbon should be synthesized in the form of spherical nanoparticles that allow such coating and offer short diffusion paths.

Thus, if the challenge of capacity fading could be overcome, the Li-S batteries may represent a highly attractive next-generation energy storage system.

## 9. APPENDIX

### 9.1. *In Situ* SAXS Study on a New Mechanism for Mesostucture Formation of Ordered Mesoporous Carbons: Thermally-Induced Self-Assembly

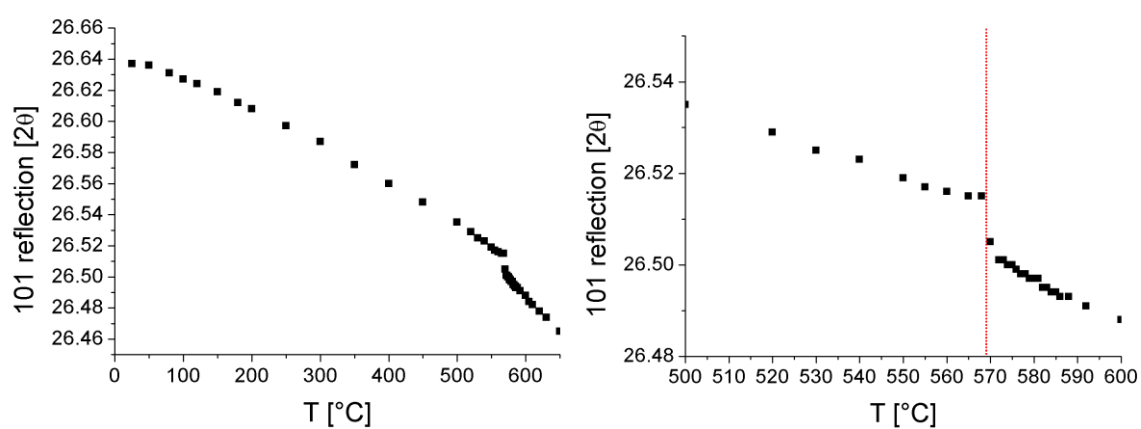


**Figure S9.1:** Peak position of the 101 reflection during heating, quartz jump around 569  $^{\circ}\text{C}$ .

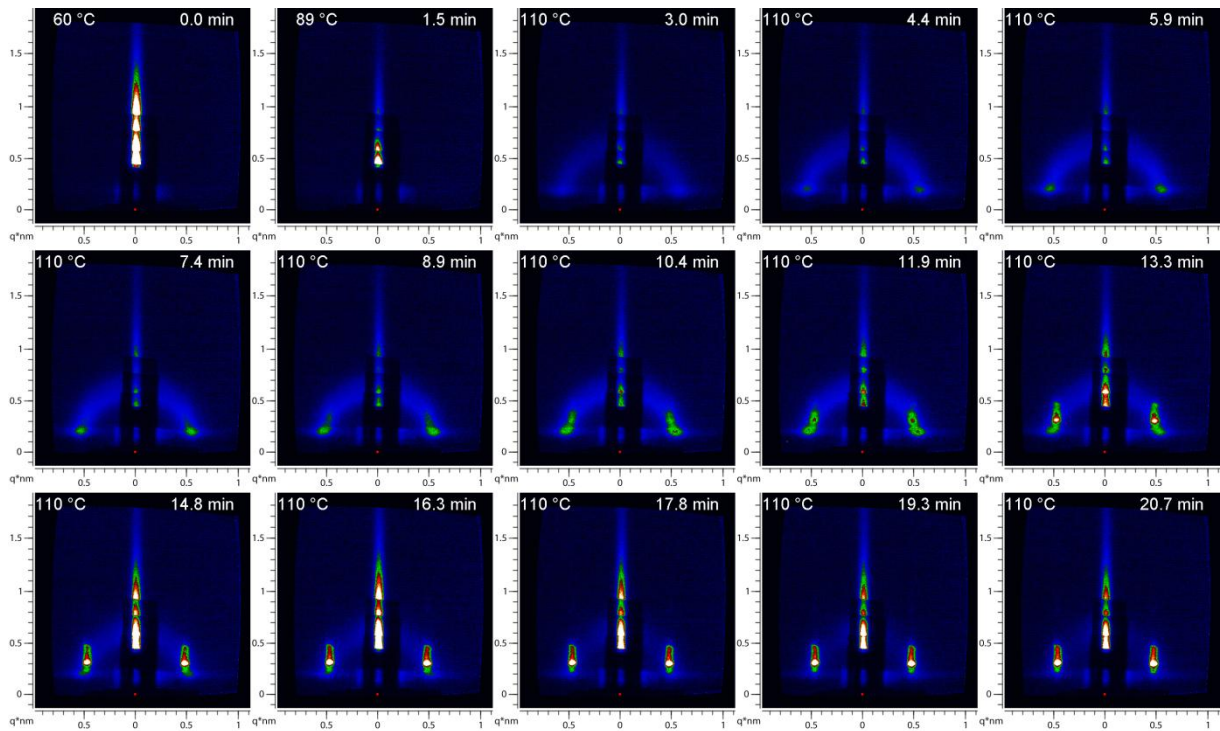


**Figure S9.2:** *In-situ* GISAXS for Film-Hex-110: Thermopolymerization at 110 °C.

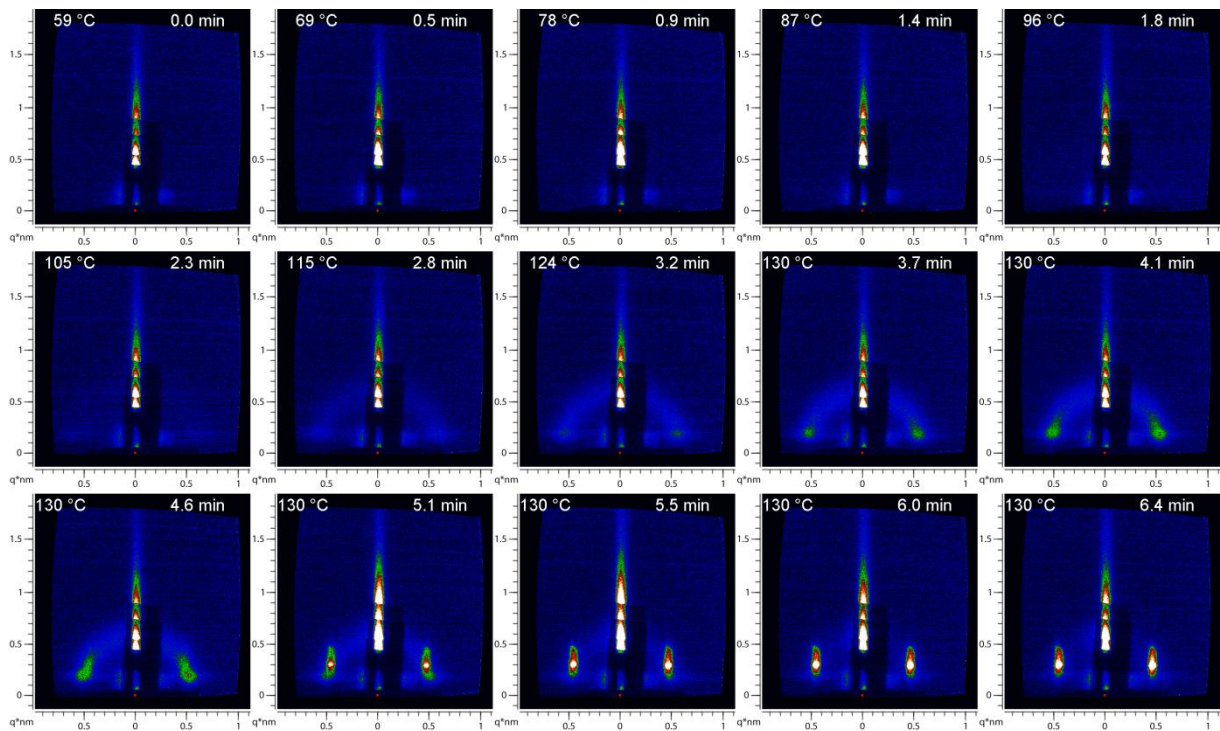


**Figure S9.3:** *In-situ* GISAXS for Film-Hex-130: Thermopolymerization at 130 °C.

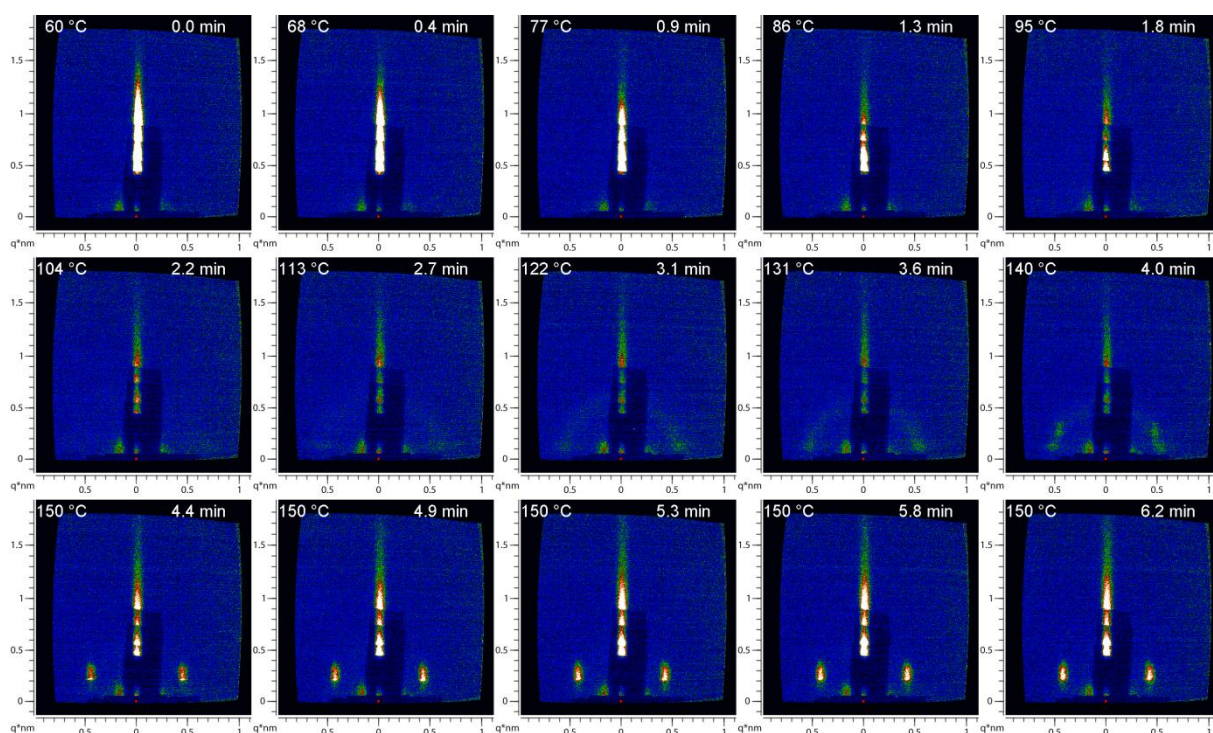


**Figure S9.4:** *In-situ* GISAXS for Film-Hex-150: Thermopolymerization at 150 °C.

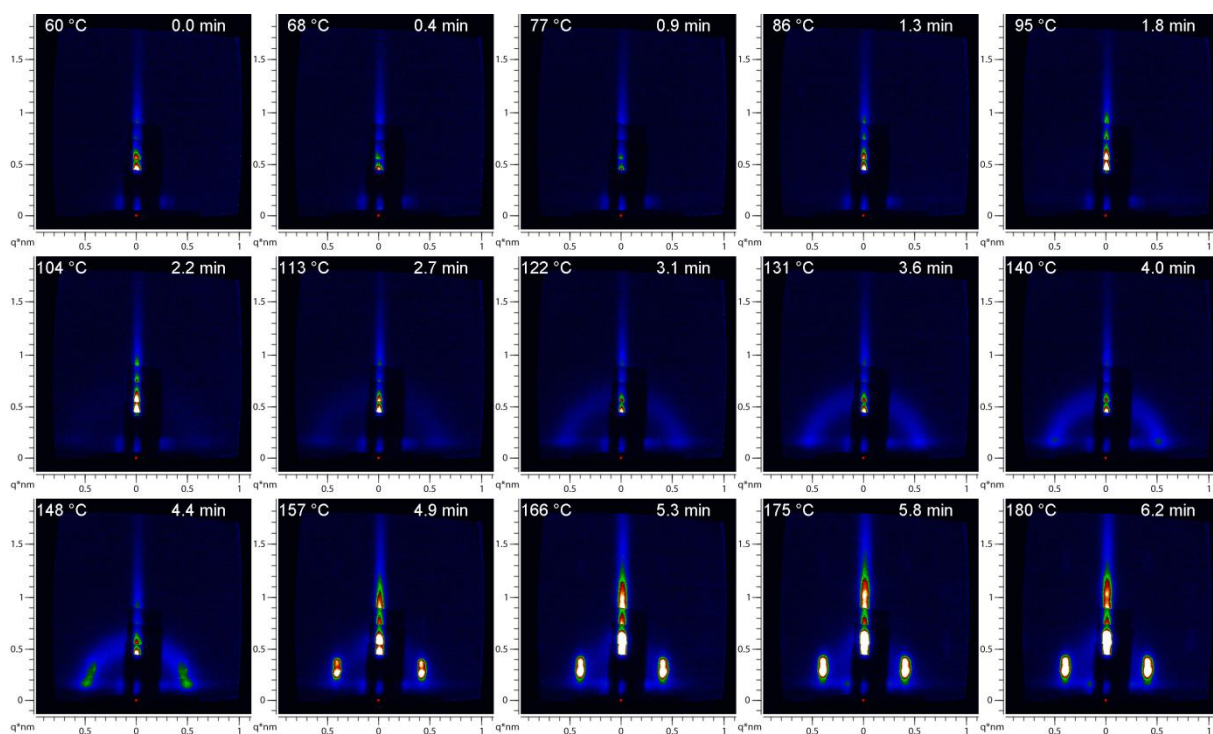


**Figure S9.5:** *In-situ* GISAXS for Film-Hex-180: Thermopolymerization at 180 °C.

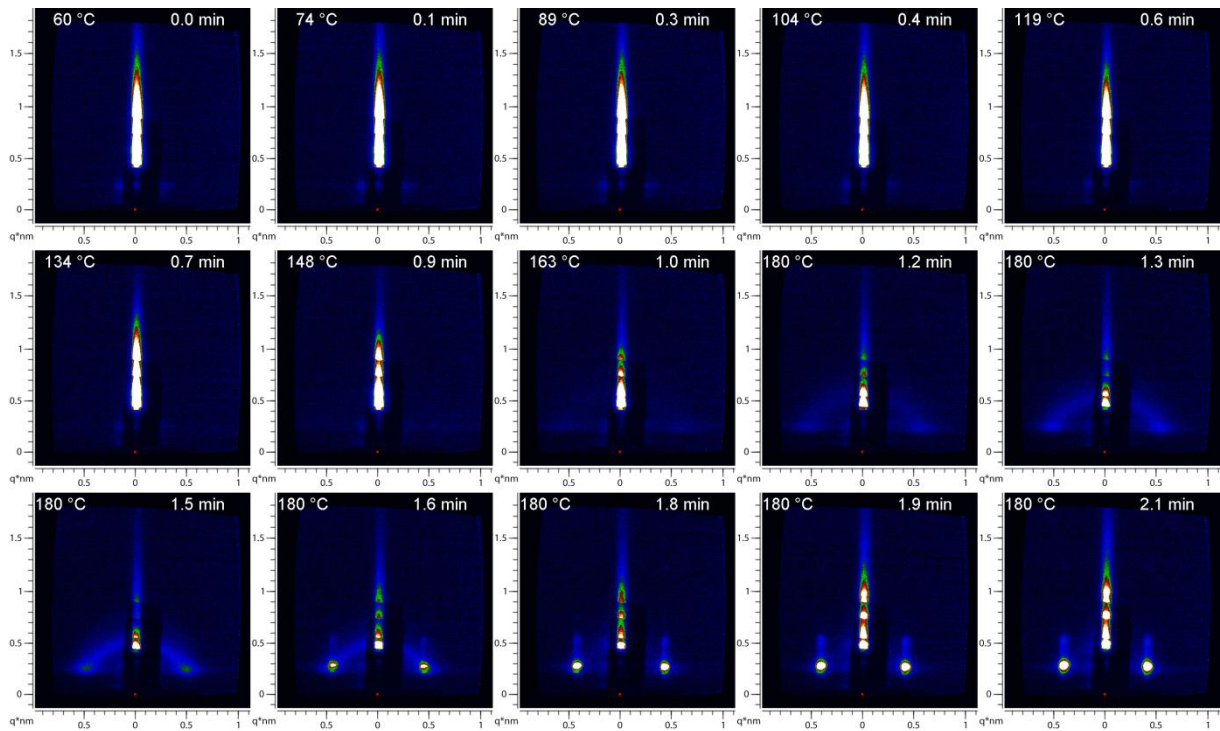


**Figure S9.6:** *In-situ* GISAXS for Film-Hex-180fast: Thermopolymerization at 180 °C heated with a ramp of 100 °C/min.

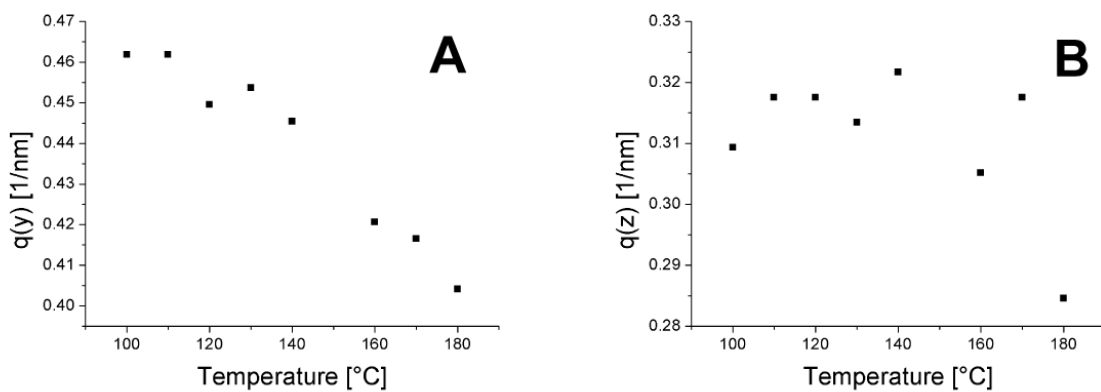


**Figure S9.7:** A)  $q(y)$  and B)  $q(z)$  values of the 10-peaks after thermopolymerization for the samples Film-Hex-T:  $q(y)$  shows a decrease for higher thermopolymerization temperatures, while no trend can be observed for  $q(z)$ .

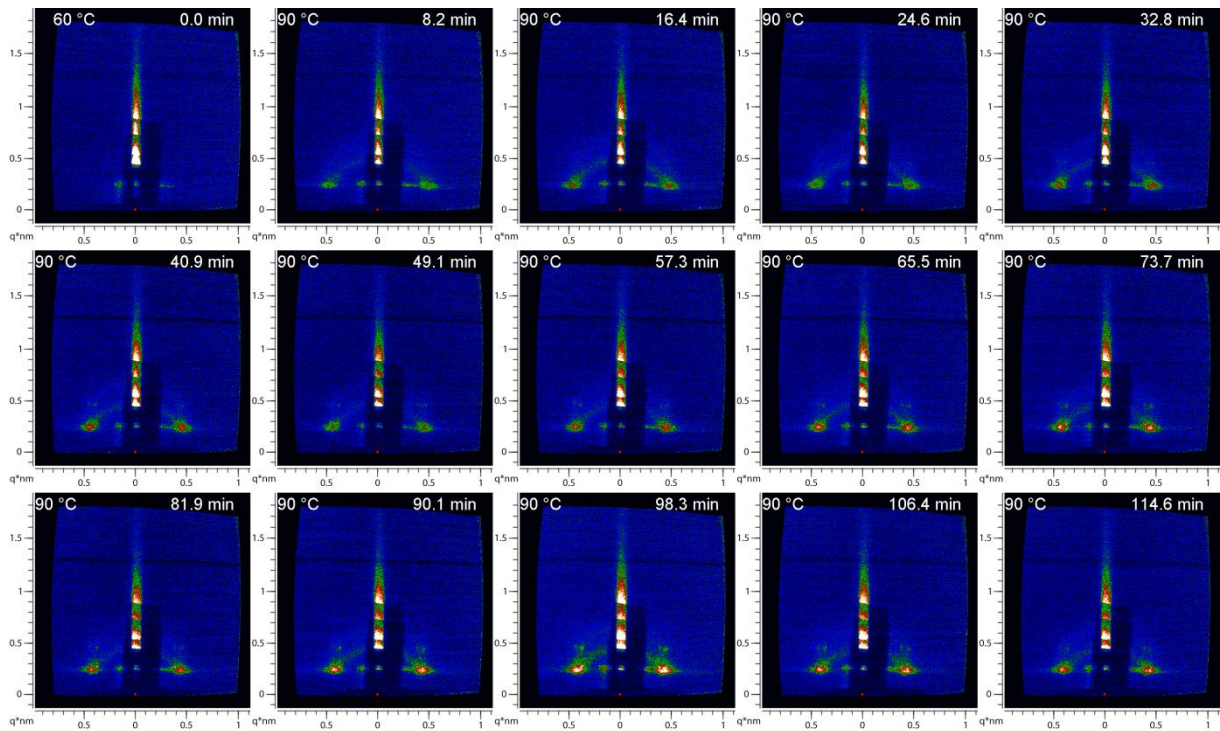


**Figure S9.8:** *In-situ* GISAXS for Film-Or-90: Thermopolymerization at 90 °C.

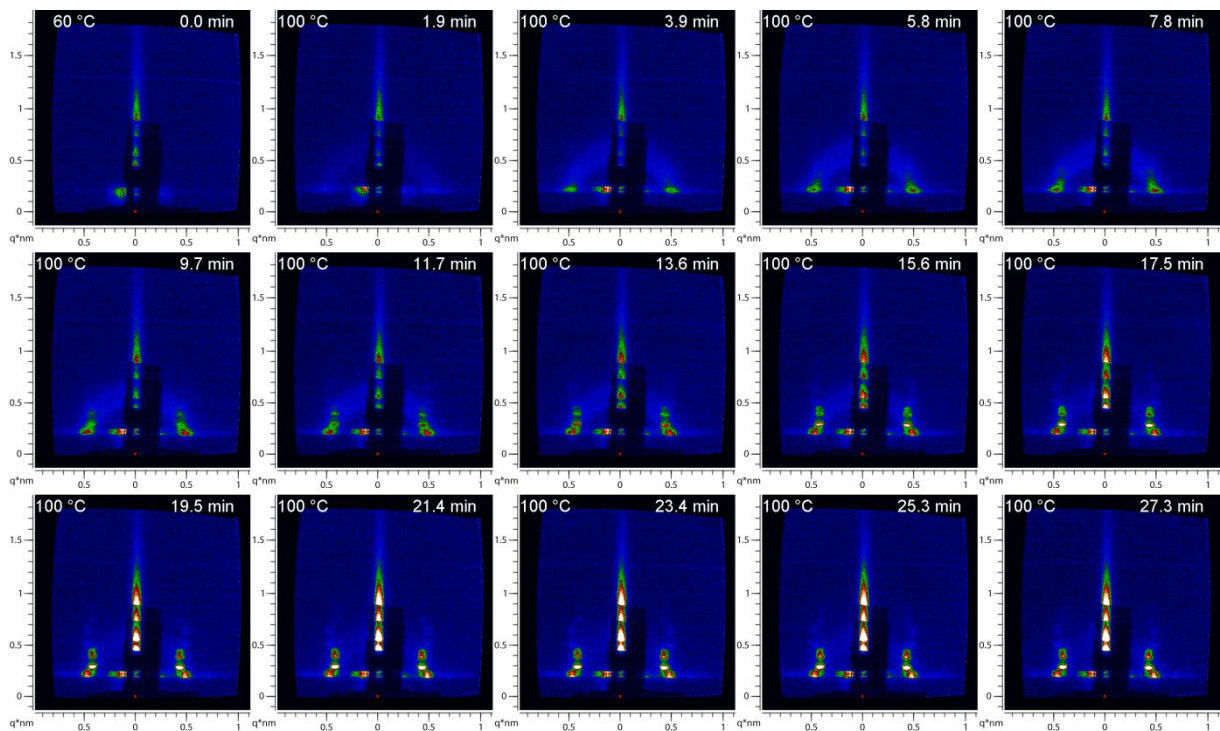


**Figure S9.9:** *In-situ* GISAXS for Film-Or-100: Thermopolymerization at 100 °C.

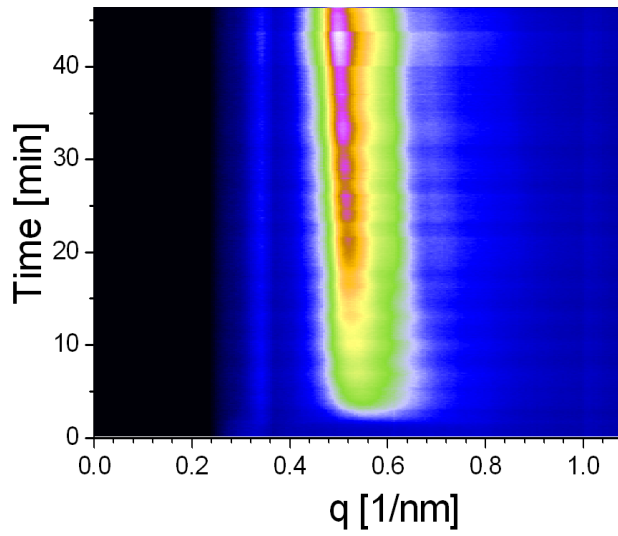


**Figure S9.10:** Plot of thermopolymerization time vs. radial integrated intensities for Film-Or-100. In-plane intensity was masked.

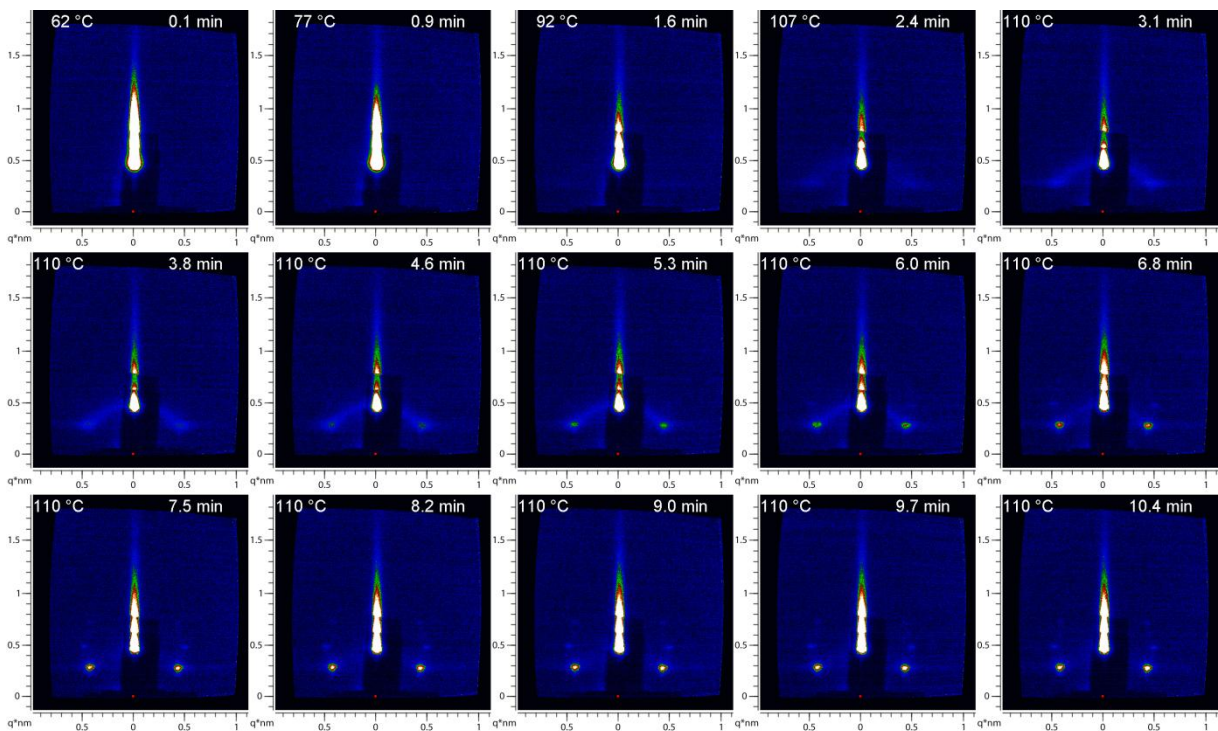


**Figure S9.11:** *In-situ* GISAXS for Film-Or-110: Thermopolymerization at 110 °C.

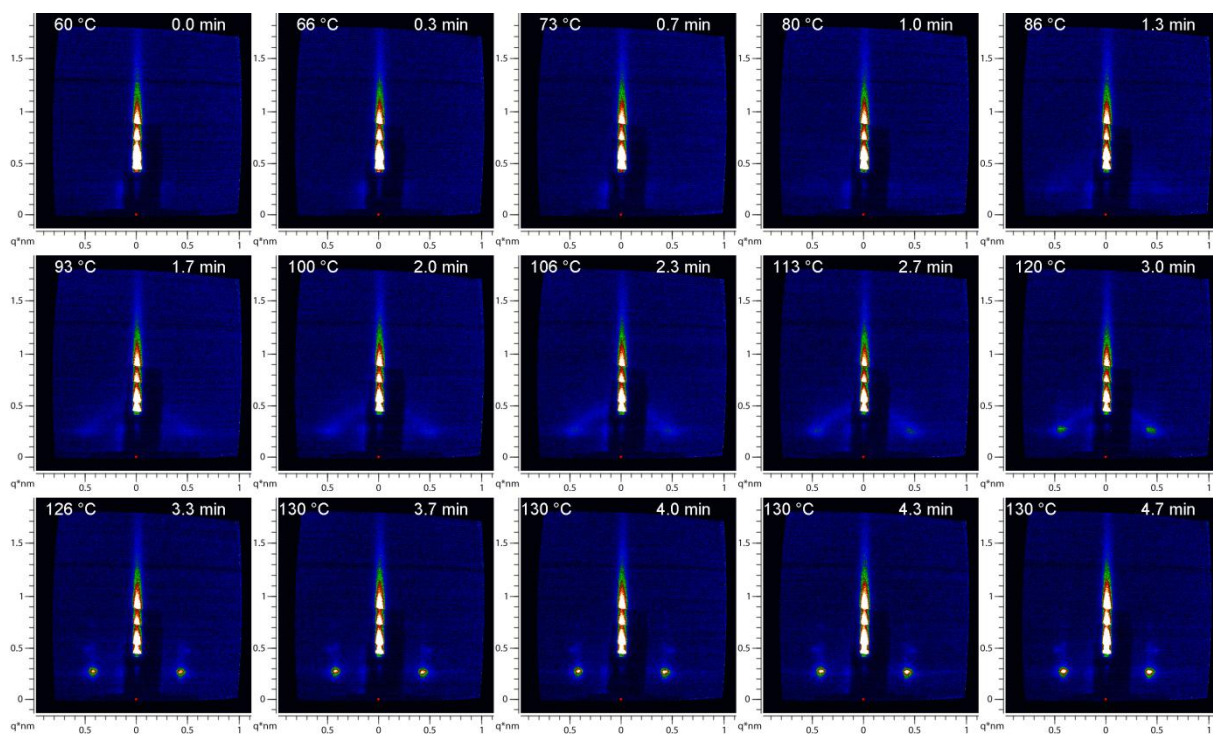


**Figure S9.12:** *In-situ* GISAXS for Film-Or-130: Thermopolymerization at 130 °C.

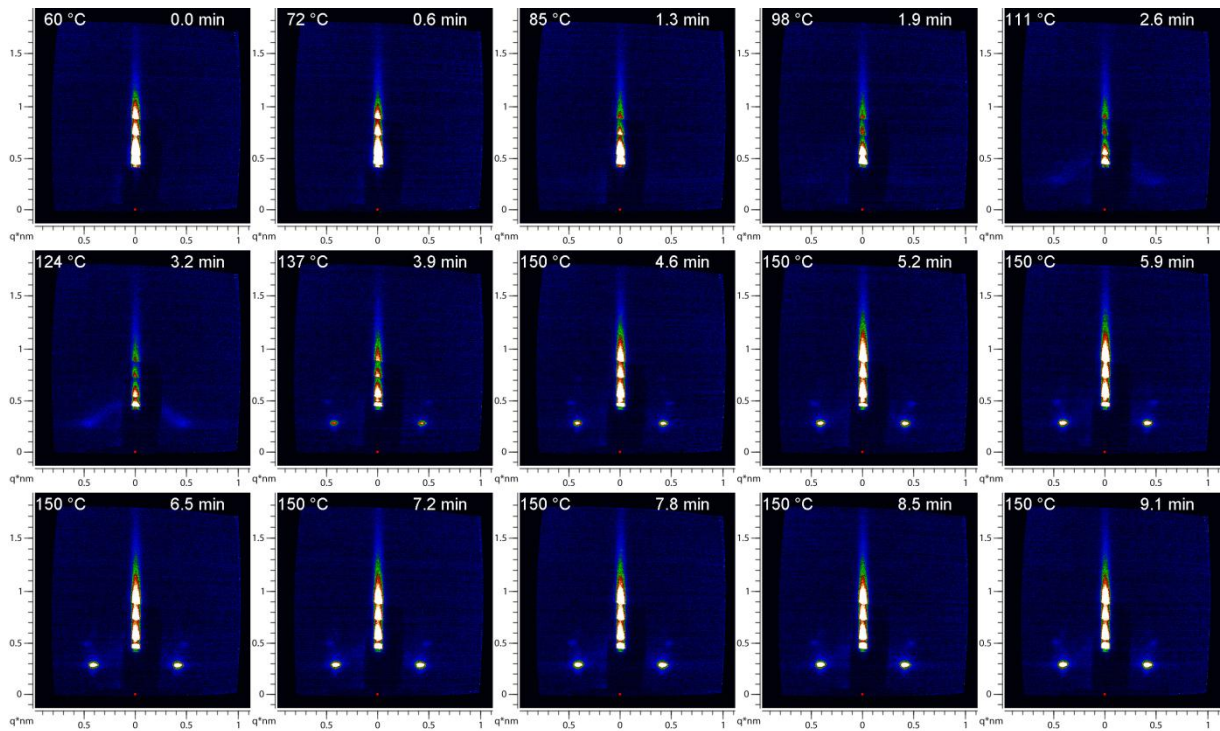


**Figure S9.13:** *In-situ* GISAXS for Film-Or-150: Thermopolymerization at 150 °C.

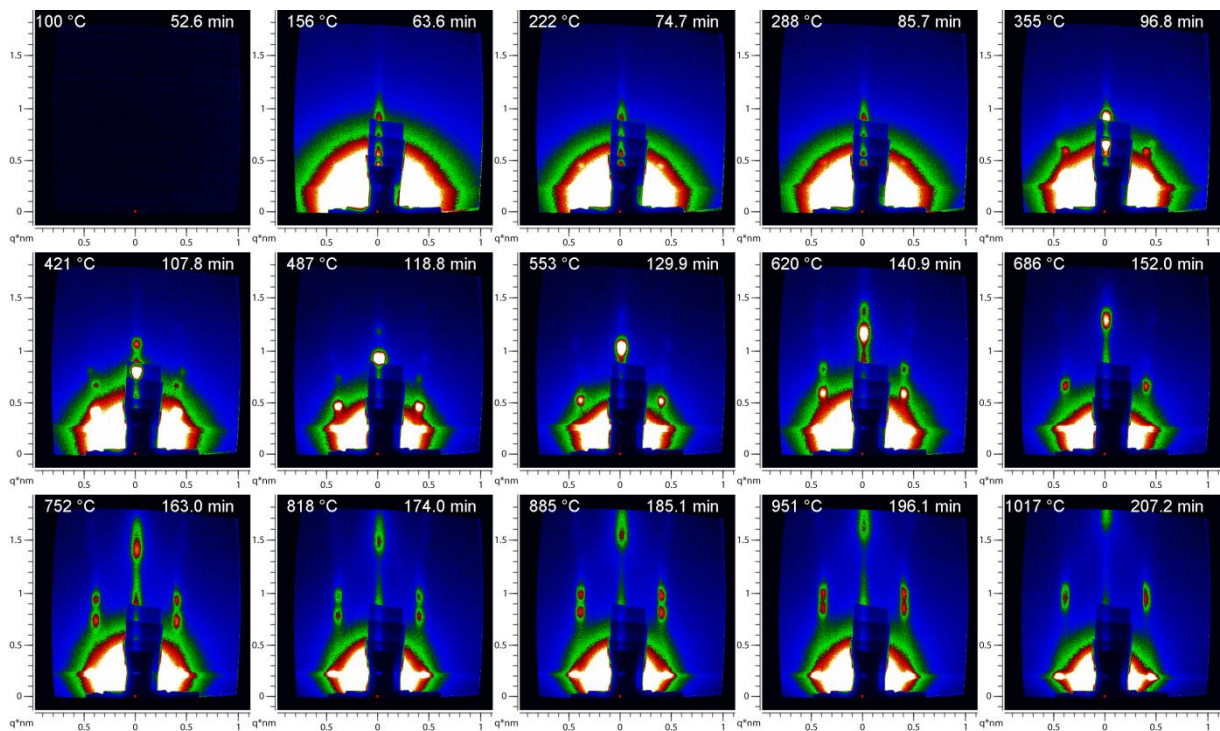


**Figure S9.14:** Carbonization of Film-Or-100: The diffuse scattering originates from the graphite dome on the heating chamber. The most intense reflections are doubled due to the grazing incidence geometry.

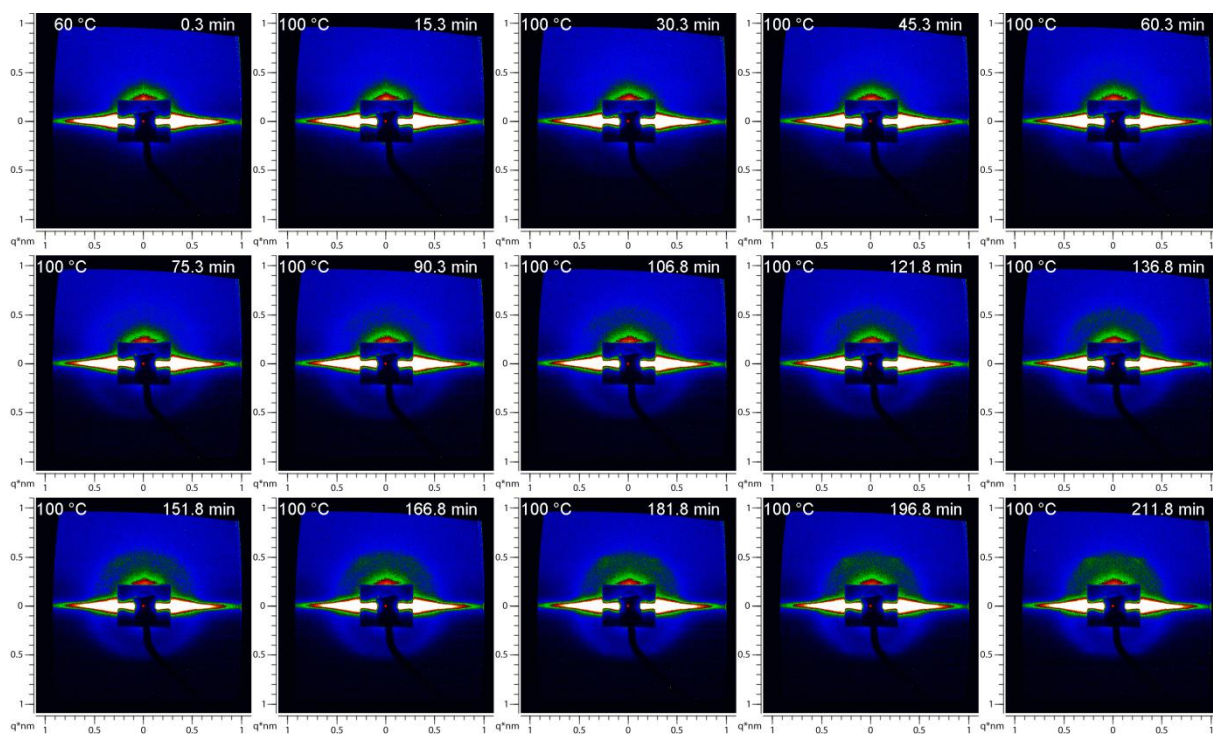


**Figure S9.15:** In-situ SAXS of AAM-Hex-100: Structure formation during thermopolymerization at 100 °C.

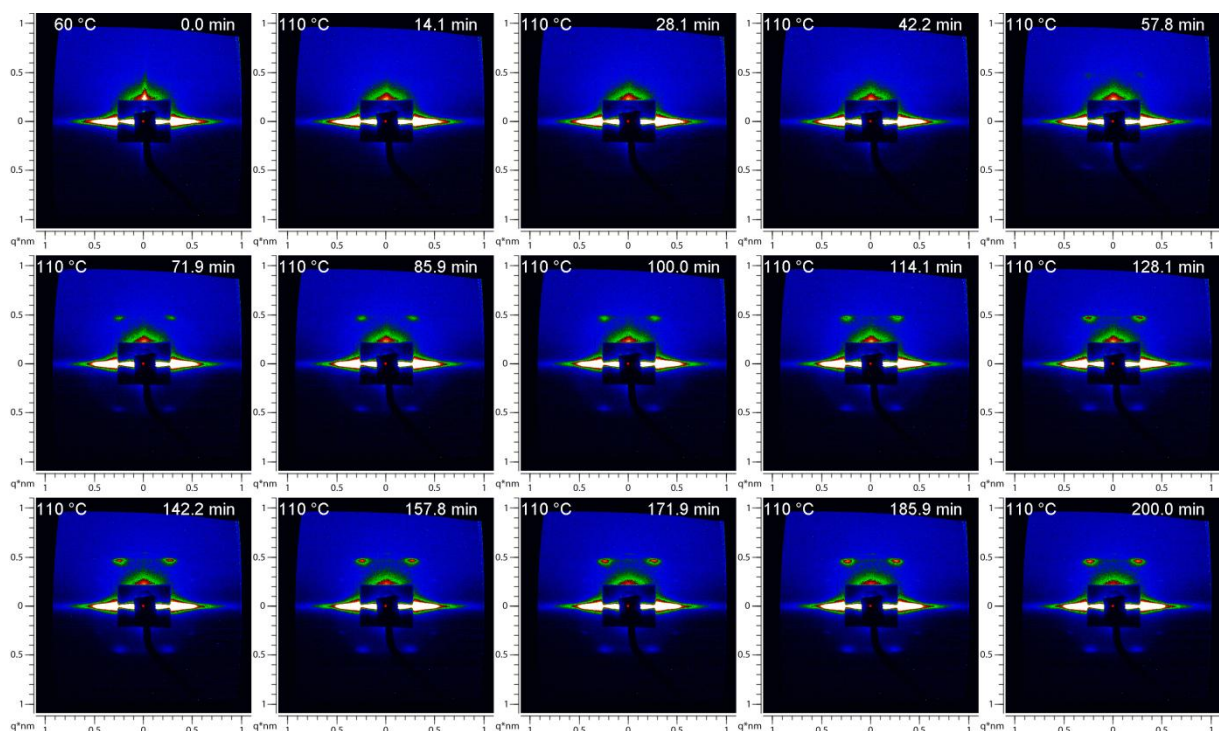


**Figure S9.16:** In-situ SAXS of AAM-Hex-110: Structure formation during thermopolymerization at 110 °C.

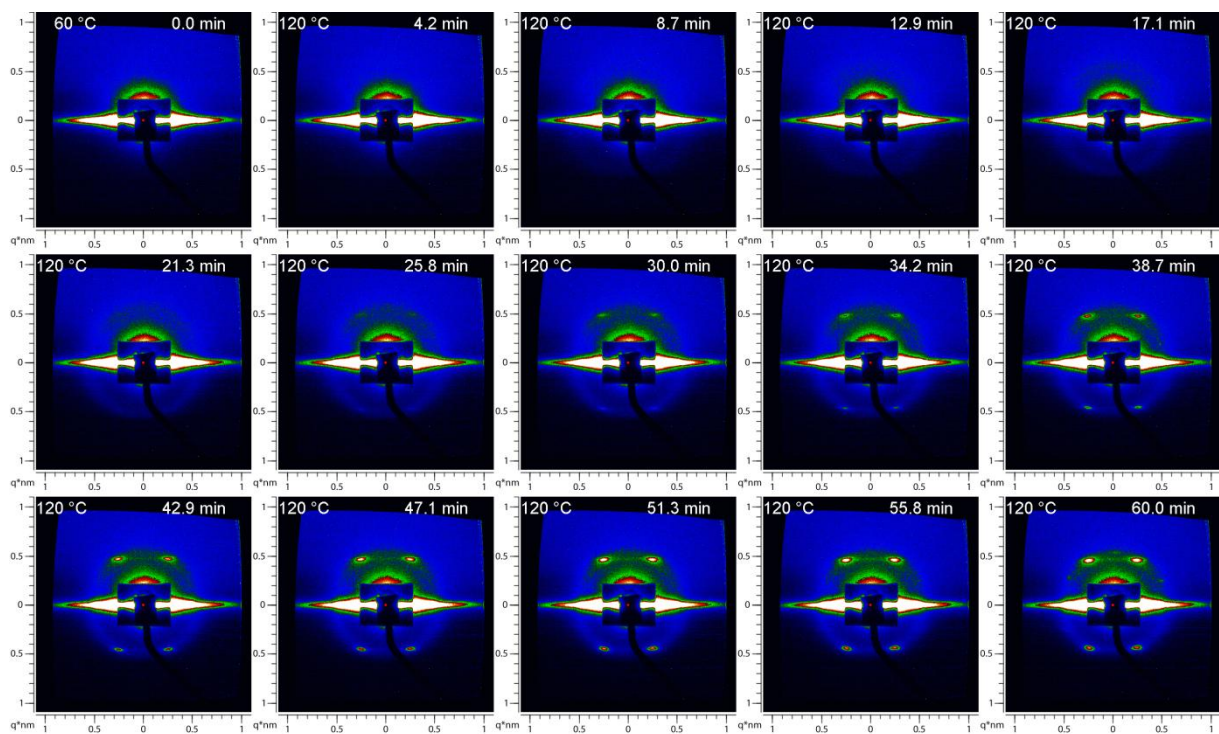


**Figure S9.17:** In-situ SAXS of AAM-Hex-120: Structure formation during thermopolymerization at 120 °C.

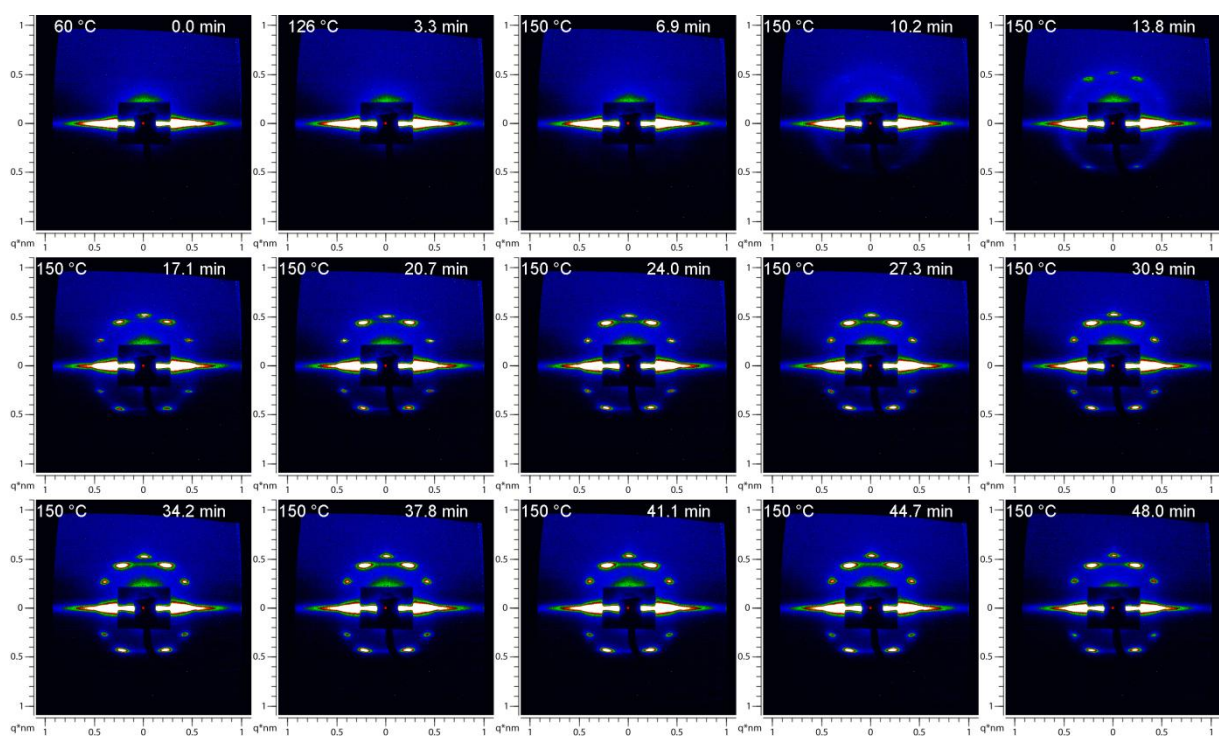


**Figure S9.18:** In-situ SAXS of AAM-Hex-150: Structure formation during thermopolymerization at 150 °C.

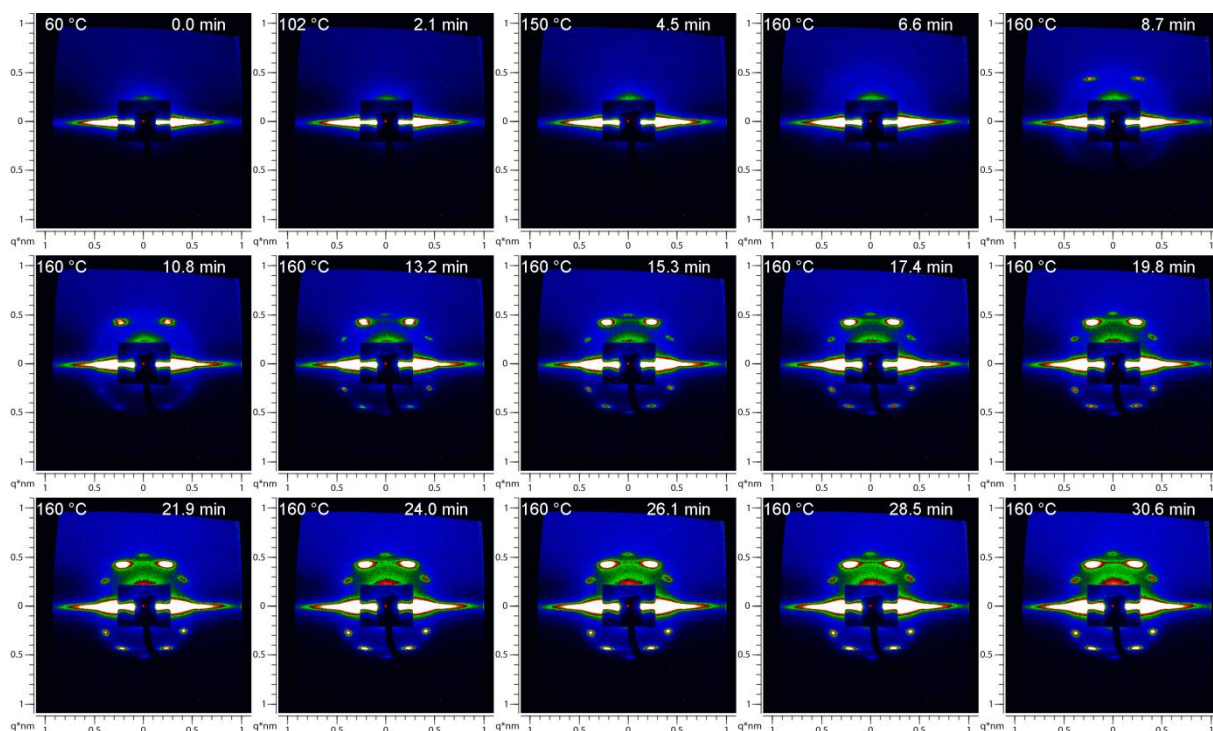


**Figure S9.19:** In-situ SAXS of AAM-Hex-160: Structure formation during thermopolymerization at 160 °C.

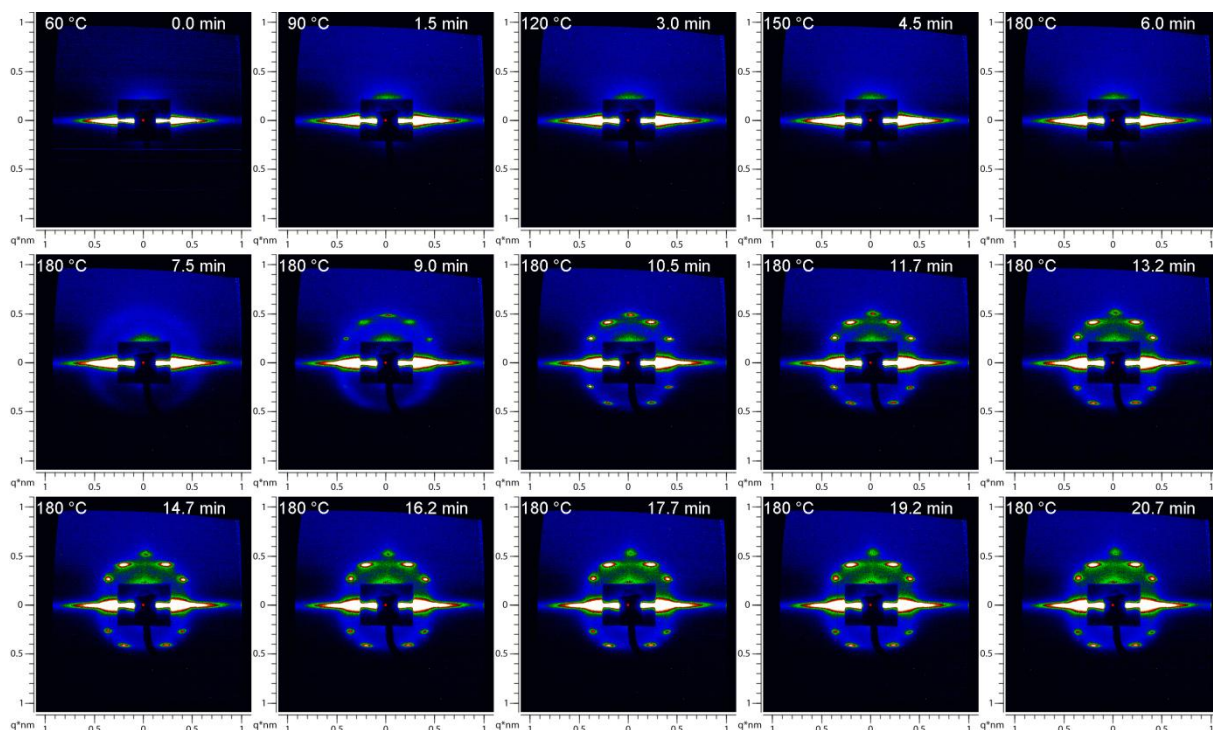


**Figure S9.20:** In-situ SAXS of AAM-Hex-180: Structure formation during thermopolymerization at 180 °C.

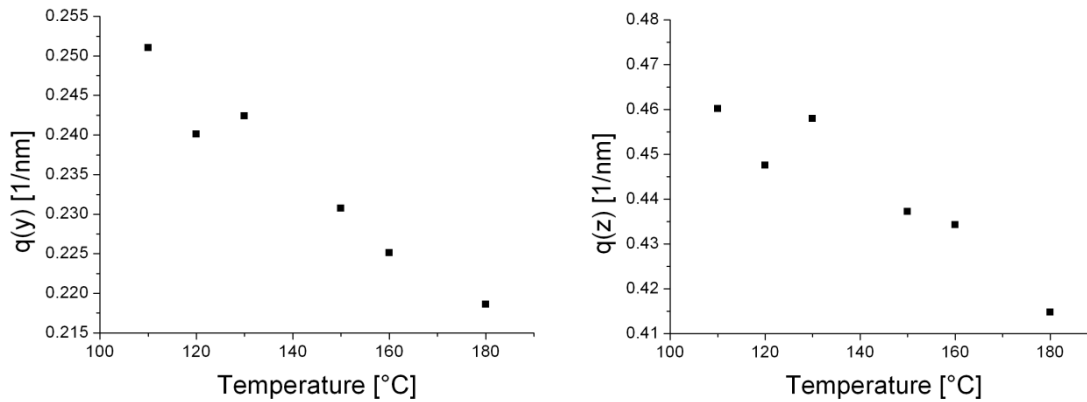


**Figure S9.21:**  $q(y)$ -values (left) and  $q(z)$ -values (right) of the 10-peaks after thermopolymerization for the samples AAM-Hex-T: Decreasing wavevectors  $q(y)$  and  $q(z)$  for higher thermopolymerization temperatures.

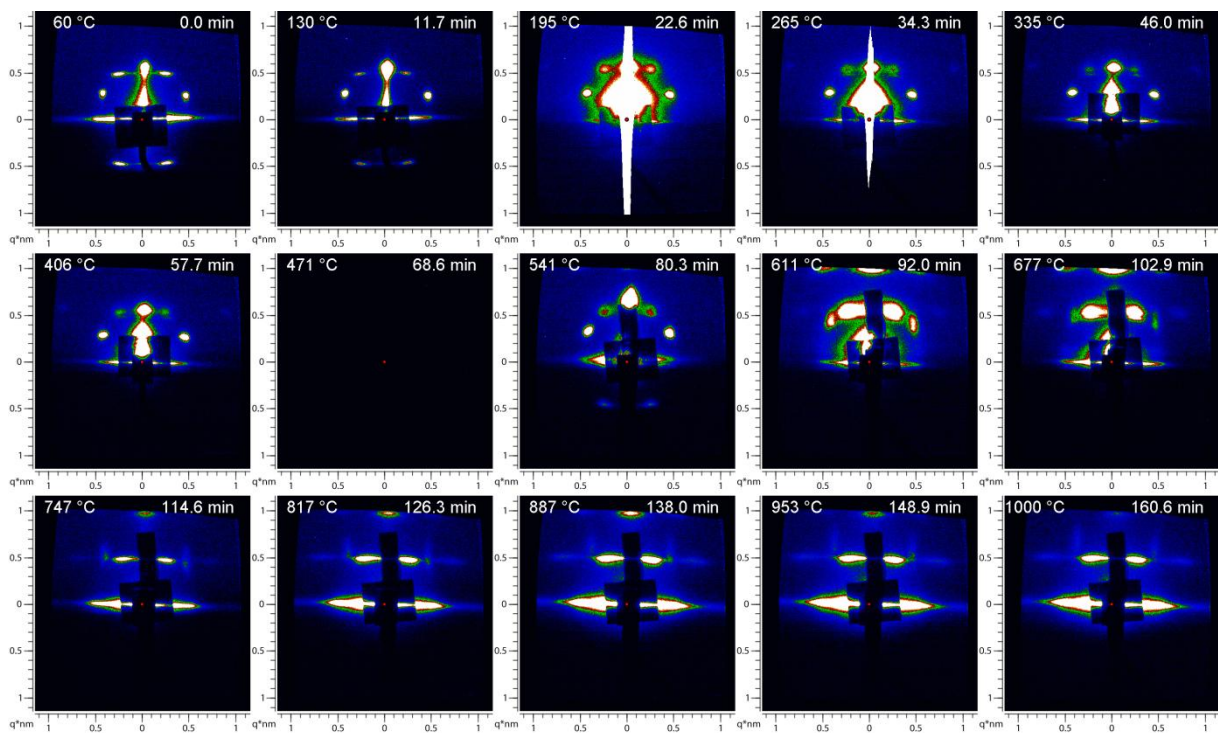


**Figure S9.22:** Carbonization of AAM-Hex-100: The overexposure is resulting from the strong intensity of diffuse scattering and reflections of the top layer which are then partially covered by additional absorbers. Those reflections are moving due to shrinkage and vanish

completely. In contrary, the reflections originated from the mesophase in the AAM pores do not shift; the shrinkage is restricted due to the confinement effect.

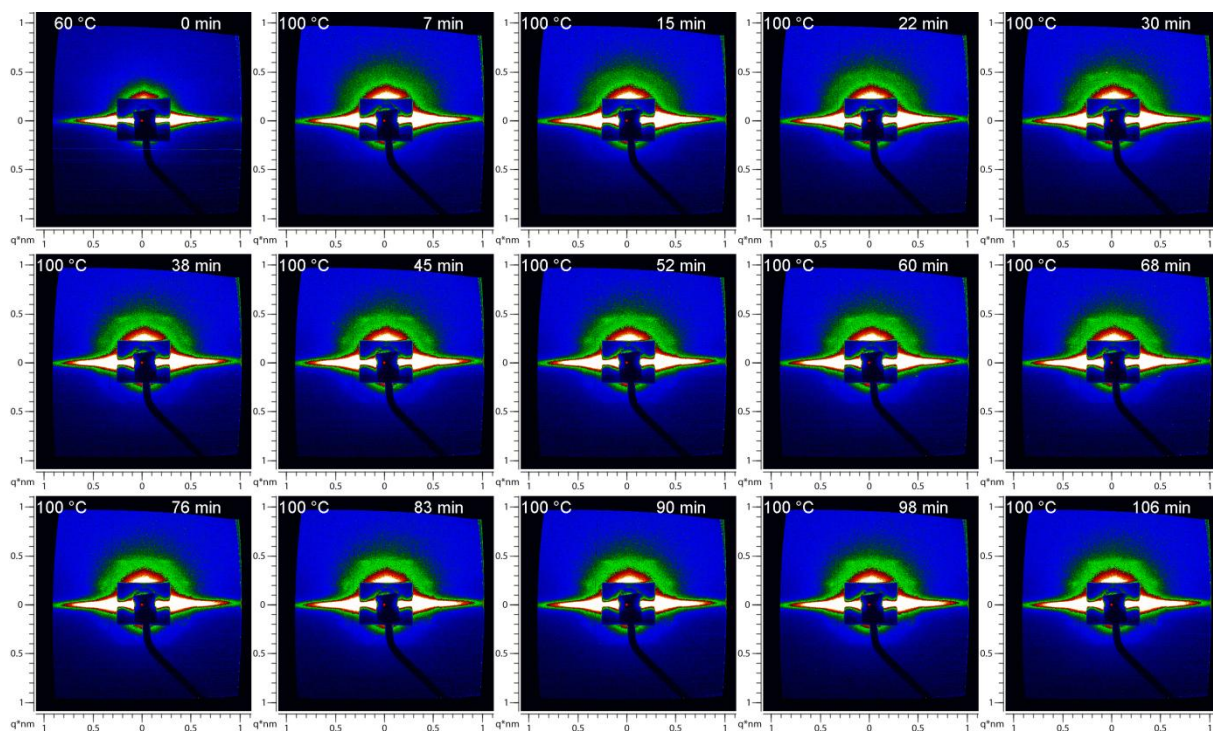


**Figure S9.23:** In-situ SAXS of AAM-Cub-100: Structure formation during thermopolymerization at 100 °C.

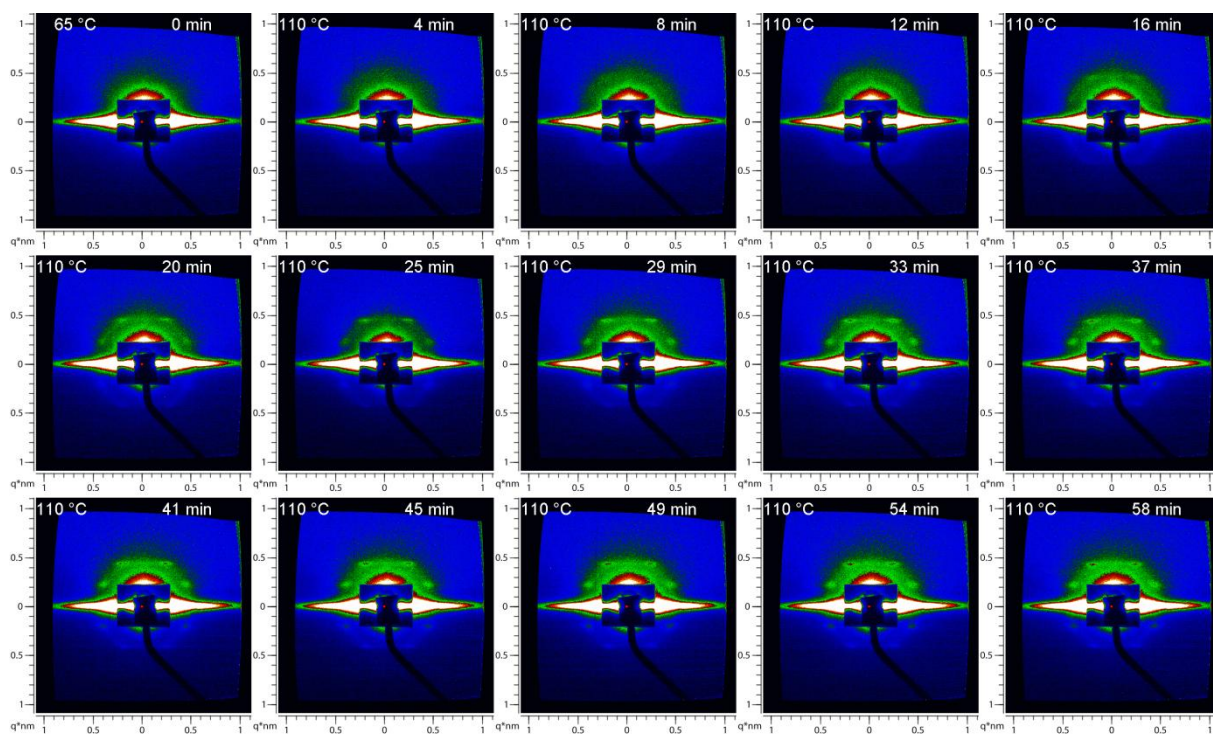


**Figure S9.24:** In-situ SAXS of AAM-Cub-110: Structure formation during thermopolymerization at 110 °C.

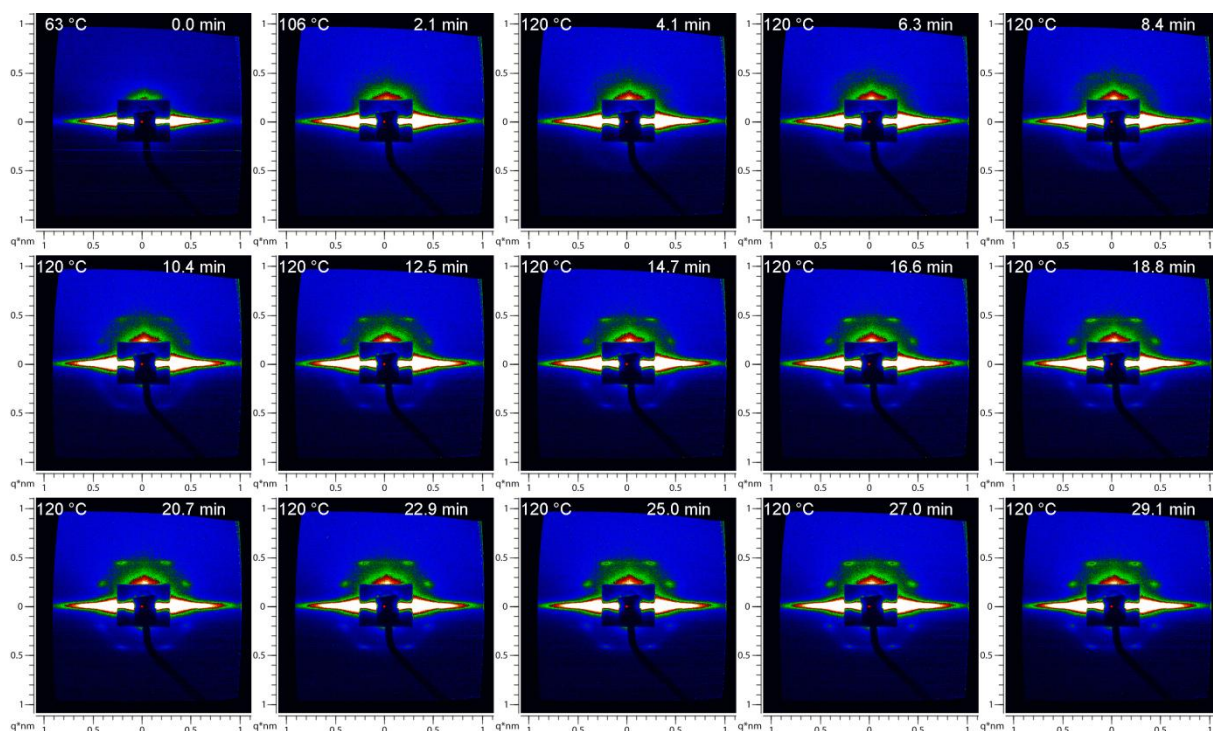


**Figure S9.25:** In-situ SAXS of AAM-Cub-120: Structure formation during thermopolymerization at 120 °C.

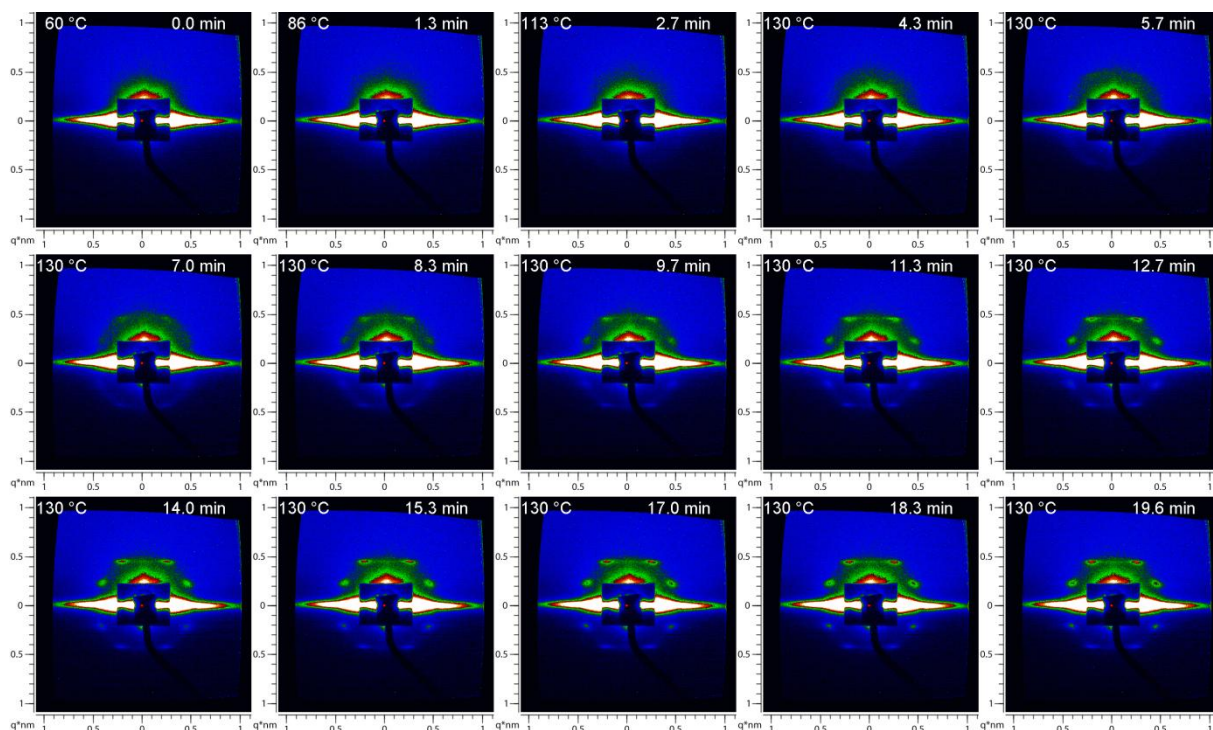


**Figure S9.26:** In-situ SAXS of AAM-Cub-130: Structure Formation during thermopolymerization at 130 °C.

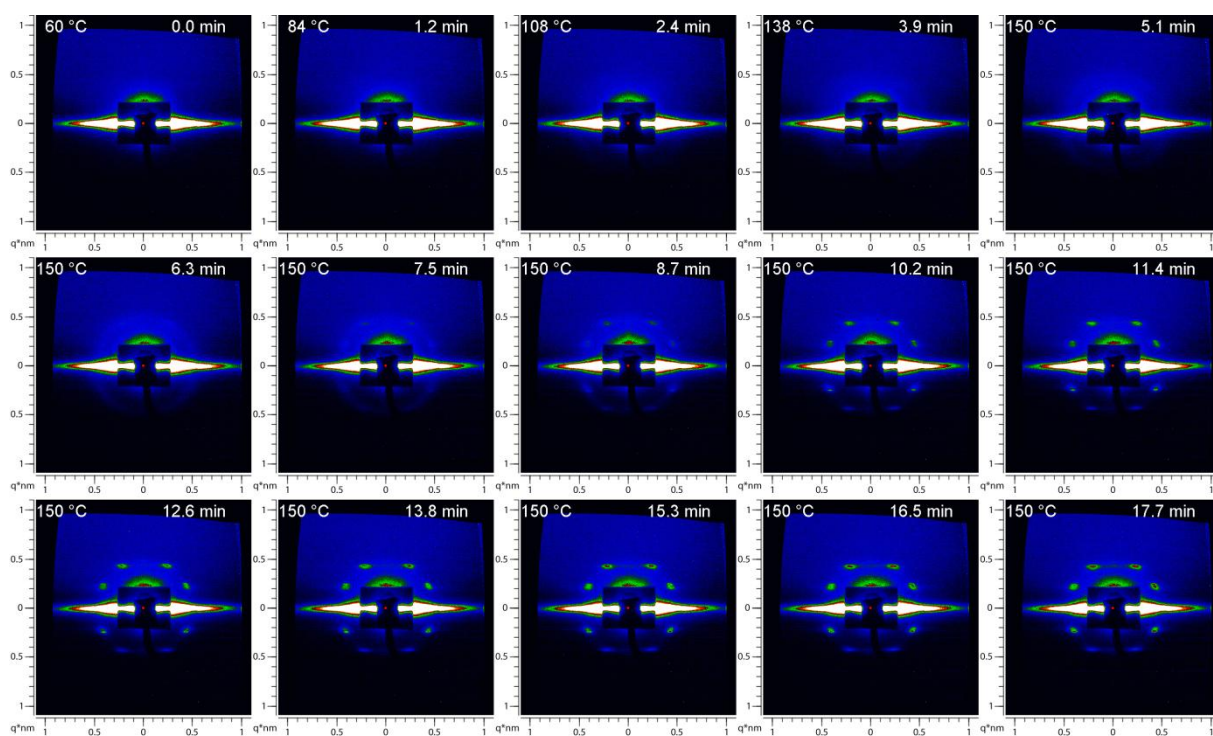


**Figure S9.27:** In-situ SAXS of AAM-Cub-150: Structure formation during thermopolymerization at 150 °C.

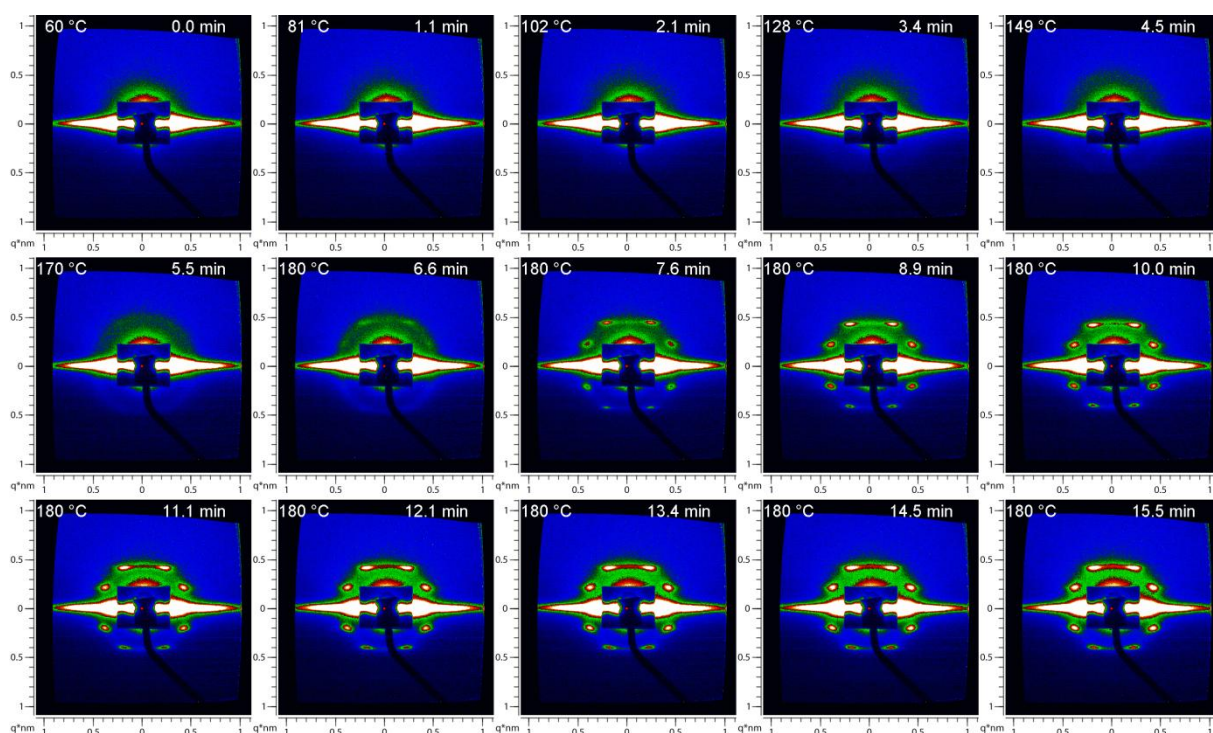


**Figure S9.28:** In-situ SAXS of AAM-Cub-180: Structure formation during thermopolymerization at 180 °C.

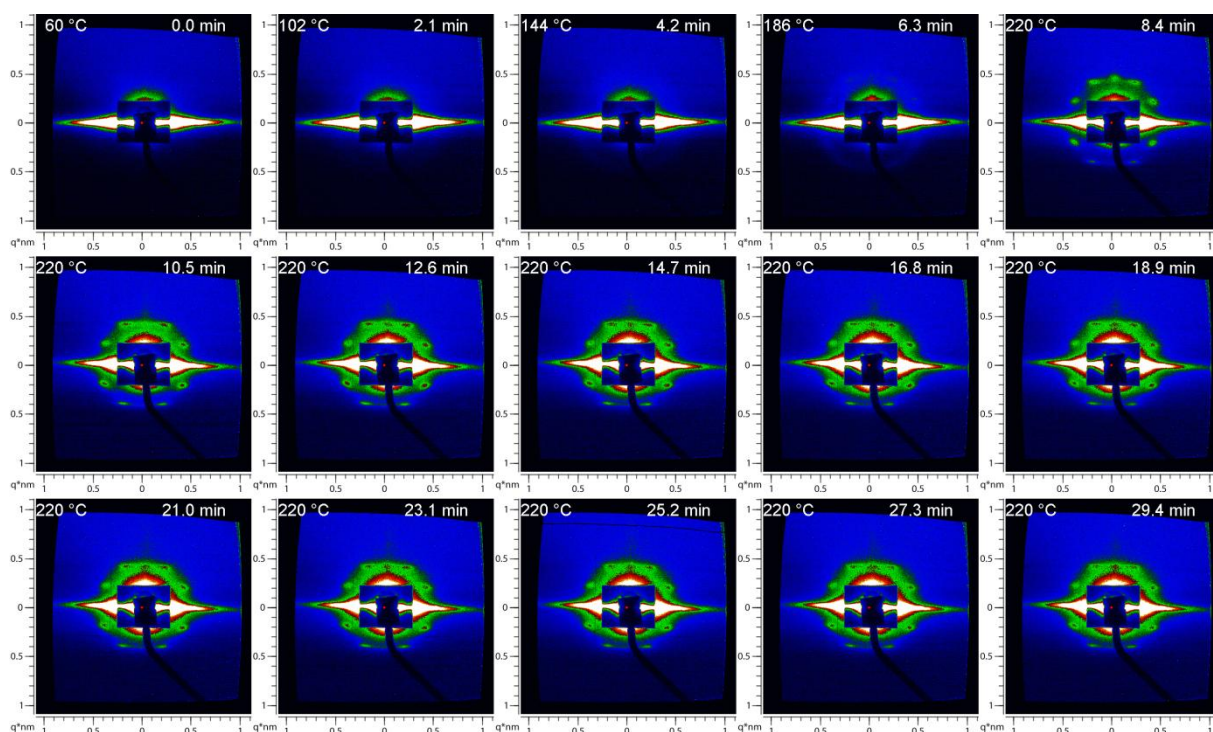


**Figure S9.29:** In-situ SAXS of AAM-Cub-220: Structure formation during thermopolymerization at 220 °C.

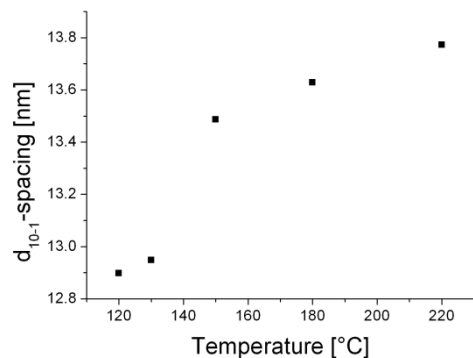


**Figure S9.30:**  $d_{10-1}$ -spacings after thermopolymerization for the samples AAM-Cub-T: increasing d-values for higher thermopolymerization temperatures. AAM-Cub-100 and AAM-Cub-110 were left out, due to the low intensities; the peak positions could therefore not be defined accurately.

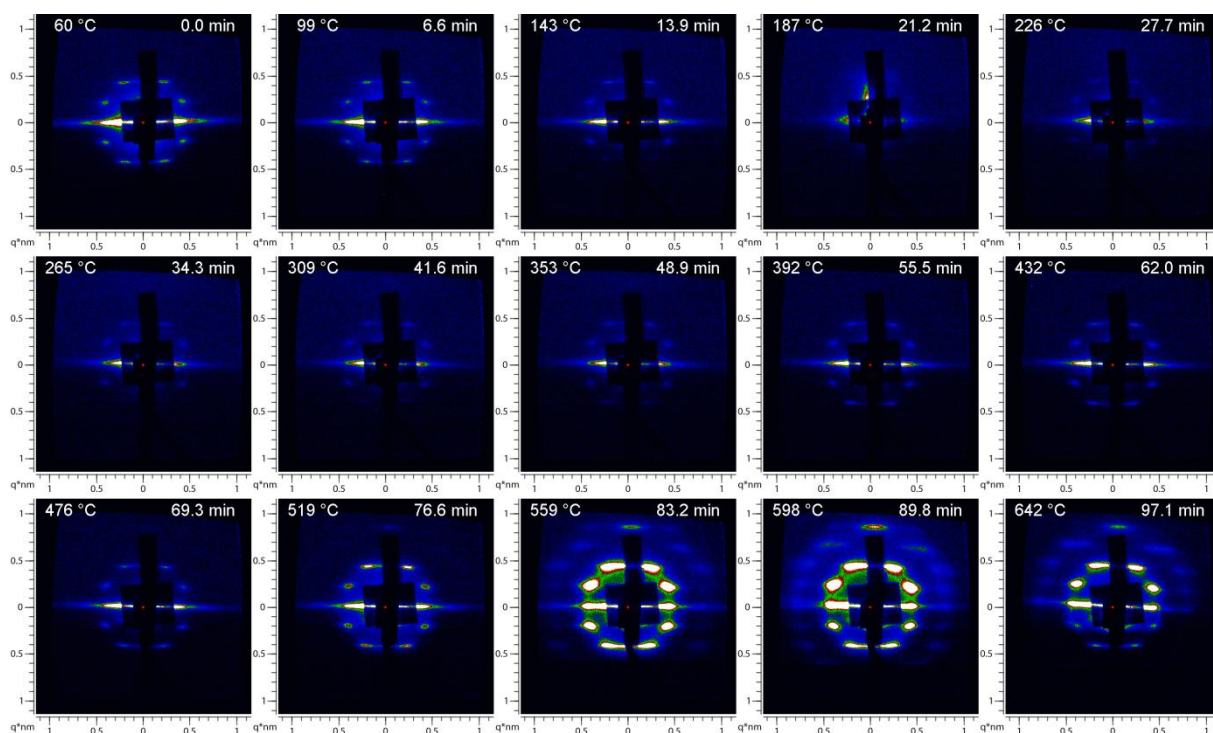


**Figure S9.31:** Carbonization of AAM-Hex-100: The reflections originated from the mesophase in the AAM pores do not shift; the shrinkage is restricted due to the confinement effect.



## 10. CURRICULUM VITAE

### Persönliche Daten

Name: Jörg David Schuster  
Geburtsdatum: 20. August 1981  
Geburtsort: Marktoberdorf  
Staatsangehörigkeit: deutsch

### Schule

09/88 – 08/92: St.-Martin Grundschule Marktoberdorf  
09/92 – 06/01: Gymnasium Marktoberdorf  
29.06.2001: *Abitur am Gymnasium Marktoberdorf*

### Studium und Promotion

10/2001 – 09/2004: Ludwig-Maximilians Universität München, Bachelorstudium Chemie und Biochemie  
03.09.2004: *Bachelor of Science (B.Sc.) Chemie und Biochemie*  
10/2004 – 06/2007: Ludwig-Maximilians Universität München, Masterstudium Chemie  
12/2006 – 06/2007: Master Arbeit an der LMU München bei Prof. Thomas Bein: „*Highly Ordered Mesoporous Phenolic Resins made by an Organic-Organic EISA Process as Films and in Anodic Alumina Membranes*“  
20.06.2007: *Master of Science (M.Sc.) Chemie*  
08/2007 – heute: Promotion an der LMU München bei Prof. Thomas Bein

### Sonstige Tätigkeiten

Seit 08/2007: Verantwortlicher wissenschaftlicher Angestellter für Ellipsometrie, Kleinwinkelröntgenbeugung (SAXS), Probenpräparation für

Transmissionselektronenmikroskopie (TEM), Infrarotspektroskopie (RA-IR), Spin-coater und Plasma-Reiniger

Seit 08/2007: Fachliche Anleitung und Ausbildung von Diplomanden und Studenten im Hauptstudium, Betreuung von Praktika in der Anorganischen und Physikalischen Chemie

### **Zusatzqualifikationen**

Sprachen: Deutsch (Muttersprache)  
Englisch (fließend)  
Französisch (Grundkenntnisse)

EDV: Microsoft Office (sehr gut)  
Adobe Illustrator und Photohop (gut)

## 11. LIST OF PUBLICATIONS AND PRESENTATIONS

### 11.1. Publications

1. Schuster, J.; Koehn, R.; Keilbach, A.; Doeblinger, M.; Amenitsch, H.; Bein, T., Two-Dimensional-Hexagonal Periodic Mesoporous Polymer Resin Thin Films by Soft Templating. *Chem. Mater.* **2009**, *21* (24), 5754-5762.
2. Schuster, J.; Keilbach, A.; Koehn, R.; Doeblinger, M.; Doerfler, T.; Dennenwaldt, T.; Bein, T., Cubic and Hexagonal Mesoporous Carbon in Pores of Anodic Alumina Membranes *Chem. Eur. J. In press.*
3. Schuster, J.; Keilbach, A.; Koehn, R.; Doeblinger, M.; Amenitsch, H.; Bein, T., In Situ SAXS Study on a New Mechanism for Mesostructure Formation of Ordered Mesoporous Carbons: Thermally-Induced Self-Assembly. *In preparation.*
4. Schuster, J.; He, G.; Nazar, L. F.; Bein, T., Large Pore Ordered Mesoporous Carbon Nanofibers with Extremely High Porosity for Lithium Sulfur Batteries. *In preparation.*
5. Schuster, J.; He, G.; Mandlmeier, B.; Nazar, L. F.; Bein, T., Spherical Ordered Mesoporous Carbon Nanoparticles with Uniform Particle Size and Extremely High Porosity for Lithium-Sulfur Batteries. *In preparation.*

### 11.2. Oral Presentations

1. Schuster, J.; Mandlmeier, B.; Keilbach, A.; Köhn, R.; Döblinger, M.; Amenitsch, H.; Dörfler, T.; Dennenwaldt, T.; Bein, T., Morphology-Control of Ordered Mesoporous

Carbons with Extremely High Porosity. 23. *Deutsche Zeolith-Tagung, Erlangen, Germany, 02.-04.03.2011.*

### 11.3. Poster Presentations

1. Schuster, J.; Keilbach, A.; Köhn, R.; Bein, T., Highly Ordered Mesoporous Thin Films Made of Phenolic Resin by an Organic-Organic EISA Process. *2nd International Symposium "Advanced micro- and mesoporous materials", Varna, Bulgaria, 06.-09.09.2007.*
2. Schuster, J.; Keilbach, A.; Döblinger, M.; Köhn, R.; Bein, T., Soft-Templating Method for Mesoporous Carbon Thin Films. *4th FEZA Conference, Paris, France, 02.-06.09.2008.*
3. Schuster, J.; Keilbach, A.; Döblinger, M.; Köhn, R.; Bein, T., Ordered Mesoporous Carbon in Confined Environments through Soft-Templating: Thin Films and Tubular Hosts. *21. Deutsche Zeolith-Tagung, Kiel, Germany, 04.-06.03.2009.*
4. Keilbach, A.; Schuster, J.; Platschek, B.; Petkov, N.; Bein, T., TP B8 –Ultradünne funktionale Nanodrähte für elektronische und optische Anwendungen. *Summarizing Workshop SFB 486 "Nanoman - Ten Years in a Nutshell" Venice, Italy, 16. 19.09.2009.*
5. Schuster, J.; Keilbach, A.; Döblinger, M.; Köhn, R.; Bein, T., Cubic and Hexagonal Mesoporous Carbon within the Pores of Anodic Aluminum Oxide Membranes. *22. Deutsche Zeolith-Tagung, Munich, Germany, 03.-05.03.2010.*
6. Schuster, J.; Köhn, R.; Keilbach, A.; Döblinger, M.; Amenitsch, H.; Bein, T., Thermally-Induced Mesostructure Formation of Polymer Resin-Surfactant Composites in

Confined Environments: An In-Situ GISAXS Study. *MRS Spring Meeting, San Francisco, USA, 05.-09.04.2010.*

7. Keilbach, A.; Schuster, J.; Li, Y.; Döblinger, M.; Bein, T., Periodic Mesoporous Organosilicas and Carbons in Confined Spaces. *16th International Zeolite Conference, Sorrento, Italy, 04.-07.07.2010.*

## 12. BIBLIOGRAPHY

1. <http://en.wikipedia.org/wiki/File:Diamond-and-graphite-with-scale.jpg>.
2. Dresselhaus, M.; Endo, M., Relation of Carbon Nanotubes to Other Carbon Materials. In *Carbon Nanotubes*, Dresselhaus, M.; Dresselhaus, G.; Avouris, P., Eds. Springer Berlin / Heidelberg: 2001; Vol. 80, pp 11-28.
3. [http://en.wikipedia.org/wiki/Carbon\\_nanotube](http://en.wikipedia.org/wiki/Carbon_nanotube).
4. Kroto, H. W.; Heath, J. R.; O'Brien, S. C.; Curl, R. F.; Smalley, R. E., *Nature* **1985**, *318* (6042), 162-163.
5. Geim, A. K.; Novoselov, K. S., *Nat Mater* **2007**, *6* (3), 183-191.
6. Liang, C.; Li, Z.; Dai, S., *Angew. Chem., Int. Ed.* **2008**, *47* (20), 3696-3717.
7. Wan, Y.; Shi, Y.; Zhao, D., *Chem. Mater.* **2008**, *20* (3), 932-945.
8. Chang, H.; Joo, S. H.; Pak, C., *J. Mater. Chem.* **2007**, *17* (30), 3078-3088.
9. Wu, C.-G.; Bein, T., *Science* **1994**, *266* (5187), 1013-15.
10. Ryoo, R.; Joo, S. H.; Jun, S., *J. Phys. Chem. B* **1999**, *103* (37), 7743-7746.
11. Lee, J.; Yoon, S.; Hyeon, T.; Oh, S. M.; Kim, K. B., *Chem. Commun.* **1999**, (21), 2177-2178.
12. Jun, S.; Joo, S. H.; Ryoo, R.; Kruk, M.; Jaroniec, M.; Liu, Z.; Ohsuna, T.; Terasaki, O., *J. Am. Chem. Soc.* **2000**, *122* (43), 10712-10713.
13. Kruk, M.; Jaroniec, M.; Kim, T.-W.; Ryoo, R., *Chem. Mater.* **2003**, *15* (14), 2815-2823.

14. Xing, W.; Bai, P.; Li, Z. F.; Yu, R. J.; Yan, Z. F.; Lu, G. Q.; Lu, L. M., *Electrochim. Acta* **2006**, *51* (22), 4626-4633.
15. Li, Z.; Dai, S., *Chem. Mater.* **2005**, *17* (7), 1717-1721.
16. Bazula, P. A.; Lu, A.-H.; Nitz, J.-J.; Schueth, F., *Microporous Mesoporous Mater.* **2008**, *108* (1-3), 266-275.
17. Wang, X.; Liu, R.; Waje, M. M.; Chen, Z.; Yan, Y.; Bozhilov, K. N.; Feng, P., *Chem. Mater.* **2007**, *19* (10), 2395-2397.
18. Vinu, A.; Hossian, K. Z.; Srinivasu, P.; Miyahara, M.; Anandan, S.; Gokulakrishnan, N.; Mori, T.; Ariga, K.; Balasubramanian, V. V., *J. Mater. Chem.* **2007**, *17* (18), 1819-1825.
19. Moriguchi, I.; Ozono, A.; Mikuriya, K.; Teraoka, Y.; Kagawa, S.; Kodama, M., *Chem. Lett.* **1999**, (11), 1171-1172.
20. Thurn-Albrecht, T.; DeRouchey, J.; Russell, T. P.; Jaeger, H. M., *Macromolecules* **2000**, *33* (9), 3250-3253.
21. Liang, C.; Hong, K.; Guiochon, G. A.; Mays, J. W.; Dai, S., *Angew. Chem., Int. Ed.* **2004**, *43* (43), 5785-5789.
22. Meng, Y.; Gu, D.; Zhang, F.; Shi, Y.; Cheng, L.; Feng, D.; Wu, Z.; Chen, Z.; Wan, Y.; Stein, A.; Zhao, D., *Chem. Mater.* **2006**, *18* (18), 4447-4464.
23. Liu, R.; Shi, Y.; Wan, Y.; Meng, Y.; Zhang, F.; Gu, D.; Chen, Z.; Tu, B.; Zhao, D., *J. Am. Chem. Soc.* **2006**, *128* (35), 11652-11662.
24. Zheng, M.; Ji, G.; Wang, Y.; Cao, J.; Feng, S.; Liao, L.; Du, Q.; Zhang, L.; Ling, Z.; Liu, J.; Yu, T.; Cao, J.; Tao, J., *Chem. Commun.* **2009**, (33), 5033-5035.
25. Schuster, J.; Keilbach, A.; Koehn, R.; Doeblinger, M.; Doerfler, T.; Dennenwaldt, T.; Bein, T., *Chem. Eur. J. In press.*

26. Schuster, J.; Koehn, R.; Keilbach, A.; Doeblinger, M.; Amenitsch, H.; Bein, T., *Chem. Mater.* **2009**, *21* (24), 5754-5762.
27. Song, L.; Feng, D.; Fredin, N. J.; Yager, K. G.; Jones, R. L.; Wu, Q.; Zhao, D.; Vogt, B. D., *ACS Nano* **2009**, *4* (1), 189-198.
28. Tanaka, S.; Katayama, Y.; Tate, M. P.; Hillhouse, H. W.; Miyake, Y., *J. Mater. Chem.* **2007**, *17* (34), 3639-3645.
29. Brinker, C. J.; Lu, Y.; Sellinger, A.; Fan, H., *Adv. Mater.* **1999**, *11* (7), 579-585.
30. Smarsly, B.; Grosso, D.; Brezesinski, T.; Pinna, N.; Boissière, C.; Antonietti, M.; Sanchez, C., *Chem. Mater.* **2004**, *16* (15), 2948-2952.
31. Song, L.; Feng, D.; Campbell, C. G.; Gu, D.; Forster, A. M.; Yager, K. G.; Fredin, N.; Lee, H.-J.; Jones, R. L.; Zhao, D.; Vogt, B. D., *J. Mater. Chem.* **2010**, *20* (9), 1691-1701.
32. Steinhart, M.; Liang, C.; Lynn, G. W.; Goesele, U.; Dai, S., *Chem. Mater.* **2007**, *19* (10), 2383-2385.
33. Wang, K.; Zhang, W.; Phelan, R.; Morris, M. A.; Holmes, J. D., *J. Am. Chem. Soc.* **2007**, *129* (44), 13388-13389.
34. Zheng, M.; Cao, J.; Ke, X.; Ji, G.; Chen, Y.; Shen, K.; Tao, J., *Carbon* **2007**, *45* (5), 1111-1113.
35. Liu, H.-J.; Wang, X.-M.; Cui, W.-J.; Dou, Y.-Q.; Zhao, D.-Y.; Xia, Y.-Y., *J. Mater. Chem.* **2010**, *20* (20), 4223-4230.
36. Peng, M.; Li, D.; Shen, L.; Chen, Y.; Zheng, Q.; Wang, H., *Langmuir* **2006**, *22* (22), 9368-9374.
37. Kim, C.; Ngoc, B. T. N.; Yang, K. S.; Kojima, M.; Kim, Y. A.; Kim, Y. J.; Endo, M.; Yang, S. C., *Adv. Mater.* **2007**, *19* (17), 2341-2346.

38. Im, J. S.; Jang, J.-S.; Lee, Y.-S., *Journal of Industrial and Engineering Chemistry* **2009**, *15* (6), 914-918.
39. Wang, Z.; Li, F.; Stein, A., *Nano Letters* **2007**, *7* (10), 3223-3226.
40. Yan, Y.; Zhang, F.; Meng, Y.; Tu, B.; Zhao, D., *Chem. Commun.* **2007**, (27), 2867-2869.
41. Tonanon, N.; Intarapanya, W.; Tanthapanichakoon, W.; Nishihara, H.; Mukai, S.; Tamon, H., *Journal of Porous Materials* **2008**, *15* (3), 265-270.
42. Kim, T.-W.; Chung, P.-W.; Slowing, I. I.; Tsunoda, M.; Yeung, E. S.; Lin, V. S. Y., *Nano Letters* **2008**, *8* (11), 3724-3727.
43. Liu, H.-J.; Cui, W.-J.; Jin, L.-H.; Wang, C.-X.; Xia, Y.-Y., *J. Mater. Chem.* **2009**, *19* (22), 3661-3667.
44. Fang, Y.; Gu, D.; Zou, Y.; Wu, Z.; Li, F.; Che, R.; Deng, Y.; Tu, B.; Zhao, D., *Angew. Chem.* **2010**, *122* (43), 8159-8163.
45. Lei, Z.; Christov, N.; Zhang, L. L.; Zhao, X. S., *J. Mater. Chem.* **2011**, *21* (7), 2274-2281.
46. Ji, X.; Nazar, L. F., *J. Mater. Chem.* **2010**, *20* (44), 9821-9826.
47. Ji, X.; Lee, K. T.; Nazar, L. F., *Nat Mater* **2009**, *8* (6), 500-506.
48. Kiessig, H., *Ann. Phys.* **1931**, *10*, 715-68.
49. Kiessig, H., *Ann. Phys.* **1931**, *10*, 769-788.
50. Patterson, A. L., *Physical Review* **1939**, *56* (10), 978.
51. Müller-Buschbaum, P., Structure Determination in Thin Film Geometry Using Grazing Incidence Small-Angle Scattering. In *Polymer Surfaces and Interfaces*, Stamm, M., Ed. Springer Berlin Heidelberg: 2008; pp 17-46.
52. Yoneda, Y., *Physical Review* **1963**, *131* (5), 2010.
53. Vineyard, G. H., *Physical Review B* **1982**, *26* (8), 4146.

54. Goodhew, P. J.; Humphreys, J.; Beanland, R., *Electron microscopy and analysis*. 3rd ed. ed.; Taylor & Francis: London, 1988.
55. Williams, D. B.; Carter, C. B., *Transmission electron microscopy : a textbook for materials science : I : basics*. Plenum: New York, 1996.
56. [http://en.wikipedia.org/wiki/File:Scheme\\_TEM\\_en.svg](http://en.wikipedia.org/wiki/File:Scheme_TEM_en.svg).
57. <http://www.ncbi.nlm.nih.gov/books/NBK21629/>.
58. Sing, K. S. W.; Everett, D. H.; Haul, R. A. W.; Moscou, L.; Pierotti, R. A.; Rouquerol, J.; Siemieniewska, T., *Pure Appl. Chem.* **1985**, *57* (4), 603-619.
59. <http://www.tcd.ie/Physics/Surfaces/ellipsometry2.php>.
60. Pang, J.; Li, X.; Wang, D.; Wu, Z.; John, V. T.; Yang, Z.; Lu, Y., *Adv. Mater.* **2004**, *16* (11), 884-886.
61. Wang, X.; Liang, C.; Dai, S., *Langmuir* **2008**, *24* (14), 7500-7505.
62. Lu, A.-H.; Spliethoff, B.; Schueth, F., *Chem. Mater.* **2008**, *20* (16), 5314-5319.
63. Kataoka, S.; Yamamoto, T.; Inagi, Y.; Endo, A.; Nakaiwa, M.; Ohmori, T., *Carbon* **2008**, *46* (10), 1358-1360.
64. Gibaud, A.; Grosso, D.; Smarsly, B.; Baptiste, A.; Bardeau, J. F.; Babonneau, F.; Doshi, D. A.; Chen, Z.; Brinker, C. J.; Sanchez, C., *J. Phys. Chem. B* **2003**, *107* (25), 6114-6118.
65. Smarsly, B.; Gibaud, A.; Ruland, W.; Sturmayer, D.; Brinker, C. J., *Langmuir* **2005**, *21* (9), 3858-3866.
66. Trick, K. A.; Saliba, T. E., *Carbon* **1995**, *33* (11), 1509-15.
67. Ferrari, A. C.; Robertson, J., *Phys. Rev. B* **2000**, *61* (20), 14095-14107.
68. Yang, Z.; Niu, Z.; Cao, X.; Yang, Z.; Lu, Y.; Hu, Z.; Han, C. C., *Angew. Chem., Int. Ed.* **2003**, *42* (35), 4201-4203.

69. Yamaguchi, A.; Uejo, F.; Yoda, T.; Uchida, T.; Tanamura, Y.; Yamashita, T.; Teramae, N., *Nature Materials* **2004**, *3* (5), 337-341.
70. Platschek, B.; Petkov, N.; Bein, T., *Angew. Chem., Int. Ed.* **2006**, *45* (7), 1134-1138.
71. Platschek, B.; Petkov, N.; Himsl, D.; Zimdars, S.; Li, Z.; Koehn, R.; Bein, T., *J. Am. Chem. Soc.* **2008**, *130* (51), 17362-17371.
72. Platschek, B.; Koehn, R.; Doeblinger, M.; Bein, T., *Langmuir* **2008**, *24* (9), 5018-5023.
73. Keilbach, A.; Doeblinger, M.; Koehn, R.; Amenitsch, H.; Bein, T., *Chemistry--A European Journal* **2009**, *15* (27), 6645-6650, S6645/1-S6645/3.
74. Wang, K.; Birjukovs, P.; Erts, D.; Phelan, R.; Morris, M. A.; Zhou, H.; Holmes, J. D., *J. Mater. Chem.* **2009**, *19* (9), 1331-1338.
75. Tanaka, S.; Doi, A.; Nakatani, N.; Katayama, Y.; Miyake, Y., *Carbon* **2009**, *47* (11), 2688-2698.
76. Cott, D. J.; Petkov, N.; Morris, M. A.; Platschek, B.; Bein, T.; Holmes, J. D., *J. Am. Chem. Soc.* **2006**, *128* (12), 3920-3921.
77. Grosso, D.; Babonneau, F.; Albouy, P.-A.; Amenitsch, H.; Balkenende, A. R.; Brunet-Bruneau, A.; Rivory, J., *Chem. Mater.* **2002**, *14* (2), 931-939.
78. Falcaro, P.; Grosso, D.; Amenitsch, H.; Innocenzi, P., *J. Phys. Chem. B* **2004**, *108* (30), 10942-10948.
79. Geranmayeh, S.; Abbasi, A.; Badiei, A., *E-J. Chem.* **2011**, *8* (1), 196-200.
80. Ghiorso, M.; Carmichael, I.; Moret, L., *Contrib. Mineral. Petrol.* **1979**, *68* (3), 307-323.
81. Tucker, M. G.; Keen, D. A.; Dove, M. T., *Mineral. Mag.* **2001**, *65* (4), 489-507.
82. Tate, M. P.; Urade, V. N.; Kowalski, J. D.; Wei, T.-c.; Hamilton, B. D.; Eggiman, B. W.; Hillhouse, H. W., *J. Phys. Chem. B* **2006**, *110* (20), 9882-9892.

83. Watanabe, R.; Iyoda, T.; Yamada, T.; Yoshida, H., *Journal of Thermal Analysis and Calorimetry* **2006**, 85 (3), 713-717.
84. Holland, B. T.; Blanford, C. F.; Stein, A., *Science* **1998**, 281 (5376), 538-540.